Observations of multiple order parameters in 5f electron systems

Elizabeth Blackburn

▶ **To cite this version:**

Elizabeth Blackburn. Observations of multiple order parameters in 5f electron systems. Condensed Matter [cond-mat]. Université Joseph-Fourier - Grenoble I, 2005. English. NNT : . tel-00011842

HAL Id: tel-00011842
https://theses.hal.science/tel-00011842

Submitted on 8 Mar 2006

HAL is a multi-disciplinary open access archive for the deposit and dissemination of scientific research documents, whether they are published or not. The documents may come from teaching and research institutions in France or abroad, or from public or private research centers.

L'archive ouverte pluridisciplinaire **HAL**, est destinée au dépôt et à la diffusion de documents scientifiques de niveau recherche, publiés ou non, émanant des établissements d'enseignement et de recherche français ou étrangers, des laboratoires publics ou privés.

Université Joseph Fourier – Grenoble I
Ecole Doctorale de Physique

T H E S E

pour obtenir le titre de
Docteur en Sciences
de l'Université Joseph Fourier – Grenoble I

Spécialité : Physique

présentée et soutenue par

Elizabeth BLACKBURN

Observations de paramètres d'ordre multiples dans les systèmes d'électrons 5*f*

Observations of multiple order parameters in 5*f* electron systems

soutenue le 16 décembre 2005

Jury :

M.	Louis-Pierre REGNAULT	Président de jury
M.	Jean-Michel MIGNOT	Rapporteur
M.	Brian RAINFORD	Rapporteur
M.	Nicholas BERNHOEFT	Examinateur
M.	Arno HIESS	Examinateur
M.	Timothy ZIMAN	Directeur de thèse

Thèse préparée à l'Institut Max von Laue-Paul Langevin, Grenoble.

Please purchase PDF Split-Merge on www.verypdf.com to remove this watermark.

Acknowledgements

First and foremost, I would like to thank my parents, Linda and Peter Blackburn, for their constant support and encouragement. Without them, I would not be where I am today.

I would also like to thank my supervisors for all of their help and patience during the preparation of this work: Nick Bernhoeft, for his careful explanations and advice; Gerry Lander, for his support and continual interest; Arno Hiess, for introducing me to neutron scattering and three-axis spectrometers, and Tim Ziman, for his time, effort and friendly ear.

Je tiens à exprimer mes remerciements aux membres de mon jury, en particulier Louis-Pierre Regnault pour m'avoir fait l'honneur de présider, et Jean-Michel Mignot et Brian Rainford d'avoir accepté d'être les rapporteurs.

During the preparation of this thesis, I have had the good fortune to work with many wonderful people, and I am most grateful for their help. This group includes Roberto Caciuffo (Università Politecnica delle Marche), Paolo Santini, Nicola Magnani, Giuseppe Amoretti (Università di Parma), Jane Brown, Mechthild Enderle, Garry McIntyre, Serge Million, Jean-Louis Ragazzoni, Maikel Rheinstädter, Fred Thomas (Institut Laue-Langevin), Pascal Boulet, Eric Colineau, Pavel Javorský, Peter Normile (Institute for Transuranium Elements), Stuart Wilkins, Carsten Detlefs, Pascale Deen, Luigi Paolosini (European Synchrotron Radiation Facility), Mike Walker (University of Toronto), Fanni Juranyi, Andrew Podlesnyak (Paul Scherrer Institute) and Wolfgang Häussler (FRM-II, Munich), amongst many others. I would particularly like to thank all of the staff at the ITU Karlsruhe for their assistance and support.

Je voudrais également remercier tout le monde à l'ILL pour m'avoir accueillie si chaleureusement, en particulier les thèsards de l'ILL, sans lesquels mon temps à Grenoble aurait été beaucoup moins drôle, en particulier Sonia Francoual, Clara Gonzalez, Alexander Grünwald, Blanka Janoušová, Martin Kempa, Lola Ruiz-Martin et Katy Wood.

Je remercie Laurence Tellier et François Sammartino pour avoir corrigés mon français. Les fautes restantes n'appartiennent qu'à moi seule.

Finally, I would like to thank the European Commission for its generous support in the framework of the 'Training and Mobility of Researchers' programme, without which I would not have had the opportunity to study abroad, and the Directors of the Institut Laue-Langevin for their hospitality.

Please purchase PDF Split-Merge on www.verypdf.com to remove this watermark.

Please purchase PDF Split-Merge on www.verypdf.com to remove this watermark.

Contents

Please purchase PDF Split-Merge on www.verypdf.com to remove this watermark.

Please purchase PDF Split-Merge on www.verypdf.com to remove this watermark.

Please purchase PDF Split-Merge on www.verypdf.com to remove this watermark.

Please purchase PDF Split-Merge on www.verypdf.com to remove this watermark.

Chapter 1

Introduction

Please purchase PDF Split-Merge on www.verypdf.com to remove this watermark.

1.1 General introduction

This thesis looks at the coexistence of different types of order generated by the same electronic system. Obviously, different forms of order are often found together, e.g. magnetic order on a crystalline lattice, but in such cases the types of order are often considered, to the first approximation, to come from different parts of the system and do not always interact (e.g. incommensurate magnetic order in itinerant electron systems), although often the symmetry requirements of the two types of order constrain each other. When more than one type of order is generated by the same components, a higher degree of correlation is to be expected.

Before going further, the definition of order needs to be clarified. An ordered state is defined by its *order parameter*. This quantity is zero in the disordered state and finite in the ordered state. The transition may be first- or second-order. In a ferromagnet, the order parameter is the macroscopic magnetization per unit volume, which is easily measured. In a superconductor, the order parameter is the complex energy gap function - a far more abstract concept.

In this thesis, multiple order parameters originating in the same electronic system are studied. Prototype multiple order parameter systems are the so-called multi-$\boldsymbol{k}$ magnetic structures where more than one propagation, or $\boldsymbol{k}$, wavevector is observed in the same volume. Two different 3-$\boldsymbol{k}$ structures are studied here. More complicated examples include the coexistence of magnetism and superconductivity, two phenomena that are often thought to be antagonistic. In the example considered here, UPd_2Al_3, the two behaviours develop from the same strongly correlated electron system.

The samples chosen are all $5f$ electron systems; a brief introduction to the physics of $5f$ electron systems is given next. The experimental probe of choice was the neutron and so some information on some of the main neutron scattering techniques used is given in Chapter 2. After this introductory material, the main work is split into three parts.

The **first part**, Chapter 3, is an inelastic neutron scattering investigation of the 3-$\boldsymbol{k}$ structure of UO_2. Full polarization analysis is used to study the spin-wave spectrum of this material, to investigate the effects of a 3-$\boldsymbol{k}$ static structure on the spin-wave fluctuations.

The **second part**, Chapters 4 and 5, covers diffraction studies of the uranium monopnictide-chalcogenide solid solutions. These uranium rocksalts show many varied types of multi-$\boldsymbol{k}$ magnetic order. In the 3-$\boldsymbol{k}$ phase of three such solid solutions, diffraction peaks are seen at unexpected points in reciprocal space. A possible explanation as to the origin of these peaks is presented, using a formalism based on geometric algebra (also known as Clifford algebra).

The **third part**, Chapter 6, looks at the antiferromagnet superconductor UPd_2Al_3 using inelastic neutron scattering. The effect of an external applied magnetic field on both the normal and superconducting states is studied. In addition, the high-resolution neutron spin-echo technique is used to determine the low-energy inelastic response to greater precision than previously managed.

Please purchase PDF Split-Merge on www.verypdf.com to remove this watermark.

Introduction générale

Cette thèse considère la coexistence de plusieurs types d'ordre. Évidemment les types d'ordre différents sont souvent remarqués en parallèle (par exemple l'ordre magnétique sur un réseau cristallin). Le développement de l'ordre impose des restrictions sur les symétries dans le matériau. Les symétries imposées par les ordres différents doivent être résolues. Si les ordres différents sont crées par les mêmes constituants, le degré de corrélation doit être plus grand, et c'est cette question qui sera traitée ici.

D'abord, la définition du paramètre d'ordre doit être examiné. Un état ordonné est défini par son paramètre d'ordre. Cette quantité est zéro dans l'état désordonné, et fini dans l'état ordonné. La transition peut être de première ou deuxième classe. Dans un matériau ferromagnétique, le paramètre d'ordre est l'aimantation dans un volume défini. Ce n'est pas difficile à mesurer. Dans un état supraconducteur, le paramètre d'ordre est le gap d'énergie - une idée beaucoup plus abstraite.

Ici, on étudie les paramètres d'ordre venant du même système électronique. Les systèmes modèles sont les structures magnétiques, appelées multi-$\boldsymbol{k}$, où $\boldsymbol{k}$ signifie le vecteur de propagation dans l'espace réciproque décrivant l'ordre. Un tel système est caractérisé par l'observation de plusieurs vecteurs dans le même volume. Un autre exemple est la coexistence de l'ordre magnétique et la supraconductivité. Normalement, ces deux phénomènes sont considérés comme antagonistes, mais dans UPd_2Al_3 ils se développent dans le même système électronique.

Pour étudier ces effets, les composés contenant les électrons $5f$ sont un choix évident, à cause de la grande variété dans les états magnétiques qu'on trouve dedans. Une introduction brève décrivant les systèmes d'électrons $5f$ est donné. La plupart des investigations présentées ici étaient faites en utilisant les neutrons comme sonde, donc le deuxième chapitre est un exposé sur les techniques utilisées. Le travail principal est décrit en trois parties.

La **première partie**, Chapitre 3, présente une investigation par la diffusion neutronique inélastique de la structure 3-$\boldsymbol{k}$ d'UO_2. Les neutrons polarisés étaient utilisés pour examiner les ondes de spin dans ce composé. L'état 3-$\boldsymbol{k}$ a un effet sur les fluctuations qui est nettement différent à ce qu'on observera dans, par exemple, l'état 1-$\boldsymbol{k}$.

La **deuxième partie**, Chapitres 4 et 5, présente une investigation par la diffraction des solutions solides U(As,Se) et U(Sb,Te). Ces solutions sont antiferromagnétiques, avec la structure NaCl. Plusieurs types d'ordre multi-$\boldsymbol{k}$ ont été vus dans la littérature. Cette partie concerne la phase 3-$\boldsymbol{k}$, où on constate l'apparition de pics de diffraction à des endroits imprévus dans l'espace réciproque. Une explication est développée dans le Chapitre 5, en utilisant l'algèbre géométrique (aussi appelé l'algèbre de Clifford).

La **troisième partie**, Chapitre 6, considère le supraconducteur antiferromagnétique UPd_2Al_3. L'effet d'un champ magnétique externe sur l'état normal et supraconducteur est présenté, sondée par la diffusion neutronique inélastique. Une étude de la réponse de basse énergie en prenant avantage de la résolution disponible avec le technique de la diffusion spin-echo est également présentée.

Please purchase PDF Split-Merge on www.verypdf.com to remove this watermark.

1.2 Uranium compounds

The actinides are one of the series in the periodic table. Each actinide atom consists of a radon-like core with 3 to 17 external electrons filling the outer $5f$, $6d$ and $7s$ shells. The ground states for the actinide atoms have been determined by atomic spectroscopy. The $7s$ shell is always filled, and as we move across the series, the $5f$ shell fills. For the lighter actinides, one or two electrons may be present in the $6d$ shell. The ground states are given in Figure 1.1.

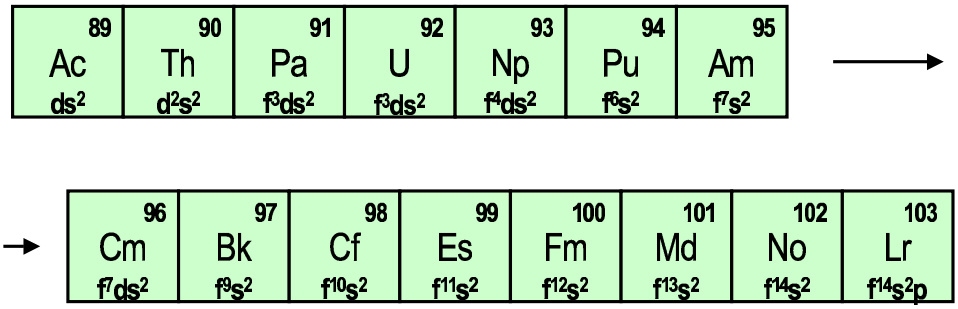

Figure 1.1: The actinide series, with the outer shell electrons labelled.

As the $5f$ shell is filled, the series does not mimic the behaviour of the $4f$ series, as was originally expected. Study of a variety of material properties, for example the atomic volume of the pure element, indicate two regimes. The light actinides (Ac-Pu) display a similar behaviour to the d transition metal series, but from Am onwards the system acts like the $4f$ lanthanides. The light actinides form a $5f$ transition series, and the heavy actinides a lanthanide-type series. This is the first indication of the strange behaviour of the $5f$ electrons.

In the lanthanides, the $4f$ electrons are localized, and can be treated as atomic electrons. This is not the case for $5f$ electrons, which are partially extended. In the metallic elements the $5f$ shells overlap, leading to the creation of $5f$ bands across the material. This is similar to the behaviour of d band transition metals. In addition, the $6d$ and $7s$ bands are close in energy and so can be expected to hybridize with the $5f$ band, creating a complex conduction band. Interestingly, for Am onwards, the overlapping is very small, if present at all, giving a good grounding to the idea that there are 'light' and 'heavy' parts of the $5f$ series.

From all of this, we can conclude that in actinide compounds, the extension of the $5f$ shell is very important in determining the electronic properties of the material, and that hybridisation of the neighbouring shells also plays an important role. The local environment of the actinide ion is therefore extremely important, and this fragility explains the wide range of different electronic behaviour observed in uranium-based compounds, ranging from highly localized moment systems (e.g. UO_2) to extended heavy fermion systems (UPt_3). This thesis concentrates on these two extremes, in particular localized multi-$\boldsymbol{k}$ structures, and the more metallic, heavy fermion compound UPd_2Al_3. A brief introduction to these two conditions is now given.

Please purchase PDF Split-Merge on www.verypdf.com to remove this watermark.

1.3 Multi-$\boldsymbol{k}$ structures

Ferromagnets and coplanar magnetic structures (e.g. Néel antiferromagnets and helical magnetic structures) can be described by an on-site term

$$\mathcal{M}_{\boldsymbol{k}_\alpha} = \mathbf{M}_{\boldsymbol{k}_\alpha} \exp(i\theta_{\boldsymbol{k}_\alpha}), \tag{1.1}$$

where $\mathbf{M}_{\boldsymbol{k}_\alpha}$ is the polarization vector (related to the magnitude of the magnetic moment) and $\theta_{\boldsymbol{k}_\alpha} = \mathbf{k}_\alpha.\mathbf{r}_i + \theta_\alpha$ is the relative phase at the i^{th} position. Such magnetic configurations are fully described by one polarization vector and one propagation vector, $\boldsymbol{k}_\alpha$, and are nominated single-$\boldsymbol{k}$ magnetic structures. In this manner, $\mathcal{M}_{\boldsymbol{k}_\alpha}$ is an order parameter, as long as more than one site is considered. For a ferromagnet $\boldsymbol{k} = 0$; in the ordered state all of the on-site terms point in the same direction.

The discovery by Kouvel and Kasper [1] of neutron diffraction patterns from Fe-Mn alloys that cannot be interpreted within this paradigm led to the proposal of multi-$\boldsymbol{k}$ configurations as a natural expansion of the single-$\boldsymbol{k}$ case. These intricate, non-collinear magnetic structures may be described by the simultaneous presence of more than one polarization and associated propagation vector at a given site. For example, a configuration is deemed 2-$\boldsymbol{k}$ when, for a given reciprocal lattice vector τ, a single domain yields magnetic Bragg peaks corresponding with two (orthogonal) wavevectors.[1] In this scheme, a 2-$\boldsymbol{k}$ configuration is defined by two (orthogonal) simultaneous on-site terms, $\mathcal{M}_{\boldsymbol{k}_\alpha} = \mathbf{M}_{\boldsymbol{k}_\alpha} \exp(i\theta_{\boldsymbol{k}_\alpha})$ and $\mathcal{M}_{\boldsymbol{k}_\beta} = \mathbf{M}_{\boldsymbol{k}_\beta} \exp(i\theta_{\boldsymbol{k}_\beta})$, and therefore two independent order parameters.

In practice, the existence of domains in high symmetry structures [3] often makes it impossible to distinguish neutron diffraction peaks generated by a polydomain single-$\boldsymbol{k}$ structure from those generated by a multi-$\boldsymbol{k}$ configuration. Indirect evidence is required to support the hypothesis of a multi-$\boldsymbol{k}$ structure. This can include magnetization data favouring a moment direction different to that required for the single-$\boldsymbol{k}$ structure [4], or, in a cubic material, the absence of an observable lattice distortion [1].

This is no substitute for direct, microscopic, information, as obtained by neutron scattering. Aid in resolving this problem is available through the application of uniaxial magnetic fields or stresses to perturb the domain population, and hence the magnitude of particular magnetic diffraction Bragg peaks. However, the perturbation may well bring about a transition from one magnetic state to another, and so neutron diffraction appears to be limited as a diagnostic tool.

To aid in the identification and understanding of multi-$\boldsymbol{k}$ states, this thesis presents two alternative studies of triple-$\boldsymbol{k}$ states, using inelastic and elastic techniques, in cubic fcc materials.

1.3.1 The stability of multi-k structures

First of all, a justification for the existence of multi-$\boldsymbol{k}$ structures on free energy grounds is given. Consider a cubic fcc magnetic structure. A spin density wave can be used to

[1] A non-orthogonal basis set can also be used; an example is the magnetic structure of neodymium [2].

Please purchase PDF Split-Merge on www.verypdf.com to remove this watermark.

describe the magnetic order. The observed quantity is

$$M(\mathbf{r}) = \mathcal{M}_{\boldsymbol{k}_\alpha} + \mathcal{M}^*_{\boldsymbol{k}_\alpha} = \mathbf{M}_{\boldsymbol{k}_\alpha} \mathrm{e}^{i(\mathbf{k}_\alpha.\mathbf{r}_i+\theta_\alpha)} + \mathbf{M}^*_{\boldsymbol{k}_\alpha} \mathrm{e}^{-i(\mathbf{k}_\alpha.\mathbf{r}_i+\theta_\alpha)} \tag{1.2}$$

where $\boldsymbol{k}$ is the propagation vector. As the magnetic moments are constrained to lie on the lattice sites, $\boldsymbol{r}_i$ must be the lattice vector for site i. In a cubic material, spin density waves along equivalent symmetry directions must have the same energy; otherwise, the cube would distort along the favoured direction. Wavevectors that are symmetry equivalent are said to belong to same star of $\{\boldsymbol{k}\}$. As a direct example, no energetic difference is expected for waves with $\boldsymbol{k} = \boldsymbol{k}_\alpha$ where $\alpha = x, y, z$. To see this, consider

$$\boldsymbol{k}_x = \frac{2\pi}{a}(\frac{1}{2}, 0, 0); \quad \boldsymbol{k}_y = \frac{2\pi}{a}(0, \frac{1}{2}, 0); \quad \boldsymbol{k}_z = \frac{2\pi}{a}(0, 0, \frac{1}{2}). \tag{1.3}$$

Using the Landau free-energy expansion, the free energy of a system can be written as a power series in terms of the order parameter. In the general case, where η represents the order parameter

$$\Phi(T, k) = \Phi_0 + a(T, k)\eta^2 + b(T, k)\eta^4 + ... \tag{1.4}$$

No odd-power terms are permitted, as the phase terms do not balance.[2]

For the spin density wave, the appropriate order parameter is given by Equation 1.1. The observed quantity is formed by considering this and its complex conjugate. As we are working in a crystal lattice, the free energy must be translationally invariant under the operation $\boldsymbol{r}_i \rightarrow \boldsymbol{r}_i - \boldsymbol{R}_n$ where $\boldsymbol{R}_n$ is a lattice vector.

In a multi-$\boldsymbol{k}$ state more than one spin density wave exist in the same volume simultaneously. The $\boldsymbol{k}_\alpha$ are drawn from the star of $\{\boldsymbol{k}\}$ (e.g. Equation 1.3). To investigate the difference between single-$\boldsymbol{k}$ and multi-$\boldsymbol{k}$ states, the simplest free energy expression involving the co-existence of more than one order parameter is

$$\begin{aligned} \Phi - \Phi_0 \quad = \quad & \sum_\alpha A(k_\alpha, T)(\mathcal{M}_{\boldsymbol{k}_\alpha} \cdot \mathcal{M}^*_{\boldsymbol{k}_\alpha}) + B_1 \sum_\alpha (\mathcal{M}_{\boldsymbol{k}_\alpha} \cdot \mathcal{M}^*_{\boldsymbol{k}_\alpha})^2 \\ & + B_2 \sum_{\alpha \neq \beta} (\mathcal{M}_{\boldsymbol{k}_\alpha} \cdot \mathcal{M}^*_{\boldsymbol{k}_\alpha})(\mathcal{M}_{\boldsymbol{k}_\beta} \cdot \mathcal{M}^*_{\boldsymbol{k}_\beta}) \end{aligned} \tag{1.5}$$

where $A(k_\alpha, T)$ is a function of the temperature and the magnitude of $\boldsymbol{k}_\alpha$. The B_n terms are assumed to be temperature independent.

For a single-$\boldsymbol{k}$ material, there is only one $\boldsymbol{k}_\alpha$ in a given volume, and so

$$(\Phi - \Phi_0)_{1-k} = A(k_\alpha, T)|\mathbf{M}_{\boldsymbol{k}_\alpha}|^2 + B_1|\mathbf{M}_{\boldsymbol{k}_\alpha}|^4. \tag{1.6}$$

Minimizing this with respect to $|\mathbf{M}_{\boldsymbol{k}_x}|^2$ results in the expression $|\mathbf{M}_{\boldsymbol{k}_x}|^2 = -A(k_x, T)/2B_1$. This can only be a stable minimum if B_1 is positive. This analysis shows that $|\mathbf{M}_{\boldsymbol{k}_x}|^2 \propto A(k_x, T)$. In the simplest approximation $A(k_x, T)$ is linear with respect to T, and so has the form $(T - T_N)$ where T_N is the order-disorder transition temperature. This means that adding a temperature dependence to the B parameters would be equivalent to adding sixth-order terms to the free energy, which can usually be safely neglected.

[2]The case of an external magnetic field is not considered here

Please purchase PDF Split-Merge on www.verypdf.com to remove this watermark.

In this given volume of single-$\boldsymbol{k}$ material, $|\mathbf{M}_{\boldsymbol{k}_y}|^2 = |\mathbf{M}_{\boldsymbol{k}_z}|^2 = 0$. Now suppose that the three order parameters exist in the same volume simultaneously (the triple-$\boldsymbol{k}$ condition). As discussed above, we assume that $|\mathbf{M}_{\boldsymbol{k}_x}|^2 = |\mathbf{M}_{\boldsymbol{k}_y}|^2 = |\mathbf{M}_{\boldsymbol{k}_z}|^2 = |\mathbf{M}|^2$ to maintain cubic symmetry.

$$(\Phi - \Phi_0)_{3-k} = 3A(k,T)|\mathbf{M}|^2 + 3B_1|\mathbf{M}|^4 + 3B_2|\mathbf{M}|^4. \tag{1.7}$$

Experimentally, it is impossible to distinguish between the single- and triple-$\boldsymbol{k}$ states by looking at the individual order parameters. The free energy from the uncoupled terms must therefore be the same. This requires that $|\mathbf{M}_{3-k}|^2 = |\mathbf{M}_{1-k}|^2/3$. For the triple-$\boldsymbol{k}$ state to be energetically favourable, $B_2 < 0$. Otherwise, a new value for $|\mathbf{M}|^2$ can always be found that will be give rise to a lower free energy for the single-$\boldsymbol{k}$ state than the triple-$\boldsymbol{k}$ state.

With this restriction in mind, the free energy can be minimized with respect to $|\mathbf{M}|^2$, giving $|\mathbf{M}|^2 = -A(k,T)/2(B_1 + B_2)$. This is a stable energy minimum if $(B_1 + B_2) > 0$. This restricts B_2 to the range $-B_1 < B_2 < 0$.

A similar analysis can be applied to a double-$\boldsymbol{k}$ state, this time with $|\mathbf{M}_{2-k}|^2 = |\mathbf{M}_{1-k}|^2/2$. This will, as for the triple-$\boldsymbol{k}$ state, only be energetically favourable if $B_2 < 0$. However, in this case, a triple-$\boldsymbol{k}$ state must always be favourable. Higher-order terms are needed to stabilize a double-$\boldsymbol{k}$ state.

2-$\boldsymbol{k}$ vs 3-$\boldsymbol{k}$ structures

As noted above, to fourth order the 3-$\boldsymbol{k}$ state is always preferred to the 2-$\boldsymbol{k}$ state. One sixth-order term that would distinguish between 3- and 2-$\boldsymbol{k}$ states has the form

$$C_2|\mathbf{M}_{\boldsymbol{k}_x}|^2|\mathbf{M}_{\boldsymbol{k}_y}|^2|\mathbf{M}_{\boldsymbol{k}_z}|^2 \tag{1.8}$$

which is only non-zero if the three spin density waves exist in the same volume. If $C_2 < 0$ this always favours a 3-$\boldsymbol{k}$ state, but $C_2 > 0$ may favour a lower-$\boldsymbol{k}$ state. This is not guaranteed as the sixth-order term is proportional to $(T - T_N)^3$, and so has a much smaller effect than the fourth order terms.

Assuming that $|\mathbf{M}|^2$ remains constant on going from the 3-$\boldsymbol{k}$ to the 2-$\boldsymbol{k}$ state the free energy difference is

$$\Phi_{3-\boldsymbol{k}} - \Phi_{2-\boldsymbol{k}} = 3B_2|\mathbf{M}|^4 + C_2|\mathbf{M}|^6 - 2B_2|\mathbf{M}|^4. \tag{1.9}$$

The 2-$\boldsymbol{k}$ state has lower energy if $C > -\frac{B_2}{|S|^2}$. $|\mathbf{M}|^2$ is proportional to $(T_N - T)$, and so near T_N, this condition is unlikely to be fulfilled, but as the temperature decreases, the system may find it energetically favourable to switch to the 2-$\boldsymbol{k}$ state. The exact crossover point depends strongly on the coefficients. This is illustrated in Figure 1.2.

1.3.2 Transverse and longitudinal structures

The direction of the polarization vector $\mathbf{M}_{\boldsymbol{k}_\alpha}$ (i.e. magnetic moment direction) is not necessarily related to the direction of the propagation vector $\boldsymbol{k}_\alpha$. In this thesis, cubic fcc antiferromagnets are studied. The magnetic moment is observed to be either parallel to

Please purchase PDF Split-Merge on www.verypdf.com to remove this watermark.

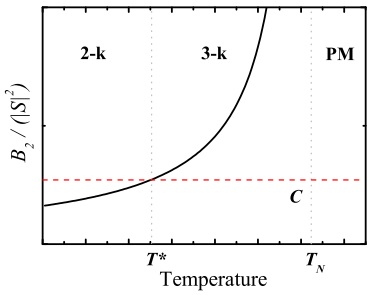

Figure 1.2: $-\frac{B_2}{|S|^2}$ versus temperature, where $|S|^2 = (T - T_N)$. C is a temperature independent coefficient (black line). C is represented by the horizontal red line. When $C = -\frac{B_2}{|S|^2}$ the 2-$\boldsymbol{k}$ $\rightarrow$ 3-$\boldsymbol{k}$ transition takes place at T^*. The two transitions are denoted by grey lines. The magnetic phase is noted; PM signifies paramagnetic.

the propagation vector (longitudinal) or perpendicular (transverse). For a 3-$\boldsymbol{k}$ magnetic structure in a cubic fcc material all of the components are present in the same volume at the same time, so there can be no magnetic K domains. However, there are three S domains: one longitudinal and two transverse structures. From the nature of the compound, the longitudinal or transverse orientation may be favoured according to the exact electronic environment. In the transverse case, the two transverse options will be degenerate. The difference between the three S domains corresponds to a re-ordering of the moments in the chemical unit cell, and is illustrated in Figure 1.3 using a 2D projection.

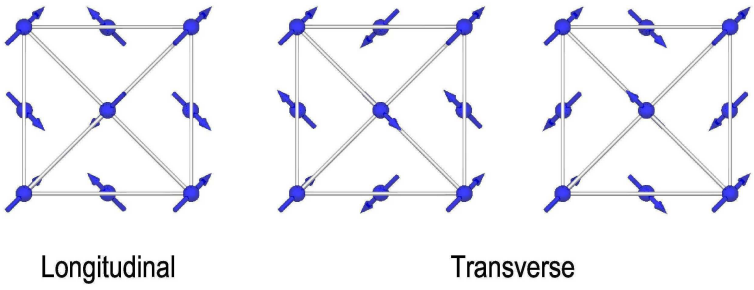

Figure 1.3: 2-D projections of longitudinal and transverse S domains of triple-$\boldsymbol{k}$ structures where $\boldsymbol{k} = \langle 001 \rangle$. Courtesy of Stuart B. Wilkins.

Please purchase PDF Split-Merge on www.verypdf.com to remove this watermark.

1.4 Heavy fermions

1.4.1 Introduction

To explain the conduction properties of metals, the itinerant electron model was developed. In this model, the electrons can move freely throughout the metal: electron bands form that extend across the sample. The transport properties of many normal metals are successfully described by the Sommerfeld model, which assumes that the electrons do not interact with each other. This is a Fermi gas, by analogy with an ideal gas. As electrons are fermions with half-integral spin, they must obey the Pauli exclusion principle; two electrons cannot have the same quantum numbers. In practice, the electrons fill up the available states. When all of the electrons are accounted for, the energy of the sample is the chemical potential, or the Fermi energy ϵ_F at $T = 0$ K.

Excitations from this ground state are limited to those electrons within $k_B T$ of the Fermi energy. This vastly reduces the number of excitations that can develop, and accounts for the reduced electronic heat capacities that were originally such a surprise in metals. The heat capacity for such a Fermi gas is linear with temperature, $C = \gamma T$, where γ is the Sommerfeld coefficient, which represents the electronic density of states at E_F.

If the electrons are forced to evolve in a periodic potential (a reasonable approximation of a lattice) the electrons may now be retarded or accelerated by the periodic potential. This can lead to an effective mass different to that of the nominal electron mass. If more complicated materials are to be described, further steps have to be taken to include the interactions in the system. To do this, Landau Fermi liquid theory is often used.

1.4.2 The Landau Fermi-liquid theory

The Sommerfeld free electron model has been successfully applied to many simple metals, but if interactions between the electrons are present, the situation becomes more complicated. Landau developed the Fermi-liquid theory to attack this problem. A one-to-one correspondence between the states of the perfect Fermi gas and the Fermi liquid is assumed. This is realized by adiabatically turning on the interactions. The Fermi liquid (and its interactions) are defined by a set of elementary excitations that possess the same spin and charge properties as the bare fermions. This is necessary as there is no 'symmetry breaking' in the adiabatic introduction of the interactions. (This means that superconductivity cannot be developed as an extension of Fermi-liquid theory.) These excitations, or *quasiparticles*, exist close to the Fermi surface, and their lifetime decreases dramatically away from the Fermi energy. The excitations of the Fermi liquid are close to those of a Fermi gas. Although the interactions may be strong, the excitations can be described as weakly interacting quasiparticles. To first order, the difference manifests as a renormalization of the particle mass, as the interactions affect the particle motion. In a Fermi liquid, the mean free time between interactions for a quasiparticle is proportional to T^{-2}, and so the resistivity ρ should have a component proportional to T^2 as the resistivity is determined by the number of collisions breaking up the flow of charged particles.

Please purchase PDF Split-Merge on www.verypdf.com to remove this watermark.

This is the most common test for a Fermi liquid, but as the constant of proportionality is determined by the effective mass, this effect is usually only visible for compounds with a large electron mass renormalization. For other transport properties, further corrections are required, often in the form of a so-called Stoner factor. These corrections are determined by the exact nature of the quasiparticle.

1.4.3 Heavy fermions

This renormalization is the origin behind the name *heavy fermion*. The observation of an apparent heavy fermion indicates that the system is strongly correlated. In fact, the name heavy fermion is usually reserved for Ce- or U-compounds, where the f electrons in the Ce- and U-compounds interact strongly with the conduction electrons at low temperatures, increasing the effective mass by one or two orders of magnitude. Examples include $CeCu_6$ and UBe_{13}. Other materials often have strongly correlated electron systems (e.g. transition metal oxides), however.

These materials may also order: antiferromagnetic order arises due to instabilities of the Fermi surface to particular antiferromagnetic wavevectors (e.g. UCu_5). Superconductivity has also been observed, and appears to involve the heavy fermions (e.g. $CeCu_2Si_2$).

All of the materials quoted above can be described in the Fermi liquid picture; however as interactions increase, it may no longer be possible to maintain the adiabatic connection between bare fermions and quasiparticles. This is suspected to be case for the 'non-Fermi-liquid' materials, such as $UCu_{5-x}Pd_x$, where the resistivity does not follow a T^2 dependence.

Please purchase PDF Split-Merge on www.verypdf.com to remove this watermark.

Chapter 2

Neutron Scattering

Please purchase PDF Split-Merge on www.verypdf.com to remove this watermark.

Sommaire

La diffusion neutronique est une sonde puissante des corrélations spatio-temporelle dans la matière condensée. Elle est particulièrement douée pour l'étude de l'aimantation, grâce au moment magnétique dont le neutron est doté. Ce moment rend le neutron sensible aux champs magnétiques dans un échantillon.

Dans ce chapitre, des méthodes mathématiques pour traiter la diffusion neutronique nucléaire et magnétique sont présentées, et les effets particuliers à un faisceau polarisé sont également donnés. Le processus suit cela de Squires [5] et Lovesey [6].

Deux techniques développées pour profiter des effets d'un faisceau polarisé sont présentées :

1) la polarimétrie sphérique neutronique, dans laquelle on peut contrôler l'état de polarisation du faisceau avant et après l'événement diffusif. Cela donne accès à des résultats dans lesquels on peut voir l'interférence entre les effets nucléaires et magnétiques, et aussi entre les effets magnétiques d'origines diverses.

2) le ≪spin-echo≫, dans lequel la polarisation des neutrons est utilisée pour porter l'information sur le transfert d'énergie entre le neutron et l'échantillon. Cela permet la résolution spatiale et énergétique d'être separée, ce qui n'est pas normalement le cas avec la diffusion neutronique. Ainsi, une résolution supérieure est achevée.

Please purchase PDF Split-Merge on www.verypdf.com to remove this watermark.

2.1 Introduction

Neutron scattering is a powerful probe of space-time correlations in condensed matter. In particular, since the neutron carries a magnetic moment, it is sensitive to the magnetic field distribution in the sample. This technique has long been exploited in studies of magnetic materials.

Here, the neutron scattering cross-section for both nuclear and magnetic scattering will be developed. The effects of using a polarized neutron beam will then be discussed, along with a description of the main techniques for polarizing neutrons and exploiting polarized neutrons. This approach follows those of Squires [5] and Lovesey [6].

2.2 The neutron scattering cross-section

The neutron is a spin-1/2 particle with a magnetic moment of $-9.65 \cdot 10^{-27}$ JT^{-1}. It interacts weakly with nuclei (via the strong force) and magnetic fields (electromagnetic interaction), and so gives rise to weak scattering, which is well described by first order perturbation theory (the Born approximation). The quantity measured is the *partial differential cross-section*: the number of scattered particles within a given energy and solid angle range. For a neutron scattered by a potential V, this is:

$$\frac{\mathrm{d}^2\sigma}{\mathrm{d}\omega\mathrm{d}\Omega} = \frac{k'}{k}\left(\frac{m}{2\pi\hbar^2}\right)^2 \sum_{\lambda,s} p_\lambda p_s \sum_{\lambda',s'} |\langle \boldsymbol{k}' s' \lambda' | \hat{V} | \boldsymbol{k} s \lambda \rangle|^2 \delta(E_\lambda - E_{\lambda'} + \hbar\omega) \tag{2.1}$$

k (k') is the incident (scattered) wavevector, s (s') is the incident (scattered) neutron spin state, λ (λ') is the state of the sample before (after) scattering, m is the mass of the neutron, E_i is the energy of state i, p_i is the occupation probability of state i, and ω is the energy transferred from neutron to sample in the scattering process. $\hat{V}$ is the operator corresponding to the scattering potential.

To derive this equation, consider a plane wave $\psi_{\boldsymbol{k}} = |\psi_{\boldsymbol{k}}|\exp(-i\boldsymbol{k}.\boldsymbol{r})$ of neutrons in a spin state s. This wave is incident on a sample in state λ, and is scattered to wavevector $\boldsymbol{k}'$ and spin state s', whilst the sample state goes to λ'. The differential cross-section, or the number of scattered particles within a given solid angle range $\mathrm{d}\Omega$, is therefore

$$\left(\frac{\mathrm{d}\sigma}{\mathrm{d}\Omega}\right)_{\lambda\to\lambda'} = \frac{1}{\Phi}\frac{1}{\mathrm{d}\Omega}\sum_{\boldsymbol{k}'} W_{\boldsymbol{k},s,\lambda\to\boldsymbol{k}',s',\lambda'} \tag{2.2}$$

where Φ is the flux of incident neutrons and $W_{\boldsymbol{k},\lambda\to\boldsymbol{k}',\lambda'}$ is the number of transitions per second from the joint state $\{\boldsymbol{k},\lambda\}$ to state $\{\boldsymbol{k}',\lambda'\}$.

To evaluate the transition rate, Fermi's golden rule is applied:

$$\sum_{\boldsymbol{k}'} W_{\boldsymbol{k},\lambda\to\boldsymbol{k}',\lambda'} = \frac{2\pi}{\hbar}\rho_{\boldsymbol{k}'}|\langle \boldsymbol{k}' s' \lambda' | \hat{V} | \boldsymbol{k} s \lambda \rangle|^2. \tag{2.3}$$

$\rho_{\boldsymbol{k}'}$ is the number of momentum states in $\mathrm{d}\Omega$ per unit energy range for neutrons in the state $\boldsymbol{k}'$.

Please purchase PDF Split-Merge on www.verypdf.com to remove this watermark.

Evaluating the density of states $\rho_{\boldsymbol{k}'}$

Suppose that the neutron-sample scattering system is contained in a box of volume V. The neutron plane waves are obliged to be periodic within this box, and so only a discrete set of $\boldsymbol{k}$ wavevectors are possible, although this set of points may be extremely dense. These wavevectors form a lattice in momentum space, with a unit cell volume

$$v_k = \frac{(2\pi)^3}{V}. \tag{2.4}$$

The quantity $\rho_{\boldsymbol{k}'}\mathrm{d}E'$ is, by definition, the number of states in $\mathrm{d}\Omega$ with energy between E' and $\mathrm{d}E'$. This corresponds to the number of wavevector points in the volume $k'^2\mathrm{d}k'\mathrm{d}\Omega$, so

$$\rho_{\boldsymbol{k}'}\mathrm{d}E' = \frac{1}{v_k}k'^2\mathrm{d}k'\mathrm{d}\Omega \tag{2.5}$$

Since $E' = \frac{\hbar^2 k'^2}{2m}$, $\mathrm{d}E' = \frac{\hbar^2}{m}k'\mathrm{d}k'$, and

$$\rho_{\boldsymbol{k}'} = \frac{1}{v_k}k'\frac{m}{\hbar^2}\mathrm{d}\Omega \tag{2.6}$$

The differential cross-section

In the scattering case, we assume that only one neutron is involved at any one time in the scattering event, and so the neutron density is $1/V$. The neutron wavefunction is therefore $\psi_{\boldsymbol{k}} = \frac{1}{\sqrt{V}}\exp(-i\boldsymbol{k}.\boldsymbol{r})$.

Using this normalised form in the matrix element of Fermi's golden rule pulls $1/V^2$ outside the matrix element, such that

$$\sum_{\boldsymbol{k}'} W_{\boldsymbol{k},\lambda\to\boldsymbol{k}',\lambda'} = \frac{2\pi}{\hbar}\frac{1}{v_k}k'\frac{m}{\hbar^2}\mathrm{d}\Omega\frac{1}{V^2}|\langle\boldsymbol{k}'s'\lambda'|\hat{V}|\boldsymbol{k}s\lambda\rangle|^2 \tag{2.7}$$

where the $\boldsymbol{k}$ variable inside the matrix element is now normalised to unity.

The flux of incident neutrons is the product of the density and the velocity, $\Phi = \hbar k/Vm$, and so the differential cross-section is

$$\begin{aligned}\left(\frac{\mathrm{d}\sigma}{\mathrm{d}\Omega}\right) &= \frac{Vm}{\hbar k}\frac{1}{\mathrm{d}\Omega}\frac{2\pi}{\hbar}\frac{V}{(2\pi)^3}k'\frac{m}{\hbar^2}\mathrm{d}\Omega\frac{1}{V^2}|\langle\boldsymbol{k}'s'\lambda'|\hat{V}|\boldsymbol{k}s\lambda\rangle|^2 \\ &= \frac{k'}{k}\frac{m}{2\pi\hbar^2}|\langle\boldsymbol{k}'s'\lambda'|\hat{V}|\boldsymbol{k}s\lambda\rangle|^2.\end{aligned} \tag{2.8}$$

The partial differential cross-section

To evaluate the energy dependence, energy must be conserved, and so, if E and E' refer to the neutron energy, and E_λ and $E_{\lambda'}$ to the sample state, $E + E_\lambda = E' + E_{\lambda'}$. The energy distribution of the scattered neutrons is given by a δ-function, i.e.

$$\int \delta(E_\lambda - E_{\lambda'} + E - E')\mathrm{d}E' = 1. \tag{2.9}$$

Please purchase PDF Split-Merge on www.verypdf.com to remove this watermark.

Using the definition of the differential cross-section

$$\left(\frac{\mathrm{d}\sigma}{\mathrm{d}\Omega}\right) = \int_0^\infty \left(\frac{\mathrm{d}^2\sigma}{\mathrm{d}\Omega \mathrm{d}E'}\right) \mathrm{d}E' \tag{2.10}$$

and taking into account the occupation factors of the sample states and neutron spin states, Equation 2.1 is obtained.

2.3 Polarized neutron scattering

Let us consider the effect of $\hat{V}$ on the neutron spin. It does nothing unless the potential is coupled to the neutron spin. As an example, consider a system of aligned nuclear spins. The scattering length will be different if the neutron spin is parallel or anti-parallel to the nuclear spins.

The simplest potential involving such an interaction is:

$$\hat{V} = \hat{A} + \hat{\boldsymbol{B}} \cdot \boldsymbol{\sigma} \tag{2.11}$$

Operators $\hat{A}$ and $\hat{\boldsymbol{B}}$ refer to the sample; $\boldsymbol{\sigma}$ refers to the Pauli spin matrices for the neutron. As we shall see later, this potential describes both nuclear and magnetic scattering.

2.3.1 Beam polarization

We are interested in the effect on the neutron spin, so a firm definition of this quantity is needed. The spin is defined as up or down relative to a quantization axis, usually set by an external magnetic field. In a beam of neutrons, the spins may point in random directions. We are interested in the ensemble of neutrons, so we define a quantity $\boldsymbol{P}$, the polarization, as the average value of the spin of the neutrons in the beam.

$$\boldsymbol{P} = \langle \boldsymbol{\sigma} \rangle \tag{2.12}$$

$P = +1$ for a perfect spin-up beam, -1 for perfect spin-down beam, and 0 for an unpolarized beam. As we are considering an ensemble of particles, a partially polarized beam is possible, but in this case we cannot give a complete quantum mechanical description of the beam. In such cases, the density matrix formalism is more useful. The density matrix operator $\hat{\rho}$ is a Hermitian matrix with unit trace, where $\mathcal{I}$ denotes the identity matrix.

$$\hat{\rho} = \frac{1}{2}(\mathcal{I} + \boldsymbol{P} \cdot \sigma) \tag{2.13}$$

2.3.2 Spin dependent cross-section

With this established, we now return to the cross-section, in particular the part that depends on the neutron spin alone.

Please purchase PDF Split-Merge on www.verypdf.com to remove this watermark.

$$\sum_s p_s|\langle s'|\hat{V}|s\rangle|^2 = \sum_{s,s'} p_s\langle s|\hat{V}^+|s'\rangle\langle s'|\hat{V}|s\rangle \quad (2.14)$$

$$= \sum_s p_s\langle s|\hat{V}^+\hat{V}|s\rangle \quad (2.15)$$

$$= \sum_s \langle s|\hat{\rho}|s\rangle\langle s|\hat{V}^+\hat{V}|s\rangle \quad (2.16)$$

Here, we have used the closure relation and the property of the density matrix operator that $p_s = \langle s|\hat{\rho}|s\rangle$. If we suppose that $\hat{\rho}$ is diagonal, then $\langle s|\hat{\rho}|s\rangle = \delta_{s,s'}\langle s'|\hat{\rho}|s\rangle$. Using this identity and the closure relation again, we obtain:

$$\sum_s p_s|\langle s'|\hat{V}|s\rangle|^2 = \sum_s \langle s|\hat{V}^+\hat{V}\hat{\rho}|s\rangle \quad (2.17)$$

$$= \mathrm{Tr}(\hat{\rho}\hat{V}^+\hat{V}) \quad (2.18)$$

This trace is independent of the choice of $\hat{\rho}$, so the final result is not constrained to a diagonal choice of $\hat{\rho}$.

The partial differential cross-section is proportional to $\mathrm{Tr}(\hat{\rho}\hat{V}^+\hat{V})$. This can be evaluated using Equations 2.11 and 2.13. Bearing in mind that $\mathrm{Tr}(\boldsymbol{\sigma}) = 0$, we obtain:

$$\mathrm{Tr}(\hat{\rho}\hat{V}^+\hat{V}) = \frac{1}{2}\mathrm{Tr}\big((\mathcal{I} + \boldsymbol{P}\cdot\boldsymbol{\sigma})(\hat{A}^+ + \hat{\boldsymbol{B}}^+\cdot\boldsymbol{\sigma})(\hat{A} + \hat{\boldsymbol{B}}\cdot\boldsymbol{\sigma})\big) \quad (2.19)$$

$$= \hat{A}^+\hat{A} + \hat{\boldsymbol{B}}^+\hat{\boldsymbol{B}} + \hat{A}^+(\boldsymbol{P}\cdot\hat{\boldsymbol{B}}) + (\boldsymbol{P}\cdot\hat{\boldsymbol{B}}^+)\hat{A} + \mathrm{i}\boldsymbol{P}\cdot(\hat{\boldsymbol{B}}^+\times\hat{\boldsymbol{B}})$$

We are also interested in the effect on the polarization of the beam. The incident beam has polarization $\boldsymbol{P}$, the scattered beam $\mathbf{P}'$. The density matrix of the scattered state is $\hat{\rho}' = \hat{\rho}\hat{V}^+\hat{V}$. From Equation 2.13, $\boldsymbol{P} = \mathrm{Tr}(\boldsymbol{\sigma}\hat{\rho})$. After normalization, this gives:

$$\mathbf{P}' = \frac{\mathrm{Tr}(\hat{\rho}\hat{V}^+\boldsymbol{\sigma}\hat{V})}{\mathrm{Tr}(\hat{\rho}\hat{V}^+\hat{V})} \quad (2.20)$$

This is equivalent to:

$$\mathbf{P}'\frac{\mathrm{d}^2\sigma}{\mathrm{d}\omega\mathrm{d}\Omega} = \frac{k'}{k}\left(\frac{m}{2\pi\hbar^2}\right)^2\sum_{\lambda,\lambda'} p_\lambda \mathrm{Tr}\left(\hat{\rho}\langle k\lambda|\hat{V}^+|k'\lambda'\rangle\boldsymbol{\sigma}\langle k'\lambda'|\hat{V}|k\lambda\rangle\right)\times \quad (2.21)$$

$$\delta(E_\lambda - E_{\lambda'} + \hbar\omega)$$

We clearly need to know $\mathrm{Tr}(\hat{\rho}\hat{V}^+\boldsymbol{\sigma}\hat{V})$.

$$\mathrm{Tr}(\hat{\rho}\hat{V}^+\boldsymbol{\sigma}\hat{V}) = \hat{A}^+\hat{\boldsymbol{B}} + \hat{A}\hat{\boldsymbol{B}}^+ + \hat{A}^+\hat{A}\boldsymbol{P} + (\boldsymbol{P}\cdot\hat{\boldsymbol{B}}^+)\hat{\boldsymbol{B}} + \hat{\boldsymbol{B}}^+(\boldsymbol{P}\cdot\hat{\boldsymbol{B}}) \quad (2.22)$$

$$-\boldsymbol{P}(\hat{\boldsymbol{B}}^+\hat{\boldsymbol{B}}) + \mathrm{i}\hat{A}^+(\hat{\boldsymbol{B}}\times\boldsymbol{P}) + \mathrm{i}\hat{A}(\boldsymbol{P}\times\hat{\boldsymbol{B}}^+) - \mathrm{i}(\hat{\boldsymbol{B}}^+\times\hat{\boldsymbol{B}}))$$

Please purchase PDF Split-Merge on www.verypdf.com to remove this watermark.

These are the general forms with which to describe the spin-dependent interactions of the neutron beam. $\boldsymbol{P}$ is a vector quantity, therefore we can describe fully the spin state of the beam in 3-D space.

To briefly outline some consequences of this result, polarization is created independently of the state of the incident beam by three terms: $\hat{A}^{+}\hat{\boldsymbol{B}}$, $\hat{A}\hat{\boldsymbol{B}}^{+}$ and $-\mathrm{i}(\hat{\boldsymbol{B}}^{+}\times\hat{\boldsymbol{B}})$. The terms $\mathrm{i}\hat{A}^{+}(\hat{\boldsymbol{B}}\times\boldsymbol{P})$ and $\mathrm{i}\hat{A}(\boldsymbol{P}\times\hat{\boldsymbol{B}}^{+})$ act to rotate an incident polarization.

2.3.3 Nuclear scattering

For nuclear scattering, the Fermi pseudopotential is used as an estimate of the scattering potential. This places a δ-function at the site of each nucleus. Every isotope has its own characteristic scattering length operator, $\hat{b}$.

$$\hat{V}_n(r) = \frac{2\pi\hbar^2}{m}\hat{b}\,\delta(r) \tag{2.23}$$

As the neutron beam is assumed to be a plane wave, evaluation over $\boldsymbol{k}$ and $\boldsymbol{k}'$ gives us the Fourier transform of the scattering potential, $\hat{V}(\boldsymbol{Q})$, where $\boldsymbol{Q} = \boldsymbol{k}' - \boldsymbol{k}$.

$$\langle \boldsymbol{k}'\lambda'|\hat{V}|\boldsymbol{k}\lambda\rangle = \langle\lambda'|\hat{V}(Q)|\lambda\rangle \tag{2.24}$$

Summing over the whole sample, the nuclear potential has the form:

$$\hat{V}_n(\boldsymbol{Q}) = \sum_i \mathrm{e}^{\mathrm{i}\boldsymbol{Q}\cdot\boldsymbol{R}_i}\frac{2\pi\hbar^2}{m}\hat{\mathbf{b}}_i \tag{2.25}$$

where $\hat{\mathbf{b}} = \hat{\alpha} + \beta\boldsymbol{\sigma}\cdot\hat{\mathbf{I}}$, is the scattering length operator and $\mathbf{R}_i$ the position vector of the i^{th} nucleus. $\hat{\mathbf{I}}$ is the nuclear spin operator. As stated earlier, the nuclear scattering is spin dependent if the nucleus has a spin. There are then two distinct scattering events: $\mathbf{I}+\frac{1}{2}$ and $\mathbf{I}-\frac{1}{2}$. The operator $\hat{\mathbf{b}}$ must return two different values.

$$\begin{aligned}\hat{\mathbf{b}}|\mathbf{I}+\frac{1}{2}\rangle &= b_+|\mathbf{I}+\frac{1}{2}\rangle\\ \hat{\mathbf{b}}|\mathbf{I}-\frac{1}{2}\rangle &= b_-|\mathbf{I}-\frac{1}{2}\rangle\end{aligned}$$

For this to be true, $\hat{\alpha}$ and β have the following values, where I is the modulus of $\mathbf{I}$:

$$\hat{\alpha} = \frac{(I+1)b_+ + Ib_-}{2I+1}, \beta = \frac{b_+ - b_-}{2I+1}$$

If we compare this to Equation 2.11, we see that:

$$\hat{A} = \sum_i \mathrm{e}^{\mathrm{i}\boldsymbol{Q}\cdot\boldsymbol{R}_i}\frac{2\pi\hbar^2}{m}\hat{\alpha}_i \tag{2.26}$$

Please purchase PDF Split-Merge on www.verypdf.com to remove this watermark.

$$\hat{\boldsymbol{B}} = \sum_i \mathrm{e}^{\mathrm{i}\boldsymbol{Q}\cdot\boldsymbol{R}_i} \frac{2\pi\hbar^2}{m} \beta_i \hat{\mathbf{I}}_i \tag{2.27}$$

We can now evaluate the effects on the cross-section and beam polarization using Equations 2.20 and 2.23. We assume that the nuclear spins are oriented randomly. This is correct except at ultra-low temperatures. On averaging over the nuclear spins, any terms linear in $\hat{\mathbf{I}}$ will disappear. The last three terms in Equation 2.20 are linear in $\hat{\mathbf{I}}$. The first term is unaffected by the spin averaging, but in the second term, $\mathcal{O}\,\hat{\mathbf{I}}_i \cdot \hat{\mathbf{I}}_j = I_i(I_i+1)$ where $\mathcal{O}$ denotes the averaging over the nuclear spin variable. If we then introduce averaging over the isotope distributions (denoted by a bar), we end up with the final cross-section, split into coherent and incoherent terms.

$$\frac{\mathrm{d}^2\sigma}{\mathrm{d}\omega\mathrm{d}\Omega} = \frac{k'}{k} \sum_\lambda p_\lambda \sum_i \mathrm{e}^{\mathrm{i}\boldsymbol{Q}\cdot(\mathbf{R}_i - \mathbf{R}_j)} [\overline{\hat{\alpha}}^2 + \delta_{i,j}(\overline{\hat{\alpha}^2} - \overline{\hat{\alpha}}^2 + \overline{\beta^2 I_i(I_i+1)})] \times \delta(E_\lambda - E_{\lambda'} + \hbar\omega) \tag{2.28}$$

Therefore, the cross-section is independent of the initial polarization. The next question is how the incident polarization is altered in the scattering process. For this, we need to evaluate Equation 2.23, again averaging over the nuclear spin.

$$\mathcal{O}\mathrm{Tr}(\hat{\rho}\hat{V}^+ \boldsymbol{\sigma} \hat{V}) = \boldsymbol{P}[\hat{A}^+\hat{A} - \frac{1}{3}\mathcal{O}(\hat{\boldsymbol{B}}^+ \cdot \hat{\boldsymbol{B}})] \tag{2.29}$$

This uses the identity given below, arising from the consideration of $\hat{\mathbf{I}}$ as a vector.

$$\mathcal{O}[\hat{\boldsymbol{B}}^+(\hat{\boldsymbol{B}} \cdot \boldsymbol{P})] = \mathcal{O}[(\hat{\boldsymbol{B}}^+ \cdot \boldsymbol{P})\hat{\boldsymbol{B}}] = \frac{1}{3}\boldsymbol{P}\mathcal{O}[\hat{\boldsymbol{B}}^+ \cdot \hat{\boldsymbol{B}}] \tag{2.30}$$

After averaging over isotope distributions,

$$\boldsymbol{P}'\frac{\mathrm{d}^2\sigma}{\mathrm{d}\omega\mathrm{d}\Omega} = \frac{k'}{k} \sum_\lambda p_\lambda \sum_i \mathrm{e}^{\mathrm{i}\boldsymbol{Q}\cdot(\mathbf{R}_i - \mathbf{R}_j)} \times \boldsymbol{P}[\overline{\hat{\alpha}}^2 + \delta_{i,j}(\overline{\hat{\alpha}^2} - \overline{\hat{\alpha}}^2 - \frac{1}{3}\overline{\beta^2 I_i(I_i+1)})]\delta(E_\lambda - E_{\lambda'} + \hbar\omega) \tag{2.31}$$

In this equation, the nuclear coherent and isotope incoherent scattering do not change the final polarization. However, for the incoherent scattering due to random nuclear spin orientation, the scattered polarization is $-\frac{1}{3}\boldsymbol{P}$. To obtain this fraction, one third of the scattering ($\boldsymbol{\sigma}_z \hat{I}_z$) does not flip the spin, and two thirds ($\boldsymbol{\sigma}_x \hat{I}_x + \boldsymbol{\sigma}_y \hat{I}_y$) do.

2.3.4 Magnetic scattering

The scattering potential here is rather more complicated than for nuclear scattering.

$$\hat{V}_m(\boldsymbol{Q}) = r_0 \boldsymbol{\sigma} \cdot \hat{\mathbf{M}}_\perp \tag{2.32}$$

Please purchase PDF Split-Merge on www.verypdf.com to remove this watermark.

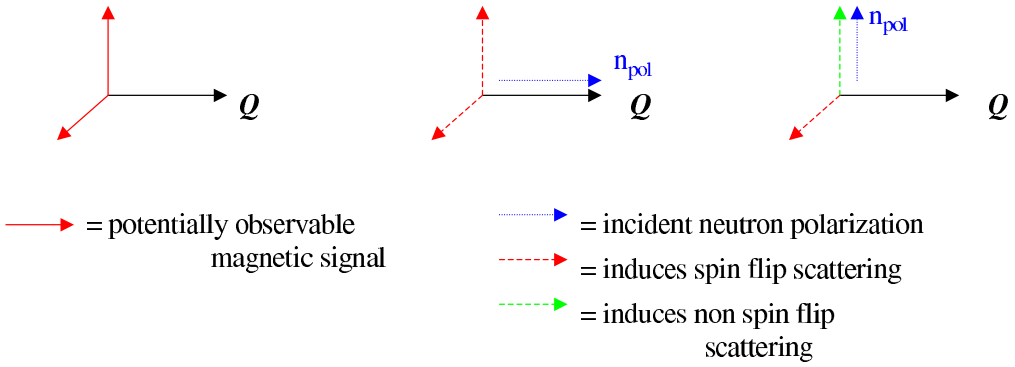

Figure 2.1: A cartoon displaying the relative geometry of the neutron spin and the scattering vector $\vec{Q}$ as described in the text.

$$\hat{\mathbf{M}}_{\perp} = \tilde{\boldsymbol{Q}} \times (\hat{\mathbf{M}} \times \tilde{\boldsymbol{Q}}) \tag{2.33}$$

$$\hat{\mathbf{M}} = -\frac{1}{2\mu_B}\boldsymbol{M}(\kappa) \tag{2.34}$$

$\boldsymbol{M}(\kappa)$ is the Fourier transform of the magnetic field distribution in the sample. This can be derived by considering scattering off a single electron. From Equation 2.33, it is clear that only those parts of $\hat{\mathbf{M}}$ perpendicular to the scattering vector $\boldsymbol{\kappa}$ are involved. $\tilde{\kappa}$ is the unit vector parallel to the scattering vector $\boldsymbol{\kappa}$. r_0 is the constant of proportionality.

The first thing to note is that this potential has no $\hat{A}$ component, and $\hat{\boldsymbol{B}} = r_0\hat{\mathbf{M}}_{\perp}$. This reduces our expressions for the spin-dependent cross-section and scattered polarization considerably.

$$\mathrm{Tr}(\hat{\rho}\hat{V}_m^{+}\hat{V}_m) = \hat{\boldsymbol{B}}^{+}\hat{\boldsymbol{B}} + \mathrm{i}\boldsymbol{P}\cdot(\hat{\boldsymbol{B}}^{+} \times \hat{\boldsymbol{B}}) \tag{2.35}$$

The cross-section depends explicitly on the incident polarization and its relation to the magnetic field distribution inside the sample.

$$\mathrm{Tr}(\hat{\rho}\hat{V}^{+}\boldsymbol{\sigma}\hat{V}) = (\boldsymbol{P}\cdot\hat{\boldsymbol{B}}^{+})\hat{\boldsymbol{B}} + \hat{\boldsymbol{B}}^{+}(\boldsymbol{P}\cdot\hat{\boldsymbol{B}}) - \boldsymbol{P}(\hat{\boldsymbol{B}}^{+}\hat{\boldsymbol{B}}) - \mathrm{i}(\hat{\boldsymbol{B}}^{+} \times \hat{\boldsymbol{B}})) \tag{2.36}$$

As noted above, the chiral $\mathrm{i}(\hat{\boldsymbol{B}}^{+} \times \hat{\boldsymbol{B}})$ term indicates that a non-collinear magnetic structure will polarize an unpolarized beam. From the other three terms, we see that if the polarization is parallel to $\hat{\boldsymbol{B}}$, the polarization will be unchanged (non-spin-flip scattering), whereas if it is perpendicular, the polarization will be flipped. This is illustrated in Figure 2.1.

2.3.5 Nuclear and magnetic scattering

In a real material, we have both nuclear and magnetic scattering at the same time, as spins are always attached to atoms. It is clear that $\hat{A}$ will always be solely nuclear,

Please purchase PDF Split-Merge on www.verypdf.com to remove this watermark.

whereas $\hat{\boldsymbol{B}}$ may contain components deriving from both nuclear and magnetic origins. In a real experiment, this all has to be accounted for. We come back to Equation 2.23. This is reshown here for clarity.

$$\begin{aligned}\mathrm{Tr}(\hat{\rho}\hat{V}^{+}\boldsymbol{\sigma}\hat{V}) &= \hat{A}^{+}\hat{\boldsymbol{B}} + \hat{A}\hat{\boldsymbol{B}}^{+} + \hat{A}^{+}\hat{A}\boldsymbol{P} + (\boldsymbol{P}\cdot\hat{\boldsymbol{B}}^{+})\hat{\boldsymbol{B}} + \hat{\boldsymbol{B}}^{+}(\boldsymbol{P}\cdot\hat{\boldsymbol{B}}) \\ &\quad -\boldsymbol{P}(\hat{\boldsymbol{B}}^{+}\hat{\boldsymbol{B}}) + \mathrm{i}\hat{A}^{+}(\hat{\boldsymbol{B}}\times\boldsymbol{P}) + \mathrm{i}\hat{A}(\boldsymbol{P}\times\hat{\boldsymbol{B}}^{+}) - \mathrm{i}(\hat{\boldsymbol{B}}^{+}\times\hat{\boldsymbol{B}}))\end{aligned}$$

Several terms that disappear in the purely nuclear case are maintained here. In particular, we have the creation of polarization by symmetric nuclear-magnetic interference terms $(\hat{A}^{+}\hat{\boldsymbol{B}} + \hat{A}\hat{\boldsymbol{B}}^{+})$. We also see rotation of the incident polarization in the antisymmetric nuclear magnetic-interference terms $\mathrm{i}\hat{A}^{+}(\hat{\boldsymbol{B}}\times\boldsymbol{P}) + \mathrm{i}\hat{A}(\boldsymbol{P}\times\hat{\boldsymbol{B}}^{+})$.

It is often a useful approximation to associate $\hat{\boldsymbol{B}}$ solely with the magnetic part of the scattering potential. Many materials do not have isotopes of different spin. In this case, the nuclear component of $\hat{\boldsymbol{B}}$ is zero. For those that do, they are only ordered at extremely low temperatures and so for the majority of neutron scattering measurements, can be treated as discussed in Section 2.3.3.

In subsequent sections, correlations coming from the $\hat{A}$ operator may be labelled N (nuclear in origin) and those coming from the $\hat{\boldsymbol{B}}$ operator may be labelled M (magnetic in origin).

2.4 Correlation functions

The scattering cross-section can be directly related to the microscopic auto-correlation functions. The evaluation of the matrix element in Equation 2.1 is obviously crucial in understanding the observed scattering. The cross-section picks up the thermal average of the operators. For nuclear scattering this represents correlations in the positioning of the nuclei. The thermal averaging over the matrix element, neglecting spin states for the moment, is

$$\int \sum_{jj'} \langle \exp[i\boldsymbol{Q}\cdot\boldsymbol{R}_j(0)] \exp[i\boldsymbol{Q}\cdot\boldsymbol{R}'_j(t)]\rangle \exp[-i\omega t]dt \tag{2.37}$$

where $\boldsymbol{Q} = \boldsymbol{k} - \boldsymbol{k}'$ and $\boldsymbol{R}_j(t)$ is the time-dependent positioning vector of the j^{th} nucleus. An intermediate scattering function can therefore be defined as

$$S(Q,t) = \frac{1}{N}\sum_{jj'} \langle \exp[i\boldsymbol{Q}\cdot\boldsymbol{R}_j(0)] \exp[i\boldsymbol{Q}\cdot\boldsymbol{R}'_j(t)]\rangle \tag{2.38}$$

where N is the number of nuclei in the system. The scattering function then steps fully into reciprocal space in both the momentum and energy variables:

$$S(Q,\omega) = \frac{1}{2\pi\hbar}\int I(Q,t)\mathrm{e}^{-i\omega t}\mathrm{d}\omega. \tag{2.39}$$

The coherent cross-section can therefore be written as

$$\frac{\mathrm{d}^2\sigma}{\mathrm{d}\omega\mathrm{d}\Omega} = \frac{\sigma_{coh}}{4\pi}\frac{k'}{k}NS(Q,\omega). \tag{2.40}$$

Please purchase PDF Split-Merge on www.verypdf.com to remove this watermark.

$S(Q,\omega)$ is the Fourier transform in time and space of the time-dependent pair-correlation function. The sample can be probed through either neutron energy loss or neutron energy gain. For neutron energy gain, the number of excitations, related to the temperature becomes important. To account for this, detailed balance factor has to be applied:

$$S(Q,\omega) = \exp(\hbar\omega/k_BT)S(-Q,-\omega). \tag{2.41}$$

For magnetic scattering, the current-density auto-correlation function is probed. The neutron creates a magnetic field. The response of the sample to this field is characterized by the complex susceptibility $\chi(Q,\omega)$. In the static limit at $Q = 0$ this is the static susceptibility divided by $g\mu_B$ where g is the Landé factor. Using the fluctuation-dissipation theorem and Equation 2.41, the imaginary part of the susceptibility is linked to the current-density correlations

$$S(Q,\omega) \propto \frac{\chi''(Q,\omega)}{1-\exp(-\hbar\omega/k_BT)}. \tag{2.42}$$

The spatial distribution of the individual scattering unit must also be considered. The Fourier transform of this distribution imposes an intensity envelope (the magnetic form factor) on the observed scattering, and for magnetism the effects are usually cause the signal to diminish for large Q.

2.5 Polarizing Neutron Beams

The neutron beam generated by either a reactor or spallation source is unpolarized. To polarize a beam, neutrons with a given polarization must be extracted, and the rest thrown away. This can be accomplished in several different ways, two of which are discussed below.

2.5.1 Polarizing monochromators

From our discussion above an unpolarized beam can be polarized by either the nuclear-magnetic interference $\hat{A}^+\hat{\boldsymbol{B}} + \hat{A}\hat{\boldsymbol{B}}^+$ or the chiral magnetic $-\mathrm{i}(\hat{\boldsymbol{B}}^+ \times \hat{\boldsymbol{B}})$ terms in Equation 2.23. If we assume that the nuclear spins are randomly oriented, then for the first term to exist, nuclear and magnetic scattering must be generated by the same scattering vector. This is fulfilled in ferromagnets. The second term is purely magnetic, and is zero unless the moment directions in the material are non-collinear.

Polarizing monochromators usually belong to the first category. A typical example, commonly used at the Institut Laue-Langevin, is the Heusler alloy Cu_2MnAl. Using the (111) reflection, the purely nuclear $(\hat{A}^+\hat{A})$ scattering is minimized, so that a high polarization (in excess of 90%) can be obtained.

Polarizing supermirrors have also been developed. By stacking multilayers of ferromagnetic material, extremely high levels of polarization can be achieved using poor polarizers such as iron. At each layer, more neutrons of the desired polarization are reflected back.

Please purchase PDF Split-Merge on www.verypdf.com to remove this watermark.

2.5.2 Polarizing filters

Helium-3 is a spin-1/2 nucleus. It has a very strongly spin-dependent neutron capture cross-section. Effectively, all neutrons with anti-parallel spins are absorbed, leaving the spin-parallel neutrons. Therefore, in an ideal filter containing a gas of perfectly polarized He^3 nuclei, an incident unpolarized beam would be perfectly polarized after transmission through the filter.

Unfortunately, it is not possible to create a perfectly polarized gas of He^3. Polarization can be generated by optical pumping methods. Two such methods are currently being pursued. In spin exchange optical pumping, a gas of, for example, rubidium ions is polarized using circularly polarized light, and then this is used to polarize the helium through direct spin exchange. In metastable exchange optical pumping, the helium is compressed and then polarized directly using the circularly polarized light. It is then brought to the desired pressure. This produces higher polarizations, but cannot be performed *in situ*. In both cases, the He^3 polarization has a given relaxation time.

2.5.3 Maintaining and controlling neutron polarization

To preserve the polarization of a neutron beam, the chosen quantization axis must remain constant. This is usually achieved by setting up a stable magnetic field through which the beam moves. The direction of magnetic field lies parallel to the neutron polarization.

If the direction of the field is changed adiabatically, then the polarization can be rotated without loss of polarization.

If the field direction is changed non-adiabatically, i.e. very suddenly, the beam polarization will not follow, but will instead start to precess about the new field direction. The problem is getting the change in field to occur sharply enough. This can be achieved using superconducting Meissner shields to separate two fields (this is done in CRYOPAD (see Section 2.6.3)).

Another type of spin flipper is the Mezei spin flipper. In the simplest form, this involves a thin rectangular solenoid, at an angle to a guide field. The neutrons enter and leave the coil non-adiabatically, and inside the coil, the polarization precesses through an angle determined by the internal field, the thickness of the coil, and the neutron's velocity. The guide field remains constant on either side, but the neutron beam's polarization can be completely determined. This is often used to set up π or $\frac{\pi}{2}$ spin flippers.

2.6 Experimental setups

2.6.1 Flipping ratio measurements

In the simplest experiments involving polarized neutrons, a polarized incident beam is generated and a π spin flipper placed before the sample. The cross-section is measured with the spin flipper off, and then with the spin flipper on. This gives the cross-sections when the polarization is reversed. This gives us the flipping ratio for a particular scattering vector and energy transfer.

Please purchase PDF Split-Merge on www.verypdf.com to remove this watermark.

$$F.R. = \frac{(\frac{\mathrm{d}^2\sigma}{\mathrm{d}\omega\mathrm{d}\Omega})_{\text{spin up}}}{(\frac{\mathrm{d}^2\sigma}{\mathrm{d}\omega\mathrm{d}\Omega})_{\text{spin down}}} \tag{2.43}$$

As a part of the cross-section depends on the incident polarization, and so can be extracted from such measurements. This is particularly useful for studies of the magnetic form factor of ferromagnets, where the nuclear and magnetic parts occur at the same scattering vector.

2.6.2 XYZ polarization

By placing a spin flipper before and after the sample, four separate cross-sections can be measured: $\langle\uparrow \mid \uparrow\rangle$, $\langle\uparrow \mid \downarrow\rangle$,$\langle\downarrow \mid \uparrow\rangle$ and $\langle\downarrow \mid \downarrow\rangle$. As discussed in the theory section, this allows us to select particular components of the cross-section, for example spin dependent isotope incoherent scattering.

Further control can be added by using adiabatic guide fields to rotate the polarization prior to entering the sample region. By this means, three orthogonal directions can be selected and investigated. The direction must be maintained during the course of a measurement, and as the guide field must be present across the sample space, ferromagnetic samples cannot be investigated. A sample spectrometer is shown in Figure 2.2.

A common notation for the directions has arisen. x is parallel to the scattering vector, y is perpendicular to the scattering vector in the scattering plane, and z is perpendicular to the scattering plane.

In magnetic scattering, signal parallel to the scattering vector is not visible. This gives us extra directional information concerning the magnetic field distribution in the sample. It means that, assuming no spin-dependent nuclear scattering term, we can cleanly separate out magnetic and non-magnetic signal by comparing the spin-flip and non-spin-flip cross-sections when the polarization is parallel to the scattering vector. Furthermore, if no nuclear signal is present, we can then distinguish the direction of the magnetic signal by comparing the spin-flip and non-spin-flip cross-sections with the polarization perpendicular to the scattering vector. This is all illustrated in Figure 2.1.

2.6.3 Spherical neutron polarimetry

The XYZ polarization technique outlined above maintains a guide field at all times, to preserve the axis of quantization and hence the beam polarization. This can be avoided by careful management of the sample environment. With this change, all possible cross-sections in three dimensions can be accessed. The scattering event can be described by a polarization tensor, $\boldsymbol{P}$. Previously, we had access to the diagonal elements. By full control of the sample environment, all of the elements become accessible.

$$\boldsymbol{P} = \begin{pmatrix} P_{xx} & P_{xy} & P_{xz} \\ P_{yx} & P_{yy} & P_{yz} \\ P_{zx} & P_{zy} & P_{zz} \end{pmatrix} \tag{2.44}$$

Please purchase PDF Split-Merge on www.verypdf.com to remove this watermark.

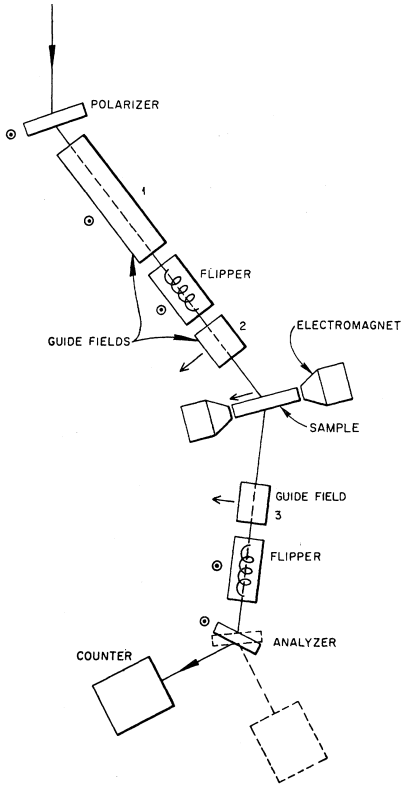

Figure 2.2: Schematic arrangement of the polarization spectrometer first designed by Moon *et al.* [7] at the Oak Ridge National Laboratory.

To achieve this, the CRYOPAD sample environment has been developed at the ILL. This device can be inserted into any spectrometer equipped to generate polarized neutrons. The basic principle is as follows. An incident polarization is selected. The beam enters a zero field region surrounding the sample. It interacts with the sample, and the scattered beam then exits the zero field region. A particular polarization is selected for analysis.

The beam is polarized by some method, such as using a Heusler monochromator. At this point, it has polarization P_0 parallel to the direction of motion. This beam enters the incident nutator, where the polarization is rotated to an angle θ with respect to the vertical axis (out of the page in Figure 2.3). The beam then passes through the outer Meissner shield. These shields are superconducting niobium cylinders, cooled inside a μ-metal box to prevent stray magnetic fields from entering the volume inside the cylinder.

Between the two Meissner shields, the primary toroidal coil generates a horizontal magnetic field $\boldsymbol{B}_p$. A secondary coil is wound over a 45° segment of this solenoid, and allows tangential/horizontal fields to vary for $\boldsymbol{k}_i$ and $\boldsymbol{k}_f$. Two rotatable dipole electromagnets (nutators) complete the device. The first nutator is used to rotate adiabatically the neutrons spins (the spin component parallel to the magnetic field $\boldsymbol{B}_{in}$ is conserved along the neutron path), so that the polarization $\boldsymbol{P}$ at the surface of the outer Nb shield is orthogonal to the incident wavevector $\boldsymbol{k}_i$ and forms an angle θ_{in} to the vertical axis,

Please purchase PDF Split-Merge on www.verypdf.com to remove this watermark.

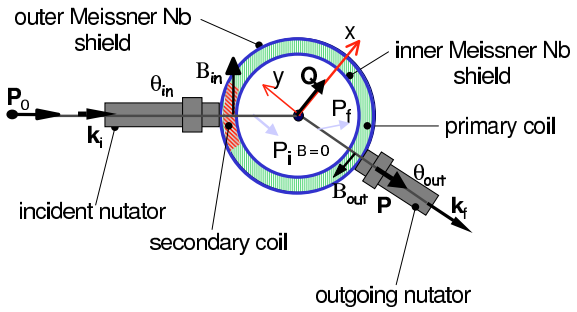

Figure 2.3: Schematic layout of CRYOPAD-II.

defined by the nutator orientation. The passage into the annular region between the two Meissner shields is non-adiabatic, causing the polarization $\boldsymbol{P}$ to rotate around $\boldsymbol{B}_p$ by an angle $\chi_{\rm in}$. By choosing appropriate values for $\theta_{\rm in}$ and for the electrical currents in the toroidal coils, the polarization of the incident beam, $\boldsymbol{P}_i$, can be driven to *any* spatial orientation. By controlling the orientation $\theta_{\rm out}$ of the second nutator, and the precession angle $\chi_{\rm out}$ that the beam polarization undergoes when the scattered neutrons cross the annular region, any of the three Cartesian components of the final polarization, $\boldsymbol{P}_f$, can be analyzed. In the following, the x-axis of the reference frame is defined to be parallel to the momentum transfer $\mathbf{Q} = \boldsymbol{k}_i - \boldsymbol{k}_f$, the y-axis is perpendicular to $\boldsymbol{Q}$ and lies in the scattering plane, and the z-axis is perpendicular to the scattering plane (vertical). This means that in a given scan across reciprocal space, only the z-axis remains constant in physical space.

The field strengths necessary to deliver the full scattered polarization along the correct direction to maximise detection using, for example, a Heusler analyser crystal, can be computed. This is described by Brown *et al.* [8]. In this way, all sixteen correlation functions defining the most general expression of magnetic neutron scattering [9, 10] can be measured. Spherical neutron-spin polarimetry has proved to be very useful in determining both complicated magnetic structures and materials where nuclear-magnetic interference is strong. This interference can only be observed when magnetic signal is found at the same scattering vector as nuclear signal.

Most previous studies have used elastic scattering. As an example, a thorough study of the formation of magnetoelectric domains in Cr_2O_3 was possible (see Brown *et al.* [11]). To summarize briefly, Cr_2O_3 is a collinear antiferromagnet with magnetic and nuclear scattering phase shifted by 90°. It is anti-centrosymmetric and so information on the 180° domains cannot be obtained from the cross-section or XYZ polarization analysis. By cooling under various conditions of electric and magnetic fields, an imbalance in domain populations was created. Then, the crystal was measured in zero field. The magnetic structures produced in given cooling conditions were obtained, along with the zero field form factor. In principle, the form factor of *any* antiferromagnetic material can now be measured by this technique.

This technique has not, as yet, often been associated with inelastic scattering stud-

Please purchase PDF Split-Merge on www.verypdf.com to remove this watermark.

ies. Although general expresssions for the cross-section and polarisation of the scattered neutrons were derived in the early 1960s [9, 10] only one recent paper can be found in the literature where the results of inelastic scattering experiments with three-dimensional polarization analysis are reported [12]. Such experiments can, in principle, give a wealth of information on the interaction between electronic, spin and vibrational degrees of freedom, and have the potential to play an important role in the study of strongly correlated electron systems. However, the low flux associated with polarised neutrons combined with the small intensity of the inelastic excitations has limited the use of this technique. In Chapter 3 such an inelastic experiment is described, carried out on UO_2.

2.6.4 Neutron spin-echo

The neutron spin-echo technique, first developed by Mezei [13], uses polarized neutrons, in a completely different way. In a spin-echo experiment, the neutron polarization is used to encode the energy transfer between the neutron and the sample. This allows the energy and spatial resolution of the neutron to be separated, and very good energy resolution can be obtained.

The incident neutron beam is fully polarized perpendicular to a magnetic field B_1. On entering field B_1 the polarization precesses over a given distance l_1 before hitting the sample, acquiring a precession angle $\phi_1 = \gamma l_1 B_1 / v_1$, where γ is the neutron's gyromagnetic ratio and v_1 is the neutron's velocity. The incident neutron beam is typically only loosely monochromatized, and so has a large spread of velocities, each of which ends up with a different total precession angle at the sample, meaning that there is no overall beam polarization at the sample.

At the sample, the beam is scattered, possibly leading to a momentum and/or energy transfer, and then passes through a second arm of length l_2 and magnetic field B_2, acquiring a precession angle $\phi_2 = \gamma l_2 B_2 / v_2$. The total precession angle is therefore $\Delta\phi = \phi_1 + \phi_2$. For elastic scattering $v_1 = v_2$, and so if $l_1 B_1 = -l_2 B_2$, $\Delta\phi = 0$ for all incoming neutron velocities. This is the 'symmetric' case. All of the neutrons are 'unwound' correctly, and so at the detector the beam polarization parallel to the original direction, P_{NSE} is recovered, taking into account any effects of scattering on the polarization.

$$P_{NSE} = P_s \langle \cos(\Delta\phi) \rangle \tag{2.45}$$

where the averaging includes information about the scatterer and P_s is the polarization after scattering by the sample. By altering the field slightly in one arm, $\Delta\phi$ is shifted away from zero, and oscillations in P_{NSE} can be measured. The amplitude of this *echo group* is a measure of the scattering intensity involved, and the envelope represents the velocity spread of the incident beam. By measuring the echo group, the measurement of the amplitude is ensured, even considering the high sensitivity of the system to small changes in the magnetic field.

Experimentally, the echo condition is obtained by keeping the magnetic field in the two arms parallel and using a π spin flip to alter the sense of precession. This can be done by an external π-flipper placed after the sample, but if the sample creates spin-dependent scattering (e.g. magnetic) this may bring about an appropriate π flip. This has the added

Please purchase PDF Split-Merge on www.verypdf.com to remove this watermark.

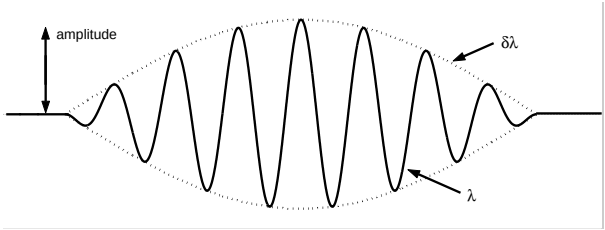

Figure 2.4: An echo group. λ is the nominal wavelength of the scattered neutron beam and $\delta\lambda$ the wavelength spread.

advantage that all non-flipped scattering does not meet the echo condition, and so is not measured in the echo. This is discussed in more detail in Section 2.6.4.

In the inelastic case, the echo condition is not so obvious, but the key effect needed is that the total precession angle is stationary over the whole beam (and spread of velocities therein):

$$\left.\frac{\partial\phi}{\partial v}\right|_{beam} = 0. \tag{2.46}$$

The energy transfer, like $\Delta\phi$, is a function of the initial and final velocities of a particular neutron. The energy transfer is positive for neutron energy gain.

$$\Delta\phi = \gamma\left(\frac{l_1B_1}{v_1} - \frac{l_2B_2}{v_2}\right), \qquad \hbar\omega = \frac{m}{2}\left(v_2^2 - v_1^2\right). \tag{2.47}$$

$\Delta\phi$ is then used to probe $\omega(v_1, v_2)$. As the functional dependence on $v_{1,2}$ is different, this is only valid for first order variations in velocity about an arbitrary reference point, denoted by a bar.

$$\Delta\phi = \phi - \bar{\phi} = \tau(\omega - \bar{\omega}) \tag{2.48}$$

where τ is a constant of proportionality with units of time and

$$\bar{\phi} = \gamma\left(\frac{l_1B_1}{\bar{v}_1} - \frac{l_2B_2}{\bar{v}_2}\right), \qquad \hbar\bar{\omega} = \frac{m}{2}\left(\bar{v}_2^2 - \bar{v}_1^2\right). \tag{2.49}$$

This only holds for first order variations in the velocities: $\delta v_i = v_i - \bar{v}_i$. Applying this approximation gives

$$\phi - \bar{\phi} = \gamma\frac{l_2B_2}{\bar{v}_2^2}\delta v_2 - \gamma\frac{l_1B_1}{\bar{v}_1^2}\delta v_1 \tag{2.50}$$

and

$$\omega - \bar{\omega} = \frac{m}{\hbar}(\bar{v}_2\delta v_2 - \bar{v}_1\delta v_1). \tag{2.51}$$

Applying this to Equation 2.48 gives an expression for the constant of proportionality τ and the ratio of magnetic fields in the two arms necessary to fulfil the condition.

$$\frac{l_1B_1}{l_2B_2} = \frac{\bar{v}_1^3}{\bar{v}_2^3}, \qquad \tau = \hbar\gamma\frac{l_iH_i}{\bar{v}_i^3} = \frac{\hbar\bar{\phi}_i}{2\bar{E}_i} \tag{2.52}$$

Please purchase PDF Split-Merge on www.verypdf.com to remove this watermark.

For the elastic case, this gives $l_1 B_1 = l_2 B_2$. The value of τ is set by the precession field. For the inelastic case, the choice of magnetic fields is keyed to the desired energy transfer, for the nominal wavelength of the neutron beam. For a reasonably monochromatic beam, an echo group may be formed.

Returning to Equation 2.45

$$\begin{aligned} P_{NSE} &= P_s \langle \cos(\phi - \bar{\phi}) \rangle = P_{init} \langle \cos(\tau(\omega - \bar{\omega})) \rangle \\ &= P_s \frac{\int S(Q,\omega) \cos(\tau(\omega - \bar{\omega})) \mathrm{d}\omega}{\int S(Q,\omega) \mathrm{d}\omega}. \end{aligned} \tag{2.53}$$

The effect of scattering is included, here assuming no Q dependence. The observed polarization is the Fourier transform of the scattering function $S(Q,\omega)$. For this reason, τ is referred to as the Fourier time.

As an example, consider a quasielastic response, assumed to have a Lorentzian lineshape, centred at the elastic echo condition, $\bar{\phi} = \bar{\omega} = 0$. In the high-temperature limit this is

$$S(Q,\omega) \propto \frac{\Gamma}{\Gamma^2 + \omega^2} \tag{2.54}$$

where Γ is the half-width.

$$P_{NSE} = P_s \frac{\int \frac{\Gamma \cos(\omega\tau)}{\Gamma^2 + \omega^2} \mathrm{d}\omega}{\int \frac{\Gamma}{\Gamma^2 + \omega^2} \mathrm{d}\omega} \tag{2.55}$$

$$= P_s \mathrm{e}^{-\Gamma\tau}. \tag{2.56}$$

If the spectrometer is tuned to the elastic condition, the Fourier time constant for a given measurement is the time, t, representing the de-correlation time for the response being probed.

P_{NSE} can be measured at a series of Fourier times by altering the magnetic fields in the arms (Equation 2.52). At the elastic echo condition $P_{NSE}(\tau) = P_s \mathrm{Re}\, S(Q,\tau)/S(Q,0)$, i.e. it is the intermediate scattering function, as τ is the de-correlation time, normalized to $S(Q,0) = \int S(Q,\omega)\mathrm{d}\omega$.

A real spin-echo spectrometer

Figure 2.5 is a sketch of real spin-echo spectrometer, the IN11A spectrometer at the Institut Laue-Langevin. The neutron beam is polarized by a supermirror section, and is then flipped by $\pi/2$, to place it perpendicular to the field in the solenoid arms, so that it will precess appropriately. In the figure, the fields H_0 and H_1 are B_1 and B_2 respectively in the text above.

Please purchase PDF Split-Merge on www.verypdf.com to remove this watermark.

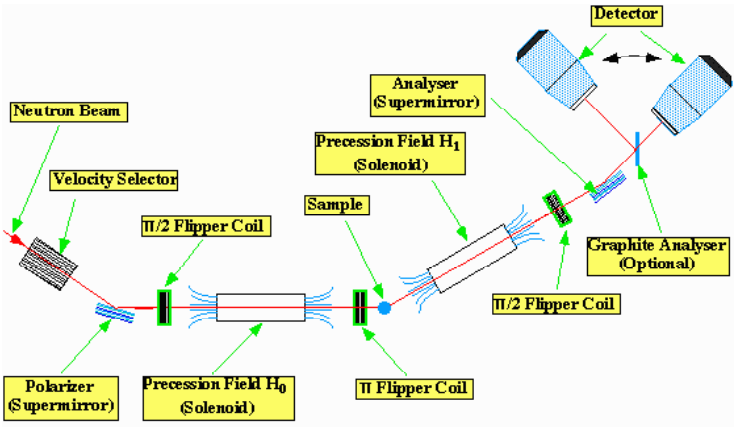

Figure 2.5: The IN11A spin-echo spectrometer at the ILL. Taken from the ILL's Yellow Book.

Magnetic spin-echo scattering

Magnetic scattering is spin-dependent and so the incident beam polarization will be changed by the scatterer (Section 2.3.2). This must be taken into account if the beam is to unwind correctly in the second arm.

Here, only systems with zero total magnetization will be considered (paramagnets and antiferromagnets). However, neutron spin-echo can be performed on ferromagnetic samples, and the appropriate method is given by Mezei [13]. As there is no macroscopic magnetization, the magnetic correlations $\langle M_i \rangle = 0$, where $i = x, y, z$, three orthogonal directions. For an isotropic magnetic system (e.g. a perfect paramagnet), the correlations in the three orthogonal directions are independent, such that $\langle M_i^* M_j \rangle = 0$ for $i \neq j$, and $\langle M_i^* M_i \rangle = \langle M_j^* M_j \rangle \neq 0$. From Equation 2.36, as the chiral term is zero, the scattered polarization is

$$\begin{aligned} \boldsymbol{P'} &= \frac{\langle \boldsymbol{M}_\perp^* (P_y M_y + P_z M_z) \rangle + \langle (P_y M_y^* + P_z M_z^*) \boldsymbol{M}_\perp \rangle}{\langle M_y^* M_y + M_z^* M_z \rangle} - \boldsymbol{P} \\ &= \frac{2P_y \langle M_y^* M_y \rangle \hat{y} + 2P_z \langle M_z^* M_z \rangle \hat{z}}{\langle M_y^* M_y + M_z^* M_z \rangle} - \boldsymbol{P} \end{aligned} \tag{2.57}$$

if the scattering vector is assumed to be parallel to x. In the spin-echo experiment, the plane of precession of the neutron polarization isassumed to be rotated so that it contains the scattering vector. For the isotropic sample Equation 2.57 reduces to $\boldsymbol{P'} = -\hat{\boldsymbol{\kappa}}(\boldsymbol{P} \cdot \hat{\boldsymbol{\kappa}})$.

The final polarization can be split into two components, each with half the magnitude of the original polarization (Figure 2.6b), one of which receives a π flip. Magnetic echoes will be seen without using an external flipper. This has the great advantage that nuclear scattering no longer meets the echo condition, and so does not contribute. However, the converse is not true. If a π-flipper is used, the second magnetic component will contribute.

The scattered magnetic polarization is half the initial polarization. This is true for all cases except when $\boldsymbol{P}$ is parallel to x or y. When $\boldsymbol{P}$ lies parallel to the scattering vector,

Please purchase PDF Split-Merge on www.verypdf.com to remove this watermark.

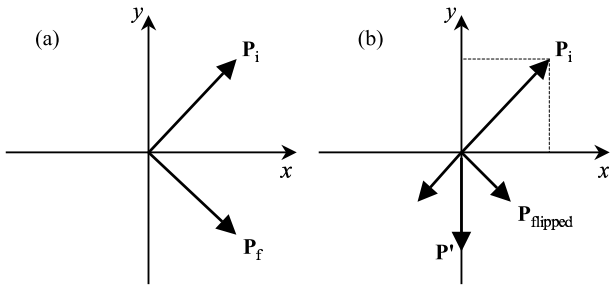

Figure 2.6: (a) The effect of a π-flipper on the neutron spin with the polarization in the $x-y$ plane. $\boldsymbol{P}_i$ is the incident polarization, and $\boldsymbol{P}_f$ that after the flipper. (b) The effect of isotropic magnetic scattering on a neutron spin polarized in the $x-y$ plane, where x is parallel to the scattering vector. $\boldsymbol{P'}$ shows the effect of the magnetic scattering and $\boldsymbol{P}_{flipped}$ is the component that contributes to the echo.

the entire polarization is π flipped. When $\boldsymbol{P}$ is perpendicular to the scattering vector, there is no π flip at all. For all other positions, a π flipped component of magnitude $P/2$ can be extracted. However, in a typical spin-echo experiment, a spread of polarizations are expected at the sample, and so these effects average out.

The next case of interest is a tetragonal single crystal with $\langle M_y^* M_y \rangle - \langle M_z^* M_z \rangle = A\langle M_y^* M_y + M_z^* M_z \rangle \neq 0$. The system is anisotropic, and the direction of this anisotropy is represented by A. This could occur in an antiferromagnet, or as critical fluctuations in a paramagnet. From Equation 2.57

$$\boldsymbol{P'} = (-P_x, AP_y, -AP_z) \tag{2.58}$$

If the precession plane is $\hat{x} - \hat{y}$, this can again be split into two components:

$$\boldsymbol{P'} = \left(\frac{1-A}{2}\right)(-P_x, -P_y, 0) + \left(\frac{1+A}{2}\right)(-P_x, P_y, 0). \tag{2.59}$$

The second term has been π flipped and contributes to the observed echo.

Please purchase PDF Split-Merge on www.verypdf.com to remove this watermark.

Chapter 3

Inelastic investigations of 3-k structures

Please purchase PDF Split-Merge on www.verypdf.com to remove this watermark.

Sommaire

Ce chapitre concerne l'identification des structures magnétiques dites ≪multi-$\boldsymbol{k}$≫, en utilisant les neutrons inélastiques. En 1981, Jensen et Bak [14] ont vu que les ondes de spin dans le composé USb peuvent être comprises si la structure n'était pas 1-$\boldsymbol{k}$ (avec un vecteur de propagation $\boldsymbol{k}$ pour décrire la structure), mais un type de phase 3-$\boldsymbol{k}$ (trois vecteurs de propagations sont nécessaires pour décrire la structure). Dans USb, les moments magnétiques se trouvent parallèles au vecteur de propagation, donc on appelle cela la phase 3-$\boldsymbol{k}$ longitudinale. Dans ce chapitre, ce principe est utilisé pour identifier le cas 3-$\boldsymbol{k}$ transverse (le moment magnétique est perpendiculaire du vecteur de propagation). L'exemple donné est la phase 3-$\boldsymbol{k}$ transverse dans le dioxyde d'uranium.

Antérieurement, la structure statique n'a jamais permis l'identification d'une structure multi-$\boldsymbol{k}$, et c'est pour cela que l'on est obligé de chercher des informations dans la réponse dynamique. UO_2 est un bon exemple d'une structure souhaitée. Les mesures indirectes donnent une grande probabilité que la structure est 3-$\boldsymbol{k}$ transverse, et les ondes de spin sont bien définies, si peu comprises. Une introduction aux études antérieures du dioxyde d'uranium est donnée.

Parce que les moments ne sont pas parallèles aux vecteurs de propagation, les neutrons polarisés sont nécessaires pour identifier l'anisotropie des ondes de spin. La polarimétrie sphérique neutronique est utilisée pour faire l'analyse. Les résultats donnent une description détaillée de l'anisotropie des fluctuations collectives dans les directions principales de l'espace réciproque. On confirme aussi la nature magnétique des excitations dans l'UO_2 et on en donne une description théorique. Ce comportement semble d'être caractéristique d'un structure 3-$\boldsymbol{k}$.

Les calculs souffrent du problème bien connu du dioxyde d'uranium - le nombre d'ondes de spin dans le zone de Brillouin [15]. Il y en a trois modes, mais la théorie présentée ici n'en donne que deux. Cela veut dire que les calculs ne sont pas exactement les-mêmes que les résultats, mais globalement ils donnent le comportement observé. Les deux modes théoriques correspondent à la mode acoustique et un des deux modes optiques. Cela est démontré quand on voit que l'anisotropie observée se développe intégralement dans un structure 3-$\boldsymbol{k}$. Pour le voir dans un structure 1-$\boldsymbol{k}$, les paramètres du modèle ne sont pas du tout réalistes. En conclusion, l'anisotropie des ondes de spin est particulier à un structure 3-$\boldsymbol{k}$.

Il sera intéressant de faire des mesures similaires sur d'autres composés 3-$\boldsymbol{k}$. Deux exemples déjà identifiés sont USb [16] et NpBi [17] (3-$\boldsymbol{k}$ longitudinale les deux). Les mesures ici peuvent confirmer, ou le contraire, la théorie sur l'USb. Il sera également intéressant d'étudier un échantillon magnétique moins complexe, par exemple le MnF_2, pour voir l'anisotropie dans un système mieux compris.

Please purchase PDF Split-Merge on www.verypdf.com to remove this watermark.

3.1 Introduction

This chapter discusses the use of inelastic scattering techniques to identify multi-$\boldsymbol{k}$ phases, in particular 3-$\boldsymbol{k}$ phases. Jensen and Bak [14] realised, in 1981, that the spin-wave spectra of USb could only be explained if the structure was assumed to be longitudinal 3-$\boldsymbol{k}$, and *not* single-$\boldsymbol{k}$. In this chapter this is extended to the transverse 3-$\boldsymbol{k}$ case, illustrating that the nature of the spin-wave excitations can be used to identify a 3-$\boldsymbol{k}$ structure.

To this end, a material with a transverse 3-$\boldsymbol{k}$ structure and strong dispersive inelastic excitations is required. UO_2 is an obvious candidate. It is a well-studied compound, thought to have a 3-$\boldsymbol{k}$ state, with a detailed spin-wave spectrum. An introduction to the physics of UO_2 is given below, followed by an analysis of the spin-wave spectrum using spherical neutron polarimetry. The results obtained give a detailed description of the anisotropy of the collective magnetic fluctuations modes propagating along the main symmetry directions in UO_2, a cubic 3-**k** antiferromagnet in which quadrupolar and magnetovibrational interactions are known to be far from negligible. These results confirm the magnetic character of the excitations observed in UO_2, and complete the phenomenological picture by providing a detailed description of the anisotropy of the fluctuation amplitudes. This behavior is then shown to be characteristic of a (transverse) 3-$\boldsymbol{k}$ structure.

3.2 The physics of uranium dioxide

The physical properties of uranium dioxide have been extensively investigated, principally because of its importance in the nuclear industry as both a fuel element and as a stable phase in which to store uranium. It also possesses interesting magnetic properties. Even now, over fifty years after the first experiments were carried out, the theoretical description of the magnetic structure and its excitations is still not complete.

As discussed earlier, the electronic state of a uranium ion is strongly influenced by its physical environment, and the level of localization of the $5f$ electrons is highly variable. In UO_2, the uranium ions are tetravalent, with the $5f^2$ levels sitting in a 6 eV gap between the valence and the conduction bands [18], and so the $5f$ electrons (and hence the magnetic moments) are highly localized.

Above $T_N = 30.8$ K, UO_2 is a paramagnetic semiconductor with the cubic fluorite structure and a Γ_5-triplet crystal field ground state [19]. The uranium lattice is fcc, with each uranium surrounded by a cubic oxygen cage. At room temperature the lattice parameter is $a = 5.470$ Å.

Below T_N there is a first order transition to Type-I antiferromagnetic order ($\boldsymbol{k} = \langle 001 \rangle$), with $\mu_{\rm ord} = 1.74\ \mu_B$ at $T = 4.2$ K. This is lower than expected for a Γ_5 state ($\sim 2.06\ \mu_B$). The magnetic transition is first order and is accompanied by a small internal distortion of the oxygen sublattice [20]. The overall symmetry remains cubic within experimental resolution and the point symmetry at the U site reduces to C_{3h} and the space group to $P3a$.

Please purchase PDF Split-Merge on www.verypdf.com to remove this watermark.

3.2.1 Magnetic structure

The magnetic transition was first observed as an anomaly in the heat capacity by Jones, Gordon and Long [21]. Powder neutron diffraction [22] found the propagation vector to be $\langle 001 \rangle$, with the uranium moments ordered $(+-)$ in planes along the axis of propagation. In this arrangement, magnetic Bragg reflections appear at (and only at) the systematic absences of the (nuclear) fcc structure, perfectly separating the nuclear and magnetic Bragg peaks. The moment direction was determined to be along the $\langle 111 \rangle$ directions.

Single crystal studies were carried out by Frazer *et al.* [23] and Willis and Taylor [24], placing the moment direction in the (110) plane, transverse to the propagation wavevector, contradicting the powder diffraction results. They also confirmed the $5f$ character of the valence electrons from form factor measurements of the magnetic signal. This work was extended by Faber and Lander [20], who established that the ordered magnetic moment was $1.74 \pm 0.02\ \mu_B$ per uranium atom at 4.2 K. They also deduced that the oxygen atoms were displaced from the ideal fluorite sites, because of a discrepancy between the theoretical and measured form factor at large scattering vectors. This is brought about by a static distortion of the oxygen cages, which gives rise to a nuclear Bragg peak at the same position as certain magnetic reflections. The authors were unable to distinguish experimentally between two models describing the shear necessary to reproduce the results. One model placed the shear parallel to the magnetic propagation vector, the other perpendicular. The authors deemed that the perpendicular model was more likely from the shape of the U^{4+} ion, arguing that the electrostatic interactions set up in this case were favourable. This model then called for four magnetic sublattices, not two as previously assumed, and therefore a non-collinear structure.

3.2.2 Spin-lattice interaction

Concurrently, the excitations in UO_2 were being investigated by Cowley and Dolling, who measured the phonons in 1965 [25] and the magnons in 1967 [26]. They noted significant magnon-phonon interaction between the magnons and the transverse phonons, principally close to the zone boundaries. This was broadly confirmed by Caciuffo *et al.* [15] in 1999, who used polarized neutrons to unambiguously separate magnetic and vibrational signals. Figure 3.1 (taken from Ref. [15]) shows the spin-wave dispersion as measured at 16.5 K along the principal crystallographic directions. There are three magnetic modes close to the magnetic zone centre, and two at the boundaries. In the left panel an anti-crossing effect is clearly visible; a phonon is present at this point, and hence the suspected cause is a magnon-phonon interaction.

Brandt and Walker [27] also saw evidence for a strong spin-lattice interaction in their studies of the elastic constants. All of the elastic constants change significantly at the antiferromagnetic transition, in particular the C_{44} constant (which measures shear strains) appeared to go to zero at the transition and then rose extemely sharply. Over 100 K above the transition, C_{44} continues to change considerably.

Allen developed a theory in 1968 [28, 29] to bind together all of these results. In two elegant papers, he describes a microscopic theory of the electronic ground state and

Please purchase PDF Split-Merge on www.verypdf.com to remove this watermark.

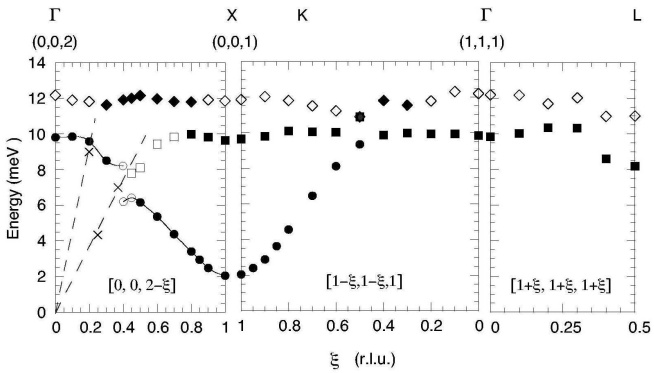

Figure 3.1: Spin-waves dispersion curves measured at 16.5 K along the principal crystallographic directions. The broken lines and crosses correspond to acoustic phonon branches measured at 270 K. Open symbols indicate qualitatively smaller magnon intensity than the filled points. The solid line in the left hand panel is a guide to the eyes. Taken from Ref. [15].

elementary electronic excitations that fits the spin wave measurements reasonably and that can be set up to give a first order transition. This is summarized in the following two paragraphs.

The degeneracy of the ground state of the uranium ion is *not* broken by the exchange interaction, as the uranium ion is orbitally degenerate and has an even number of electrons. Therefore, further interactions are required to bring about the magnetically ordered state. These interactions could arise from, for example, electrostatic quadrupole-quadrupole interactions, or Jahn-Teller distortions of the oxygen cages.

From the work on the magnetic dispersions and the elastic constants, it seemed clear that there was a spin-lattice interaction, and so Allen constructed his Hamiltonian on this basis, considering the interaction of the quadrupole moment on the U^{4+} ion with the eight surrounding O^{2-} ions. Using this, Allen reproduced the magnetic structure, *as it was understood at the time*, and gave a reasonable estimate of the magnetic excitations. He calculated that all external distortions cancelled out, leaving only distortions internal to the unit cell (i.e. rotations of the oxygen cage), in spite of the large anisotropies. He was also able to reproduce a first order transition (although the details of the temperature dependence were not exact) in which both the magnetic moments and the Jahn-Teller distortions order. This explains the behaviour of the C_{44} elastic constant: the distortion is always present, but at higher temperatures it is dynamic [30]. The internal distortion also affects the magnetic ground state: Ippolito, Martinelli and Bevilacqua [31] have found that a dynamical Jahn-Teller coupling of the Γ_5 ground state with a trigonal phonon mode gives the correct moment reduction.

This agreed nicely with the observations of Faber and Lander [20], with several key differences. Allen had considered a simple collinear magnetic structure, whereas Faber and Lander showed that, in fact, the structure was non-collinear. Because of this change in the basic assumptions, Allen's predictions may no longer be considered accurate (for

Please purchase PDF Split-Merge on www.verypdf.com to remove this watermark.

example, the oxygen cage distortion observed was not that predicted), but this does not detract from his central thesis: the importance of the spin-lattice interaction in the physics of uranium dioxide.

3.2.3 Three-k structure

Subsequently, further elastic diffraction was carried out by Burlet *et al.* [32] under magnetic fields, strongly suggesting that the magnetic structure and (by extension) the lattice distortion were both 3-$\boldsymbol{k}$ in nature. Burlet *et al.* observed that under an applied magnetic field, the relative strength of the $\langle 001 \rangle$ magnetic reflections did not change. Each of these peaks selects a different member of the star of $\{\boldsymbol{k}\}$ and so equal intensities indicate no change in the underlying K domain populations. Whilst not a positive proof, as the magnetic field might be too small to cause domain repopulation, one possible explanation for this behaviour is that the material has a triple-$\boldsymbol{k}$ structure, and hence no K domains.

An analysis of the crystal field splittings carried out by Amoretti *et al.* [19] found that the triple-$\boldsymbol{k}$ structure model reproduced the observed behaviour better than other models. However, one major problem is that the single-$\boldsymbol{k}$ structure was found to be energetically favourable with respect to the 3-$\boldsymbol{k}$ structure. Nuclear magnetic resonance experiments carried out by Ikushima *et al.* [33] indicate that the structure is 3-$\boldsymbol{k}$ on the basis of the symmetry of the electric field gradient observed. The experimental results presented in this thesis add to this weight of evidence that the structure is indeed transverse triple-$\boldsymbol{k}$.

Although a 3-$\boldsymbol{k}$ structure has no K domains, three S, or phase, domains are possible in a 3-$\boldsymbol{k}$ structure. 2D projections of these are illustrated in Figure 3.2. UO_2 is transverse, as magnetic peaks are seen at (001). Many neutron studies, in particular of the form factor [20], have shown that the intensities are consistent with an incoherent addition of the contributions from the two transverse S domains. This has recently been verified using resonant x-ray scattering [34], if the 3-$\boldsymbol{k}$ structure is assumed.

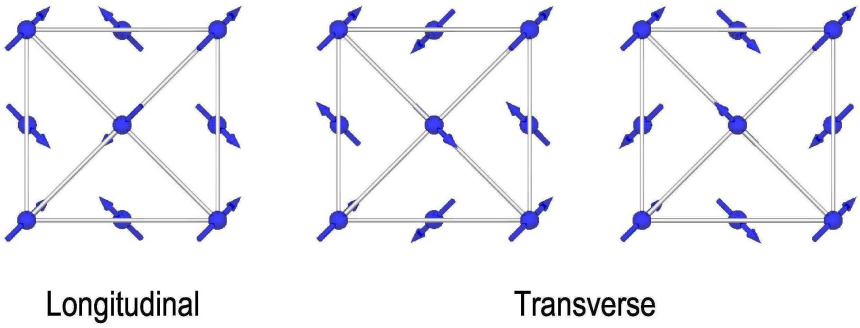

Figure 3.2: 2-D projections of longitudinal and transverse triple-$\boldsymbol{k}$ structures where $\boldsymbol{k} = \langle 001 \rangle$. Courtesy of Stuart B. Wilkins.

Please purchase PDF Split-Merge on www.verypdf.com to remove this watermark.

3.2.4 Spin wave dispersion

Much theoretical work on this material has tried to reproduce the observed spin wave dispersions. In the observed spectrum, three modes can be distinguished at the magnetic zone centre, one of which is weaker than the others. In a purely dipolar model two branches are predicted. If quadrupolar two-ion interactions are included [35] two further branches might appear, bringing the total to four, but these additional two branches should be much weaker than the others. In Giannozzi's work [36] the missing quadrupolar mode was supposed to have an intensity 10^{-2} of the neighbouring spin excitations, and so would not have been visible above the background even in the inelastic polarized neutron scattering experiments carried out.

Assuming that this split into spin and quadrupolar modes is correct, the 'spin' wave dispersions can be calculated, following a methodology developed for USb and CeSb [14, 37]. This will be described in more detail later, but essentially involves treating the uranium spins as independent spins, coupled via nearest neighbour Heisenberg interactions. As the spins are highly localized, this is a good approximation. Dipolar, anisotropic and crystal field terms are included in the Hamiltonian, which is then analyzed using the Holstein-Primakoff transformation. By this method, the dispersion of two branches can be adequately modelled, but only if the exchange interaction is assumed to be anisotropic, with a sign of the anisotropy that favours a longitudinal structure over the experimentally observed transverse structure. The parameters used also lead to a transition temperature $T_N = 45$ K. To improve this value, the anisotropy must be increased further in favour of a longitudinal structure. Similar problems are extant in the model of the dispersion developed using the model of Giannozzi, which relies on calculating the magnetic susceptibility directly.

Please purchase PDF Split-Merge on www.verypdf.com to remove this watermark.

3.3 Experimental Details

The technique of spherical neutron polarimetry (SNP) was used to investigate the spin-wave spectrum in UO_2, using the thermal-neutron three-axis spectrometer IN20 at the Institut Laue-Langevin, equipped with the CRYOPAD-II device. Further details on this technique are given in Section 2.6.3.

The experiment was performed on a single crystal of ~ 9 cm^3 in volume, cut from a melt-growth crystal boule of depleted uranium dioxide, supplied by P. duPlessis of the Witwatersrand University, South Africa. It proved to be single phase and close to stoichiometry, with a homogeneous mosaic spread of about 0.4 degrees. This sample was the same as that used by Caciuffo *et al.* [15].

IN20 was operated in the fixed-$\boldsymbol{k}_f$ mode ($k_f = 2.662$ Å^{-1}), with the standard polarized neutron setup: Heusler monochromator-Heusler analyser configuration (the Heusler alloy used was Cu_2MnAl). The sample was mounted on a mini-goniometer, and accurately oriented with the $[1\bar{1}0]$ direction vertical prior to installation in the CRYOPAD-II device.

Before starting the experiment, the CRYOPAD-II device was aligned and calibrated using the (004) Bragg reflection of a pyrolytic graphite crystal. An incident polarization $P_0 = 0.910(3)$ was obtained along three perpendicular directions. Measurements on the nuclear (002) Bragg peak of UO_2 with incident polarization parallel to z gave a scattered polarization $P = 0.891(1)$. The rotation of the neutron polarization as scattered elastically by magnetic Bragg reflections was then measured and found to be consistent with a transverse 3-$\boldsymbol{k}$ magnetic structure with an $\langle 001 \rangle$ propagation vector. The UO_2 crystal (99 g) was aligned with the scattering plane [001]-[110]. The neutron polarization axes x, y and z are illustrated for two points in this scattering plane in Figure 3.3.

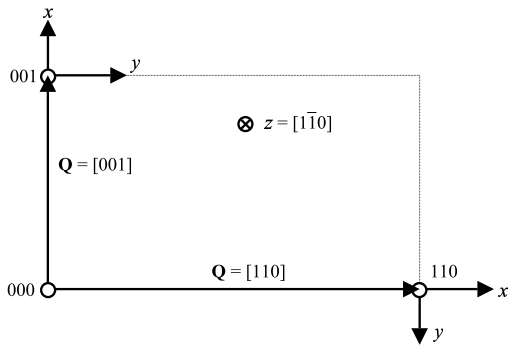

Figure 3.3: The [001]-[110] scattering plane of UO_2. The x and y neutron polarization directions are shown for $\boldsymbol{Q} = [001]$ and $\boldsymbol{Q} = [110]$. The z neutron polarization direction is always parallel to $[1\bar{1}0]$.

To recap the relevant results from Section 2.3 on polarized neutrons (neglecting the chiral magnetic term), in the presence of certain magneto-vibrational interference terms

Please purchase PDF Split-Merge on www.verypdf.com to remove this watermark.

the neutron polarization will be rotated. For example,

$$P_{fy}\sigma = (N^*M_{\perp y} + NM^*_{\perp y}) + i(N^*M_{\perp z} - NM^*_{\perp z})P_{ix} \tag{3.1}$$

so that a beam initially polarized along the x direction should have a small y polarization component after being scattered. In Eq. 3.1, σ is the double differential cross-section, N indicates the vibrational scattering amplitude, generated by the operator $\hat{A}$ and $M_{\perp\alpha}$ are Cartesian components of the inelastic magnetic scattering operator, generated by $\hat{\boldsymbol{B}}$. The magneto-vibrational term, responsible for the rotation of $\boldsymbol{P}$, involves correlation functions which couple the time dependences of the spin components perpendicular to $\boldsymbol{Q}$ and the time dependences of atomic displacements parallel to $\boldsymbol{Q}$ at the same position and time.

For $\boldsymbol{P}_i \parallel x$, the unrotated polarization is given by:

$$P_{fx}\sigma = a + NN^*P_i - (M_{\perp y}M^*_{\perp y} + M_{\perp z}M^*_{\perp z})P_{ix} \tag{3.2}$$

where a is a polarization-independent background term. Scattering from lattice vibrations, proportional to NN^*, gives rise to a non-spin-flip (NSF) signal, whereas magnetic scattering reverses the polarization of the beam, and hence leads to a spin-flip (SF) signal. On the other hand, with $\boldsymbol{P}_i \parallel y$ and negligible magneto-vibrational interference, one has

$$P_{fy}\sigma = NN^*P_i + (M_{\perp y}M^*_{\perp y} - M_{\perp z}M^*_{\perp z})P_{iy}. \tag{3.3}$$

Components of the magnetic fluctuation perpendicular to $\boldsymbol{Q}$ but parallel to $\boldsymbol{P}_i$ also give rise to NSF scattering, whereas components perpendicular to both $\boldsymbol{Q}$ and $\boldsymbol{P}_i$ produce SF scattering. P_{fz} behaves similarly.

The final polarization is extracted from SF and NSF measurements, where the SF measurement is taken with the fields in the second nutator inverted.

$$P_f = \frac{I_{NSF} - I_{SF}}{I_{NSF} + I_{SF}} \tag{3.4}$$

where I is the integrated intensity and the background should be subtracted as appropriate.

3.4 Results

3.4.1 At the magnetic zone centres

Measurements were performed at inelastic positions spanning the whole magnetic Brillouin zone. Some example scans taken at the magnetic zone centres are shown in Figure 3.4. The three panels on the left show constant-$\boldsymbol{Q}$ scans taken at $\boldsymbol{Q} = [001]$. The label $\alpha - \beta$ indicates that the initial polarization is along the α direction and that the final polarization is analyzed along the β direction. The three panels on the right show similar scans taken with the $x - x$, $y - y$ and $z - z$ geometry at $\boldsymbol{Q} = [110]$. The open and filled symbols correspond, respectively, to neutrons scattered either spin up (NSF) or spin

Please purchase PDF Split-Merge on www.verypdf.com to remove this watermark.

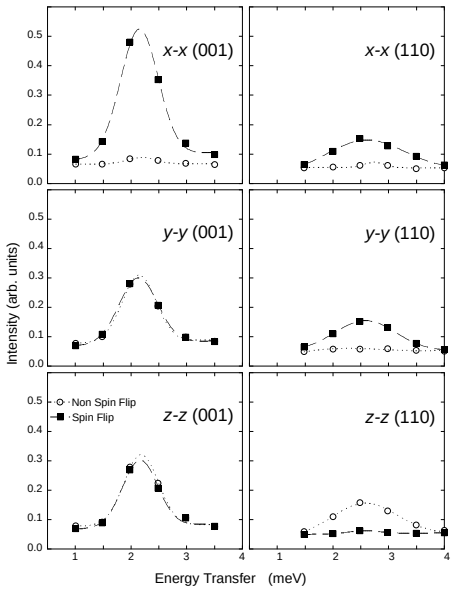

Figure 3.4: Constant-$\boldsymbol{Q}$ scans taken at (001) (left hand side) and (110) (right hand side). The neutron $x-x$, $y-y$ and $z-z$ spin-flip (SF = black squares) and non spin-flip (NSF = open circles) cross-sections are shown. The error bars are smaller than the point size.

down (SF) with respect to the chosen analysis direction, where the incident polarisation is defined to be spin up. A difference between these two counts implies a polarisation of the scattered beam.

The absence of NSF scattering in the $x-x$ measurement indicates that the excitation centered about 2.5 meV is purely magnetic in nature. The $y-y$ and $z-z$ cross-sections can then be used to gain further information on the polarisation of the fluctuations (see Equation 3.3).

At $\boldsymbol{Q}$ = [001], y is in the [110] direction, and z in the [1$\bar{1}$0] direction. In both the $y-y$ and $z-z$ channels, the SF and NSF signals are equal, indicating that fluctuations in the y and z directions have equal amplitudes leading to equal scattering intensity in both directions - there are isotropic fluctuations in the accessible plane.

At $\boldsymbol{Q}$ = [1 1 0], y corresponds to the [001] direction. For neutron polarization in the y direction, signal appears in the SF channel only, whereas for polarization along z, it is in the NSF channel only. This indicates that there are no magnetic fluctuations along the [001] direction (parallel to y). The $z-z$ data independently measures the same information as the $y-y$ data. This absence of fluctuations is also responsible for the weaker intensity measured at (110): only one component of the fluctuations is visible, as compared to two in the (001) case. This leads to the intensity difference (ratio 4:1) observed at the two positions. In principle some of the results presented here could be obtained by careful measuring of intensities obtained using unpolarized neutrons, but one would need to be confident that the difference was physical in origin, and not a resolution effect, for example. However, unexpected variations in intensity might be a sign that polarization analysis would be useful.

Please purchase PDF Split-Merge on www.verypdf.com to remove this watermark.

The above discussion focusses on the low-energy (acoustic) magnetic fluctuations. Figure 3.5 shows similar data taken at larger energy transfer, examining the less-dispersive magnetic modes. Again, the signal is all magnetic, but at (110) the 10 meV mode has equal amplitudes of fluctuation along y [001] and z [1$\bar{1}$0]. The (less intense) 12.5 meV mode shows a slightly larger magnetic amplitude along y than along z, evidenced by the small difference in NSF and SF scattering for the y direction, which is inverted with the polarization along the z direction. This indicates that the effect observed at low-energy transfers is a real difference and not simply due to the change in the magnetic cross-section due to a shift in scattering vector. The high-energy (optic) modes correspond to isotropic magnetic fluctuations, with amplitudes of comparable size along [001], [110] and [1$\bar{1}$0].

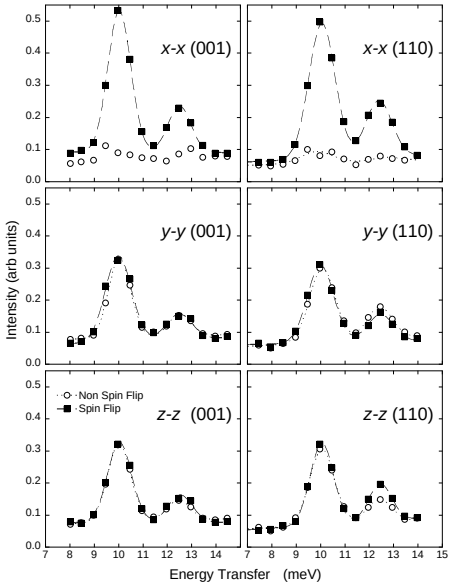

Figure 3.5: Constant-$\boldsymbol{Q}$ scans taken at (001) (left hand side) and (110) (right hand side) for an energy transfer of 8 - 14 meV. The $x-x$, $y-y$ and $z-z$ cross-sections are shown. SF scattering is indicated by filled squares and NSF scattering by open circles. The error bars are smaller than the point size.

3.4.2 Across the Brillouin zone

Data treatment

Information gathered from similar data sets taken at different $\boldsymbol{Q}$ positions was used to monitor the fluctuations of the collective modes propagating along the symmetric directions Δ, Σ and Γ throughout the whole Brillouin zone, from the (001) and (110) reciprocal lattice points. This information is collated in Figs. 3.6 - 3.11.

For each point, $x-x$, $y-y$ and $z-z$ measurements were taken and the excitations observed were fitted using Gaussian profiles to extract an intensity and centre-of-mass for each spin-wave. The centre-of-mass of the excitations in the $x-x$ scans was used to

Please purchase PDF Split-Merge on www.verypdf.com to remove this watermark.

establish the dispersions, and is plotted in the upper panels in Figures 3.6 - 3.11. For all of the points shown in these figures, no signal was observed in the $x-x$ NSF channel, indicating that the scattering at each point is magnetic in origin. For the $y-y$ and $z-z$ measurements, the fitted intensities were used to calculate a spin-flip fraction for each measurement, $I_{SF}/(I_{SF}+I_{NSF})$ where I_{SF} (I_{NSF}) represents the integrated intensity in the spin-flip (non spin-flip) channel. This is 1 if the scattering is all SF, and 0 if it is all NSF. This contains all of the information available from these measurements on the anisotropy of the fluctuations in the excitations with respect to the y and z directions.

Each figure contains an insert illustrating the positioning of the scattering vector $\boldsymbol{Q}$ in the scattering plane. The $\boldsymbol{P} \parallel y$ and $\boldsymbol{P} \parallel z$ data sets provide two independent measurements of the same quantity, with the z data expected to be the mirror image of the y data, and this comparison emphasises the robust nature of the data. The spin-flip fraction of each point in the dispersion plots can be identified by matching up the symbols.

Results

In Figures 3.6 and 3.7, the behavior of the modes propagating along $[\zeta\zeta 0]$ is illustrated. With $\boldsymbol{Q} \parallel [110]$, magnetic fluctuations in the plane $[001]-[1\bar{1}0]$ are accessible. With incident neutrons polarized along y (i.e. $[001]$), NSF scattering is absent if fluctuations along $[001]$ are negligible. This is observed in Figure 3.6 for the dispersive mode when $\zeta < 0.5$, whereas for $\zeta > 0.5$ the spin-flip fraction is about 0.5, suggesting that after the branches merge, fluctuations along $[001]$ and $[1\bar{1}0]$ have comparable magnitude. Results obtained with incident neutrons polarized along $[1\bar{1}0]$ (lower panel of Figure 3.6) confirm these conclusions. Figure 3.7 looks at the same branches again, but this time moving away from the (001) magnetic zone center. In this geometry, fluctuations along the $[110]$ direction are probed in place of the $[001]$ fluctuations.

Combining the data from Figures 3.6 and 3.7, at the magnetic zone center ($\zeta = 0$) all of the modes have equal amplitude fluctuation in the $[110]-[1\bar{1}0]$ plane, and the acoustic mode has no fluctuations in the $[001]$ direction. Around the magnetic zone-boundary ($\zeta = 0.5$) the excitation mode around 10 meV is polarized in the $[1\bar{1}0]$ direction, whereas the branch near 12 meV shows a small preference for fluctuations in the $[11\bar{1}]$ direction.

The modes propagating along $\langle\zeta\zeta\zeta\rangle$ are shown in Figures 3.8 and 3.9. For small ζ values in Figure 3.8, fluctuations in the $[001]-[1\bar{1}0]$ plane are explored. At low ζ, the acoustic branch is polarized along $[1\bar{1}0]$, whilst the non-dispersive branches at higher energy are almost isotropic in the plane perpendicular to $\boldsymbol{Q}$, with fluctuations along $[001]$ and $[1\bar{1}0]$ having finite amplitude. The behavior of the acoustic branch changes on approaching the zone boundary as fluctuations in the scattering plane increase in amplitude until the mode becomes isotropic in the plane perpendicular to $\boldsymbol{Q}$ for $\zeta = 0.5$. The plane explored in Figure 3.9 remains close to $[110]-[1\bar{1}0]$; anisotropic fluctuations develop for ζ larger than about 0.25, as the three modes start to merge. Then, the mode at 10 meV (the middle branch) becomes mostly $[1\bar{1}0]$ polarized, as does the mode propagating along $[\zeta\zeta 0]$ from the (001) position. In the 12 meV mode the fluctuation amplitude along $[1\bar{1}0]$ diminishes relative to the fluctuation amplitude in the scattering

Please purchase PDF Split-Merge on www.verypdf.com to remove this watermark.

plane.

In Figures 3.10 and 3.11 the [00ζ] magnons are investigated. From the (110) point, they are investigated in transverse geometry. Close to $\boldsymbol{Q} = [110]$, the accessible fluctuations are in a plane close to [001]-[1$\bar{1}$0]. The high-energy branches are isotropic in this plane, in contrast to the behavior of the low-energy mode, which has been assumed to hybridise strongly with the transverse Δ_5 acoustic phonon. At the magnetic zone center in fact, the [001] fluctuation is not present in the lowest energy magnon branch. In longitudinal geometry (Figure 3.11) the acoustic mode has equal amplitudes along [001] and [1$\bar{1}$0], like the two optic modes.

Cross-terms

Particular attention was devoted to the region where the magnon-phonon interaction was observed [26]. In the position where the anti-crossing occurs ($\sim$ (0 0 1.5)), a magneto-vibrational interaction should rotate the neutron spin, as outlined in Equation 3.1, and cross terms of the form $x-y$, $x-z$, etc. should be observed. We looked carefully for such a rotation, but none was observed (see Figure 3.12). In the cross-term channels, a signal was observed at the inelastic magnetic excitation, but there was no observable difference between the spin-flip and non spin-flip terms. From Equation 3.1, this indicates that $N^* M_{\perp z} - N M^*_{\perp z} = 0$; either there are no magneto-vibrational terms present, although the presence of polarization independent scattering indicates that there may be some, or the in-phase and out-of-phase contributions are equal. The lack of a polarization dependent signal could also be due to the low intensity of the magnon at this point in reciprocal space, or a weak phonon cross-section due to the small value of Q.

Please purchase PDF Split-Merge on www.verypdf.com to remove this watermark.

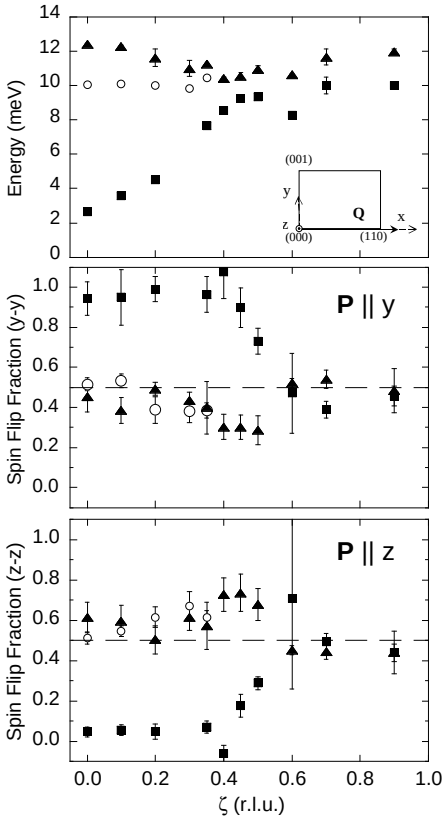

Figure 3.6: The modes in the [$\zeta\zeta$0] direction from the 110 magnetic zone center to 220. The upper panel shows the dispersion, and the insert indicates the scattering geometry and coordinate system for the neutron polarization. The lower panels show the ratio of SF to NSF (SF/(SF+NSF)) scattering for each mode, identified by symbol type, with data taken from the $y-y$ and $z-z$ cross-sections respectively.

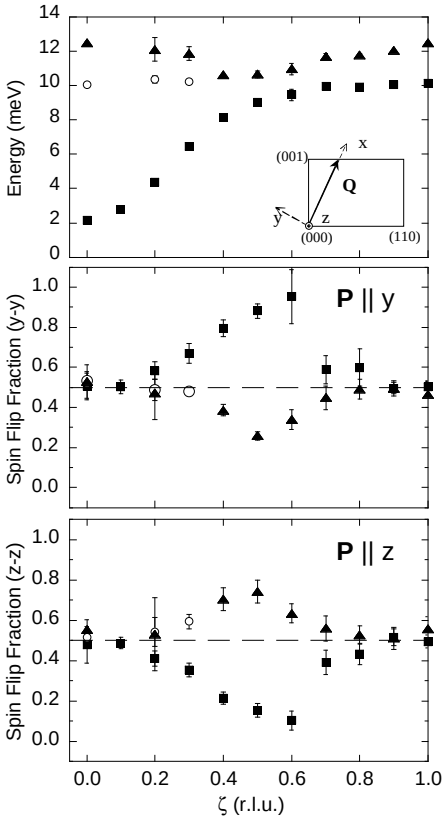

Figure 3.7: The modes in the [$\zeta\zeta$0] direction from the 001 magnetic zone center to 111. The upper panel shows the dispersion, and the insert indicates the scattering geometry and coordinate system for the neutron polarization. The lower panels show the ratio of SF to NSF (SF/(SF+NSF)) scattering for each mode, identified by symbol type, with data taken from the $y-y$ and $z-z$ cross-sections respectively.

Please purchase PDF Split-Merge on www.verypdf.com to remove this watermark.

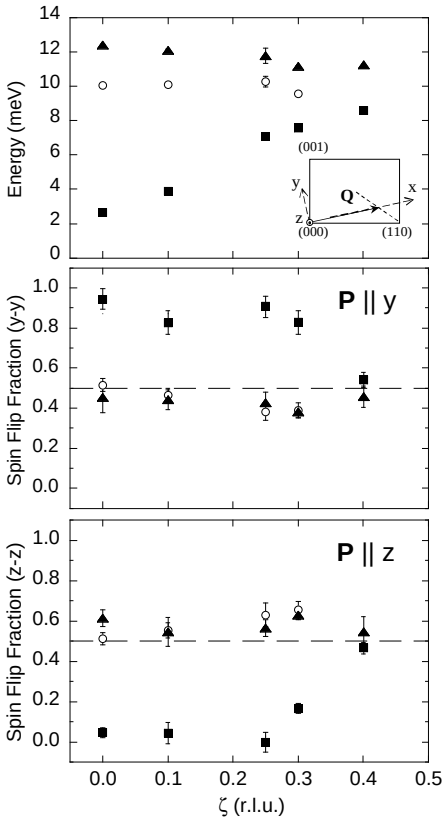

Figure 3.8: The normal modes of magnetic fluctuations in the $[\overline{\zeta}\zeta\zeta]$ direction from the (110) magnetic zone center to $\frac{1}{2}\frac{1}{2}\frac{1}{2}$. The upper panel shows the dispersion relation; the insert indicates the scattering geometry and coordinate system for the neutron polarization. The lower panels show the ratio of SF to NSF (SF/(SF+NSF)) scattering for each mode, identified by symbol type, with data taken from the $y-y$ and $z-z$ cross-sections respectively.

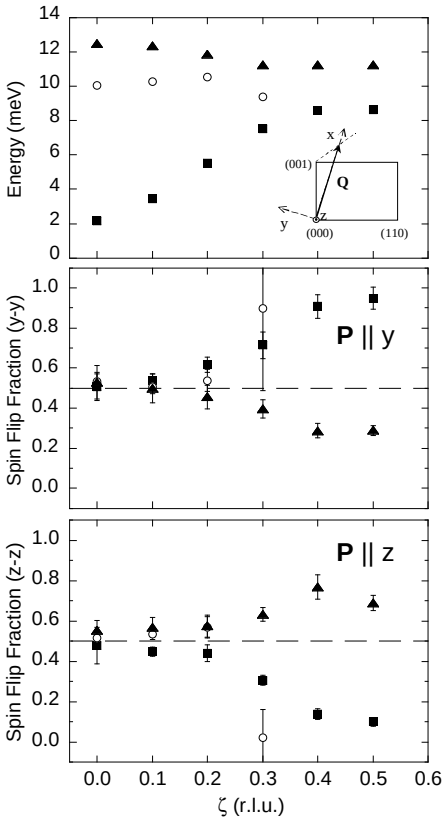

Figure 3.9: The normal modes of magnetic fluctuations in the $[\zeta\zeta\zeta]$ direction from the (001) magnetic zone center to $\frac{1}{2}\frac{1}{2}\frac{3}{2}$. The upper panel shows the dispersion relation; the insert indicates the scattering geometry and coordinate system for the neutron polarization. The lower panels show the ratio of SF to NSF (SF/(SF+NSF)) scattering for each mode, identified by symbol type, with data taken from the $y-y$ and $z-z$ cross-sections respectively.

Please purchase PDF Split-Merge on www.verypdf.com to remove this watermark.

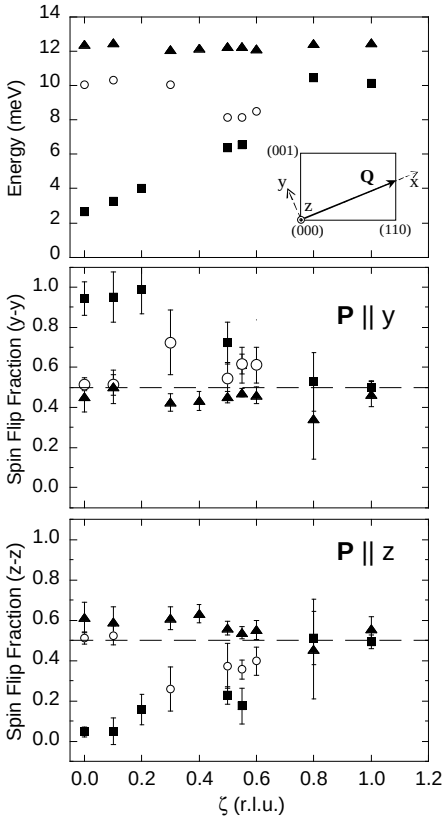

Figure 3.10: The normal modes in the [00ζ] direction from the (110) magnetic zone center to 111. The upper panel shows the dispersion relation; the insert indicates the scattering geometry and coordinate system for the neutron polarization. The lower panels show the ratio of SF to NSF (SF/(SF+NSF)) scattering for each mode, identified by symbol type, with data taken from the $y-y$ and $z-z$ cross-sections respectively.

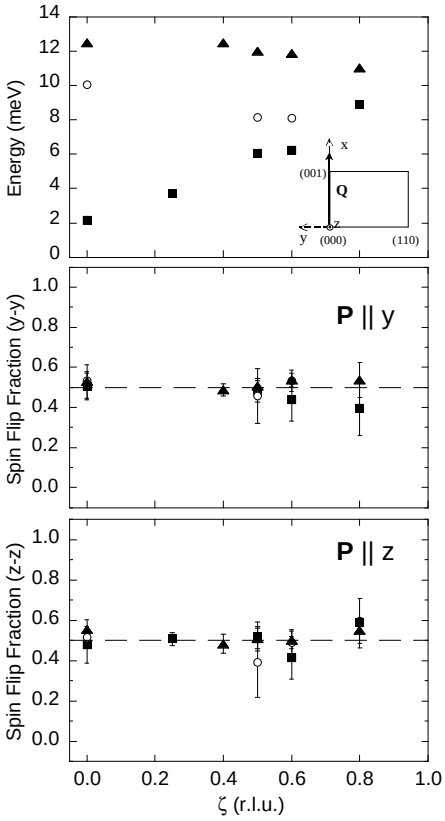

Figure 3.11: The normal modes in the [00ζ] direction from the (001) magnetic zone center to 002. The upper panel shows the dispersion relation; the insert indicates the scattering geometry and coordinate system for the neutron polarization. The lower panels show the ratio of SF to NSF (SF/(SF+NSF)) scattering for each mode, identified by symbol type, with data taken from the $y-y$ and $z-z$ cross-sections respectively.

Please purchase PDF Split-Merge on www.verypdf.com to remove this watermark.

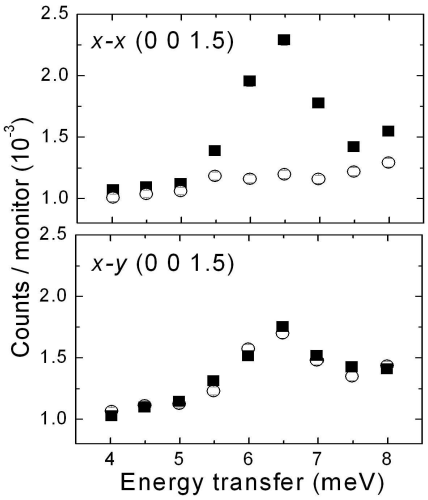

Figure 3.12: Constant-$\boldsymbol{Q}$ scans taken at (0,0,1.5). The x-x (upper panel) and x-y (lower panel) spin-flip (black squares) and non spin-flip (open circles) cross-sections are shown. The x-x data illustrates the presence of magnetic signal. In the x-y channel, no difference is observed between the spin-flip and non spin-flip cross-sections. The error bars are smaller than the point size, where not shown.

Please purchase PDF Split-Merge on www.verypdf.com to remove this watermark.

3.5 Model and Discussion

The results presented above indicate that the [001] fluctuations are always absent in the acoustic spin-wave mode. This work asserts that this is characteristic of a transverse 3-$\boldsymbol{k}$ magnetic structure, and that, more generally, an $\langle 001 \rangle$ fluctuation will be absent in a 3-$\boldsymbol{k}$ structure, building on the work of Jensen and Bak [14] on USb. Here, their model is summarized, and the extension to UO_2 considered. Finally, this is made more rigorous by calculating the expected susceptibility.

3.5.1 The Jensen and Bak model

USb is a cubic, NaCl-type material with a longitudinal 3-$\boldsymbol{k}$ structure, with the uranium atoms on fcc sites. Like UO_2 it is a Type-I antiferromagnet ($\boldsymbol{k} = \langle 001 \rangle$). Figure 3.2 illustrates the differences between the transverse and longitudinal 3-$\boldsymbol{k}$ structures using a 2-D projection.

The magnetic excitations in USb were first measured by Lander and Stirling [16]. They noticed that the acoustic excitation was present at $\boldsymbol{Q} = (110)$, but not at $\boldsymbol{Q} = (001)$. From Eq. 2.33, this means that this excitation consists of fluctuations in the [001] direction only. At the (001) magnetic Bragg reflection, only the component of the magnetic moment parallel to [001] contributes to elastic scattering (since this is a longitudinal material). If this were the only component involved in the inelastic scattering, then the excitation would have to involve longitudinal fluctuations of the magnetic moment. Whilst not unheard of, this is unusual.

Jensen and Bak [14] assumed that all three components of the magnetic moment (the three $\boldsymbol{k}$ values) were involved in the inelastic process. This placed the moment directions along the $\langle 111 \rangle$ directions, as illustrated in Figure 3.13. They then considered transverse fluctuations of these spins, and found that when the spins precess in phase (a reasonable approximation for the lowest energy mode) the [100] and [010] fluctuations cancel out. (This behaviour has also been observed in NpBi [17], another longitudinal 3-$\boldsymbol{k}$ structure.)

This can be generalized to the transverse structure of UO_2. The moments are large and well localized, and can be treated as classical vectors. For the structure in Figure 3.13, only the [100] fluctuation remains. For the second type of transverse structure, only the [010] fluctuation remains. This phenomenological argument explains the absence of the [001] fluctuation in the acoustic modes.

These results emphasise the difference between the elastic and inelastic scattering in these multi-$\boldsymbol{k}$ compounds. At any one magnetic Bragg reflection, the elastic scattering cross-section filters out two of the components. At all positions in reciprocal space, the inelastic scattering cross-section involves all of the components, apparently correlated from site to site. Secondly, the [110] and $[1\bar{1}0]$ fluctuations are equal in the acoustic mode. On the basis of the phenomenological model, either only one of the transverse S-domains is present, or they are both present in equal volume. Recent x-ray resonant scattering experiments on UO_2 have found this second case to be true [34].

Please purchase PDF Split-Merge on www.verypdf.com to remove this watermark.

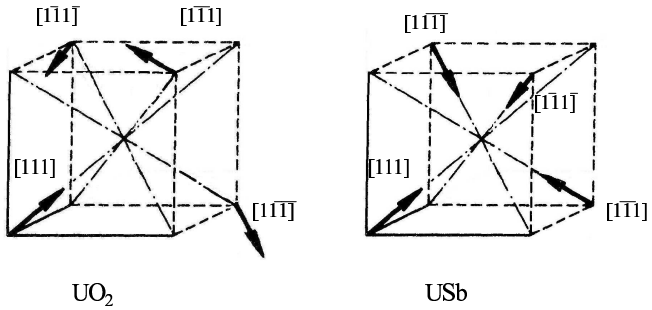

Figure 3.13: One eighth of the real space unit cells of UO2 and USb, with spin directions labelled.

3.5.2 Spin-wave calculations

Although spin waves in UO_2 have been experimentally investigated since the 1960s, a satisfactory theoretical understanding is still lacking. In particular, calculations of spin waves for the initially assumed 1-$\boldsymbol{k}$ magnetic structure could be brought into satisfactory agreement with experiment [26], whereas the actual 3-$\boldsymbol{k}$ structure is much more difficult to reconcile with the observed spin-wave spectra. In particular, whereas three branches are experimentally observed, two branches are predicted by purely dipolar models. If quadrupolar two-ion interactions are included [35] two further branches might appear, bringing the total to four. These additional two branches should be much weaker than the others.

Preliminary calculations

Preliminary calculations were done using the Hamiltonian of Jensen and Bak [14]. This has three terms: a nearest neighbour Heisenberg exchange, a dipolar anisotropic term and the crystal field term. This last term fixes the $\langle 111 \rangle$ directions as the easy axes, to model the three Fourier components as one simple vector.

$$\begin{aligned} H &= H_{iso} + H_{aniso} + H_{cef} \\ H_{iso} &= -\sum_{nn} J_1 \boldsymbol{S}_i.\boldsymbol{S}_j \\ H_{aniso} &= -\sum_{nn} J_D(\boldsymbol{S}_i.\boldsymbol{r}_{ij})(\boldsymbol{S}_j.\boldsymbol{r}_{ij}) \\ H_{cef} &= S_x^4 + S_y^4 + S_z^4 \end{aligned} \tag{3.5}$$

Please purchase PDF Split-Merge on www.verypdf.com to remove this watermark.

The sums are over nearest neighbours. Because of the transverse nature of UO_2, the $\boldsymbol{r}_{ij}$ in the anisotropic term describe an easy plane defined by the oxygen atoms. The equations of motion were found and the eigenvalues and eigenvectors evaluated using the Holstein-Primakoff transformations. As expected for this simple model, the calculated dispersions were not exact, but acoustic and optic branches were clearly identifiable. From the eigenvectors, the $y-y$ spin-flip fraction for a mode at a particular $\boldsymbol{Q}$ could be calculated; qualitatively along the $[\zeta\zeta 0]$ direction from the 110, there were no [001] fluctuations in the acoustic branch and the optic branch had a spin-flip fraction of ~ 0.5.

Dynamical susceptibility calculations

As these basic calculations indicate that the 3-$\boldsymbol{k}$ structure may be responsible for the observed behaviour, more detailed calculations of the dynamical susceptibility were carried out in collaboration with N. Magnani and P. Santini at the Universitá di Parma.

In the following, for the static 3-$\boldsymbol{k}$ structure a mean-field model similar to that adopted in Ref. [35] is used. This is based on anisotropic exchange and effective lattice-mediated quadrupolar interactions. Each U ion has an associated $S=1$ pseudospin corresponding to the Γ_5-triplet crystal-field ground state. This multiplet carries magnetic-dipole and Γ_3, Γ_5 electric-quadrupole degrees of freedom. In addition to the usual two-ion dipolar superexchange, effective quadrupole interactions are expected to arise from the magnetoelastic coupling. Excited crystal-field states lie above 150 meV and are not expected to produce qualitative changes in the low temperature behaviour.

Although there are four inequivalent sites, in the mean-field approximation the problem can be reduced to the study of a single self-consistent effective Hamiltonian

$$H_{MF} = -JS\langle S\rangle - KQ\langle Q\rangle, \tag{3.6}$$

where $S = \boldsymbol{n}(i)\cdot\boldsymbol{S}(i)$ is the component of the spin along the direction of the moment $\boldsymbol{n}(i)$ in the i^{th} sublattice (parallel to one of the four cube diagonals), and $Q = [(\boldsymbol{n}(i)\cdot\boldsymbol{S}(i))^2 - 2/3]$ is the quadrupole operator describing an axial distortion of the charge distribution along $\boldsymbol{n}(i)$. The first term in H_{MF} drives the order, and the second is needed to account for the first-order character of the phase transition. Since Q and S commute, the eigenstates of H_{MF} do not depend on the values of the J and K parameters, but the eigenvalues obviously do.

Spin-wave excitations are calculated within a random-phase-approximation approach [37]. This is equivalent to the method used in Ref. [35], apart from the fact that quadrupolar interactions between fluctuations are neglected. Indeed, these effects are expected to be minor [35], as the main role of quadrupolar terms in the dynamics being a modification of the single-ion energy gaps (the latter determines the overall energy scale of spin waves). The exchange is limited for simplicity to nearest-neighbour ions, and is parameterized by J and a second parameter, δ, which represents the anisotropic part of exchange [37]. The relation between the parameters here and those of Ref. [37] is $J = 2J_0$, whilst we define $\delta = (J_1^l - J_1^t)/|J_1^t|$. The off-diagonal exchange parameter J_1^a has no effect on spin-waves in the high-symmetry directions considered here. For isotropic exchange, $\delta = 0$. The stability of the transverse structure requires $\delta > 0$.

Please purchase PDF Split-Merge on www.verypdf.com to remove this watermark.

The wavevector- and frequency-dependent dynamical susceptibility tensor $\chi_{\alpha\beta}(\boldsymbol{Q},\omega)$, whose poles and residues correspond to the frequencies and neutron-scattering intensities of spin-wave excitations, is obtained by starting from the single-ion dynamical susceptibilities calculated with H_{MF}, and by implementing the random-phase-approximation scheme of Ref. [37]. The calculation of the cross-section for polarized neutrons is obtained by using the general expression [6] which describes the final polarization $\boldsymbol{P}_f$ of a scattered neutron beam as a function of the incident beam polarization $\boldsymbol{P}_i$. Defining the **x**-axis as parallel to $\boldsymbol{Q}$ and choosing $\boldsymbol{P}_i \perp \mathbf{x}$ one obtains

$$P_{f\alpha}\left(\frac{d^2\sigma}{d\omega d\Omega}\right) \propto \{P_{iy}\left[S_{\alpha y}(\boldsymbol{Q},\omega)+S_{y\alpha}(\boldsymbol{Q},\omega)\right]+P_{iz}\left[S_{\alpha z}(\boldsymbol{Q},\omega)+S_{z\alpha}(\boldsymbol{Q},\omega)\right]$$

$$-P_{i\alpha}\left[S_{yy}(\boldsymbol{Q},\omega)+S_{zz}(\boldsymbol{Q},\omega)\right]\}, \tag{3.7}$$

where

$$S_{\alpha\beta}(\boldsymbol{Q},\omega)=\frac{\chi''_{\alpha\beta}(\boldsymbol{Q},\omega)}{\pi\left[1-\exp\left(-\hbar\omega/k_BT\right)\right]}. \tag{3.8}$$

For a given $\boldsymbol{Q}$, $S(\boldsymbol{Q},\omega)$ has three poles (two of which are always degenerate), corresponding to two spin-wave branches. For the $\boldsymbol{Q}$ directions considered here, each diagonal term of the susceptibility tensor $\chi''_{\alpha\alpha}(\boldsymbol{Q},\omega)$ in the cubic reference frame contributes a pole $\omega^{\alpha\alpha}(\mathbf{Q})$. For instance, for $\boldsymbol{Q}$ along [001] or [110], two of the dispersion curves $\omega^{xx}(\boldsymbol{Q})$, $\omega^{yy}(\boldsymbol{Q})$, and $\omega^{zz}(\boldsymbol{Q})$ are degenerate, have equal intensity, and correspond to the optical mode, whereas the third one (ω^{xx} or ω^{yy} depending on which of the two possible S-domains is considered) corresponds to the acoustic branch.

As in the central panel of Figures 3.6-3.11, the **y**-axis is defined to be parallel to the incident-beam polarization $\boldsymbol{P}_i$ (the **x**-axis is parallel to $\boldsymbol{Q}$). The **z**-axis is defined by $\mathbf{x}\times\mathbf{y}$. In the following, the cubic-axes reference frame will be denoted by $\bar{x}$, $\bar{y}$, $\bar{z}$. For $\boldsymbol{P}_f \parallel \mathbf{y}$, the measured spin-flip fraction for a given spin-wave mode of frequency $\omega_0(\boldsymbol{Q})$ is given by $I_{zz}/(I_{yy}+I_{zz})$, where $I_{\alpha\alpha}=S_{\alpha\alpha}(\boldsymbol{Q},\omega_0(\boldsymbol{Q}))$, and α refers to the chosen ($\boldsymbol{Q}$-dependent) reference frame. For instance, by rotating the generalized susceptibility tensor to a reference frame x, y, z matching the one used in Figure 3.6, one has that

$$\chi_{yy}=\chi_{\bar{z}\bar{z}};\chi_{zz}=\frac{\chi_{\bar{x}\bar{x}}+\chi_{\bar{y}\bar{y}}}{2}. \tag{3.9}$$

For both S domains, this leads to a $y-y$ spin-flip fraction (central panel of Figure 3.6) equal to 1 for the acoustic branch. In fact, for this branch $I_{yy}=0$ because it has no fluctuations along the cubic $\bar{z}$-axis. This is a consequence of the general behavior expected for a transverse 3-$\boldsymbol{k}$ structure, as discussed in the paragraphs following Equation 3.8. For $\boldsymbol{Q}$ lying in the scattering plane [001]-[110], the eigenvalue $\omega_{\bar{z}\bar{z}}$ is associated to the optical branch, so that the acoustic branch amplitude has no contribution from $\chi_{\bar{z}\bar{z}}$. In the reference frame of the experiment (for instance the one of Figure 3.6), $\chi_{yy}=\chi_{\bar{z}\bar{z}}$ is therefore zero. The spin flip fraction is about 1/3 for the optical branch since for the latter $I_{yy}\sim 2I_{zz}$ (in fact, in the second equality of Equation 3.9, only one of the two terms in the numerator is nonzero). The corresponding $z-z$ spin-flip fractions are simply their complements to one. This is perfectly compatible with the experimental data in the

Please purchase PDF Split-Merge on www.verypdf.com to remove this watermark.

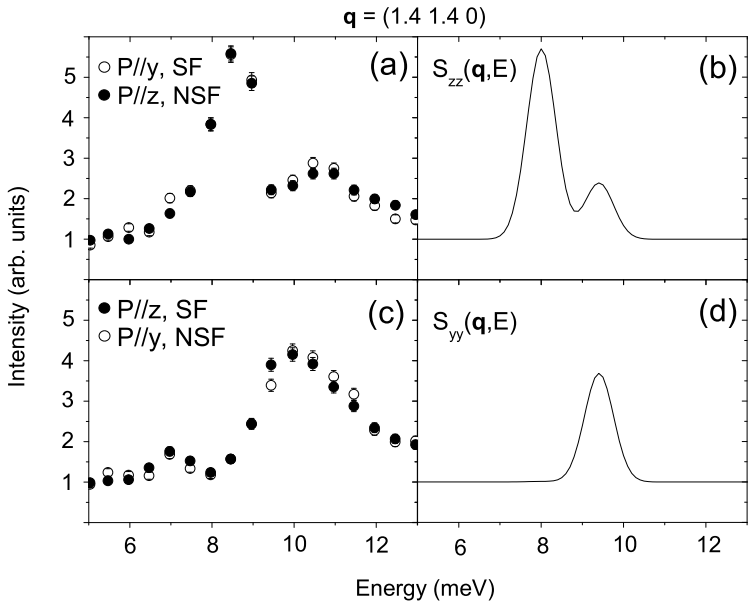

Figure 3.14: Measured and calculated inelastic neutron scattering spectra at $\boldsymbol{Q}$ = (1.4 1.4 0) in the scattering geometry of Figure 3.6. Panel (a) shows the fluctuations parallel to the z direction and panel (c) the fluctuations parallel to the y direction. The 8.5 meV peak in panel (a) corresponds to the acoustic branch, and the 10.5 meV peak to the two optical branches. The 7 meV peak is non-magnetic in nature. The theoretical cross-sections in panels (b) and (d) have been gaussian-broadened to match the experimental resolution. The single plotted curve in panels (b) and (d) should match both data sets in panels (a) and (c) respectively.

region where the acoustic and the optical branches are well separated ($\zeta \leq 0.5$). It should be noted that, although (as stated above) one of the two optical branches is missing in the model, experimentally these display very similar polarization properties. An example of comparison between measured and calculated inelastic neutron scattering spectra is shown in Figure 3.14.

As for Figure 3.11, the generalized susceptibility tensor rewritten in the suitable reference frame gives

$$\chi_{yy} = \chi_{zz} = \frac{\chi_{\bar{x}\bar{x}} + \chi_{\bar{y}\bar{y}}}{2}. \tag{3.10}$$

Of course, this experimental configuration cannot detect any anisotropic behaviour in the magnetic fluctuations; this is confirmed by the present experimental result, as a spin-flip ratio 1/2 is detected for all branches.

On the other hand, returning to Figure 3.6 but supposing the 3-$\boldsymbol{k}$ structure to be longitudinal, the acoustic branch can be identified with $\omega^{\bar{z}\bar{z}}(\mathbf{Q})$ and the optical branch with $\omega^{\bar{x}\bar{x}}(\mathbf{Q})$ and $\omega^{\bar{y}\bar{y}}(\boldsymbol{Q})$; therefore, the $y-y$ spin-flip fraction would be 0 for the former ($I_{zz} = 0$) and 1 for the latter ($I_{yy} = 0$). As this is not compatible with the experimental data, polarization analysis clearly discriminates between 3-$\boldsymbol{k}$ longitudinal and 3-$\boldsymbol{k}$ trans-

Please purchase PDF Split-Merge on www.verypdf.com to remove this watermark.

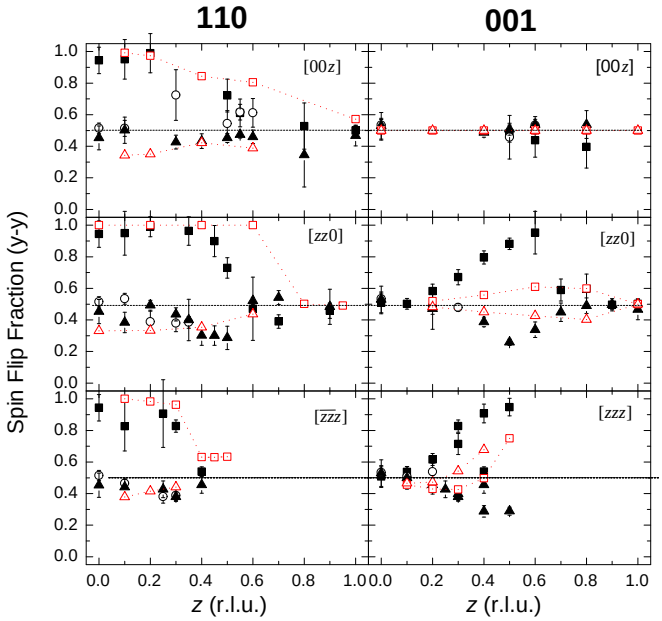

Figure 3.15: Measured (black) and calculated (red) $y-y$ spin flip fractions for directions from the 110 (right-hand side) and 001 (left-hand side) magnetic zone centres.

verse excitations. Of course, this is more readily shown by the absence of the elastic (001) Bragg peak in the case of a longitudinal structure.

As far as all other investigated directions are concerned, the calculated polarizations well reproduce the measured ones whenever optical and acoustic branches are energetically well separated (Figure 3.15). The modelled data applies to the two branches (squares and triangles in the previous notation). The model data have the same qualitative form as the real data, although the exact values are not perfectly matched. The major difference between model and theory occurs along the $[\zeta\zeta\zeta]$ branch off 001.

The above results do not depend on the precise values of the three parameters of the model (J, K, δ). The correct range for these values has been set by a qualitative matching of the model with the observed static properties and spin-wave frequencies. For all three parameters we obtain values close to those used in Ref. [35]. In particular, a slightly larger value of T_N (40 K) with respect to the experimental one had to be assumed in order to match spin-wave energies. No attempts were made to precisely fit the experimental dispersion curves, since the presence of three branches makes it difficult as only two branches are allowed by the present model. However, it was verified that the calculated spin-flip fractions are unchanged if the values of J and K are varied in the range consistent with macroscopic behavior. This is also true when different values of the anisotropic exchange ratio are used.

When acoustic and optical branches are well separated, the agreement between the

Please purchase PDF Split-Merge on www.verypdf.com to remove this watermark.

theoretical and experimental spin-flip fractions is very good, and in particular the peculiar behaviour of the acoustic mode is confirmed. Instead, for $\boldsymbol{Q}$-values where acoustic and optical branches are close in energy, the spin-flip fractions extracted from the experimental data appear to deviate from the calculated ones. These deviations are not understood at present. They might be due to effects not included in the present model (e.g., spin-phonon interactions, or whatever produces the third spin-wave branch). However, we cannot completely rule out that the deviations are an artefact, due to the difficulty of assigning the measured total scattering intensity to the different spin-wave modes, when their energies are closer than the experimental energy resolution. In fact, the deviation of the experimental ratios from the calculated ones resembles that expected for not fully discriminated spin-wave peaks.

3.6 Conclusions and summary

The polarization of the spin-wave modes in the ordered 3-$\boldsymbol{k}$ state of UO_2 has been examined experimentally using three-dimensional polarisation analysis techniques. The information obtained allows the directions and relative amplitudes of fluctuations giving rise to the inelastic scattering event to be assessed. Fluctuations along three axes of symmetry (Δ, Σ, Γ) have been investigated. The measured polarizations of acoustic and optical branches of UO_2 are consistent with those expected for the 3-$\boldsymbol{k}$ static ordered structure, at least at points in reciprocal space where branches are well separated in energy. Exact quantitative calculations suffer from the well-known problems of calculating the exact dispersion relations in UO_2, but the qualitative results obtained here are not strongly influenced by changes of the model parameters within physically reasonable limits. No direct evidence for magnon-phonon interactions was found.

An important issue in the calculations is that the observed polarization behavior emerges in a natural way under the assumption of 3-$\boldsymbol{k}$ order. Assuming a 1-$\boldsymbol{k}$ structure, a similar behavior can in principle be obtained, but only for anisotropic exchange parameters satisfying particular conditions. That is, whereas for a 3-$\boldsymbol{k}$ structure the observed anisotropic fluctuations occurs whatever the coupling strength, in a 1-$\boldsymbol{k}$ structure it could only be the result of an accident. This indicates that the behaviour observed here is the generalisation of the observations of Jensen and Bak [14] in the longitudinal 3-$\boldsymbol{k}$ material USb to all 3-$\boldsymbol{k}$ systems, and indicates that the $\boldsymbol{k}$ wavevectors give a correlated response.

It would be interesting to perform similar measurements on other 3-$\boldsymbol{k}$-ordering compounds, such as USb [16] or NpBi [17]. For instance, the latter orders in a longitudinal structure, with well-defined spin-waves whose dispersion and intensities are well reproduced by a model of localized $5f$-electrons in a crystal-field [14, 37]. Spin-wave polarization measurements could be used to test quite selectively the correctness of the theoretical picture for USb. Indeed, this picture has been put into question several times because the excited crystal-field states the model predicts have not yet been experimentally observed [38].

Please purchase PDF Split-Merge on www.verypdf.com to remove this watermark.

Chapter 4

Elastic observations in 3-k structures

Please purchase PDF Split-Merge on www.verypdf.com to remove this watermark.

Sommaire

Dans le chapitre 3, on a vu que la structure magnétique 3-$\boldsymbol{k}$ possède des dynamiques fondamentalement différentes de celles observées dans un structure 1-$\boldsymbol{k}$. Les résultats indiquent que les trois composantes de Fourier pour la description de l'aimantation doivent être corrélées pour expliquer le comportement des ondes de spin. Pour mémoire, une phase 3-$\boldsymbol{k}$ est ainsi nommée parce que trois vecteurs de propagation $\boldsymbol{k}$ dans le même volume sont obligatoires pour expliquer la structure observée. Si on prend ce modèle, la question est : Y a-t-il des corrélations entre ces trois paramètres de l'ordre magnétique ? Et si c'est le cas, peut-on les voir ?

Dans ce chapitre, la recherche pour ces corrélations est présentée. Les composés choisis pour la cherche sont des composés d'uranium de type NaCl. Ils montrent beaucoup de structures multi-$\boldsymbol{k}$, grâce aux qualités de l'ion d'uranium et des électrons $5f$ (Section 1.2). Les composés utilisés sont présentés, avec une courte discussion sur les différentes possibilités d'une corrélation, ou cohérence entre les trois paramètres de l'ordre magnétique.

La diffusion neutronique et photonique montrent tous les deux qu'il y a des pics de Bragg faibles aux positions $\boldsymbol{k}_3 = \tau + \langle 1/2\ 1/2\ 1/2\rangle$, où τ est un vecteur du réseau réciproque et 1/2 est dans les unités du réseau réciproque. Ces pics sont indépendants de l'échantillon. L'origine n'est pas une petite phase separée dans le cristal. D'abord, un tel vecteur de propagation $\langle 1/2\ 1/2\ 1/2\rangle$ n'a jamais été vu avant dans des composés d'uranium type NaCl. La largeur des pics est un argument plus persuasif : c'est la même pour les pics $\boldsymbol{k}_3$ et pour les pics magnétiques normaux. Cela montre que ces deux groupes de pics sont ordonnés sur la même échelle de distance - le cristal entière. Les expériences montrent que ces pics $\boldsymbol{k}_3$ ne sont pas le résultat des événements de diffusion multiples.

Cela laisse un objet avec l'ordre à grande distance, et une direction favorisée parallèle à $\langle 111\rangle$. Une distorsion du réseau n'est pas soutenue par ces observations. La mesure avec les neutrons confirme que ces pics existent sur une échelle de temps thermodynamique ($\sim 10^{-11}$ à 10^{-12} s). Le facteur de forme pour ces pics n'est pas facile à extraire des données, parce que la structure magnétique derrière ces pics n'est pas connu. Néanmoins, on peut deviner, en utilisant les absences systématiques observées, mais le résultat ne semble pas en accord avec les facteurs de forme traditionelles. Le chapitre 5 donne une justification pour l'observation de ces pics $\boldsymbol{k}_3$, et ses propriétés.

Please purchase PDF Split-Merge on www.verypdf.com to remove this watermark.

4.1 Introduction

The previous chapter showed that a 3-$\boldsymbol{k}$ structure has different dynamics to those expected for a single-$\boldsymbol{k}$ structure, and the apparent involvement of all three Fourier components in creating the spin-wave spectrum indicates that the three $\boldsymbol{k}$ wavevectors, or order parameters, are correlated.

To recap, a 3-$\boldsymbol{k}$ phase is so called because a consistent interpretation of the positions and symmetries of the magnetic Bragg peaks is not possible within the confines of a model magnetic order parameter based on a single propagation wavevector. Instead three (orthogonal) propagation vectors, with their associated magnetic moments, are required to exist simultaneously in the same volume.[1] Taking this as a working model a natural question is whether or not long-range coherent correlations exist between the conjectured order parameters, as hinted at by the inelastic scattering results. If so, what form would this take, and how might it be brought to light by known diffraction techniques?

To investigate this problem, the uranium rock-salts have been chosen for study. As a group, they display many different multi-$\boldsymbol{k}$ structures, due to the unique qualities of the uranium ion and its $5f$ electrons (Section 1.2). In this chapter, the particular compounds studied are introduced, followed by a short discussion of the search for order parameter correlations in these compounds. Experimental evidence for these correlations is then presented. The subsequent chapter attempts to place this in a theoretical context.

4.2 Uranium rock-salts

The uranium monopnictide-monochalcogenide solid solutions were well studied in the 1980s (for a comprehensive review, see Ref. [39]). These materials display a wide range of magnetic properties. Physically, they are all NaCl-type structures, and the pnictides and chalcogenides are perfectly soluble. The lattice parameters of the solid solution crystals follow Vegard's law. Magnetically, the monopnictides are typically antiferromagnetic, with a range of multi-$\boldsymbol{k}$ structures observed. The monochalcogenides are usually ferromagnetic. For this work, two different solutions were considered, $UAs_{1-x}Se_x$ and $USb_{1-x}Te_x$. In both cases the addition of the chalcogenide acts to reduce the number of electrons in the conduction band, and hence alters the electronic environment of the magnetic $5f$ level.

4.2.1 $UAs_{1-x}Se_x$

Kuznietz *et al.* [40] carried out a series of neutron diffraction experiments and uncovered a rich phase diagram, filled with longitudinal multi-$\boldsymbol{k}$ and incommensurate phases. This work was redone recently using x-ray resonant scattering by Longfield *et al.* [41]. The $x = 0.2$ composition, whose phase diagram as a function of temperature is shown in Figure 4.1, was selected for study as it contains both 2-$\boldsymbol{k}$ and 3-$\boldsymbol{k}$ phases. The lattice parameter is 5.78 Å at room temperature, and the ordered magnetic moment is $\sim 2\ \mu_B$ at 4.2 K.

[1] Some authors use a non-orthogonal basis set.

Please purchase PDF Split-Merge on www.verypdf.com to remove this watermark.

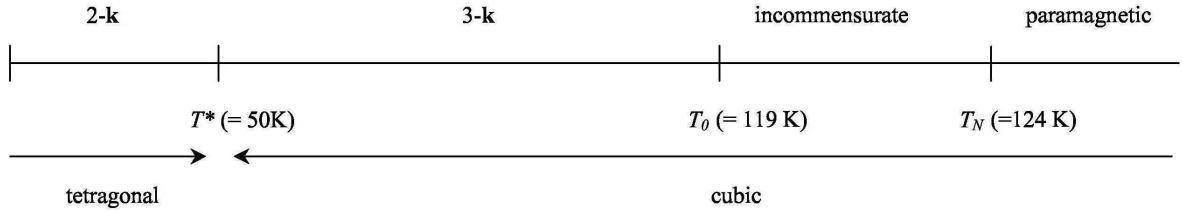

Figure 4.1: Phase line for $UAs_{0.8}Se_{0.2}$ as a function of temperature. $\boldsymbol{k} = \langle 00\frac{1}{2}\rangle$.

Below $T_N = 124$ K, the compound enters an incommensurate ordered magnetic state. At $T_0 = 119$ K, this develops into a commensurate 3-$\boldsymbol{k}$ configuration with propagation vector $\langle 00\frac{1}{2}\rangle$ in reciprocal lattice units (rlu). At $T^* = 50$ K the cubic symmetry is broken and the low-temperature commensurate 2-$\boldsymbol{k}$ phase develops. The crystal structure is now tetragonal. A rationale for this transition was given in Section 1.3.1. The change in the crystal structure is small, but definitely present, as shall be seen later (Section 4.4).

Heat capacity of $UAs_{0.8}Se_{0.2}$

All of the transitions can be seen clearly in the heat capacity (Figure 4.2). In an external magnetic field, the antiferromagnet-paramagnet transition remains essentially unchanged, but the transition at T^* shifts and broadens.

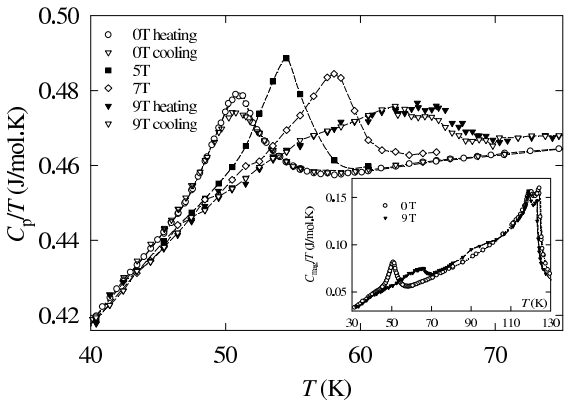

Figure 4.2: C_p/T for $UAs_{0.8}Se_{0.2}$ under applied magnetic field, measured on an 80 mg single crystal in a Quantum Design PPMS-9 calorimeter. The inset is C_{mag}/T over a broader temperature range. C_{mag} has been calculated by comparison with a thorium blank. This figure courtesy of Pavel Javorský. The lines are guides for the eye.

Magnetization of $UAs_{0.8}Se_{0.2}$

The M/H magnetization ratio, where M is the magnetization and H the magnetic field, was measured by sweeping the temperature at a given magnetic field H parallel to the

Please purchase PDF Split-Merge on www.verypdf.com to remove this watermark.

[100] axis (Figure 4.3). The magnetization observed at a constant temperature whilst sweeping the magnetic field was found to be consistent. In a magnetic field the anomaly at T^* become more pronounced. The location of the anomaly shifts upwards and matches perfectly with the changes in the heat capacity.

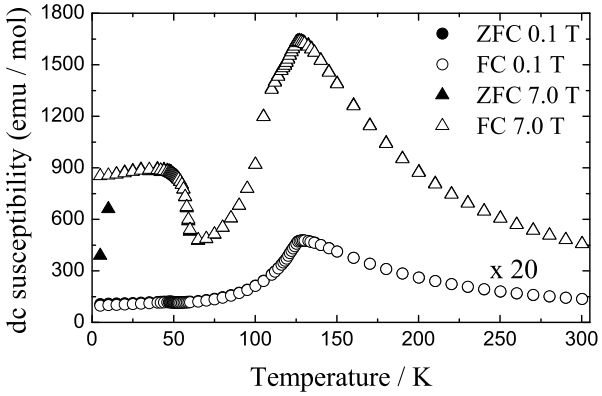

Figure 4.3: The ratio M/H for an 80 mg single crystal of $UAs_{0.8}Se_{0.2}$ as measured in a Quantum Design MPMS-7 SQUID magnetometer. M is the magnetization and H the magnetic field. The open (closed) points are zero field cooled (field cooled). The data at 0.1 T have been vertically scaled by a factor of 20. The error bars are smaller than the point size.

As illustrated in Figure 4.3 below T^* there are differences between the zero-field- and field-cooled results. This is assigned to domain repopulation in the 2-$\boldsymbol{k}$ phase. There are no observable differences above T^*, as expected for the 3-$\boldsymbol{k}$ state in this material. Figure 4.4 is a phase diagram marking $T^*(H)$ and the domain repopulation transition extracted from these measurements.

Description of samples used

In the experiments described here two batches of single crystals were used. Both were prepared at ETH Zurich by K. Mattenberger and O. Vogt. The second batch was prepared twenty years after the first. Within the estimated experimental error (± 1 K), T_N was the same in all samples of $UAs_{0.8}Se_{0.2}$. A polycrystalline sample was also used in some experiments. This was prepared in two batches (denoted I and II) at the ITU Karlsruhe by P. Boulet. This was found to contain a small amount ($< 1\%$) of UO_2 impurity.

The heat capacities of the single crystal, used in the the neutron diffraction experiments, and Batch I, as used in the time-of-flight experiments, are shown in Figure 4.5a. T^* is 51 K for the single crystal and 57 K for Batch I. Batch II displays similar behaviour, but T^* is 60 K. The microscopic origin of this sensitivity to sample preparation is unknown. It may be a further measure of the hysteretic nature of the discontinuous crystalline and magnetic transitions at this point. The M/H ratios, where M is the magnetization and $H = 1000$ gauss is the magnetic field, of the single crystal and of Batch I are given in Figure 4.5b.

Please purchase PDF Split-Merge on www.verypdf.com to remove this watermark.

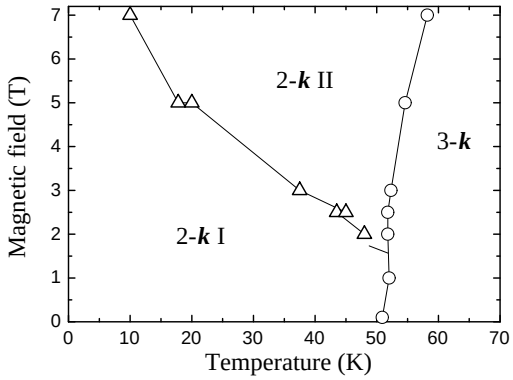

Figure 4.4: The magnetic field-temperature phase diagram for $UAs_{0.8}Se_{0.2}$, as determined from measurements of the magnetization ratio M/H. In the phase 2-$\boldsymbol{k}$ I, the three possible domains are all present. In 2-$\boldsymbol{k}$ II, the external field perturbs the domain populations.

4.2.2 $USb_{1-x}Te_x$

Burlet *et al.* [4] carried out neutron diffraction on this particular solid solution, and observed (longitudinal) magnetic ordering with propagation wavevectors parallel to the fourfold cubic axes. Here, the compositions $USb_{0.85}Te_{0.15}$ and $USb_{0.88}Te_{0.12}$ are considered, as they both possess a 3-$\boldsymbol{k}$ phase. The lattice parameters for these two compositions are very close ($\sim$ 6.19 Å at room temperature), and the magnetic moment is of the order of 2.7 μ_B/U. These two compositions have the same T_N ($\sim$ 210 K), below which an incommensurate phase develops. At $\sim$ 190 K a commensurate phase forms with $\boldsymbol{k} = \langle 00\frac{1}{2} \rangle$ which persists down to the lowest temperatures measured, although a second incommensurate phase is observed to develop in parallel. A part of the phase diagram for $USb_{0.88}Te_{0.12}$ is shown in Figure 4.6c, which contains magnetic neutron diffraction data from $USb_{0.88}Te_{0.12}$. The wavevector range (2 k 0) was studied, where $0.5 < k < 0.6$ in reciprocal lattice units (rlu). This samples only one of the three order parameters. Panel (a) shows the initial incommensurate phase. The main commensurate phase is 3-$\boldsymbol{k}$ and a re-entrant incommensurate phase is observed below 130 K. Panel (b) shows the intensity summed over all of the observed magnetic scattering in the given range, and represents the best estimate of $|S_i|^2$. The moment saturates if all of the phases are taken into account, indicating that there are no missing phases. Panel (c) illustrates the temperature dependence of the propagation wavevectors.

The first incommensurate phase can be modelled as a lock-in transition, analogous to that seen with charge density waves (see e.g. Moncton, Axe and diSalvo [42]). The nature of the second, re-entrant incommensurate phase is unknown. It is not obviously related to the lock-in transition, and is not discussed further here. In the commensurate phase, the apparent wavevector shifts; this is a temperature effect as the system was calibrated at 135 K.

Please purchase PDF Split-Merge on www.verypdf.com to remove this watermark.

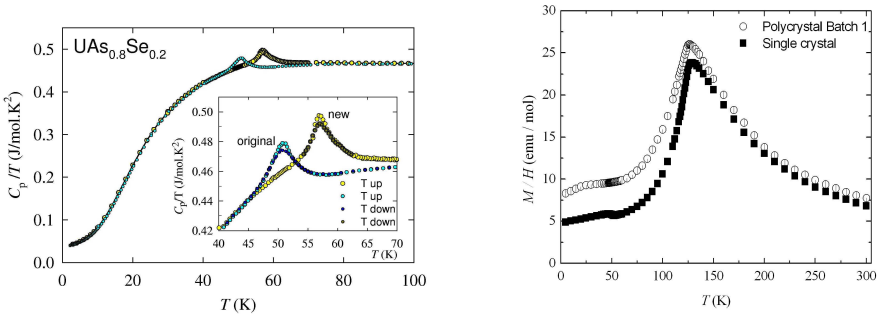

Figure 4.5: Left-hand panel: The linear coefficient of the heat capacity of the 80 mg single crystal of $UAs_{0.8}Se_{0.2}$, labelled 'original', and Batch I of the polycrystalline $UAs_{0.8}Se_{0.2}$, labelled 'new'. The insert shows data on an expanded scale around T^*, illustrating the amplitude hysteresis at the 2-$\boldsymbol{k}$ to 3-$\boldsymbol{k}$ transition, and a marked sample dependence of T^*, which is not seen in the area under the anomaly (i.e. the change in entropy) or at T_N. Right-hand panel: The M/H ratio at $H = 1000$ gauss of the 80 mg single crystal (squares) and Batch I (circles) of $UAs_{0.8}Se_{0.2}$. Whilst the polycrystal has a higher dc susceptibility, T_N (defined by the point of maximum slope) is similar ($\pm$ 1 K) in both samples.

The commensurate-incommensurate lock-in transition

The lock-in transition, as described by Moncton, Axe and diSalvo [42] for charge density waves, can be applied to spin density waves. A term is postulated to exist in the free energy (see Section 1.3 for further discussion on the basics of the free energy of such a system) corresponding to an additional (secondary) wavevector $\boldsymbol{q}'_\alpha = \boldsymbol{k}_\alpha - 3\boldsymbol{\delta}$. Although the system is stable at the (measured) incommensurate wavevector $\boldsymbol{q}_\alpha = \boldsymbol{k}_\alpha + \boldsymbol{\delta}$, the existence of the second order parameter acts to pull $\boldsymbol{\delta}$ towards zero to minimize stresses.

$\boldsymbol{\delta}$ could be a vector in any direction; we assume that it is parallel to $\boldsymbol{k}_\alpha$, the local high symmetry direction. The existence of a secondary order parameter with wavevector $\boldsymbol{q}'_\alpha$ is then postulated, as a translationally invariant addition to the free energy of the form

$$A(q'_i, T) \sum_\alpha |\boldsymbol{M}'_{\boldsymbol{q}_\alpha}|^2 + B_3 \sum_\alpha (\boldsymbol{M}^3_{\boldsymbol{q}_\alpha} \boldsymbol{M}'_{\boldsymbol{q}_\alpha} + \boldsymbol{M}^{*3}_{\boldsymbol{q}_\alpha} \boldsymbol{M}'^{*}_{\boldsymbol{q}_\alpha}) \tag{4.1}$$

can be created.[2] For a given $\boldsymbol{M}_{\boldsymbol{q}_\alpha}$ the vector components are all parallel so the vector dependence can be neglected.

Minimizing this with respect to the secondary order parameter $M'^{*}_{q_\alpha}$ gives

$$M'_{q_\alpha} = -\frac{B_3}{A(q'_\alpha, T)} M^{3*}_{q_\alpha} \tag{4.2}$$

and so the terms in Equation 4.1 are both sixth-order additions to the free energy. The

[2]The terms relating to multi-$\boldsymbol{k}$ states have been neglected, and are assumed to have little effect in the incommmensurate phase.

Please purchase PDF Split-Merge on www.verypdf.com to remove this watermark.

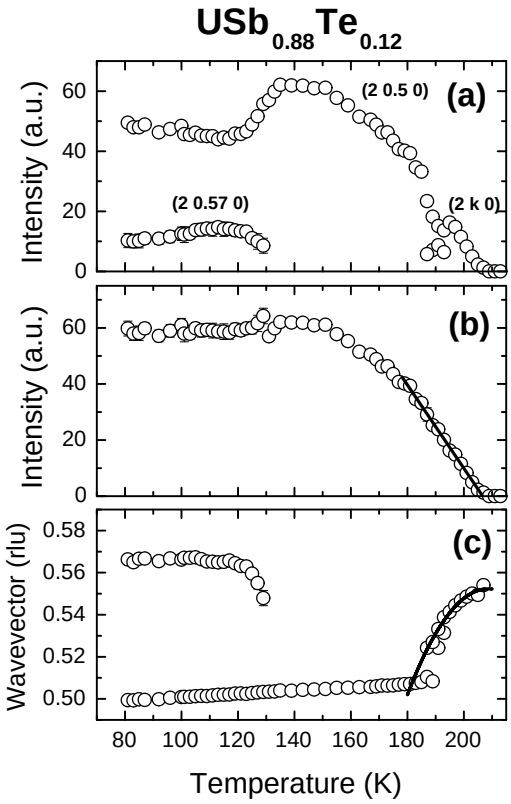

Figure 4.6: The temperature dependence of (a) the integrated intensity of the magnetic Bragg peaks found in the range (2 0.5-0.6 0) in the reciprocal space of $USb_{0.88}Te_{0.12}$, (b) the total integrated intensity summed over all of the observed peaks, and (c) the wavevectors of the observed magnetic Bragg peaks. The lines are described in the text.

Please purchase PDF Split-Merge on www.verypdf.com to remove this watermark.

free energy can therefore be written, after summation over all wavevectors, as

$$\Phi - \Phi_0 = A(q_i, T)|M_{q_\alpha}|^2 + B'|M_{q_\alpha}|^4 + \left(C - \frac{B_3^2}{A(q_i', T)}\right)|M_{q_\alpha}|^6. \tag{4.3}$$

including other sixth-order terms via C. This form emphasises the behaviour of the wavevector and applies to both single- and multi-$\boldsymbol{k}$ phases. Close to T_N, $|M_{q_\alpha}|^2$ is assumed to be small, and so sixth-order terms can be neglected in establishing its value. Minimization gives $|M_{q_\alpha}|^2 = -A(q_i, T)/B'$ and so $|M_{q_\alpha}|^2 \propto (T_N - T)$ (the line in Figure 4.6b close to T_N). The simplest form for $A(q_i, T)$ is

$$A(q, T) = \alpha(T - T_N) + \beta(q - q_c)^2. \tag{4.4}$$

This is a minimum for $q_i = q_c$, as required for the primary order parameters. At k_i', A will have a larger value.

Now consider the effect of a small shift in the incommensurate wavevector, such that $\delta \rightarrow \delta_0 + \epsilon$, where $q_c = k_i + \delta_0$. $A(q, T)$ now depends on ϵ. If ϵ is small, $A^{-1}(q_i', T) \approx (D - E\epsilon)$ to first order in ϵ, and minimization of the free energy with respect to ϵ gives

$$\epsilon = \frac{E}{\beta}|S|^4 \tag{4.5}$$

and so $\epsilon \propto (T - T_N)^2$ in the limit close to the transition (the line in Figure 4.6c). Due to the presence of the secondary wavevector, the wavevector will tend to decrease (as ϵ increases) to minimize the total energy until it locks into the commensurate state. An obvious test for this would be look for the secondary wavevector $\boldsymbol{q}_i'$. However, from the temperature dependences, the 'lock-in' transition seems to be a reasonable description.

4.3 Experimental motivation

Assuming that the 3-$\boldsymbol{k}$ state can be used as a model system in which there are coherent correlations between order parameters, how might this be observable? The two main experimental issues are, firstly, the location in reciprocal space of an experimental signature, and secondly, would it be sufficiently long-time correlated to be imaged by diffraction techniques, or would it be fundamentally dynamic in origin?

The ordinary, or single-$\boldsymbol{k}$ magnetic reflections in these materials are found at scattering vectors of the type $\boldsymbol{k}_1 = \boldsymbol{\tau} + \langle 00\frac{1}{2}\rangle$, where $\boldsymbol{\tau}$ is a reciprocal lattice vector. In a naïve picture, ignoring the quantization of angular momentum, the vectorial sum of the three conceptual moments assumed to be responsible for the $\boldsymbol{k}_1$ Bragg peaks, yields a net moment of cube triad $\langle 111\rangle$ symmetry. This suffers two unfortunate problems at the level of both the x-ray and neutron diffraction cross sections. First, since the moment auto-correlation,

$$\begin{aligned}\langle (\boldsymbol{M}_{\boldsymbol{k}_x} e^{i(\boldsymbol{k}_x.\boldsymbol{r}+\theta_x)} + \boldsymbol{M}_{\boldsymbol{k}_y} e^{i(\boldsymbol{k}_y.\boldsymbol{r}+\theta_y)} + \boldsymbol{m}_{\boldsymbol{k}_z} e^{i(\boldsymbol{k}_z.\boldsymbol{r}+\theta_z)}) \\ \times (\boldsymbol{M}_{\boldsymbol{k}_x} e^{i(\boldsymbol{k}_x.\boldsymbol{r}'+\theta_x)} + \boldsymbol{M}_{\boldsymbol{k}_y} e^{i(\boldsymbol{k}_y.\boldsymbol{r}'+\theta_y)} + \boldsymbol{M}_{\boldsymbol{k}_z} e^{i(\boldsymbol{k}_z.\boldsymbol{r}'+\theta_z)})\rangle,\end{aligned} \tag{4.6}$$

Please purchase PDF Split-Merge on www.verypdf.com to remove this watermark.

is a 2-site correlator it produces terms of the form $\langle \boldsymbol{M}_{\boldsymbol{k}_i} e^{i(\boldsymbol{k}_i.\boldsymbol{r}+\theta_i)} \boldsymbol{M}_{\boldsymbol{k}_j} e^{i(\boldsymbol{k}_k.\boldsymbol{r}'+\theta_j)} \rangle$ only and so cannot reveal the desired coherences between the three order parameters.

Secondly, even if this defect is ignored and diffraction from three coherent objects (as a 'secondary' order parameter) is postulated to exist, symmetry analysis based on the wavevector dependence of the three 'primary' order parameters leads to a conceptual moment aligned along the $\langle 111 \rangle$ directions (see Section 5.2 for further details). At each site the $\langle 111 \rangle$ director is then given by the sum of the underlying order parameter wave vectors, $\sum k_i$. However, the geometric structure factor of such a construct is zero for wave vectors of the form $\langle \frac{1}{2}\frac{1}{2}\frac{1}{2} \rangle$, i.e. just those compatible with the symmetry requirements of the cube. This is illustrated pictorially in Figure 4.7 and mathematically in Appendix 4.A. For these reasons it is not clear where diffraction from this third-order correlator might appear, if it exists.

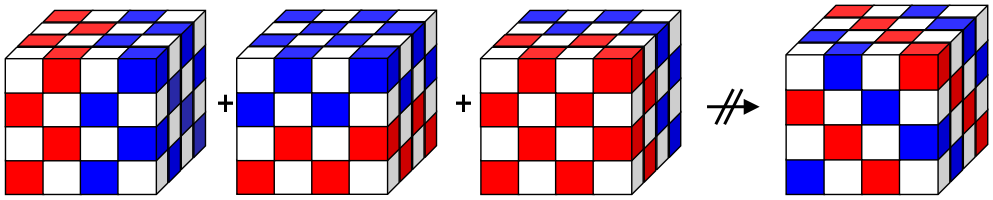

Figure 4.7: The cubes are cartoon representations of the magnetic structure in a $2 \times 2 \times 2$ block of unit cells in $UAs_{0.8}Se_{0.2}$. Each coloured block is a uranium ion, and the blue and red colours represent antiparallel moments. The white blocks are empty space. The first three blocks correspond with the three $\boldsymbol{k}_1$ propagation vectors. The fourth block is the structure with the propagation wavevector $[\frac{1}{2}\frac{1}{2}\frac{1}{2}]$.

Recently, however, it was claimed that direct evidence for multi-$\boldsymbol{k}$ coherence might be seen in x-ray resonant scattering from the $E1F^{(2)}$ term in the cross-section (an introduction to the x-ray resonant scattering cross-section is given in Section 4.4). This represents the 2-site correlator as given above, observed through the interaction of two order parameters. Therefore, in principle this type of scattering should be seen in any multi-$\boldsymbol{k}$ configuration at positions set by the wavevector dependence, i.e. in this case at $\boldsymbol{k}_2 = \boldsymbol{\tau} + \langle 0kk \rangle$. This was reported by Longfield *et al.* [43] in $UAs_{0.8}Se_{0.2}$.

Armed with this unpromising theoretical outlook, but reasoning that if the third-order phase correlator existed it might well be transient and hence best exposed on the electronic hopping time scale of x-ray resonant scattering, investigations were made in the cubic 3-$\boldsymbol{k}$ phase of $UAs_{0.8}Se_{0.2}$ at wavevectors of the form, $\boldsymbol{k}_3 = \boldsymbol{\tau} + \langle \frac{1}{2}\frac{1}{2}\frac{1}{2} \rangle$. Surprisingly, at just such positions a weak, but long-range ordered, signal was observed. The data supporting this observation are now presented, followed by neutron scattering data in which this diffraction event is also observed.

Please purchase PDF Split-Merge on www.verypdf.com to remove this watermark.

4.4 X-ray resonant scattering studies

4.4.1 The x-ray resonant scattering cross-section

X-ray diffraction is based on the electromagnetic interaction between the x-ray photon (a spin-1 particle) and the electric field generated by the electrons in the sample. As the wavelength of the x-ray photon is on the atomic lengthscale, simple diffraction patterns result. Diffraction by the magnetic field of the electrons is possible, but weaker by a factor $(\hbar\omega/mc^2)^2$. This can be overcome by exploiting the phenomenon of atomic absorption. Close to the absorption energy, a two-step coherent elastic scattering process takes place. The incoming photon promotes a core-electron into an empty state above the Fermi energy, and this is followed by the decay of the virtually excited electron into the core-hole, generating the scattered photon. This process typically takes 10^{-15} seconds. Unlike neutron scattering, this type of scattering strongly perturbs the sample. The resonant-exchange process is particularly sensitive to sample magnetization because of the effects of magnetic order on the electron states. For uranium ions, the absorption process probed is usually M_{IV} or M_V.

$$\begin{array}{lll} \text{U } M_{IV}\text{:} & 3d_{3/2} \rightarrow & 5f_{5/2} \\ \text{U } M_{V}\text{:} & 3d_{5/2} \rightarrow & 5f_{5/2} \text{ or } 5f_{7/2} \end{array}$$

The dipole scattering amplitude[3] has been calculated by Hannon *et al.* [44] as an expansion of spherical harmonics and reformulated by Hill and McMorrow [45] into a basis more readily related to experiment. In the formalism of the latter, the dipole scattering amplitude is

$$f_{jE1} = \boldsymbol{\epsilon}' \cdot \boldsymbol{\epsilon} F^{(0)} + -i(\boldsymbol{\epsilon}' \times \boldsymbol{\epsilon}) \cdot \hat{\boldsymbol{m}}_j F^{(1)} + (\boldsymbol{\epsilon}' \cdot \hat{\boldsymbol{m}}_j)(\boldsymbol{\epsilon} \cdot \hat{\boldsymbol{m}}_j) F^{(2)} \tag{4.7}$$

where $\hat{\boldsymbol{m}}_j$ is the unit vector in the direction of the j^{th} magnetic moment and $\boldsymbol{\epsilon}'(\boldsymbol{\epsilon})$ are the final (initial) x-ray photon polarization states. The terms $F^{(n)}$ give rise to the resonance phenomena, and contain the dependence of the scattering amplitude on the ordered magnetic moment.

Experimentally, an x-ray beam as generated by a synchrotron source has σ polarization (linear polarization perpendicular to the horizontal scattering plane). Scattering into the π polarization channel (parallel to the scattering plane) can be separated by using an analyzer crystal, so the $\sigma \rightarrow \sigma$ and $\sigma \rightarrow \pi$ scattering channels can be probed. Ignoring the $F^{(0)}$ term as it is independent of the magnetic moment direction, these two channels have scattering amplitudes of the form

$$f_j^{\sigma\rightarrow\sigma} = \frac{[(\hat{\boldsymbol{k}}_f \times \hat{\boldsymbol{k}}_i) \cdot \hat{\boldsymbol{m}}_j]^2}{[1 - (\hat{\boldsymbol{k}}_f \cdot \hat{\boldsymbol{k}}_i)^2]} F^{(2)} \tag{4.8}$$

and

$$f_j^{\sigma\rightarrow\pi} = i\hat{\boldsymbol{k}}_f \cdot \hat{\boldsymbol{m}}_j F^{(1)} + \frac{[(\hat{\boldsymbol{k}}_i \cdot \hat{\boldsymbol{k}}_f)\hat{\boldsymbol{k}}_f \cdot \hat{\boldsymbol{m}}_j - \hat{\boldsymbol{k}}_i \cdot \hat{\boldsymbol{m}}_j][(\hat{\boldsymbol{k}}_f \times \hat{\boldsymbol{k}}_i) \cdot \hat{\boldsymbol{m}}_j]}{[1 - (\hat{\boldsymbol{k}}_f \cdot \hat{\boldsymbol{k}}_i)^2]} F^{(2)} \tag{4.9}$$

[3]Multipole transitions are always possible, but are not considered here.

Please purchase PDF Split-Merge on www.verypdf.com to remove this watermark.

where $\hat{\boldsymbol{k}}_i$ and $\hat{\boldsymbol{k}}_f$ are the unit initial and final scattering vectors.

4.4.2 Experimental details

The experiments described here were performed on the ID20 beamline at the European Synchrotron Radiation Facility (ESRF), Grenoble. The x-ray beam is generated using an undulator, with σ incident polarization (99.0 $\pm$ 0.5 %). Polarization analysis was carried out using an Au (111) analyzer crystal. The beamline was tuned to the U M_{IV} edge, as this gives the largest enhancement for moments associated with the $5f$ states, although the existence of the diffraction events observed was confirmed at the M_V edge as well.

Two single crystals of $UAs_{0.8}Se_{0.2}$ were studied. Sample I was that used in the heat capacity (Figure 4.2) and susceptibility (Figure 4.3) measurements. The results presented here are from Sample I unless otherwise indicated, although all results were confirmed with the second sample. The results presented here were all reproduced in a single crystal of $USb_{0.85}Te_{0.15}$.

4.4.3 Results

Resonant diffraction events

Representative reflections for the $\langle k00\rangle$, $\langle kk0\rangle$ and $\langle kkk\rangle$ peaks in $UAs_{0.8}Se_{0.2}$ are illustrated in Figure 4.8, where scans were taken along the [001] direction. These reflections are subsequently labelled $\boldsymbol{k}_1$, $\boldsymbol{k}_2$ and $\boldsymbol{k}_3$ accordingly, following the conventions established earlier. These data were taken at 60 K with an Au (111) analyzer and their sharp width is indicative of long-range order. They all have a Lorentzian squared lineshape profile.

Figure 4.9 displays the dependence of these same reflections on incident photon energy, using an Au (111) analyzer to discriminate the $\sigma \rightarrow \sigma$ and $\sigma \rightarrow \pi$ channels; they are all resonant peaks. The intensity ratio is $\boldsymbol{k}_1 : \boldsymbol{k_2} : \boldsymbol{k_3} = 1 : 10^{-2} : 10^{-4}$. Both the (0 0 5/2) and (1/2 1/2 5/2) peaks are only resonant in the $\sigma \rightarrow \pi$ channel, and they both have the same lineshape. The reflection at (1/2 0 5/2) is resonant in both channels, but is not centered at the absorption M_{IV} edge, and has an unexpected lineshape. This is discussed in Ref. [43], and will not be discussed further here.

Temperature dependences

The $\boldsymbol{k}_3$ peaks are only observed in the 3-$\boldsymbol{k}$ phase. At T^*, the onset of the tetragonal distortion corresponds with the disappearance of the $\boldsymbol{k}_3$ peak (Figure 4.10). The temperature dependence close to T_N is discussed in Section 4.5 in comparison with the temperature dependence as observed by neutrons. The intensity of all of the observed reflections diminishes with temperature before disappearing above T_N.

Azimuthal (Renninger) scans of the $\boldsymbol{k}_3$ reflections

Figure 4.11 shows the azimuthal dependence of the intensity of the $\boldsymbol{k}_3$ reflections (1/2 1/2 5/2) and (-1/2 1/2 5/2) in the $\sigma \rightarrow \pi$ channel. The smooth variation of the intensity

Please purchase PDF Split-Merge on www.verypdf.com to remove this watermark.

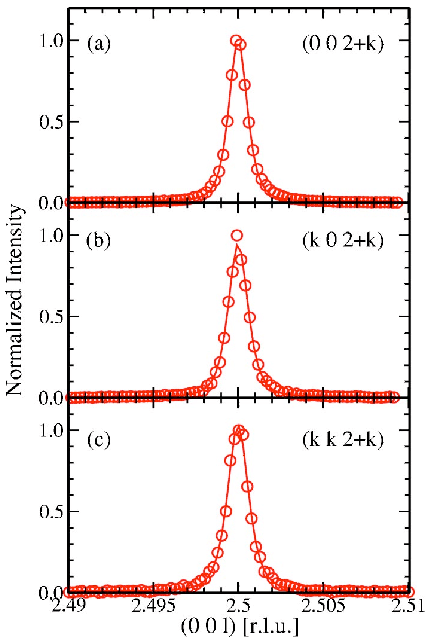

Figure 4.8: Scans along the [001] direction of the reflections (0 0 5/2), (1/2 0 5/2) and (1/2 1/2 5/2). The solid lines are a fit to a Lorentzian squared line shape. The data were taken at a temperature of 60 K.

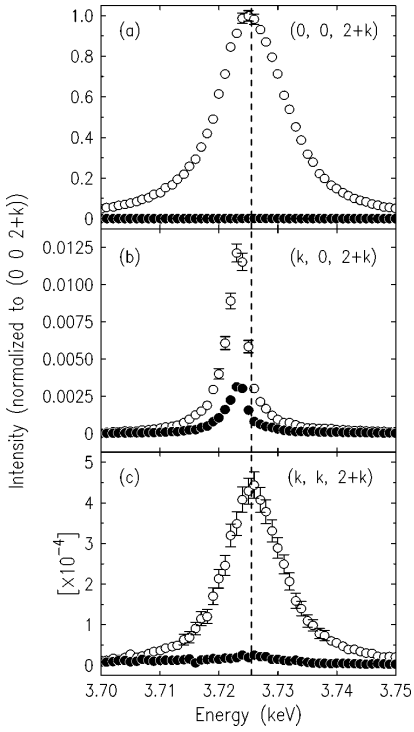

Figure 4.9: Scans of the incident photon energy with polarization analysis of the scattered beam for the three reflections in Figure 4.8, at the U M_{IV} edge (dashed vertical line). The open points are in the $\sigma \rightarrow \pi$ channel and the closed points n the $\sigma \rightarrow \sigma$ channel. The temperature was 70 K, and $k = \frac{1}{2}$.

Please purchase PDF Split-Merge on www.verypdf.com to remove this watermark.

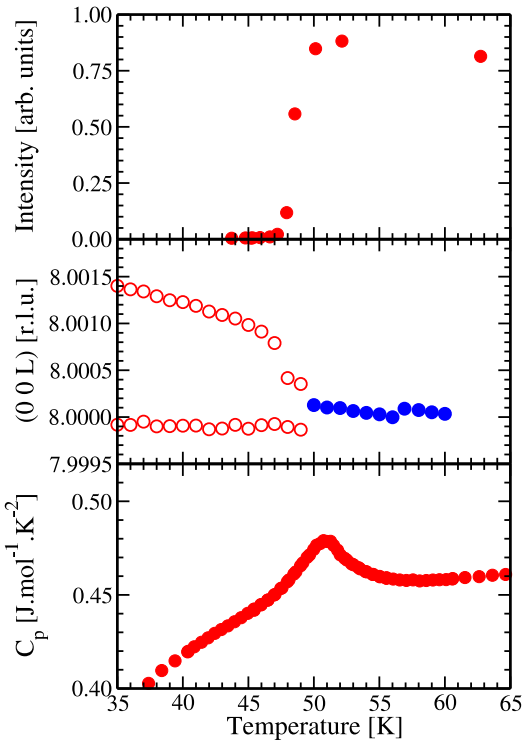

Figure 4.10: The upper panel is the integrated intensity of the $\boldsymbol{k}_3$ peak (1/2 1/2 5/2), as a function of temperature. The middle panel is the position of the charge peak at (008) as measured by (non-resonant) x-ray diffraction on ID20. These measurements were made on Sample II. The lower panel is the heat capacity of $UAs_{0.8}Se_{0.2}$ (Sample I).

Please purchase PDF Split-Merge on www.verypdf.com to remove this watermark.

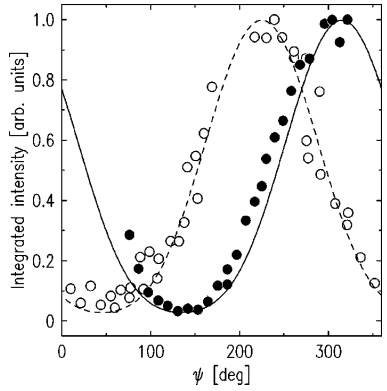

Figure 4.11: Azimuthal scans in the $\sigma \rightarrow \pi$ channel about the scattering vector (1/2 1/2 5/2) (open points) and (-1/2 1/2 5/2) (closed points) reflections from $UAs_{0.8}Se_{0.2}$. The lines are described in the text. For all azimuthal angles the intensity in the $\sigma \rightarrow \sigma$ channel is zero.

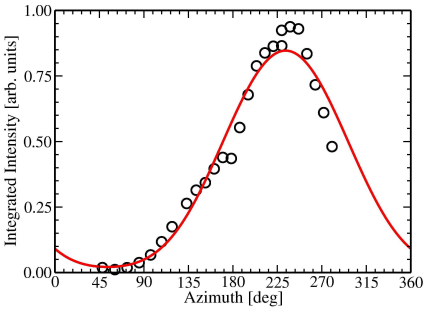

Figure 4.12: Azimuthal scans in the $\sigma \rightarrow \pi$ channel about the scattering vector (-1/2 -1/2 5/2) from $USb_{0.85}Te_{0.15}$. The lines correspond to the analysis described in the text. Note that for all azimuthal angles the intensity in the $\sigma \rightarrow \sigma$ channel is zero.

eliminates multiple scattering as a possible source for these peaks.

Discussion

The $\boldsymbol{k}_3$ diffraction events are observed in the 3-$\boldsymbol{k}$ phase only. They disappear below T^*, in the 2-$\boldsymbol{k}$ phase, when the cubic symmetry disappears. From Figure 4.8, they are generated by long-range order. The smooth variation of the azimuthal scans eliminates a multiple scattering origin. The energy resonance of the $\boldsymbol{k}_3$ peak looks identical to that of the $\boldsymbol{k}_1$ peak, and is only present in the $\sigma \rightarrow \pi$ channel, suggesting that it too is generated from the $F^{(1)}$ dipole $E1$ scattering amplitude.

The lines through the azimuthal dependences in Figure 4.11 are calculated from the $F^{(1)}$ term of the $E1$ cross-section, assuming a symmetry-breaking vector parallel to the reduced wavevector $\langle kkk \rangle$. The outline of such a calculation is given in Appendix 4.B. The symmetry breaking vectors required to fit the data at the different peaks plotted were

Reflection	Symmetry breaking vector
(1/2 1/2 5/2)	[111]
(-1/2 1/2 5/2)	$[\bar{1}11]$
(-1/2 -1/2 5/2)	$[\bar{1}\bar{1}1]$

In each case, the symmetry breaking vector is parallel to the propagation wavevector that generates the given reflection. It is not obvious that this is generated by a magnetic moment.

Please purchase PDF Split-Merge on www.verypdf.com to remove this watermark.

From Equations 4.8 and 4.9 the absence of a $\sigma \rightarrow \sigma$ term indicates that either $F^{(2)} = 0$ or that $(\hat{\boldsymbol{k}}_f \times \hat{\boldsymbol{k}}_i) \cdot \hat{\boldsymbol{m}}_j = 0$. For the (1/2 1/2 5/2) reflection the scattering plane is [110]-[001]. The azimuthal dependences indicate that the signal at the $\boldsymbol{k}_3$ positions is generated by a symmetry breaking vector parallel to $\langle 111 \rangle$. To give a null result in the $\sigma \rightarrow \sigma$ channel, we therefore require that $F^{(2)} = 0$. Note that this assumes that the scattering is purely dipolar.

As mentioned above, the x-ray probe operates on a very short timescale. The $\boldsymbol{k}_3$ diffraction events may therefore be short-time phenomena. To investigate this, neutron diffraction, which averages over a longer time and probes the bulk of the material, was an obvious next step.

4.5 Neutron diffraction

Experimental details

Single crystal neutron diffraction studies were carried out on the four-circle diffractometer D10 at the Institut Laue-Langevin (ILL), Grenoble. To maximise the signal-to-noise ratio, the diffractometer was operated in three-axis mode using a pyrolytic graphite (002) analyser crystal (estimated acceptance of $\pm$ 0.5 meV at full width half maximum) and a He^3 detector with maximal incident flux ($5 \cdot 10^6$ neutrons $cm^{-2}s^{-1}$) at the calibrated wavelength $\lambda = 2.3622(3)$ Å. In order to suppress $\lambda/2$ contamination, a pyrolytic graphite filter was placed in the path of the incident beam.

The sample of $UAs_{0.8}Se_{0.2}$ used was the 80 mg single crystal used in the x-ray resonant scattering (Figures 4.8 and 4.9) experiment, as well as in heat capacity (Figure 4.2) and susceptibility (Figure 4.3) measurements. The crystal was indexed on D10 at room temperature using the 66 accessible nuclear Bragg reflections, and checked at lower temperatures, giving a lattice parameter of 5.7694(11) Å at 65 K, with the error in λ included [46].

The sample of $USb_{0.88}Te_{0.12}$ used was a 0.7 g single crystal prepared at ETH Zurich. The crystal was indexed using 102 reflections, giving a lattice parameter 6.2013(4) Å at 135 K [46]. The magnetic phase diagram obtained for this particular composition (Figure 4.6) was the same as that observed by Burlet *et al.* [4]. The nuclear structure factors calculated in this case are tabulated in Appendix 4.C to give an example.

The $\boldsymbol{k}_1$ reflections

Bragg reflections indexed at $\boldsymbol{k}_1 = \langle 11\frac{1}{2} \rangle$ confirm the presence of the single-$\boldsymbol{k}$ order parameters for $T < T_0$. The temperature dependence of three such $\boldsymbol{k}_1$ reflections in $UAs_{0.8}Se_{0.2}$ is given in Figure 4.13. The three orthogonal propagation wavevectors are present with equal strength in the 3-$\boldsymbol{k}$ phase ($T^* - T_0$), reflecting the long-range phase coherence of the three order parameters in the 3-$\boldsymbol{k}$ state. Below T^*, in the 2-$\boldsymbol{k}$ state, the domain populations are approximately equal. This is consistent with the behaviour noted by Kuznietz *et al.* [40]. Similar information is given for $USb_{0.88}Te_{0.12}$ in Figure 4.6. Systematic absences are observed at positions like (0 0 1/2) and (0 0 3/2), indicating that the

Please purchase PDF Split-Merge on www.verypdf.com to remove this watermark.

magnetic moment is parallel to the propagation vector.

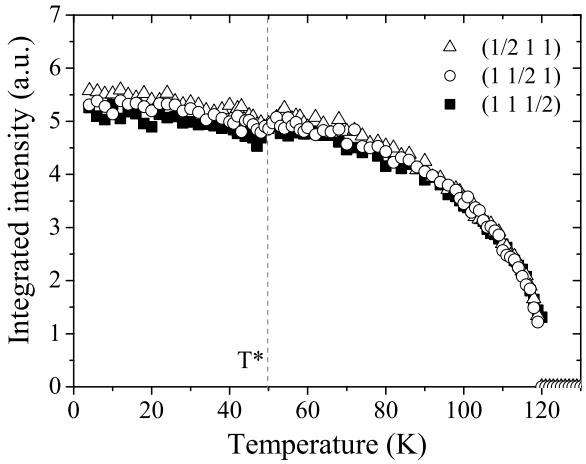

Figure 4.13: Integrated intensity of $\langle 11k \rangle$ reflections of $UAs_{0.8}Se_{0.2}$ as a function of temperature, measured by neutron diffraction on D10 (ILL). The sample is the same as that used in the x-ray resonant scattering studies.

The $\boldsymbol{k}_3$ reflections

The three frames in Figure 4.14 show measurements from $UAs_{0.8}Se_{0.2}$ at the (3/2 -1/2 -1/2) $\boldsymbol{k}_3$ position for $T < T^*, T^* < T < T_N$ and $T > T_N$ respectively. The peak is only present between T^* and T_N, i.e. in the 3-$\boldsymbol{k}$ phase. The intensity of this peak is approximately 10^{-3} of the strongest single-$\boldsymbol{k}$ magnetic reflections. As in the x-ray resonant diffraction, the wavevector response is sharp.

In $USb_{0.88}Te_{0.12}$, the $\boldsymbol{k}_3$ peak was investigated at $T = 135$ K on the basis of the phase diagram, as no parasitic incommensurate phases were present. Scans at the $\boldsymbol{k}_3$ positions at 135 K and 220 K (inside the paramagnetic phase) are shown in Figure 4.15 for two reflections. The reflections again had an intensity approximately 10^{-3} of the $\boldsymbol{k}_1$ peaks.

In both materials, a series of reflections were measured over a range of momentum transfers. The variation in the intensity of these peaks is reported on in Section 4.5.1. Whilst $\mathbf{k_3}$ peaks are observed at positions where τ is not parallel to $\langle kkk \rangle$, they are (apparently systematically) absent at $\mathbf{k_3}$ positions such as (1/2 -1/2 -1/2) and (3/2 -3/2 -3/2).

Temperature dependence

The temperature dependence of the (3/2 -1/2 -1/2) $\mathbf{k_3}$ peak is given in Figure 4.16, together with the $\mathbf{k_1}$ data, and overlaid onto the equivalent x-ray data for the reflections (0 0 5/2) and (1/2 1/2 5/2). Although the neutron diffraction data are relatively poorly defined and few in number, the behaviour is qualitatively similar to the x-ray data from the same sample. It is clear that the two types of reflection have qualitatively different temperature dependences.

Please purchase PDF Split-Merge on www.verypdf.com to remove this watermark.

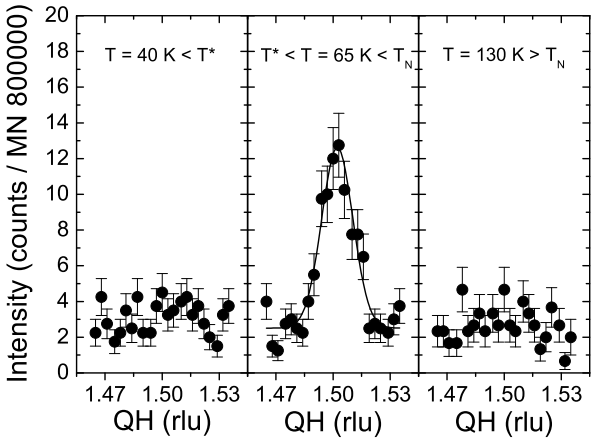

Figure 4.14: Scans taken on D10 (ILL) along the [100] direction through $\boldsymbol{Q}$ = (3/2 -1/2 -1/2) at T = 40 K (left hand panel), T = 65 K (central panel) and T = 130 K (right hand panel). The line in the central panel is a Gaussian fit to the reflection profile; the width is similar to that observed in the $\boldsymbol{k}_1$ reflections. The $\lambda/2$ contamination is of the order of 1 to 2 counts on this scale. The monitor of 800000 represents a counting time of $\sim$ 2 minutes.

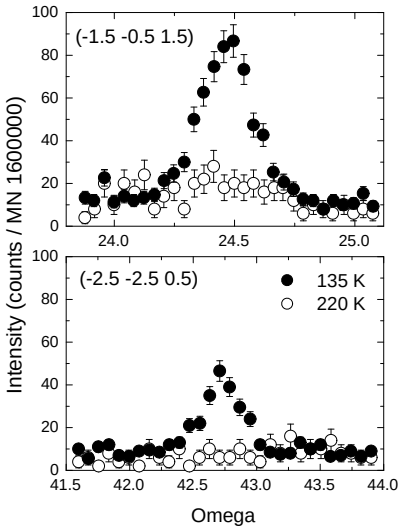

Figure 4.15: The (-1.5 -0.5 1.5) and (-2.5 -2.5 0.5) Bragg diffraction peaks in $USb_{0.88}Te_{0.12}$ at 135 K (closed circles) and 220 K (open circles). The data were taken on D10 (ILL) in the three-axis mode. The monitor used corresponds to $\sim$ 4 minutes.

Please purchase PDF Split-Merge on www.verypdf.com to remove this watermark.

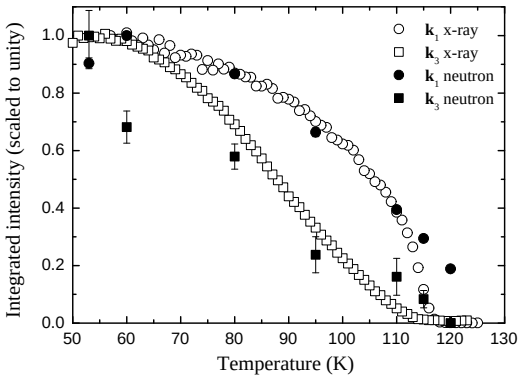

Figure 4.16: Temperature dependences of the $\mathbf{k_1}$ (circles) and $\mathbf{k_3}$ (squares) integrated intensities as measured by neutron diffraction (closed points) and resonant x-ray scattering peak intensity (open points) on the same single crystal of $UAs_{0.8}Se_{0.2}$. The data have been individually scaled to a common low temperature value.

Azimuthal dependence and multiple scattering

A Renninger scan was made with the $USb_{0.88}Te_{0.12}$ sample for the $\boldsymbol{k}_3$ reflection at (-1.5 -0.5 1.5), covering 35° of the ψ angle. Unlike an x-ray azimuth scan, this should be smooth and unmodulated. As this scan is smooth and considerably above the estimated background level, the peak does not appear to be generated by multiple scattering events.

For the $UAs_{0.8}Se_{0.2}$ sample limited azimuthal scans were carried on a selected $\mathbf{k_3}$ reflection and revealed no evidence for multiple scattering. To generate a $\mathbf{k_3}$ peak by a multiple scattering process would require three $\mathbf{k_1}$ reflections. In this context, estimates of the expected magnitude of multiple scattering reflections are helpful. The $(11\frac{1}{2})$ $\mathbf{k_1}$ peak has 8.5% of the integrated intensity of the (002) nuclear reflection at 60 K. A multiple scattering signal was observed at positions of the $\boldsymbol{k}_2$ type, as confirmed by a Renninger scan. This had an intensity similar to that of the $\boldsymbol{k}_3$ peak. It requires a double scattering event, and this gives a reflectivity of $\sim 1\%$ for the (002). The implied multiple scattering event for a $\mathbf{k_3}$ reflection would therefore have a reflectivity of $6 \cdot 10^{-8}$ with respect to the (002) nuclear peak, leading to 10^{-2} counts on the scale shown in Figure 4.14. To obtain the observed signal via multiple scattering the reflectivity of the (002) would have to be ~ 25 %.

Discussion

The $\boldsymbol{k}_3$ peaks have been observed by neutron diffraction, and have a sharp wavevector response, confirming the existence and long-range order of the $\boldsymbol{k}_3$ response as a bulk property of the 3-$\boldsymbol{k}$ state, the phase coherence time window ($\sim 4 \cdot 10^{-12}$s) remains relatively coarse, being on the same scale as typical thermal excitations at these temperatures.

Please purchase PDF Split-Merge on www.verypdf.com to remove this watermark.

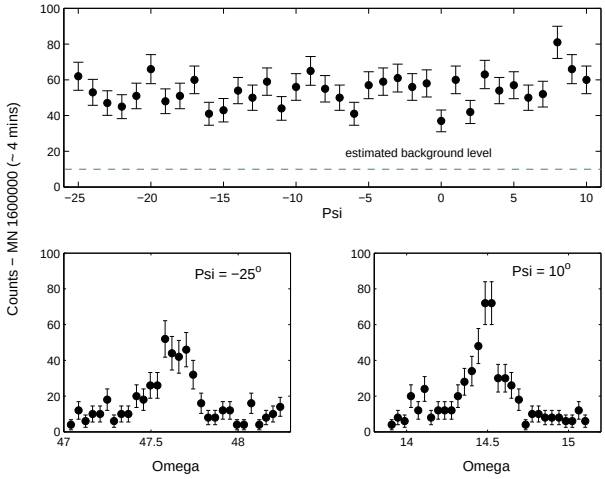

Figure 4.17: A Renninger scan taken at the maximum of the (-1.5 -0.5 1.5) reflection as measured by neutron diffraction from $USb_{0.88}Te_{0.12}$ over 35°. The dashed line is the estimated background level. The two lower panels are rocking scans at the extremal ψ values of the Renninger scan.

The azimuthal scans and intensity analysis indicate that the peaks are not generated by multiple scattering events. The sharp widths of the responses, as seen by both x-rays and neutrons, argue against the existence of parasitic phases, or small regions ($\sim 10^{-3}$ of the crystal volume) with an ordering wavevector $\langle \frac{1}{2}\frac{1}{2}\frac{1}{2} \rangle$. As an aside, single-$\boldsymbol{k}$ ordering with such a wavevector has, to date, never been reported in NaCl-type uranium compounds. In this case, the observed temperature dependences would have to be completely fortuitous. These observations all suggest that the $\boldsymbol{k}_3$ reflections as seen by neutrons are not a product of local chemical or structural disorder.

The apparent systematic absences reported by neutron diffraction indicate that the effective magnetic dipole creating the scattering amplitude lies parallel to the propagation wavevector generating the scattering for both the $\boldsymbol{k}_1$ and $\boldsymbol{k}_3$ peaks. The inference from these two observations is that: (i) in common with the results obtained from the azimuth dependence of x-ray resonant scattering, the effective scattering object for the $\boldsymbol{k}_3$ peak may be parameterised by a moment which lies along the $\langle 111 \rangle$ directions, and (ii) for the $\boldsymbol{k}_1$ peak, the polarization vector is parallel to the $\langle 001 \rangle$ directions. Whilst these two deductions can be reconciled at the classical level as a vector sum of 'components', this construction is unable to give a finite geometric structure factor at the $\boldsymbol{k}_3$ positions (see Appendix 4.A) and, furthermore, any such linear combination of independent angular momenta appears to lack a sound microscopic basis.

The observed temperature dependences in both the x-ray and neutron data match, and together with the apparent long-range order and effective dipolar nature of the appropriate order parameter, suggests that the x-ray (near surface) and neutron (bulk) probes are imaging the same object. The dependence close to T_N is not the same for the two types of reflection. This is discussed by Lander and Bernhoeft [47], who looked at the x-ray temperature dependence and found that close to T_N the $\boldsymbol{k}_1$ integrated in-

Please purchase PDF Split-Merge on www.verypdf.com to remove this watermark.

tensity varied as $(T_N - T)^{0.4}$, whereas the $\boldsymbol{k}_3$ reflections had a temperature dependence proportional to $(T_N - T)^{1.5}$.

Having established that the $\boldsymbol{k}_3$ reflections are brought about by a physical process associated with a dipolar scattering object, attention now turns to its origin. Reflections at different $\boldsymbol{Q}$ vectors were measured to investigate the form factor; this is now addressed.

4.5.1 The form factor

Introduction

In magnetic neutron scattering, the intensity of the magnetic signal is determined by an envelope function labelled the magnetic form factor. This is the Fourier transform of the magnetization density of the individual unit that orders to give rise to the coherent Bragg diffraction event. Usually, this is the magnetization distribution for a single magnetic ion, and most measured form factors can be calculated using electron atomic orbitals for a single ion in the dipole approximation [48]. There are some specific exceptions, for example O_2, where the moment is carried by the whole molecule, and so the free orbitals of a single molecule have to be used in the calculation [49].

For U(Sb,Te) and U(As,Se) the relevant ion is the uranium ion. The form factors for the different uranium states are all reasonably similar, so that it can be difficult to establish the ground state of the single ion from form factor measurements alone. For a deeper discussion on magnetic form factors in uranium ions, see Freeman *et al.* [50].

Experimental details

The integrated intensity of the $\boldsymbol{k}_1$ and $\boldsymbol{k}_3$ peaks was measured from $\theta - 2\theta$ scans in $USb_{0.88}Te_{0.12}$, taking advantage of the larger crystal. Some intensities of $\boldsymbol{k}_3$ peaks were also taken from the $UAs_{0.8}Se_{0.2}$ sample. For the $\boldsymbol{k}_3$ this was experimentally difficult as the peaks were very weak and had to be measured in the single-detector, three-axis mode of D10. The 2D detector option on D10 provides a more accurate measure of the intensity but the signal-to-noise ratio is worse. The $\boldsymbol{k}_1$ reflections were measured using both the three-axis mode and the 2D detector, to provide a control of the accuracy of three-axis mode. The accuracy of the single detector could therefore be controlled. All of the peaks observed could be fitted using a Gaussian lineshape.

To evaluate the integrated intensities a trapezoidal numerical integration was used, with a background subtraction calculated using a linear fit of the first and last six points. The errors were estimated by repeating the calculation at the extremes of the errors on the individual data points. This integrated intensity then has to be corrected to establish the form factor.

$$f^2(Q) \propto \frac{I_{hkl}}{LAy} \frac{1}{[\hat{Q} \times (\hat{\mathbf{M}} \times \hat{Q})]^2} \tag{4.10}$$

where $f^2(Q)$ is the structure factor, I_{hkl} is the integrated intensity of reflection (hkl), L is the Lorentz factor, A is the absorption correction, y is the extinction correction, and the final term is the geometrical interaction between the scattering vector $\boldsymbol{Q}$ and the direction

Please purchase PDF Split-Merge on www.verypdf.com to remove this watermark.

of the magnetization $\mathbf{M}$ in the sample. The effect of absorption was neglected. The Lorentz factor corrects for the time-of-reflection opportunity for a given reciprocal-lattice point, based on its position and the type of scan and detector used. The appropriate factor here is $L = 1/\sin(2\theta)$. The other factors will be discussed below.

The $\boldsymbol{k}_1$ peaks

The $\boldsymbol{k}_1$ peak intensities were measured over a range of scattering vectors for the crystal of $USb_{0.88}Te_{0.12}$ only. The $[\hat{Q} \times (\hat{\boldsymbol{M}} \times \hat{Q})]^2$ factor was calculated using the established magnetic structure: moment directions longitudinal to the propagation vectors along the cube four-fold axes. The 2D detector and analyzer measurements match very well (Figure 4.18). The line $\exp(-0.07Q^2)$ in the lower panel of Figure 4.18 is a good approximation to the uranium form factor [39]. To illustrate this, data taken from the literature for UAs [51] and USb [52] have been added to the lower panel. These two compounds are both cubic antiferromagnets, although in both cases the type of antiferromagnetism is different, and the propagation vector is $\langle 001 \rangle$.

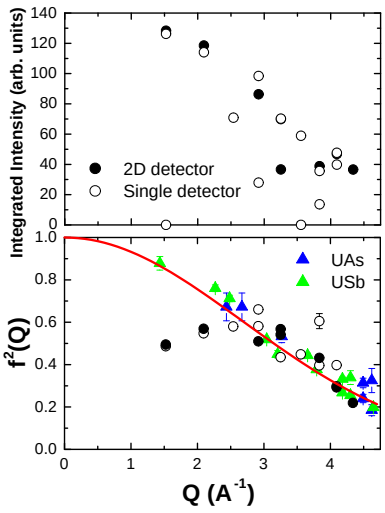

Figure 4.18: The upper panel shows the uncorrected integrated intensities for the $\boldsymbol{k}_1$ peaks from $USb_{0.88}Te_{0.12}$. The open (closed) points were obtained from the 1D (2D) detector. The 2D detector data have been vertically scaled. The lower panel shows the data corrected for the Lorentz factor and the direction of the magnetic moments. It has then been scaled to the red line, $\exp(-0.07Q^2)$, a common approximation for the uranium form factor. The triangles are similar data for pure UAs (Ref. [51]) and pure USb (Ref. [52]).

The data taken for $USb_{0.88}Te_{0.12}$ fits the trend for high $\boldsymbol{Q}$ values, but the first two points are clearly lower than the curve. This is almost certainly due to extinction effects in the large sample. The nuclear peaks suffer from some extinction (see Appendix 4.C). The numerical effects of the extinction could not be determined, as no measurements

Please purchase PDF Split-Merge on www.verypdf.com to remove this watermark.

were made at a different incident wavelength, and a standard refinement of the magnetic reflections was not able to give a good fit [46]. However, the comparison with the UAs and USb data indicates that the data measured here obey the usual uranium form factor.

The $\boldsymbol{k}_3$ peaks

To evaluate the integrated intensity of the $\boldsymbol{k}_3$ peaks, a trapezoidal numerical integration was used, with a background subtraction calculated using a linear fit of the first and last six points. The errors were estimated by repeating the calculation at the extremes of the errors on the individual data points. Of the 20 peaks studied in $USb_{0.88}Te_{0.12}$, several were permutations of each other. These permutations all had similar intensities and so were summed to improve statistics, leaving 11 data points. In the integration process used, the intensity at the points with positions with $\boldsymbol{\tau} \parallel \langle 111 \rangle$ was zero. This was not the case for any of the other peaks, reinforcing the interpretation of these null intensities as systematic absences. In $UAs_{0.8}Se_{0.2}$ 10 reflections were measured, contributing 7 distinct data points.

Table 4.1 gives the integrated intensities, with error, and the appropriate Lorentz correction for the eleven peaks. Here, extinction should not be an issue as the peaks have very low intensities. Figure 4.19 plots these data as a function of momentum transfer. A limited data set was collected for $UAs_{0.8}Se_{0.2}$, and this is shown in the same figure. The points shown here represent the limits of the accessible portion of reciprocal space for crystals with a lattice parameter $\sim$ 5-6 Å on D10. Although the wavelength could be changed, 2.36 Å represents the best flux for D10, and it is not clear that the peaks could be seen if the noise level were higher.

$\langle hkl \rangle$	Q ($Å^{-1}$)	Integrated intensity (arb. units)	Error (arb. units)	$\sin(2\theta)$
$\langle 3/2\ 1/2\ 1/2 \rangle$	1.68	10.67	0.97	0.60
$\langle 3/2\ 3/2\ 1/2 \rangle$	2.21	20.10	0.86	0.76
$\langle 3/2\ 3/2\ 3/2 \rangle$	2.64	-0.02	0.02	0.86
$\langle 5/2\ 1/2\ 1/2 \rangle$	2.64	9.67	0.65	0.86
$\langle 5/2\ 3/1\ 1/2 \rangle$	3.00	7.84	0.61	0.93
$\langle 5/2\ 3/2\ 3/2 \rangle$	3.33	1.62	0.16	0.98
$\langle 5/2\ 5/2\ 1/2 \rangle$	3.63	15.12	1.05	0.99
$\langle 7/2\ 1/2\ 1/2 \rangle$	3.63	2.22	0.22	0.99
$\langle 5/2\ 5/2\ 3/2 \rangle$	3.90	8.61	0.60	0.99
$\langle 7/2\ 3/1\ 1/2 \rangle$	3.90	13.75	1.14	0.99
$\langle 7/2\ 3/2\ 3/2 \rangle$	4.16	7.38	0.69	0.98

Table 4.1: The integrated intensities of the grouped peaks at the $\boldsymbol{k}_3$ positions in $USb_{0.88}Te_{0.12}$.

To convert the integrated intensities into a form factor, the magnetic structure must be known. The appropriate structure for the $\boldsymbol{k}_3$ events is not evident. However, it is

Please purchase PDF Split-Merge on www.verypdf.com to remove this watermark.

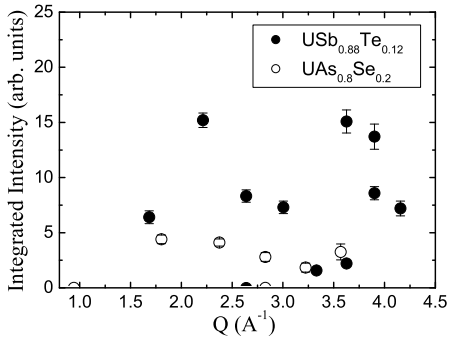

Figure 4.19: The integrated intensity of $\boldsymbol{k}_3$ peaks from $USb_{0.88}Te_{0.12}$ (closed points), corrected for the Lorentz factor, as a function of momentum transfer, as measured on D10 (ILL). The open points are the same data from $UAs_{0.8}Se_{0.2}$. At 2.67 Å^{-1} the $UAs_{0.8}Se_{0.2}$ data point has been shifted to avoid point overlay.

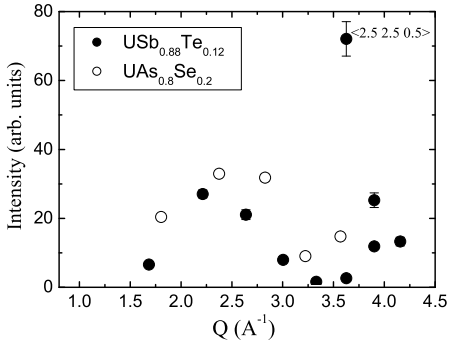

Figure 4.20: The integrated intensity of $\boldsymbol{k}_3$ peaks from $USb_{0.88}Te_{0.12}$ (closed points), corrected for the Lorentz factor and the magnetic structure model described in the text, as a function of momentum transfer. The open points are the same data from $UAs_{0.8}Se_{0.2}$, now vertically scaled by a factor of 3. At 2.67 Å^{-1} the $UAs_{0.8}Se_{0.2}$ data point has been shifted to avoid point overlay.

clear that these data do not resemble the usual uranium ion form factor. The integrated intensity is clearly anisotropic, as the two points at 3.63 Å^{-1} have very different intensities. One of these (-2.5 -2.5 0.5), is illustrated in Figure 4.15b, confirming that it is not obviously spurious in origin, although the high temperature background appears to have increased. On the basis of the x-ray azimuthal analysis and the systematic absences noted earlier, assumes the existence of moments parallel to the propagation wavevector $\langle \frac{1}{2}\frac{1}{2}\frac{1}{2} \rangle$ generating a given reflection. The correction for this structure is shown in Figure 4.20. This issue is addressed in the following chapter.

4.5.2 Time-of-flight analysis

Whilst the D10 data confirms the existence and long-range order of the $\mathbf{k_3}$ response as a bulk property of the 3-$\boldsymbol{k}$ state, the phase coherence time window ($\sim 4 \cdot 10^{-12}$s) remains

Please purchase PDF Split-Merge on www.verypdf.com to remove this watermark.

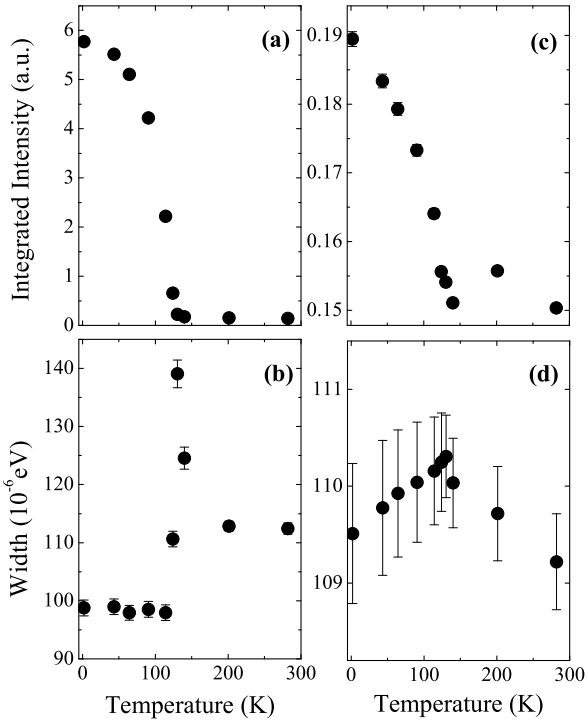

Figure 4.21: Time-of-flight data from a polycrystalline ingot of $UAs_{0.8}Se_{0.2}$, measured on IN5 (ILL). Panels (a) and (b) show the integrated intensity (over an energy transfer range $-0.15 \leq \Delta E \leq 0.15$ meV) and energy linewidth of the elastic peak at the $\langle 1\ 1\ 1/2 \rangle$ position. Panels (c) and (d) give equivalent information for data averaged over the momentum transfer range $0.42 \leq Q \leq 1.41$ Å^{-1}, i.e. for scattering angles below the magnetic Bragg cut off value. The data in (c) have been adjusted for the integrated scattered solid angle to be comparable to (a).

relatively coarse, being on the same scale as typical thermal excitations at these temperatures. When looking at low-level signals in $UAs_{0.8}Se_{0.2}$ a longer integration time may be important since inelastic neutron scattering on pure UAs shows a pronounced response, broad in wavevector and energy transfer, at temperatures below T_N [53]. To assess the degree of long-time order present in the correlations leading to the $\mathbf{k_3}$ response, the basis set of $\mathbf{k_1}$ diffraction peaks has been investigated by high resolution time-of-flight spectroscopy on a polycrystalline sample (see Section 4.2.1 for further sample information). Attaining the necessary high resolution limits the count rate, rendering the $\mathbf{k_3}$ peaks unobservable.

Time-of-flight experiments have been carried out using the IN5 and FOCUS spectrometers, at the ILL and the Paul Scherrer Institute (PSI), Villigen, Switzerland, respectively. The spectrometers were operated at incident wavelengths (4.85, 5.13 and 5.30 Å) close to twice that used on D10, giving an elastic energy resolution better than 0.1 meV. The two-site de-coherence time can then be determined from the integrated elastic response on scales up to $\sim 4 \cdot 10^{-11}$s. The large solid angle detector banks enable a survey of the

Please purchase PDF Split-Merge on www.verypdf.com to remove this watermark.

Brillouin zone for $0.25 \leq Q \leq 2.3$ Å^{-1}.

At the scattering angle corresponding with $\langle 1\ 1\ 1/2\rangle$ magnetic reflections, the temperature dependences of the integrated elastic peak intensity, over an energy transfer range $-0.15 \leq \Delta E \leq 0.15$ meV, and energy width are shown in panels (a) and (b) of Figure 4.21 respectively. In parallel with Figure 4.13 (single crystal data), they clearly show the transition from paramagnetism to magnetic order. The energy linewidth of the peak, panel (b), tracks the transition in the manner expected for a developing order parameter. In the paramagnetic phase, slow fluctuations with low amplitude generate a weak broadening of the elastic linewidth. In the immediate neighbourhood of T_N, the rapidly increasing fluctuation amplitude leads to a step-like increase in the measured width, followed by a sharp fall in the ordered phase. The reduced energy linewidth below T_N, despite the increasing integrated intensity, confirms the narrowing of the intrinsic linewidth and the long-time order of the independent single-$\boldsymbol{k}$ order parameters on time scales $\sim 10^{-11}$s. This result, which establishes the existence on thermodynamic space-time scales of the order parameter basis set for both the 2- and 3-$\boldsymbol{k}$ magnetic configurations, is important in view of the apparent conflicting requirements of angular momentum quantization with orthogonal magnetic moments in the given 3-$\boldsymbol{k}$ structure [40].

In addition to this response at the $\mathbf{k_1}$ positions, a significant increase in the intensity with *decreasing* temperature is seen across the full range of reciprocal space covered for all $T \leq T_N$ (Figure 4.21c). At all temperatures measured this integrated elastic scattering has a similar energy width (Figure 4.21d) to that observed at the $\mathbf{k_1}$ position in the paramagnetic phase above T_N (Figure 4.21b). Its broad extent in momentum transfer indicates that the response is generated by local, long-time correlations, the amplitude of which mimics the temperature dependence of the $\mathbf{k_1}$ antiferromagnetic Bragg peaks. It stays on a similar dynamic scale in both the paramagnetic and ordered phases.

4.6 Experimental summary

To summarize, the present results show x-ray and neutron diffraction peaks at $\mathbf{k_3}$ positions. These peaks are sample independent properties of 3-$\boldsymbol{k}$ phases where $\boldsymbol{k} = \langle 00\frac{1}{2}\rangle$. They are not caused by multiple scattering events. Information on the nature and space-time coherence scales of this response has also been presented.

A brief survey of possible origins of the $\boldsymbol{k}_3$ peaks is given. A simple explanation would be that, at the level of 10^{-3} of the total volume, there are regions that exhibit an ordering with the wavevector $\boldsymbol{k} = \langle 1/2\ 1/2\ 1/2\rangle$. This would explain the observed x-ray energy dependence. However, a number of observations contradict such a scenario. Firstly, the similar, sharp momentum space widths of the $\boldsymbol{k}_1$ and $\boldsymbol{k}_3$ reflections indicate that the $\boldsymbol{k}_3$ peaks represent (bulk) long-range order. Secondly, the temperature dependence relationships noted above would have to be completely fortuitous in origin. Moreover, a propagation vector of the type $\langle 1/2\ 1/2\ 1/2\rangle$ has, to date, never been reported in uranium NaCl-type compounds. These observations suggest that the $\boldsymbol{k}_3$ reflections are not a product of local chemical or structural disorder, but are intimately related to the primary long-range magnetic order parameters.

Please purchase PDF Split-Merge on www.verypdf.com to remove this watermark.

From both the x-ray and neutron data, the effective symmetry-breaking direction lies along the reduced wavevector $\langle 111 \rangle$. Any combined lattice distortion or charge density wave at $\langle kk0 \rangle$ coupled with a magnetic dipole $\langle k00 \rangle$ is not supported by these observations. Furthermore, there is no experimental evidence for either a distortion or a charge density wave in the cubic phase.

The observation by diffraction of thermal neutrons is important since (i) the neutron is a weak probe of the electronic state thus eliminating possible distortions of the core and valence wavefunctions as a cause, (ii) the neutron scattering amplitude is well established and carries information on the shape of the scattering object (the form factor), unlike the x-ray resonant scattering amplitude which is based on approximate treatments of a strongly perturbative probe, and (iii) the time scale of the auto-correlation function of the $\boldsymbol{k}_3$ peaks is in the thermodynamic regime $\sim 10^{-11}$ to 10^{-12} s. Furthermore, the long-range, long-time order observed with respect to the three primary order parameters through $\mathbf{k_1}$ peaks on both D10 and the time-of-flight spectrometers in single crystal and polycrystalline samples respectively shows them to be representative of a thermodynamic magnetic configuration. By analogy, the same is likely to be the case for the 3-$\boldsymbol{k}$ state realised in $USb_{0.85}Te_{0.15}$ and $USb_{0.88}Te_{0.12}$.

The further evidence furnished by neutron time-of-flight analysis (Figure 4.21c,d) shows that local, slow, long-time dynamics persist into the paramagnetic phase. This suggests that the scattering associated with the long-range magnetic order parameters may originate from local magnetic scattering units, which appear to characterise the multi-$\boldsymbol{k}$ magnetic configuration, supporting arguments previously advanced on the basis of the x-ray resonant scattering data [47]. In conjunction with this, the measured lower limit for the phase coherence time scale in the 3-$\boldsymbol{k}$ state imposes significant constraints on any theoretical interpretation.

The form factor for the $\boldsymbol{k}_3$ cannot easily be extracted from the data. As the magnetic structure is not known the correction factor based on the magnetic moment direction is not easily applied. Using an estimate based on the x-ray azimuthal data and the observation of systematic absences in the neutron diffraction the integrated peak intensity appears to oscillate over a momentum transfer range of 0.9 - 4.2 Å^{-1} nearing a minimum at 3.5 Å^{-1}.

In the next chapter, a justification for the appearance $\boldsymbol{k}_3$ diffraction event is given, and some of the questions raised by the data are answered.

Please purchase PDF Split-Merge on www.verypdf.com to remove this watermark.

4.A Geometric structure factor

In $UAs_{0.8}Se_{0.2}$ and $USb_{0.88}Te_{0.12}$, the magnetic ions are arranged in a face centred cubic structure. In a triple-**k** structure, we consider the simultaneous existence of three ordering wavevectors: $\mathbf{k}_x = [1/2\ 0\ 0]$, $\mathbf{k}_y = [0\ 1/2\ 0]$ and $\mathbf{k}_z = [0\ 0\ 1/2]$. The structure factor for this arrangement is given by:

$$F(\tau) = \sum_i \mathbf{m}_i e^{i\tau.\mathbf{d}_i} \tag{4.11}$$

where $\mathbf{d}_i$ is the position of the magnetic moment $\mathbf{m}_i$ in real space. For the triple-**k** case, $\mathbf{m}_i$ is usually considered as the sum of Fourier components. These are considered to be longitudinal on the basis of neutron scattering data.

$$\mathbf{m}_i = \mathbf{m}_x e^{i\mathbf{k}_x.\mathbf{d}_i} + \mathbf{m}_y e^{i\mathbf{k}_y.\mathbf{d}_i} + \mathbf{m}_z e^{i\mathbf{k}_z.\mathbf{d}_i} \tag{4.12}$$

Let us consider the z component only, evaluated over a $2 \times 2 \times 2$ block of unit cells. The magnitude of $\mathbf{m}$ is set to unity.

$$\begin{aligned} F(\tau)_z &= (1 - e^{i2\pi\tau_z})(1 + e^{i2\pi\tau_x} + e^{i2\pi\tau_y} + e^{i2\pi(\tau_x+\tau_y)}) \\ &\quad (1 + e^{i\pi(\tau_x+\tau_z)} + e^{i\pi(\tau_x+\tau_y)} + e^{i\pi(\tau_y+\tau_z)}) \end{aligned} \tag{4.13}$$

$$\tag{4.14}$$

In this equation, the first bracket is generated by the periodicity along the z axis. The second bracket describes the phase coherence of the plane perpendicular to the z axis. The third bracket contains information on the relative phase of the four moments contained in the nuclear unit cell.

To obtain the x and y components of $F(\tau)$, $\tau_{x,y,z}$ must be cyclically permuted. At $\tau = (1/2\ 1/2\ 1/2)$, each of these components is necessarily zero. This arises from the second bracket.

Please purchase PDF Split-Merge on www.verypdf.com to remove this watermark.

4.B Azimuthal dependence in x-ray resonant scattering

Following the treatment of Hill and McMorrow [45], the dipole scattering amplitude is written as

$$\begin{aligned} f_{jE1} &= \begin{pmatrix} \sigma\to\sigma & \pi\to\sigma \\ \sigma\to\pi & \pi\to\pi \end{pmatrix} = F^{(0)} \begin{pmatrix} 1 & 0 \\ 0 & \cos(2\theta) \end{pmatrix} \\ &\quad -iF^{(1)} \begin{pmatrix} 0 & z_1\cos\theta + z_3\sin\theta \\ z_3\sin\theta - z_1\cos\theta & -z_2\sin(2\theta) \end{pmatrix} \\ &\quad +F^{(2)} \begin{pmatrix} z_2^2 & -z_2(z_1\sin\theta - z_3\cos\theta) \\ z_2(z_1\sin\theta + z_3\cos\theta) & -\cos^2\theta(z_1^2\tan^2\theta + z_3^2) \end{pmatrix} \end{aligned} \tag{4.15}$$

where θ is the Bragg scattering angle and z_i are the (orthonormal) components of the magnetization vector $\hat{\boldsymbol{m}}_j$ in the basis $[\boldsymbol{u}_1, \boldsymbol{u}_2, \boldsymbol{u}_3]$ where $\boldsymbol{u}_1$ is perpendicular to the scattering vector and in the scattering plane and $\boldsymbol{u}_3$ antiparallel to the scattering vector. The cross-section is sensitive to the local symmetry-breaking field and the $F^{(1)}$ are therefore not necessarily in proportion to the thermodynamic magnetic moment.

The azimuthal dependence is determined by expanding z_i in terms of the components μ_i of the symmetry breaking vector along orthogonal crystallographic unit vectors $\boldsymbol{x}_i$.

$$\begin{aligned} z_1 &= \mu_x\sin\alpha_1\cos(\psi+\delta_1) + \mu_y\sin\alpha_2\cos(\psi+\delta_2) + \mu_z\sin\alpha_3\cos(\psi+\delta_3) \\ z_2 &= \mu_x\sin\alpha_1\sin(\psi+\delta_1) + \mu_y\sin\alpha_2\sin(\psi+\delta_2) + \mu_z\sin\alpha_3\sin(\psi+\delta_3) \\ z_3 &= \mu_x\cos\alpha_1 + \mu_y\cos\alpha_2 + \mu_z\cos\alpha_3, \end{aligned} \tag{4.16}$$

where α_i is the angle between $\boldsymbol{x}_i$ and $\boldsymbol{u}_3$ at $\psi = 0$, and δ_i is the angle between $\boldsymbol{x}_i^\perp$ and $\boldsymbol{u}_1$ at $\psi = 0$. $\boldsymbol{x}_i^\perp$ is the projection of $\boldsymbol{x}_i$ onto the plane perpendicular to $\boldsymbol{Q}$. ψ is the azimuthal angle.

Please purchase PDF Split-Merge on www.verypdf.com to remove this watermark.

4.C Structure factors of $USb_{0.88}Te_{0.12}$

The nuclear Bragg peaks were measured using the 2D detector option on D10, and the integrated intensities were extracted using a Gaussian fitting procedure. The structure factor F_{hkl} was then calculated using

$$F_{hkl}^2 \propto \frac{I_{hkl}}{LAy} \tag{4.17}$$

where I_{hkl} is the integrated intensity of reflection (hkl), L is the Lorentz factor, A is the absorption correction and y is the extinction correction. The effect of absorption was neglected. Two thermal parameters were included. The scale factor, the extinction and the thermal parameters were refined with the Cambridge Crystallographic Subroutine Library [46], which uses a least squares refinement procedure.

hkl	F_{obs} (arb. units)	F_{calc} (arb. units)	$(F_{obs} - F_{calc})$ (arb. units)	$\sigma(F_{obs} - F_{calc})$ (arb. units)	y^2
200	332.433	381.007	-48.57370	-9.72	0.8532
400	361.704	373.017	-11.31308	-1.87	0.9008
220	358.602	384.799	-26.19736	-3.76	0.8837
420	368.618	381.007	6.01535	1.96	0.8979
111	96.764	381.007	4.16661	3.85	0.9897
311	97.765	94.781	2.89367	6.39	0.9931
331	95.373	96.329	-0.95638	-2.98	0.9925
222	367.148	380.599	-13.45050	-2.26	0.8964
422	356.562	346.645	9.91757	2.42	0.8801

Table 4.2: The structure factor listing for $USb_{0.88}Te_{0.12}$. The scale factor for this refinement is 81.7809 and $\chi^2 = 31.9$.

Please purchase PDF Split-Merge on www.verypdf.com to remove this watermark.

Chapter 5

Order parameter correlation in 3-k structures

Please purchase PDF Split-Merge on www.verypdf.com to remove this watermark.

Sommaire

Dans les deux derniers chapitres, des signes de la cohérence à grande distance entre les paramètres d'ordres magnétiques dans les états 3-$\boldsymbol{k}$ ont été vu. En particulier, des pics de Bragg ont été vu dans des endroits imprévus. Dans ce chapitre, une explication pour ces observations est présentée.

Dans cette explication, les pics $\boldsymbol{k}_3 = \tau + \langle 1/2\ 1/2\ 1/2 \rangle$, où τ est un vecteur du réseau réciproque et $1/2$ est dans les unités du réseau réciproque, sont considérés comme les signes de corrélations quantiques ordonnées, vus pour la première fois dans la matière condensée cristalline. Les corrélations quantiques ont été discutées avant dans le contexte des systèmes d'électrons fortement corrélés.

Une méthode pour développer les corrélations entre les paramètres d'ordre est établie dans l'algèbre géometrique, aussi nommé l'algèbre de Clifford. Cette algèbre est une algèbre vectorielle avec des règles pour développer un produit éxterieur. Cette algèbre a été utilisé pour étudier la résonance magnétique nucléaire et les intricats quantiques. Une introduction à cette algèbre est donnée dans l'annexe 5.A .

Cette méthode est ainsi utilisée pour exprimer les équations pour la diffusion neutronique, et on voit qu'une terme avec la symétrie et position des pics $\boldsymbol{k}_3$ apparaît. L'origine de cette terme est un corrélateur quantique entre les trois paramètres d'ordre ; une partie du produit géometrique des trois paramètres.

Pour essayer de mettre ces arguments sur une base numerique, ces arguments ont été appliqué aux orbites électroniques $5f$ pour voir si cela explique le facteur de forme neutronique. Dans la symétrie cubique pour les électrons $5f$, il y a trois types d'orbites : un singulet, nommé β, et deux triplets, δ et ϵ. Si les trois orbites δ sont correlés dans la manière décrite par l'algèbre géometrique, on réussit à reproduire le facteur de forme observé. En conclusion, les paramètres d'ordre sont corrélés dans ces composés 3-$\boldsymbol{k}$, et on peut identifier une signature de cette corrélation quantique aux températures relativement hautes.

Please purchase PDF Split-Merge on www.verypdf.com to remove this watermark.

5.1 Introduction

In the previous two chapters, signs of long-range coherence between the magnetic order parameters in 3-$\boldsymbol{k}$ states have been reported. In particular, diffraction events have been seen that are not yet accounted for within the conventional approach to multi-$\boldsymbol{k}$ structures. In this chapter, a possible explanation for these unexpected observations is presented.

The $\boldsymbol{k}_3$ peaks described in Chapter 4 are considered as signs of ordered quantum correlators, visible for the first time in periodic bulk condensed matter. Quantum correlations have been discussed both in the context of few-atom Bose condensates and strongly correlated electron systems such as the joint superconducting-magnetic state, which has been the subject of recent interest [54, 55]. Inspired by the success of the ideal gas model and associated developments, many approaches to the mesoscopic problem involve a conceptual fragmentation of the system into quasiparticle states as per the Landau Fermi-liquid model. Interactions are then included as a corrective glue to partially re-instate the broken correlations. Whilst a significant range of experimental data may be consistently treated within such a framework, albeit often requiring different quasiparticles to explain different thermodynamic and transport properties, the results presented in the previous Chapter appear to lie outside the paradigm.

A formalism to describe these order parameter correlations is developed using geometric algebra (GA), also known as Clifford algebra. Geometric algebra is an extended vector algebra with well-defined rules for treating outer vector products. It has been found useful when discussing, for example, nuclear magnetic resonance and quantum entanglement (see e.g. [56, 57]). An introduction to GA is given in Appendix 5.A, although the approach in the main text is self-contained. This formalism is then inserted into the neutron scattering cross-section and is shown to give rise to a diffraction event at the scattering vector $\boldsymbol{k}_3 = \boldsymbol{\tau} + \langle \frac{1}{2}\frac{1}{2}\frac{1}{2} \rangle$. The model is then used to examine the 'form factor' for the $\boldsymbol{k}_3$ reflections.

5.2 Motivation

Experimental motivation

To recap the principal experimental results that need to be accounted for, in the 3-$\boldsymbol{k}$ state in cubic antiferromagnets, cubic symmetry is maintained and the three $\boldsymbol{k}_1$ (single-$\boldsymbol{k}$) type reflections are present in equal quantities. A Bragg diffraction event is seen at scattering vector $\boldsymbol{k}_3 = \boldsymbol{\tau} + \langle \frac{1}{2}\frac{1}{2}\frac{1}{2} \rangle$. As discussed in the previous chapter, this peak cannot be obtained by a simple sum or product of the $\boldsymbol{k}_1$ order parameters. From both the neutron and x-ray resonant scattering data, the origin of these peaks appears to be a magnetic dipole pointing along the $\langle 111 \rangle$ directions parallel to the propagation vector $\langle \frac{1}{2}\frac{1}{2}\frac{1}{2} \rangle$.

The evidence presented in Chapter 4 indicates that these reflections are generated by the 3-$\boldsymbol{k}$ state, and not by any parasitic phase. From the time- and length-scales that have been probed, the scattering appears to be both long-time and long-range ordered.

Please purchase PDF Split-Merge on www.verypdf.com to remove this watermark.

Free energy arguments

First of all, the free energy of the system is examined, to see what it can tell us. The free energy for a multi-$\boldsymbol{k}$ structure was explored in Section 1.3, considering only the primary spin density waves corresponding with the three orthogonal propagation wavevectors $\boldsymbol{k}_\alpha$. To account for the $\boldsymbol{k}_3$ reflections, by both neutron and x-ray resonant scattering methods, a dipolar moment organized with a propagation wavevector of the type $\langle \frac{1}{2}\frac{1}{2}\frac{1}{2}\rangle$ is needed.

The order parameter for such scattering would have to have the form

$$\mathcal{M}_{\boldsymbol{k}'} = \mathbf{M}_{\boldsymbol{k}'} \mathrm{e}^{i(\boldsymbol{k}'\cdot\boldsymbol{r}+\theta_{\boldsymbol{k}'})} \tag{5.1}$$

where $\boldsymbol{k}' = \langle \frac{1}{2}\frac{1}{2}\frac{1}{2}\rangle (= \boldsymbol{k}_x + \boldsymbol{k}_y + \boldsymbol{k}_z)$. If this is to play a role in the free energy, it must contribute to terms that are translationally invariant with respect to the lattice vectors. Two types of term are obvious candidates:

$$A(k', T)(\mathcal{M}_{\boldsymbol{k}'} \cdot \mathcal{M}^*_{\boldsymbol{k}'}) \quad \text{and} \quad B_4 \mathcal{M}_{\boldsymbol{k}_x} \mathcal{M}_{\boldsymbol{k}_y} \mathcal{M}_{\boldsymbol{k}_z} \mathcal{M}^*_{\boldsymbol{k}'}. \tag{5.2}$$

where $\mathcal{M}_{\boldsymbol{k}_x} = \mathbf{M}_{\boldsymbol{k}_x} \mathrm{e}^{i(\boldsymbol{k}_x\cdot\boldsymbol{r}+\theta_{\boldsymbol{k}_x})}$ and $\theta_{\boldsymbol{k}'} = \theta_{\boldsymbol{k}_x} + \theta_{\boldsymbol{k}_y} + \theta_{\boldsymbol{k}_z}$ describe the single-$\boldsymbol{k}$ order parameters. If the B_4 term is to be translationally invariant, it is helpful to relabel $\mathcal{M}_{\boldsymbol{k}'}$ as $\mathcal{M}_{\boldsymbol{k}_{xyz}}$. Eight terms of the B_4 type must exist by cubic symmetry, with equal magnitudes. This means that $\mathcal{M}_{\boldsymbol{k}_{xyz}}$ must be invariant under cyclic permutations of the three coordinate axes. Such a permutation leaves $\boldsymbol{k}_{xyz}$ invariant, indicating that $\mathcal{M}_{\boldsymbol{k}_{xyz}}$ is longitudinal with respect to the propagation vector. This agrees with experimental observations.

Terms in the free energy must be real scalar quantities. For the A term, involving a dot product of two vectors, this is not a problem. For the B_4 term, the approach is not so clear. For the single-$\boldsymbol{k}$ components $\mathcal{M}_{\boldsymbol{k}_\alpha} \parallel \boldsymbol{k}_\alpha$, so the three components are orthogonal. The triple vector product is therefore zero. The triple scalar product gives a scalar, and so for the B_4 term to exist, B_4 must be a vector. Although such a term may exist in the free energy, we are no closer to identifying the origin of the $\boldsymbol{k}_3$ peaks.

Theoretical motivations

Having identified the need to go beyond the usual quasiparticle auto-correlation function to have a basis for understanding the appearance of the $\boldsymbol{k}_3$ Bragg peaks, an approach has been developed based in geometric algebra. Hestenes [58] and the Cambridge GA group [56] have evaluated the single-particle case and extended it to deal with multi-particle correlators. This is developed here, following the approach of Doran and Lasenby [56]. This is then generalized to cover multi-order parameter systems and applied to the neutron dipole scattering amplitude, firstly for a single electron, and then for a lattice. We stay in the non-relativistic limit. Appendix 5.A is a detailed introduction to the basics of 3D Clifford geometric algebra in this limit.

5.3 Quantum correlations in geometric algebra

A geometric algebra exists in a linear vector space within which the rules for vector multiplication are expanded. The *geometric* product of two vectors $\boldsymbol{a}$ and $\boldsymbol{b}$ is $\boldsymbol{ab} =$

Please purchase PDF Split-Merge on www.verypdf.com to remove this watermark.

$\boldsymbol{a} \cdot \boldsymbol{b} + \boldsymbol{a} \wedge \boldsymbol{b}$, where $\boldsymbol{a} \cdot \boldsymbol{b}$ is the inner product (in this case the normal scalar product) and $\boldsymbol{a} \wedge \boldsymbol{b}$ is the outer product. This second term is nominated a *bivector*, and is the first new element of the algebra. This grade-2 entity encodes an oriented plane, with a sense of rotation. The plane with the opposite sense of rotation is $\boldsymbol{b} \wedge \boldsymbol{a} = -\boldsymbol{a} \wedge \boldsymbol{b}$ (orthogonal vectors anti-commute). The bivector is related to, but distinct from, the Gibbs vector cross product characteristic to three-dimensional space. On using higher grade elements in place of the vectors $\boldsymbol{a}$ and $\boldsymbol{b}$, further terms are generated, up to the closure requirements of the GA as imposed by the number of dimensions of the vector space. The span of the algebra consists of a scalar, the set of basis vectors and the higher-order generalised products. The general element of the GA is termed a multivector and comprises a sum of elements of different grades.

For the GA of a 3-D Euclidean space, the (orthonormal) basis vectors $\boldsymbol{e}_k$ can be mapped to the three Pauli spin matrices $\hat{\sigma}_k$ and thereby generate an algebra isomorphic with that of Pauli spinor mechanics. To see this, consider the geometric product of two basis vectors

$$\boldsymbol{e}_i \boldsymbol{e}_j = \boldsymbol{e}_i \cdot \boldsymbol{e}_j + \boldsymbol{e}_i \wedge \boldsymbol{e}_j = \delta_{ij} + I \epsilon_{ijk} \boldsymbol{e}_k \tag{5.3}$$

where $I = \boldsymbol{e}_i \boldsymbol{e}_j \boldsymbol{e}_k$ is the unit *trivector* for the algebra. This new grade-3 element is a directed volume element; $\boldsymbol{e}_i \boldsymbol{e}_k \boldsymbol{e}_j = -I$. In a 3-D space there can only be one independent trivector, and it commutes with all of the basis vectors. $I \boldsymbol{e}_k = \boldsymbol{e}_i \boldsymbol{e}_j$, where $\boldsymbol{e}_k$ is the vector perpendicular to the plane defined by the bivector $\boldsymbol{e}_i \boldsymbol{e}_j$.

Equation 5.3 is isomorphic with the equation defining the properties of the Pauli matrices in quantum spinor mechanics.

5.3.1 A spin-1/2 particle

The Pauli spin operators

$$\hat{s}_k = \frac{\hbar}{2} \hat{\sigma}_k, \tag{5.4}$$

where $k = \{x, y, z\}$, together with an appropriate set of 2-component spinors,

$$|\psi\rangle = \begin{pmatrix} \alpha \\ \beta \end{pmatrix} \qquad \alpha, \beta \in \mathbb{C} \tag{5.5}$$

are used to describe states involving spin-1/2 particles. Here α and β are complex numbers that relate to the probability of observing the spin-up and spin-down states respectively, relative to the axis of quantization, labelled z.

The mapping of the spinor to GA

The $\hat{\sigma}_k$ Pauli operators are represented in GA as basis vectors labelled $\boldsymbol{e}_k$. In this notation the axis of quantization is $\boldsymbol{e}_3$. We now consider the observable

$$s_k = \frac{\hbar}{2} n_k = \langle \psi | \hat{s}_k | \psi \rangle \tag{5.6}$$

Please purchase PDF Split-Merge on www.verypdf.com to remove this watermark.

where $n_k = \langle\psi|\hat{\sigma}_k|\psi\rangle$. This can be expressed as a classical vector $\boldsymbol{n} = (n_x, n_y, n_z)$ with $|\boldsymbol{n}|^2 = (|\alpha|^2 + |\beta|^2) = \langle\psi|\psi\rangle^2 = 1$ for normalized states. In spherical polar coordinates, this vector is

$$\boldsymbol{n} = \sin\theta\,(\cos\phi\,\boldsymbol{e}_1 + \sin\phi\,\boldsymbol{e}_2) + \cos\theta\,\boldsymbol{e}_3. \tag{5.7}$$

θ determines the rotation of the spin relative to the axis of quantization. ϕ determines the rotation of the $\boldsymbol{e}_3 - \boldsymbol{n}$ plane, but for a single spin, this rotation is irrelevant (gauge invariance). Using this classical interpretation, the spinor can be rewritten in terms of the angles θ and ϕ.

$$|\psi\rangle = \begin{pmatrix} \cos(\theta/2)\mathrm{e}^{-i\phi/2} \\ \sin(\theta/2)\mathrm{e}^{i\phi/2} \end{pmatrix} \mathrm{e}^{i(\gamma+\delta)/2} \tag{5.8}$$

where $\phi = \delta - \gamma$. The overall phase factor $(\gamma+\delta)$ can be thought of as the alignment of the spin space. For a single spin, this is irrelevant, but when more than one spin is involved, this term can be difficult to deal with. In the GA approach, all of this information is included in $\boldsymbol{n}$. Assuming for the moment that the overall phase factor can be safely ignored, the spinor is now described in terms of half-angles, and looks like a rotor: the rotation of the axis of quantization onto $\boldsymbol{n}$.

In GA, this rotation of the $\boldsymbol{e}_3 - \boldsymbol{n}$ plane by the angle ϕ can be described by a rotor of the form $\exp[-B\phi/2]$, where B is the bivector defining the plane of rotation, $\boldsymbol{e}_1\boldsymbol{e}_2$. To show this we can write, using the orthonormal nature of the basis vectors,

$$\begin{aligned} (\cos\phi\,\boldsymbol{e}_1 + \sin\phi\,\boldsymbol{e}_2) &= (\cos\phi + \boldsymbol{e}_2\boldsymbol{e}_1\sin\phi)\boldsymbol{e}_1 \\ &= \exp[-\boldsymbol{e}_1\boldsymbol{e}_2\phi]\boldsymbol{e}_1 = \exp[-I\boldsymbol{e}_3\phi]\boldsymbol{e}_1 \\ &= \exp[-I\boldsymbol{e}_3\phi/2]\exp[-I\boldsymbol{e}_3\phi/2]\boldsymbol{e}_1 \\ &= \exp[-I\boldsymbol{e}_3\phi/2]\boldsymbol{e}_1\exp[I\boldsymbol{e}_3\phi/2]. \end{aligned} \tag{5.9}$$

The first step, obtaining the exponential form, uses the face that $(\boldsymbol{e}_1\boldsymbol{e}_2)(\boldsymbol{e}_1\boldsymbol{e}_2) = -1$, and so $\boldsymbol{e}_1\boldsymbol{e}_2 = I\boldsymbol{e}_3$ acts like i in the exponential expansion $\mathrm{e}^{i\theta} = \cos\theta + i\sin\theta$. Following a similar procedure for the θ variable

$$\begin{aligned} \boldsymbol{n} &= \exp[-\phi I\boldsymbol{e}_3/2]\exp[-\theta I\boldsymbol{e}_2/2]\boldsymbol{e}_3\exp[\theta I\boldsymbol{e}_2/2]\exp[\phi I\boldsymbol{e}_3/2] \\ &= R\boldsymbol{e}_3R^\dagger. \end{aligned} \tag{5.10}$$

This is simply the rotation of the axis of quantization of the spinor, and suggests that the rotor R is a map to the spinor. By expanding the rotors, the mapping for the Pauli spinor $\leftrightarrow$ GA is obtained. Explicitly,

$$\begin{aligned} R &= \exp[-\phi I\boldsymbol{e}_3/2]\exp[-\theta I\boldsymbol{e}_2/2] \\ &= 1 - \frac{\phi}{2}I\boldsymbol{e}_3 - \frac{\theta}{2}I\boldsymbol{e}_2 + \frac{\phi}{2}\frac{\theta}{2}I\boldsymbol{e}_3I\boldsymbol{e}_2 + \text{h.o.t.} \end{aligned}$$

The higher order terms simply add to the four basic terms presented here, changing the coefficients, and as the spinor can be written as

$$|\psi\rangle = \begin{pmatrix} a^0 + ia^3 \\ -a^2 + ia^1 \end{pmatrix} \tag{5.11}$$

Please purchase PDF Split-Merge on www.verypdf.com to remove this watermark.

the a^i terms are identified with the four basic components of the rotor, giving the mapping

$$|\psi\rangle = \begin{pmatrix} a^0 + ia^3 \\ -a^2 + ia^1 \end{pmatrix} \leftrightarrow \psi = a^0 + a^k I\boldsymbol{\sigma}_k \tag{5.12}$$

so that $|\uparrow\rangle = 1$ and $|\downarrow\rangle = -I\boldsymbol{e}_2$. The spinor is a rotor.

The operator

The spinor has now been written as a GA multivector. The operators $\{\hat{\sigma}_k\}$ also require mapping. This is done by example.

$$\hat{\sigma}_1|\psi\rangle = \begin{pmatrix} -a^2 + ia^1 \\ a^0 + ia^3 \end{pmatrix} \leftrightarrow -a^2 + a^1 I\boldsymbol{e}_3 - a^0 I\boldsymbol{e}_2 + a^3 I\boldsymbol{e}_1 \tag{5.13}$$

Using Equation 5.12 the right-hand-side of this can be written as follows:

$$\begin{aligned} -a^2 + a^1 I\boldsymbol{e}_3 - a^0 I\boldsymbol{e}_2 + a^3 I\boldsymbol{e}_1 &= \boldsymbol{e}_1(a^0 + a^1 I\boldsymbol{e}_1 + a^2\boldsymbol{e}_2 + a^3 I\boldsymbol{e}_3)\boldsymbol{e}_3 \\ &= \boldsymbol{e}_1\psi\boldsymbol{e}_3. \end{aligned} \tag{5.14}$$

suggesting that the general operator mapping requires right multiplication by $\boldsymbol{e}_3$.

$$\hat{\sigma}_k|\psi\rangle \leftrightarrow \boldsymbol{e}_k\psi\boldsymbol{e}_3 \tag{5.15}$$

This can be verified by example for all of the operators.

The quantum mechanical imaginary

One further quantity needs to be evaluated: the unit imaginary as used in quantum mechanics. In Pauli algebra, the unit imaginary matrix, is given by $\hat{\sigma}_1\hat{\sigma}_2\hat{\sigma}_3$ suggesting that pre-multiplication by i be considered as an operator and so, on translation to GA,

$$i|\psi\rangle \leftrightarrow \boldsymbol{e}_1\boldsymbol{e}_2\boldsymbol{e}_3\psi(\boldsymbol{e}_3)^3 = \psi I\boldsymbol{e}_3 \tag{5.16}$$

i.e. right multiplication by the bivector $I\boldsymbol{e}_3$.

Single particle observables

An observable is formed in wave mechanics by taking an inner product, where, in the bra-ket notation the 'bra' wavefunction is the Hermitian conjugate. In GA, this operation corresponds with the reversal of the order of the GA elements. A quantity must be assembled to give the correct scalar projection. By direct expansion one obtains the mapping

$$\langle\psi|\phi\rangle = \mathrm{Re}\langle\psi|\phi\rangle - i\mathrm{Re}\langle\psi|i\phi\rangle \leftrightarrow \langle\psi^\dagger\phi\rangle - \langle\psi^\dagger\phi I\boldsymbol{e}_3\rangle I\boldsymbol{e}_3 \tag{5.17}$$

where the angular brackets on the right-hand-side indicate that the scalar projection of the geometric product is to be taken, i.e the scalar components are extracted. Using Equations 5.15 and 5.17 the expectation value for a spin in the k direction is therefore mapped as

$$\langle\psi|\hat{\sigma}_k|\psi\rangle \leftrightarrow \langle\psi^\dagger\boldsymbol{e}_k\psi\boldsymbol{e}_3\rangle - \langle\psi^\dagger\boldsymbol{e}_k\psi I\rangle I\boldsymbol{e}_3. \tag{5.18}$$

Please purchase PDF Split-Merge on www.verypdf.com to remove this watermark.

5.3.2 Multi-particle states

So far, we have discussed a single spin-1/2 particle, described by a state multivector basis set $\{1, \boldsymbol{e}_j^1\}$ in the GA. A second, identical, particle is added, with its own basis set $\{1, \boldsymbol{e}_k^2\}$ where the superscript is the particle label. In ordinary spinor mechanics a state-vector of arbitrary angular momentum is generated by successive application of spinor operators (e.g. $|\psi\rangle = |\phi_1\rangle \otimes |\phi_2\rangle \otimes |\phi_3\rangle$). In GA simply involves multiplying together the appropriate multivectors.

The basis elements of the direct product are therefore

$$\{1, \boldsymbol{e}_j^1, \boldsymbol{e}_k^2, \boldsymbol{e}_j^1 \boldsymbol{e}_k^2\} \tag{5.19}$$

This has sixteen degrees of freedom; a two-spin system is known to have only eight. This difference arises because here there are two quantum mechanical 'imaginaries', $I^1\boldsymbol{e}_3^1$ and $I^2\boldsymbol{e}_3^2$. (From now on, the trivector I will be assumed to have the same superscript label as the following $\boldsymbol{e}_k$.) By equating the action of these two imaginaries, the degrees of freedom are reduced to eight.[1]

$$\psi I \boldsymbol{e}_3^1 = \psi I \boldsymbol{e}_3^2 \tag{5.20}$$

which can be rearranged to give

$$\psi = -\psi I \boldsymbol{e}_3^1 I \boldsymbol{e}_3^2 = \psi \frac{1}{2}(1 - I\boldsymbol{e}_3^1 I \boldsymbol{e}_3^2). \tag{5.21}$$

defining

$$E_2 = \frac{1}{2}(1 - I\boldsymbol{e}_3^1 I \boldsymbol{e}_3^2). \tag{5.22}$$

which has the property $E_2^2 = E_2$ as a *projection operation*. Applied to states of the system, this enforces compliance with the restrictions of standard Pauli spinor mechanics and reduces the system to eight degrees of freedom. In a direct product state vector this is given as,

$$\psi = \phi^1 \phi^2 E_2 \tag{5.23}$$

where ϕ^i are the spinors for the individual particles.

The compound imaginary

A quantum correlator of odd symmetry may also be defined,

$$J_2 = E_2 I \boldsymbol{e}_3^1 = E_2 I \boldsymbol{e}_3^2 = \frac{1}{2}(I\boldsymbol{e}_3^1 + I\boldsymbol{e}_3^2). \tag{5.24}$$

This has the property $J_2^2 = -E_2$. Even though $E_2 \neq 1$, J_2 has the nature of a generalised quantum imaginary for a two-spin state.

[1] This ties together the arbitrary phase terms in Equation 5.7.

Please purchase PDF Split-Merge on www.verypdf.com to remove this watermark.

General multi-particle states

This formalism can be extended to higher multiplicities. The key is E_n, which is, for higher particle numbers

$$E_n = \prod_{b=2}^{n} \frac{1}{2}(1 - I\boldsymbol{e}_3^1 I\boldsymbol{e}_3^b). \tag{5.25}$$

J_n is then constructed via the condition,

$$J_n = E_n I\boldsymbol{e}_3^a \qquad \forall\ a \tag{5.26}$$

5.3.3 Multiple order parameters

The nature of the quantum correlator

In the approach outlined above, a distinct copy of the GA has been associated with each (quasi)particle. This is easily visualized. From the macroscopic perspective, however, the nature of the quasiparticle is not always evident. The copies of the GA can instead be considered as independent configuration spaces out of which the quantum correlator is projected, and so the quasiparticle need not be defined.

These configuration spaces each have their own frame of reference relative to the external frame of reference. An example would be the three magnetic order parameters seen experimentally in Chapter 4. Each order parameter is a defined parameter space with its own frame of reference (defined by the direction of the polarization vector), and they are mutually orthogonal. Another example would be electronic orbitals, each with its own frame of reference relative to the external frame of reference and set of appropriate Pauli spin operators. If these spaces are correlated a particle evolving inside them will be affected by the correlation between them, and so obey the correlators derived above. For three magnetic order parameters, there are three configuration spaces, and so the third-order correlatior is of interest.

The third-order correlators

For a three-spin state, the correlators E and J can be developed using Equations 5.25 and 5.26.

$$\begin{aligned} E_3 &= \frac{1}{4}(1 - I\boldsymbol{e}_3^1 I\boldsymbol{e}_3^2)(1 - I\boldsymbol{e}_3^1 I\boldsymbol{e}_3^3) \\ &= \frac{1}{4}(1 - I\boldsymbol{e}_3^1 I\boldsymbol{e}_3^2 - I\boldsymbol{e}_3^1 I\boldsymbol{e}_3^3 + I\boldsymbol{e}_3^1 I\boldsymbol{e}_3^2 I\boldsymbol{e}_3^1 I\boldsymbol{e}_3^3) \\ &= \frac{1}{4}(1 - I\boldsymbol{e}_3^1 I\boldsymbol{e}_3^2 - I\boldsymbol{e}_3^1 I\boldsymbol{e}_3^3 - I\boldsymbol{e}_3^2 I\boldsymbol{e}_3^3) \end{aligned} \tag{5.27}$$

$$\begin{aligned} J_3 &= E_3 I\boldsymbol{e}_3^1 = E_3 I\boldsymbol{e}_3^2 = E_3 I\boldsymbol{e}_3^3 \\ &= \frac{1}{4}(1 - I\boldsymbol{e}_3^1 I\boldsymbol{e}_3^2 - I\boldsymbol{e}_3^1 I\boldsymbol{e}_3^3 - I\boldsymbol{e}_3^2 I\boldsymbol{e}_3^3) I\boldsymbol{e}_3^1 \\ &= \frac{1}{4}(I\boldsymbol{e}_3^1 + I\boldsymbol{e}_3^2 + I\boldsymbol{e}_3^3 - I\boldsymbol{e}_3^1 I\boldsymbol{e}_3^2 I\boldsymbol{e}_3^3) \end{aligned} \tag{5.28}$$

Please purchase PDF Split-Merge on www.verypdf.com to remove this watermark.

The observable for a order-n correlated state

As mentioned, J takes the role of the unit imaginary, and the expectation value of spin in the $\hat{\sigma}_k^1$ subspace in direction k is given as

$$\langle\psi|\hat{\sigma}_k^1|\psi\rangle \leftrightarrow \langle\psi^\dagger \boldsymbol{e}_k^1\psi\boldsymbol{e}_3^1\rangle - \langle\psi^\dagger \boldsymbol{e}_k^1\psi\boldsymbol{e}_3^1 J\rangle J. \tag{5.29}$$

The second term has no scalar part, and, after a little algebra taking into account the higher-order correlator, one arrives at

$$\langle\psi|\hat{\sigma}_k^1|\psi\rangle \leftrightarrow -2^{n-1}\langle I\boldsymbol{e}_k^1\psi^\dagger J_n\psi\rangle = -2^{n-1} I\boldsymbol{e}_k^1\cdot(\psi^\dagger J_n\psi). \tag{5.30}$$

Observables involving higher odd powers of $\hat{\sigma}_i$ come from a projection of the $(\psi^\dagger J_n\psi)$ quantity, whilst terms of even power are transmitted through $(\psi^\dagger E_n\psi)$.

5.4 Neutron scattering

5.4.1 Introduction

If an interaction can be written as an expectation value for a dipole, the higher-order correlations are compactly described using J_n. In second-order (J_2) correlated states the additional quantum correlations are not projected by such probes, but the understanding of quantum correlation is considerably advanced by their study. A probe looking at the expectation value of two dipoles would, however, give rise to observable differences, via the E_2 correlator. With a single dipole probe, the first 'new' correlations will be seen from the J_3 correlator.

When looking at electrons, the neutron is a dipolar probe and so the scattering amplitude is written out explicitly as an expectation value of a single dipole, starting with the scattering from a single electron, and then moving to scattering from a periodic lattice. The expectation value for the J_3 term is then evaluated.

5.4.2 Neutron-electron interaction

To construct the scattering amplitude the combined probe-sample wavefunction is split into time intervals before and after the scattering event. This artificial fragmentation introduces a probabilistic aspect concurrent with a direction of time. At any instant, outside the (unspecified) interaction time interval, the state-vector of the electron-neutron system is taken to have distinct spatial and spinor components in the form of a direct product, $\psi_{sys}(\boldsymbol{r}_n,\boldsymbol{r}_i;\boldsymbol{s}_n,\boldsymbol{\sigma}_i;t) = \phi_{sys}(\boldsymbol{r}_n,\boldsymbol{r}_i;t)\chi_{sys}(\boldsymbol{s}_n,\boldsymbol{\sigma}_i;t)$ where $\boldsymbol{r}_n$, $\boldsymbol{r}_i$ and $\boldsymbol{\sigma}_i$, $\boldsymbol{s}_n$ are electron and neutron spatial and spin co-ordinates respectively. Possible spin-orbit terms are therefore neglected. The combined wavefunction is then separated in the first Born approximation as $\phi_{sys}(\boldsymbol{r}_n,\boldsymbol{r}_i;t) = \phi_n(\boldsymbol{r}_n;t)\phi_s(\boldsymbol{r}_i;t)$; in contrast, the spinor fragment is projected onto a stationary set of joint neutron-electron eigenstates. As the spatial location is unknown/undefined, the neutron wavefunction is taken as a plane wave. When constructing the total scattering amplitude, the neutron beam state-vector is taken as a linear summation over individual neutrons.

Please purchase PDF Split-Merge on www.verypdf.com to remove this watermark.

The neutron-electron dipole-dipole scattering amplitude arises from an effective Zeeman field. The Hamiltonian depends on the relative separation, $\boldsymbol{R} = \boldsymbol{r}_n - \boldsymbol{r}_i$, and the spin configuration of the two particles

$$\hat{H}_i = (g\mu_B\gamma\mu_N)\hat{\boldsymbol{s}}_n \cdot \nabla \times \left(\frac{\hat{\boldsymbol{\sigma}}_i \times \boldsymbol{R}}{|\boldsymbol{R}|^3}\right). \tag{5.31}$$

where $\hat{\boldsymbol{s}}_n$ and $\hat{\boldsymbol{\sigma}}_i$ are respectively the neutron and electron spin operator and the remaining symbols take on their conventional meanings (see e.g. Lovesey and Balcar [59]).

The geometrical restrictions imposed by the form of the electromagnetic interaction generate powerful selection rules. To illustrate this it is convenient to express $\boldsymbol{R}/|\boldsymbol{R}|^3$ as $\nabla \cdot (1/|\boldsymbol{R}|)$ and then decompose $(1/|\boldsymbol{R}|)$ into plane wave states. Integrating over the neutron spatial co ordinates, assuming that neutron (plane wave) is uniformly distributed in space at all times, the Fourier transform variable can be written as $\boldsymbol{Q} = \boldsymbol{k}_f - \boldsymbol{k}_i$ giving

$$\hat{H}_i = 4\pi\hat{\boldsymbol{s}}_n \cdot [\boldsymbol{Q} \times (\hat{\boldsymbol{\sigma}}_i \times \boldsymbol{Q})]\frac{e^{i\boldsymbol{Q}\cdot\boldsymbol{r}_i}}{Q^2} \tag{5.32}$$

or, since this can be written as

$$\hat{H}_i = 4\pi[(\hat{\boldsymbol{s}} \cdot \hat{\boldsymbol{\sigma}})(\boldsymbol{Q} \cdot \boldsymbol{Q}) - (\hat{\boldsymbol{s}} \cdot \boldsymbol{Q})(\hat{\boldsymbol{\sigma}} \cdot \boldsymbol{Q})]\frac{e^{i\boldsymbol{Q}\cdot\boldsymbol{r}_i}}{Q^2} \tag{5.33}$$

the $\hat{\boldsymbol{s}}_n$ and $\hat{\boldsymbol{\sigma}}_i$ operators can be interchanged

$$\hat{H}_i = 4\pi\hat{\boldsymbol{\sigma}} \cdot [\boldsymbol{Q} \times (\hat{\boldsymbol{s}} \times \boldsymbol{Q})]\frac{e^{i\boldsymbol{Q}\cdot\boldsymbol{r}_i}}{Q^2}. \tag{5.34}$$

The expression is symmetric both with respect to wave-vector and $\hat{\boldsymbol{s}}$ and $\hat{\boldsymbol{\sigma}}$ of the neutron and electron respectively for the single-electron case. Equation 5.34 gives the Hamiltonian with respect to the electron spin operators $\hat{\boldsymbol{\sigma}}$. The electron is acting in a magnetic field created by the neutron. This is a two-level system, and so the Hamiltonian can be written as $\hat{H} = a_0\hat{\sigma}_0 + a_\alpha\hat{\sigma}_\alpha$, with α as a Cartesian component.

The price of integrating out of the unknown, uniform, prior and posterior neutron spatial dependence is that the a_α are complex and the Hamiltonian of the effective two level system is non-Hermitian. Explicitly,

$$a_\alpha^{\boldsymbol{Q}}(\boldsymbol{r}_i) = (g\mu_B\gamma\mu_N)(\frac{m}{2\pi\hbar^2})(\frac{e^{i\boldsymbol{Q}\cdot\boldsymbol{r}_i}}{Q^2})\sum_\beta [Q^2\delta_{\alpha\beta} - Q_\alpha Q_\beta]\hat{s}_\beta. \tag{5.35}$$

The energy eigenvalues for this are $E_\pm = a_0 + \sqrt{a_x^2 + a_y^2 + a_z^2}$ or, more concisely $E_\pm = a_0 + |\boldsymbol{a}|\exp(i\boldsymbol{Q}\cdot\boldsymbol{r}_i)$.

It is clear that the electromagnetic interaction, and therefore the dipole-dipole scattering amplitude, vanishes when the neutron spin lies parallel to $\boldsymbol{Q}$. These problems formally vanish when it is recalled that, in the free-electron problem, as there is no lattice, the stationary phase condition of elastic scattering can only occur at $\boldsymbol{Q} = 0$. In harmony with this the joint spinor eigenstate ensures that there is no scattering.

Please purchase PDF Split-Merge on www.verypdf.com to remove this watermark.

The probabilistic scattering event must now be introduced for a second time to break the spin symmetry of H_i. Approximations and assumptions made to achieve a macroscopic scattering rate are discussed in the following section.

The expectation value of the Hamiltonian maps to GA as

$$\langle\psi|\hat{H}_i|\psi\rangle \leftrightarrow a_\alpha \boldsymbol{\sigma}_\alpha \cdot (\psi \boldsymbol{\sigma}_3 \psi^\dagger) \tag{5.36}$$

where ψ is the electron state vector. This is then re-written to express the expectation value as an interaction with an effective magnetic field $\boldsymbol{B}$ generated by the neutron.

$$\langle\psi|\hat{H}_i|\psi\rangle \leftrightarrow \boldsymbol{B} \cdot (\psi \boldsymbol{\sigma}_3 \psi^\dagger). \tag{5.37}$$

Application to the projection into the p^{th} sub-space of a mesoscopic state (Section 5.3.3) yields

$$\langle\psi|\hat{H}_i|\psi\rangle \leftrightarrow -2^{n-1} I \boldsymbol{B}^p \cdot (\psi J_n \psi^\dagger). \tag{5.38}$$

where $\boldsymbol{B}^p$ is the neutron field evaluated in the p^{th} sub-space.

5.4.3 The lattice

From the single particle analysis it is clear that there is one common Fourier $\boldsymbol{Q}$ vector for *all* components of the electron $\hat{\boldsymbol{\sigma}}$ operator, and that no products of $\hat{\boldsymbol{\sigma}}$ components (e.g. $\boldsymbol{\sigma}_1\boldsymbol{\sigma}_2$ cross terms) occur in the interaction Hamiltonian. Rather, $\hat{H}$ is the sum of the components each sitting in their own Zeeman field. This underlines the restriction of the neutron magnetic cross-section to dipole scattering. To clarify the formalism for (macroscopic) Bragg scattering it is necessary to consider the modifications in scattering amplitude arising from electronic correlations.

There are qualitative differences in the scattering amplitude for bound and spatially periodic multi-electron systems. Primarily, the joint neutron-electron spinor and wavefunction symmetries described above are broken on introducing the time-averaged macrostate. Once the electron wave function is bounded, elimination of the Fourier transform vector is most reasonably made in favour of the neutron spatial co-ordinate as it can easily be treated as a plane wave. The electromagnetic interaction becomes a perturbative, non-diagonalised term precluding direct summation of the zero-scattering independent-particle response.

A mesoscopic scattering event occurs when the stationary phase condition is fulfilled. This condition, that the total phase in the scattering amplitude at a given scattering vector be zero when summed over the space-time coherence volume of diffraction, is paraphrased in Bragg's law [60, 61], where the choice of experimental scattering vector determines the stationary phase condition probed. The mesoscopic scattering operator is constructed, over the diffraction coherence volume, as the linear sum of the free-particle scattering interaction evaluated over the periodic macroscopic state within the single quasiparticle approximation.

The mesoscopic state-vector and applied operators are projected onto a lattice of N sites. The electronic quasiparticle states are distinguished by their site index v. A modulated magnetic configuration, e.g. the Néel state, may be represented in GA by

Please purchase PDF Split-Merge on www.verypdf.com to remove this watermark.

$\boldsymbol{\sigma}_3 \rightarrow \boldsymbol{\sigma}_3 \exp(i\boldsymbol{k}.\boldsymbol{r}_v)$ where $\boldsymbol{k}$ is the characteristic ordering wave vector. This phase term represents a rotation of the frame of quantization for the correlator on site v.

These changes then have to be carried through to the J_n correlator with the stationary phase condition, $(\boldsymbol{Q}+\boldsymbol{k}-\boldsymbol{\tau}) = \text{constant}$. In a cubic lattice, projecting the level-3 quantum correlators we obtain

$$J_3 = \frac{1}{4}(I\boldsymbol{\sigma}_3^1 \mathrm{e}^{i\boldsymbol{k}_x.\boldsymbol{r}} + I\boldsymbol{\sigma}_3^2 \mathrm{e}^{i\boldsymbol{k}_y.\boldsymbol{r}} + I\boldsymbol{\sigma}_3^3 \mathrm{e}^{i\boldsymbol{k}_z.\boldsymbol{r}} - I\boldsymbol{\sigma}_3^1 \mathrm{e}^{i\boldsymbol{k}_x.\boldsymbol{r}} I\boldsymbol{\sigma}_3^2 \mathrm{e}^{i\boldsymbol{k}_y.\boldsymbol{r}} I\boldsymbol{\sigma}_3^3 \mathrm{e}^{i\boldsymbol{k}_z.\boldsymbol{r}}) \tag{5.39}$$

where the three characteristic ordering wave vectors, $\boldsymbol{k}$ are given by $\boldsymbol{k}_x$, $\boldsymbol{k}_y$ and $\boldsymbol{k}_z$ respectively.

The $\boldsymbol{k}_1$ Bragg peak symmetries in the 3-$\boldsymbol{k}$ phases of the uranium rocksalts force the representative moments to be longitudinal, i.e. parallel to the appropriate $\boldsymbol{k}_1$ vector. The pth sub-space axis of quantization, $\boldsymbol{\sigma}_3^p$ is therefore taken parallel to its $\boldsymbol{k}_1$ vector. As the term in the exponential is a scalar product, there are no problems in aggregating the exponential terms in the last term of J_3, giving rise to a stationary phase condition for peaks at $\boldsymbol{k}_3 = \boldsymbol{k}_x + \boldsymbol{k}_y + \boldsymbol{k}_z$.

The stationary phase condition of coherent Bragg diffraction enables the experimenter to exploit the scattering geometry to select a unique propagation wave-vector and hence extract the individual terms in J_3. Thus, for example, the $\boldsymbol{k}_1$ amplitudes associated with the subset $\{j^1\boldsymbol{\sigma}_z^1, j^2\boldsymbol{\sigma}_z^2, j^3\boldsymbol{\sigma}_z^3\} \sim \{m_x, m_y, m_z\}$ are selected by tuning the spectrometer to their respective wave-vectors $\{\boldsymbol{k}_x, \boldsymbol{k}_y, \boldsymbol{k}_z\}$ where the effective interaction of a given spin operator in frame of quantization (1) with a field of magnitude B_α is $\mu_B\langle B_\alpha \hat{\sigma}_\alpha^1\rangle = -j\mu_B B_\alpha \boldsymbol{\sigma}_\alpha^1 \cdot (\psi J_3 \psi^\dagger)$. These terms give rise to Bragg peaks at the same positions as the J_1 quantum correlator.

The new third-order scattering amplitude of the 3-$\boldsymbol{k}$ term is projected by the $\boldsymbol{k}_3$ propagation vector at $\boldsymbol{Q} = \langle \frac{1}{2}\frac{1}{2}\frac{1}{2}\rangle + \boldsymbol{\tau}$ with an amplitude proportional to $j\boldsymbol{\sigma}_z^1 j\boldsymbol{\sigma}_z^2 j\boldsymbol{\sigma}_z^3$. The propagation vector of the $\boldsymbol{k}_3$ term reveals that it arises from a periodic array of ferromagnetic sheets perpendicular to $\langle 111\rangle$ with antiferromagnetic phasing.

Furthermore, in the 3-$\boldsymbol{k}$ state, no matter which sub-space p in the orthogonal set, $p \in \{1, 2, 3\}$, is projected onto by $-jB_\alpha \boldsymbol{\sigma}_\alpha^p \cdot (\psi J_3 \psi^\dagger)$, the expectation value must be the same under the cubic symmetry, indicating that the direction of $(\psi J_3 \psi^\dagger)_1$ lies along the $\langle 111\rangle$ directions. This is consistent with the symmetries established by the free energy arguments and explains the systematic absences noted in neutron diffraction [62] and the x-ray azimuth dependence [63].

5.4.4 Summary

The mapping of a spin-1/2 particle from its spinor to GA has been developed and extended to multi-particle systems. This has been applied to the neutron scattering dipole amplitude, where the effect of a lattice is explored. This translation to GA and its extension to cover the mesoscopic level-3 quantum correlator provides a rationale for the observation of magnetic dipole scattering at $\boldsymbol{k}_3$ positions in the cubic 3-$\boldsymbol{k}$ phase of the uranium rock salts. The azimuth dependence of x-ray resonant scattering $\boldsymbol{k}_3$ peaks as reported in Fig. 4.11 may be evaluated as shown and the systematic absences in neutron

Please purchase PDF Split-Merge on www.verypdf.com to remove this watermark.

diffraction at positions where $\boldsymbol{\tau} \parallel \langle kkk \rangle$ can be understood in this picture. The intensity dependence (a ratio $\boldsymbol{k}_1 : \boldsymbol{k}_3 = 1{:}10^{-3}$) seems reasonable given the origin of the $\boldsymbol{k}_3$ peak in this model.

5.5 The spatial distribution of the magnetization

5.5.1 Introduction

The magnetic form factor as measured by neutrons is the Fourier transform of the spatial magnetization distribution of the individual scattering unit. The form factor is obtained from measurements of the wavevector-dependent integrated intensity envelope that applies to the magnetic Bragg peaks. After correction for instrumental effects and the geometrical constraints imposed by the magnetic structure, this is typically compared with calculations based on the radial integrals for free single ions.

Form factors of this type were calculated in the 1970s and are tabulated in the Neutron Data Booklet [48]. The original calculations for uranium were carried out by Freeman *et al.* [50], who used the relativistic Dirac-Fock equations to evaluate the free-ion radial integrals of several U ions. There is very little observable difference between the U^{3+}, U^{4+} and U^{5+} in the Q range typically accessible for a crystal with a lattice parameter of 5-6 $Å^{-1}$. The different radial integrals for the U^{4+} ion are illustrated in Figure 5.1.

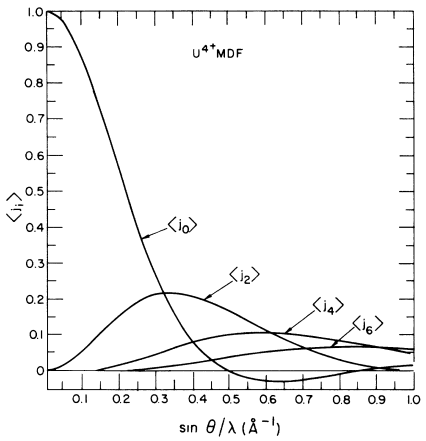

Figure 5.1: Radial $\langle j_i \rangle$ integrals obtained with Dirac-Fock solutions for U^{4+}. Taken from Freeman *et al.* [50].

It is somewhat surprising that these single-ion form factors work so well for ions in lattices, where the crystal field environment distorts the spherical symmetry of the free ion, but they have been observed experimentally on many occasions. The effect of a crystal field is often accounted for by altering the balance of the different radial components, and this can also be used to estimate the ratio of spin and orbital components in the angular momentum of the electron (for an example, see Ref. [64]). From the

Please purchase PDF Split-Merge on www.verypdf.com to remove this watermark.

integrated intensities seen for the $\boldsymbol{k}_3$ peaks in Chapter 4, it is not clear that the single-ion form factor can be applied.

In Section 5.3 a quantum correlator was derived for three correlated electronic configuration spaces (defined as three independent sets of applicable Pauli operators). A configuration space may be thought of as an electronic orbital, possessing its own axis of quantization and frame of reference. As shown in Section 5.4, the quantum correlator of three such coherent spaces leads to several terms in the neutron cross-section: a simple sum of the individual configuration spaces, so that each projects out its own apparent 'order parameter' (giving rise to the $\boldsymbol{k}_1$ peaks); and a direct product of the three spaces, giving rise to a conjugate order parameter (the $\boldsymbol{k}_3$ peaks). If three candidate orbitals can be found, the intensity modulaton of the $\boldsymbol{k}_3$ peaks should be calculable using the direct product of the three orbitals as the spatial magnetization distribution. For the uranium rocksalts, the uranium ion is in a crystal field of cubic symmetry.

5.5.2 $5f$ electrons in cubic symmetry

In a cubic environment, the seven $5f$ orbitals have three (degenerate) irreducible representations: a singlet (β) and two triplets (δ and ϵ). In the Bethe notation these are Γ_2, Γ_4 and Γ_5 states respectively [65]. These orbitals have the form

$$\begin{aligned} 5f(\beta) &= \left\{\frac{xyz}{r^3}\right\}, \\ 5f(\epsilon) &= \left\{\frac{(x(z^2-y^2))}{r^3}, \frac{(y(x^2-z^2))}{r^3}, \frac{(z(y^2-x^2))}{r^3}\right\}, \\ 5f(\delta) &= \left\{\frac{(5x^3-3xr^2)}{r^3}, \frac{(5y^3-3yr^2)}{r^3}, \frac{(5z^3-3zr^2)}{r^3}\right\}. \end{aligned}$$

Representations are shown in Figure 5.2. As the $\boldsymbol{k}_1$ peaks appear to be symmetrically identical, they must all be generated by members of the same irreducible representation (i.e. there is no cross-correlation between orbitals from different sets). This limits us to three scenarios: β, ϵ and δ. As we are expecting three configuration spaces (orbitals) one of the triplets seems a more likely origin.

5.5.3 Results

The scattering amplitudes of the $\boldsymbol{k}_1$ and $\boldsymbol{k}_3$ Bragg events have been calculated from first principles by N. Bernhoeft, forming the relevant matrix elements from the U $5f^{3+/4+}$ ionic configurations with radial integrals as tabulated in the Neutron Data Booklet [48]. As is common with the U $5f$ ion, the differences in ion have little effect on the observed magnetic Bragg peak intensities. The calculations are then corrected for the effect of the magnetic moment direction and the Lorentz correction, so that they can be compared with the raw measured integrated intensities. There are no free parameters, apart from a vertical scaling factor. The raw data used for comparison was measured in single-detector mode (see Section 4.5.1). Further details are given below.

Please purchase PDF Split-Merge on www.verypdf.com to remove this watermark.

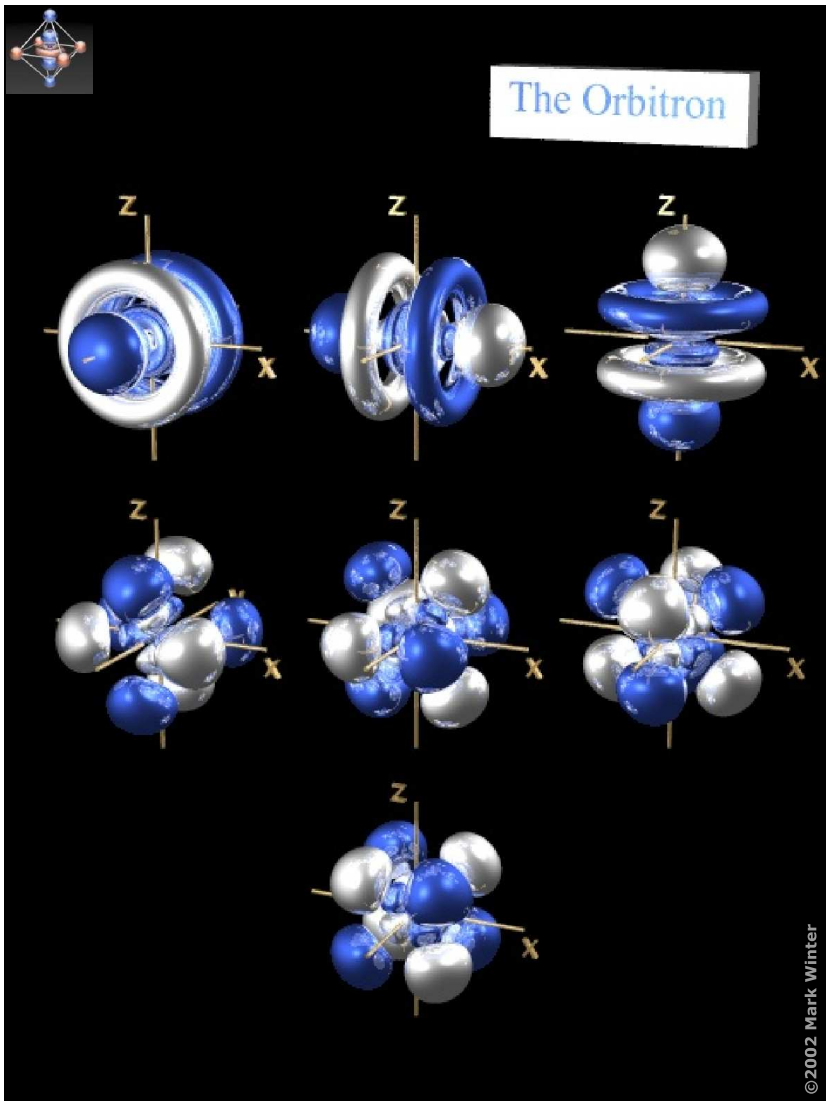

Figure 5.2: The cubic set of $5f$ orbitals. The top line is the δ orbitals, the middle line the ϵ orbitals, and the bottom line the β orbital. These representations were created by Dr. M. Winter, University of Sheffield (http://www.shef.ac.uk/chemistry/orbitron/).

Please purchase PDF Split-Merge on www.verypdf.com to remove this watermark.

The $\boldsymbol{k}_1$ peaks

The magnetic moment directions for the $\boldsymbol{k}_1$ peaks are easily determined as they are longitudinal to the propagation vector generating the peak. In the calculations (Figure 5.3) the point group symmetries of the ionic orbitals in a cubic environment have been respected; however, the radial extent of the orbitals differs from the free ion values in the metallic state. To assess the spatial extent of the $5f$ wavefunctions a calculation of the $\boldsymbol{k}_1$ Bragg intensities has been made in which the set $\{j_0, j_4, j_6\}$ of ionic Bessel functions compatible with cubic symmetry[2] are replaced by a single term, $\exp(-0.07\boldsymbol{Q}^2)^{\frac{1}{2}}$ with $|\boldsymbol{Q}|$ in Å^{-1}. This scheme, which replaces $\langle j_0 \rangle$ by $\exp(-0.07\boldsymbol{Q}^2)^{\frac{1}{2}}$ whilst setting the $\langle j_4 \rangle$ and $\langle j_6 \rangle$ coefficients to zero, is used to represent the radial extent of the uranium ion in rock-salt compounds [39, 52]. Since the $\langle j_0 \rangle$ coefficient is independent of the orientation of the scattering vector with respect to the state vector, in this approximation no information on the angular disposition of the wavefunction can be obtained.

The results are given as closed circles in the left-hand panel of Figure 5.3. This single term approximation to the $\{j_0, j_4, j_6\}$ set reproduces the wavevector dependency of the measured intensities, and enables one, in a semi-empirical manner, to address the role of bonding on the radial extent of the uranium valence shell. The lack of numerical agreement for the first two data points is attributed to extinction. The figure further demonstrates that the marked anisotropies at $|\boldsymbol{Q}| \sim 2.9$ Å^{-1}, 3.8 Å^{-1} and 4.1 Å^{-1} are correctly reproduced by the complex vector scattering amplitude of the projection of the state vector. The right-hand panel of Figure 5.3 is the transform of the integrated intensities of the left-hand panel, i.e. both experimental (open circles) and theoretical (closed circles), to a form factor together with the extinction corrected (open triangles) form factor of pure USb [52]. The latter has been used to set the integrated intensity on an absolute scale in the left-hand panel.

The $\boldsymbol{k}_3$ peaks

The magnetic moments are obtained by following the symmetry arguments presented earlier (i.e. parallel to the $\langle 111 \rangle$ vector leading to a nuclear Bragg peak). These peaks are suspected to be due to the direct product of the orbitals responsible for the $\boldsymbol{k}_1$ peaks.

Direct calculation shows that the minimal $\{\langle j_0 \rangle \rightarrow \exp(-0.07\boldsymbol{Q}^2)^{\frac{1}{2}};\ j_4 = j_6 = 0\}$ approximation is not sufficient to explain the intensity-wavevector distribution of the $\boldsymbol{k}_3$ peaks. Therefore the summed contribution from the radial $\{j_0, j_4, j_6\}$ set as determined by the cubic environment is used at each angular setting. As with the $\boldsymbol{k}_1$ peaks, ignoring the role of valence shell bonding results in $\boldsymbol{k}_3$ intensities that have poor agreement with the data since the radial extent of the wavefunction is artificially restricted. The same $\boldsymbol{k}_1$ replacement of the $\langle j_0 \rangle$ term is therefore made to allow for the bond electron density redistribution in the radial extent of the isotropic component, and, in the same vein, the calculations make use of a small, empirical, adjustment to the relative $\langle j_4 \rangle$ contribution.

Calculations of the scattering amplitude arising from the β, ϵ and δ sets of symmetry determined orbitals give a ratio of cross sections: $5f(\delta)$:$5f(\epsilon)$:$5f(\beta) = 30000$:100:1 in

[2]The $\langle j_2 \rangle$ term is not allowed in cubic symmetry.

Please purchase PDF Split-Merge on www.verypdf.com to remove this watermark.

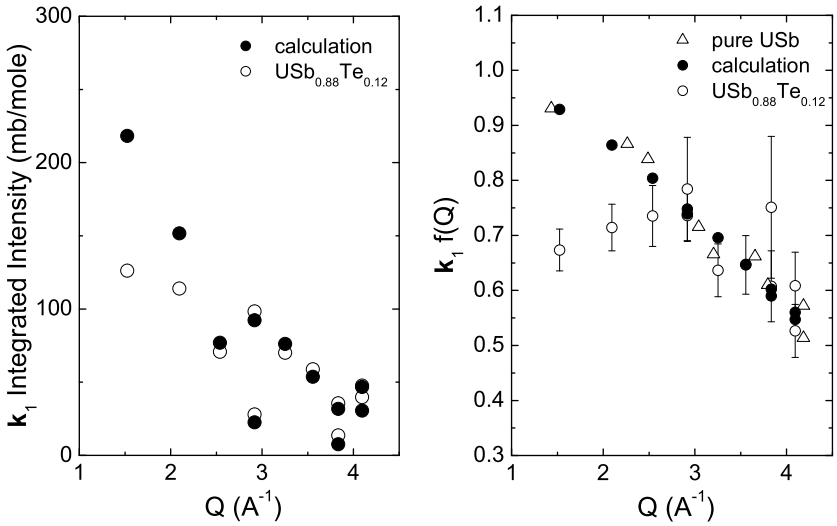

Figure 5.3: Left-hand panel: $\boldsymbol{k}_1$ scattering intensity compared with a first principles calculation (excepting a vertical scaling factor) from the degenerate $5f(\delta)$ orbitals compatible with cubic symmetry. Right-hand panel: data converted to form factor, additional triangular points are taken from the observed form factor of pure USb [52]. The latter have been used to set the integrated intensity on an absolute scale in the left hand panel (mb/mole). Key: open circles are $USb_{0.88}Te_{0.12}$; open triangles are USb; closed circles are calculation. The $USb_{0.88}Te_{0.12}$ data are not corrected for extinction.

favour of the $5f(\delta)$ orbitals. This means that the cross-section at the $\boldsymbol{k}_3$ peaks due to the δ orbitals is significantly larger than from the other two orbitals. The results for the δ orbitals are shown in Figure 5.4. The $UAs_{0.8}Se_{0.2}$ data are included, scaled to the $USb_{0.88}Te_{0.12}$ data (open circles). The coherent scattering amplitude from the $5f(\delta)$ orbitals is *uniquely* able to reproduce the observed anisotropy of the cross section. Most notably this is the case between the {(5/2 5/2 1/2), (7/2 1/2 1/2)} and {(5/2 5/2 3/2), (7/2 3/2 1/2)} pairs of reflections at 3.63 Å^{-1} and 3.90 Å^{-1} respectively. The anomalies are well captured by the δ orbitals whilst the ϵ, β and a spherically symmetric linear combination of all of the orbitals all show an anisotropy at $|\boldsymbol{Q}| = 3.63$ Å^{-1} in the opposite sense to that observed.

We note that in Figure 4.15 the high temperature measurement at the (3/2 3/2 1/2) reflection from $USb_{0.88}Te_{0.12}$ has an elevated background; there may therefore be some contamination at lower temperatures. However, this match is still better than that obtained with the other two orbital sets.

5.5.4 Discussion

At first sight, these results might be surprising in view of the systematic absences at $\boldsymbol{k}_3 \parallel \langle 111 \rangle$, particularly as the β orbital has the appropriate $\langle xyz \rangle$ symmetry, but the calculation has shown it to be weak and incapable of supporting the observed form factor. The δ orbitals provide the best match to the data and fit well with the definition provided

Please purchase PDF Split-Merge on www.verypdf.com to remove this watermark.

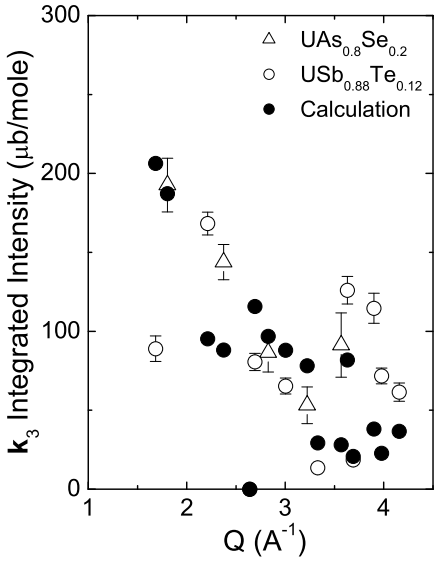

Figure 5.4: $\boldsymbol{k}_3$ scattering intensity compared with a first principles calculation (excepting a vertical scaling factor) from the degenerate $5f(\delta)$ orbitals compatible with cubic symmetry. Key: open circles = $USb_{0.88}Te_{0.12}$; open triangles = $UAs_{0.8}Se_{0.2}$; closed circles = calculation. The {(5/2 5/2 1/2), (7/2 1/2 1/2)} and {(5/2 5/2 3/2), (7/2 3/2 1/2)} pairs of reflections at 3.526 Å^{-1} and Å^{-1} respectively have been separated by 2% in their abscissa to illustrate the anisotropy. The data are set on an absolute scale as in Figure 5.3.

Please purchase PDF Split-Merge on www.verypdf.com to remove this watermark.

by the quantum correlator. The $\boldsymbol{k}_3$ peak arises from the coherent direct product of the three orbitals.

To cross-check the behaviour, at the $\boldsymbol{k}_3$ position, the scattering amplitude as calculated for the $\boldsymbol{k}_1$ peaks was gives an intensity of $2{\cdot}10^{-2}$ relative to the intensity of the $\boldsymbol{k}_3$ peak as calculated from the δ orbitals.

The absence of $\boldsymbol{k}_3$ peaks when $\boldsymbol{\tau} \parallel \langle \frac{1}{2}\frac{1}{2}\frac{1}{2} \rangle$ indicates quite strongly that at any given $\boldsymbol{k}_3$ peak the apparent dipole direction is longitudinal. This arises naturally from the geometric algebra formalism, where an inversion of $\boldsymbol{\sigma}_i$ yields an inversion of the conjugate axis in reciprocal space. This indicates that the set $\{\boldsymbol{\sigma}_z^1, \boldsymbol{\sigma}_z^2, \boldsymbol{\sigma}_z^3\}$ of vector-projected order parameters is aligned with the $\{\pm Q_x, \pm Q_y, \pm Q_z\}$ axes respectively, and *not* a mixed set, e.g. $\{\mp Q_x, \pm Q_y, \pm Q_z\}$. It follows that $\{\boldsymbol{\sigma}_z^1, \boldsymbol{\sigma}_z^2, \boldsymbol{\sigma}_z^3\}$ and $\{Q_x, Q_y, Q_z\}$ share the same chirality. The system does not favour preferentially one chirality, indicating that the sample is in reality a superposition of right- and left-hand chiral states. However, once chosen, the two are not mixed in the scattering amplitude. The $\{\boldsymbol{\sigma}_z^1, \boldsymbol{\sigma}_z^2, \boldsymbol{\sigma}_z^3\}$ element of the quantum correlator therefore changes sign on adjacent (111) planes by inversion of all three elements. This gives rise to the vectorial projections as observed in the azimuthal scans taken by x-ray resonant scattering.

Here, the system has been considered to be completely localized, or ionic. We note that some multi-$\boldsymbol{k}$ structures appear to have semimetal properties (e.g. UAs and USb). Knöpfle and Sandratskii [66] have found that the Fermi surface in USb, a 3-$\boldsymbol{k}$ antiferromagnet with propagation vector $\langle 001 \rangle$, has 3-$\boldsymbol{k}$ symmetries (Figure 5.5) and, specifically, the δ orbital symmetries. These symmetries are lowered on using pressure to enter the 1-$\boldsymbol{k}$ phase high-pressure state. These Fermi surface sheets clearly have the δ orbital symmetries. These Fermi surfaces were calculated using a modified augmented spherical wave method with a fully relativistic Hamiltonian.

Nonetheless, the effects of band hybridization on the form factor have been neglected here. Within this assumption, the experimental results presented above suggest that the electronic system is best described as a coherent superposition of the set of $5f(\delta)$ orbitals, with coherent correlations between all of the uranium ions.

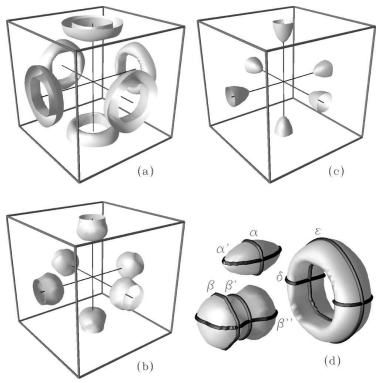

Figure 5.5: Fermi surface sheets in 3-$\boldsymbol{k}$ USb. Taken from Knöpfle and Sandratskii [66]. The sheets shown all have δ symmetry.

Please purchase PDF Split-Merge on www.verypdf.com to remove this watermark.

Because the role of the crystal field environment is paramount in explaining this behaviour, it is no surprise that the single-ion approach has problems with the $\boldsymbol{k}_3$ peaks.

5.6 Summary

The approach developed here establishes unique evidence for both (a) the existence and (b) the experimental detection of the triple quantum projector of the many-body state-vector. The quantum correlator, derived using geometric algebra, reveals that both a sum and product of three order parameters participate in the neutron scattering cross-section, permitting a consistent interpretation of the observed $\boldsymbol{k}_3$ peaks in terms of three coherent scattering amplitudes coming from the elements of the $5f(\delta)$ triplet state.

The signature of this coherence is the $\boldsymbol{\sigma_1\sigma_2\sigma_3}$ type term, which is accessible when using momentum-transfer sensitive dipolar probes, i.e. Bragg diffraction techniques. The vector component of this term is then extracted, and this gives the vectorial projections found from the resonant x-ray azimuthal dependences. It seems clear that the $\boldsymbol{k}_3$ peaks, seen in the 3-$\boldsymbol{k}$ state only, are generated by the δ orbitals

The order parameters can therefore be viewed as quantum correlators of the appropriate multi-particle state-vector, and can be equated with degenerate (symmetry connected) Pauli subspaces (the electronic orbitals).

Please purchase PDF Split-Merge on www.verypdf.com to remove this watermark.

5.A Geometric algebra: an introduction

An algebra is founded in a set of axioms with rules for handling elements. For example, a vector algebra consists of two types of element: vectors, which possess a direction, and scalars. The vector algebra is defined to be commutative and associative under addition, with an identity element of zero, and the inverse of vector **a** being **-a**. The set of vectors is closed under multiplication by a scalar, and the operation is distributive and associative, such that:

(i) $\lambda(\mathbf{a}+\mathbf{b}) = \lambda\mathbf{a} + \lambda\mathbf{b}$,

(ii) $(\lambda+\mu)\mathbf{a} = \lambda\mathbf{a} + \mu\mathbf{a}$,

(iii) $(\lambda\mu)\mathbf{a} = \lambda(\mu\mathbf{a})$, and

(iv) if $1\lambda = \lambda$ then $1\mathbf{a} = \mathbf{a}$

where λ and μ are scalars. Extending the scalars to 2D complex numbers makes it a complex vector space, which looks like the direct product of the 2D space and the ordinary vector space. In a vector space a set of basis vectors can be defined that span the space. Any vector can then be defined as an addition of basis set elements.

What happens under multiplication of two vectors? For any vector space as defined above, a scalar (inner) product can be defined: $\mathbf{a}.\mathbf{b} = \gamma$. This is usually defined as the projection of **a** onto **b**. Uniquely in the three-dimensional case, the vector cross product of two vectors $\mathbf{a} \times \mathbf{b} = \mathbf{c}$ may be defined in terms of a vector orthogonal to the initial elements.

These two operations yield a scalar (grade-0 element) and a vector (grade-1 element). Higher grade terms can be envisaged: a grade-2 'bivector', formed by the outer (or wedge) product $\mathbf{a} \wedge \mathbf{b}$, is the antisymmetric ($\mathbf{a} \wedge \mathbf{b} + \mathbf{b} \wedge \mathbf{a} = 0$) directed outer projection of two vectors, defining both a plane and a sense of circulation within it. This is related to, but clearly distinct from, the Gibbs vector cross product in 3D space. To emphasise this, $\times$ is reserved for the vector cross product and $\wedge$ used exclusively for the outer product. Introducing the bivector as a distinct geometric object provides a clean distinction between axial and (ordinary) polar vectors. Axial vectors, such as angular momentum, express circulation and are more naturally described as bivectors, whereas linear momentum is a (polar) vector.

The geometric product of two vectors is therefore defined as $\mathbf{ab} = \mathbf{a}.\mathbf{b} + \mathbf{a} \wedge \mathbf{b}$, the combination of the inner and outer products of the vectors **a** and **b**. **ab** is a multivector that projects a grade-0 term (the scalar) and a grade-2 term (the bivector). The grades possible are determined by the dimensionality of the space, such that a 2D space can have terms of grades 0, 1 and 2. A 3D space adds a grade-3 element. The linear space of interest is defined as the one containing these multivector elements, and the geometric algebra is concerned with the operation of the geometric product. This means that the geometric product can be applied to scalars and bivectors.

A full introduction to geometric algebra can be found in the book *Geometric algebra for physicists* by Doran and Lasenby [56].

Please purchase PDF Split-Merge on www.verypdf.com to remove this watermark.

5.A.1 The geometric algebra of 3D space

To explore these ideas in more detail, the 3D case is taken as an example. Consider a 3D space spanned by three orthonormal vectors: $\mathbf{e}_1$, $\mathbf{e}_2$ and $\mathbf{e}_3$. The geometric product of the basis vectors is:

$$\mathbf{e}_i\mathbf{e}_j = \mathbf{e}_i.\mathbf{e}_j + \mathbf{e}_i \wedge \mathbf{e}_j \;\rightarrow\; \mathbf{e}_i \wedge \mathbf{e}_j \text{ if } i \neq j \text{ and } \mathbf{e}_i.\mathbf{e}_j = 1 \text{ if } i = j. \tag{5.40}$$

Three independent bivectors may therefore be generated ($\mathbf{e}_1\mathbf{e}_2$, $\mathbf{e}_1\mathbf{e}_2$ and $\mathbf{e}_1\mathbf{e}_2$), describing the three orthogonal planes of 3D space. The (non-commutative) product of two distinct bivectors yields the third bivector element:

$$\begin{aligned}(\mathbf{e}_i\mathbf{e}_j)(\mathbf{e}_j\mathbf{e}_k) &= \mathbf{e}_i\mathbf{e}_j\mathbf{e}_j\mathbf{e}_k = \mathbf{e}_i\mathbf{e}_k \\ (\mathbf{e}_j\mathbf{e}_k)(\mathbf{e}_i\mathbf{e}_j) &= \mathbf{e}_j\mathbf{e}_k\mathbf{e}_i\mathbf{e}_j = \mathbf{e}_k\mathbf{e}_j\mathbf{e}_j\mathbf{e}_i = \mathbf{e}_k\mathbf{e}_i = -\mathbf{e}_i\mathbf{e}_k.\end{aligned} \tag{5.41}$$

This uses the antisymmetric nature of the bivector. The square of a bivector is -1:

$$(\mathbf{e}_i\mathbf{e}_j)(\mathbf{e}_i\mathbf{e}_j) = \mathbf{e}_i\mathbf{e}_j\mathbf{e}_i\mathbf{e}_j = -\mathbf{e}_i\mathbf{e}_i\mathbf{e}_j\mathbf{e}_j = -1. \tag{5.42}$$

To summarize, the basis bivectors square to -1 and anticommute with each other.

One further element exists in 3D space: the unit tri-vector $I = \mathbf{e}_1\mathbf{e}_2\mathbf{e}_3$. This is a directed volume element. As with the scalar quantity, in a 3D space there can only be one independent tri-vector, but in a higher dimensional space, there may be more. I commutes with the basis vectors, giving the bivector perpendicular to, and describing a right hand circulation about the original vector. The bivectors are linked by a duality transformation to a given basis vector.

$$\begin{aligned}I\mathbf{e}_1 &= \mathbf{e}_1\mathbf{e}_2\mathbf{e}_3\mathbf{e}_1 = \mathbf{e}_2\mathbf{e}_3 \\ \mathbf{e}_1 I &= \mathbf{e}_1\mathbf{e}_1\mathbf{e}_2\mathbf{e}_3 = \mathbf{e}_2\mathbf{e}_3\end{aligned} \tag{5.43}$$

The geometric product of the grade-1 vector and grade-3 trivector is limited to a grade-2 bivector, reflecting the closure condition of 3D space. As seen here, the vector and trivector commute. In fact, I commutes with all elements of the 3D algebra, and squares to -1. It therefore behaves as a unit imaginary, and in some cases is used as this, but care must be taken according to the problem in question.

$$II = \mathbf{e}_1\mathbf{e}_2\mathbf{e}_3\mathbf{e}_1\mathbf{e}_2\mathbf{e}_3 = \mathbf{e}_2\mathbf{e}_3\mathbf{e}_2\mathbf{e}_3 = -\mathbf{e}_3\mathbf{e}_3 = -1 \tag{5.44}$$

The vector cross product

Consider the geometric product of a bivector and the trivector:

$$I(\mathbf{e}_1 \wedge \mathbf{e}_2) = I\mathbf{e}_1\mathbf{e}_2\mathbf{e}_3\mathbf{e}_3 = II\mathbf{e}_3 = -\mathbf{e}_3. \tag{5.45}$$

$\mathbf{e}_3$ is the vector perpendicular to the plane $\mathbf{e}_1 \wedge \mathbf{e}_2$. This gives a definition for the vector cross product as

$$\mathbf{a} \times \mathbf{b} = -I(\mathbf{a} \wedge \mathbf{b}). \tag{5.46}$$

The vector cross product is in reality a bivector, mapped to a vector using the duality transform.

Please purchase PDF Split-Merge on www.verypdf.com to remove this watermark.

Away from the basis elements

When not working with basis elements, the results may not be so clear. To provide some examples, let us consider the geometric product of a vector $\mathbf{a}$ and a bivector B in this 3D algebra.

$$\mathbf{a}B = \mathbf{a}.B + \mathbf{a} \wedge B \tag{5.47}$$

The inner product is generalised to mean the lowest grade projection of the result, and the outer product the highest grade part of the result. In this case, the scalar product is a vector and the outer product a trivector. $\mathbf{a}$ is split into components parallel and perpendicular to the plane defined by B: $\mathbf{a} = \mathbf{a}_\parallel + \mathbf{a}_\perp$. B can then be defined as $B = \mathbf{a}_\parallel \wedge \mathbf{b}$, where $\mathbf{b}$ is orthogonal to $\mathbf{a}_\parallel$.

$$\mathbf{a}.B = \mathbf{a}_\parallel(\mathbf{a}_\parallel\mathbf{b}) = -(\mathbf{a}_\parallel\mathbf{b})\mathbf{a}_\parallel = -B.\mathbf{a} \tag{5.48}$$

The scalar product is antisymmetric, therefore:

$$\mathbf{a}.B = \frac{1}{2}(\mathbf{a}B - B\mathbf{a}). \tag{5.49}$$

The outer product is therefore the projection involving $\mathbf{a}_\perp$:

$$\mathbf{a} \wedge B = \mathbf{a}_\perp(\mathbf{a}_\parallel\mathbf{b}) = \mathbf{a}_\parallel\mathbf{b}\mathbf{a}_\perp = B \wedge \mathbf{a}. \tag{5.50}$$

This is symmetric, so the outer product can be written as:

$$\mathbf{a} \wedge B = \frac{1}{2}(\mathbf{a}B + B\mathbf{a}). \tag{5.51}$$

The Pauli spin algebra

Staying for the moment in 3D space, the geometric product of the basis vectors can be rewritten as

$$\mathbf{e}_i\mathbf{e}_j = \mathbf{e}_i.\mathbf{e}_j + \mathbf{e}_i \wedge \mathbf{e}_j = \delta_{ij} + I\epsilon_{ijk}\mathbf{e}_k. \tag{5.52}$$

This has the same form as the Pauli algebra of quantum mechanics. The Pauli matrices are therefore a matrix representation of the 3D geometric algebra. As a reminder, the Pauli matrices are

$$\sigma_1 = \begin{pmatrix} 0 & 1 \\ 1 & 0 \end{pmatrix}, \quad \sigma_2 = \begin{pmatrix} 0 & -i \\ i & 0 \end{pmatrix}, \quad \sigma_3 = \begin{pmatrix} 1 & 0 \\ 0 & -1 \end{pmatrix} \tag{5.53}$$

where i is the unit imaginary. These matrices obey the relation

$$\sigma_i\sigma_j = \delta_{ij}\mathcal{I} + i\epsilon_{ijk}\sigma_k, \tag{5.54}$$

where $\mathcal{I}$ is the 2×2 identity matrix. If $\mathcal{I}$ is explicitly identified with the unit scalar, and i with the 3D unit trivector I, the geometric product of 3D space is recovered.

Please purchase PDF Split-Merge on www.verypdf.com to remove this watermark.

Higher-dimensional algebras

Depending on the problem, higher-dimensional algebras may be appropriate. The most common example is the 4D spacetime algebra, used for the study of relativistic physics. The even subalgebra of this 4D spacetime algebra has the same properties as the 3D algebra described above. This work concentrates on non-relativistic effects and so stays in the 3D algebra; further details on space time algebra can be found in, for example, *Space-Time Algebra*, by David Hestenes [58].

5.A.2 Axioms of geometric algebra

As this development shows, vectors play a crucial role in the geometric algebra: the vector space provides the starting point for the algebra, and the grade-1 vector defines the grading system. Three key axioms apply to vectors in all geometric algebras.

(i) $a(bc) = (ab)c = abc$. The geometric product is associative.

(ii) $a(b + c) = ab + ac$. The geometric product is distributive.

(iii) The square of any vector is a real scalar: $a^2 \in \mathbb{R}$.

By multiplying vectors together, the complete algebra is generated. The elements of the full algebra are multivectors. A geometric product involving multivectors is also associative and distributive. As for a set of vectors, the multivectors are closed under multiplication by a scalar. With these rules in mind, some useful properties of the algebra are discussed. From now on, vectors are described using lower-case italic letters.

Reflections

When a vector is reflected in a plane, the part parallel to the plane is unchanged, and the part perpendicular to the plane has its sign reversed. Consider a vector a being reflected in the plane perpendicular to the unit vector n. a can be resolved into components parallel and perpendicular to n.

$$\begin{aligned} a &= n^2 a \\ &= n(n \cdot a + n \wedge a) \\ &= a_\parallel + a_\perp \end{aligned} \tag{5.55}$$

$a_\parallel$ is easy to assign, leaving the remainder as the perpendicular contribution

$$a_\parallel = a \cdot n, \qquad a_\perp = n\, n \wedge a. \tag{5.56}$$

The reflected vector is

Please purchase PDF Split-Merge on www.verypdf.com to remove this watermark.

$$\begin{aligned} a' = a_\perp - a_\parallel &= n\,n \wedge a - a \cdot n\,n \\ &= -n \cdot a\,n - n \wedge a\,n \\ &= -nan \end{aligned} \tag{5.57}$$

To reflect a higher-grade element, each of its component vectors must be reflected. Using the bivector $B = a \wedge b$ as an example, and using the antisymmetry of the wedge product

$$\begin{aligned} B' &= (-nan) \wedge (-nbn) \\ &= \frac{1}{2}(nannbn - nbnnan) \\ &= \frac{1}{2}(n(ab - ba)n) \\ &= n(a \wedge b)n \\ &= nBn. \end{aligned} \tag{5.58}$$

Rotations

A rotation in the plane containing the two unit vectors m and n can be achieved by successive reflections in the planes perpendicular to m and n. Components perpendicular to the plane are unaffected, and the angle beween the initial vector a and the rotated vector a' is twice the angle between m and n. Therefore, if $b = -mam$ is the reflection in m, then $a' = -nbn = nmamn$, or

$$a' = RaR^\dagger \qquad \text{where } R = nm. \tag{5.59}$$

It should be clear that this will hold for bivectors, and indeed for elements of any grade. As m and n are unit vectors

$$RR^\dagger = nm(nm)^\dagger = nmmn = 1 = R^\dagger R. \tag{5.60}$$

R is labelled a rotor, and it consists of a geometric product: $R = n \cdot m + n \wedge m$, where $n \cdot m = cos\,\theta$.

$$\begin{aligned} (n \wedge m)(n \wedge m) &= (nm - n \cdot m)(m \cdot n - mn) \\ &= -nmmn + n \cdot m(nm + mn) - (n \cdot m)^2 \\ &= -nmmn + (n \cdot m)^2 \\ &= -\sin^2\theta \end{aligned} \tag{5.61}$$

The unit bivector B of the plane $m \wedge n$ is then given by

$$B = \frac{m \wedge n}{\sin\,\theta}. \tag{5.62}$$

Please purchase PDF Split-Merge on www.verypdf.com to remove this watermark.

The rotor can then be expressed as

$$R = \cos\,\theta - B\sin\,\theta. \tag{5.63}$$

By applying a power series, and remembering that $B^2 = -1$ this can be expressed as an exponential.

$$R = \exp(-B\theta) \tag{5.64}$$

This rotates through an angle of 2θ, so to rotate a by an angle θ in the B plane, the appropriate description is

$$a' = \mathrm{e}^{-B\theta/2} a \mathrm{e}^{B\theta/2}. \tag{5.65}$$

The sense of rotation is contained in the description of B. To invert it, B has to be inverted. This concept of rotation in a plane is applicable to higher dimensions.

Please purchase PDF Split-Merge on www.verypdf.com to remove this watermark.

Please purchase PDF Split-Merge on www.verypdf.com to remove this watermark.

Chapter 6

The antiferromagnetic superconductor UPd_2Al_3

Please purchase PDF Split-Merge on www.verypdf.com to remove this watermark.

Sommaire

Dans ce chapitre on laisse les systèmes localisés pour étudier un système plutôt itinerant : l'UPd_2Al_3. Ceci est un des rares matériaux où l'ordre antiferromagnétique existe en même temps que la supraconductivité. On peut essayer de trouver comment la supraconductivité se développe dans des champs magnétiques forts associée avec l'ordre magnétique, et si l'aimantation est nécessaire pour la fonctionnement de ce type de supraconductivité.

L'aimantation et la supraconductivité ont été vu ensemble dans plusieurs composés. Les matériaux haute-T_c sont soupçonnés d'avoir un médiateur magnétique, parce que quand on change l'environnement électronique par le dopage, ils deviennent magnétiques [67]. Dans les supraconducteurs de type RNi_2B_2C, R est une terre rare, et les ions des terres rares sont souvent magnétiques. Ils agissent avec les électrons conducteurs, dans certains cas pour supprimer la supraconductivité [68].

Dans les composés fermions lourds avec une base de Ce comme $CeCu_2Si_2$ et $CeIn_3$ des paramètres externes, comme la pression, peuvent être utilisés pour changer un composé entre l'ordre antiferromagnétique et la supraconductivité. Un médiateur magnétique a été également proposé pour ces composés [69].

Cela nous amène aux composés fermions lourds avec une base d'uranium. UGe_2 est ferromagnétique, mais il devient supraconducteur sous la pression [70]. Quelques composés sont antiferromagnétiques et supraconducteurs en même temps (e.g. URu_2Si_2 [71]), ce qui indique que l'environnement magnétique n'empêche pas la supraconductivité dans ces matériaux. UPd_2Al_3 est considéré comme un modèle pour ces systèmes parce que ces propriétés le rendent relativement facile à manipuler pour les expériences [72].

Les composés soupçonnés d'avoir un médiateur magnétique ont souvent un gap d'énergie non conventionnel (aussi nommé le paramètre d'ordre), avec nodes dans l'espace de momentum, et une symétrie asphérique. En fait, Monthoux, Balatsky et Pines [73] ont montré que pour un certain médiateur magnétique le gap d'energie est obligatoirement non conventionnel.

Dans les chapitres précédents, nous avons vu que les paramètres d'ordre magnétique dans le même espace sont corrélés. Ici, il y a un paramètre d'ordre magnétique et un paramètre d'ordre supraconducteur, avec une origine commune - les électrons corrélés $5f$. Le rôle de l'aimantation dans la supraconductivité est sujet à de vifs débats, et plusieurs auteurs ont postulé un médiateur magnétique pour UPd_2Al_3.

La réponse inélastique vue par les neutrons est une sonde unique de l'ordre magnétique et supraconducteur dans ce matériau. Un champ magnétique externe a des effets sur les deux types d'ordre par des mécanismes différents. Pour ces raisons, on présente les effets d'un champ magnétique externe sur la réponse inélastique. Finalement, pour conclure sur certaines questions sur la réponse de basse énergie, le ≪spin-echo≫ est utilisé pour sa haute résolution.

Please purchase PDF Split-Merge on www.verypdf.com to remove this watermark.

Les états paramagnétiques et antiferromagnétiques normaux étaient étudiés dans un champ magnétique externe. Le comportement observé était caracteristique d'un liquide de Fermi dans des champs jusqu'á 15 T. La réponse quasiélastique augmente vivement à 4 T avant un déclin dans des champs supérieurs. Ce comportement est attribué à la rotation des moments magnétiques à 4.2 T. Dans le champ magnétique externe, on voit aussi un changement dans la dispersion du pic inélastique dit de haute-énergie. Ces changements sont en accord avec la théorie pour les ondes de spin dans un composé hexagonal, comme UPd_2Al_3 [74]. Une réponse additionnelle était vue dans les champs hauts (11.6 T) à 4 meV. L'origine de cette réponse est pour le moment inconnue, mais quelques origines possibles sont décrites.

Le changement de la réponse en quittant l'état supraconducteur était étudié. Avec le technique spin-echo, nous avons confirmé que, dans la limite de la résolution possible, au profond de l'état supraconducteur, il n'y a pas de diffusion quasiélastique. Les mesures descendent jusqu'à $T = 50$ mK. Cette observation est liée avec le surface de Fermi et l'impacte pour la compréhension de l'état supraconducteur est discuté.

Pour cette étude, on a utilisé un cristal unique d'UPd_2Al_3. Pour le spin-echo sur les composés magnétique, il y a certains effets secondaires qui deviennent de plus en plus importants avec un cristal unique comme échantillon. Ces effets sont présentés dans l'annexe 6.A.

Please purchase PDF Split-Merge on www.verypdf.com to remove this watermark.

6.1 Introduction

This chapter now shifts focus away from highly localized systems to a heavy-fermion material, UPd_2Al_3. This is one of the rare class of materials in which antiferromagnetic order and superconductivity coexist, and as such, provides a model system for questioning how the superconductivity survives in the strong magnetic fields found in an ordered state, and whether or not the magnetism is crucial in creating the superconducting phase coherent state. Typically the internal fields of a magnetically ordered phase far exceed the fields necessary to destroy superconductivity.

Magnetism and superconductivity are thought to interact in several different groups of compounds. The high-T_c ceramics are often suspected of having a magnetic mediator, as when the electronic environment is altered by doping, the superconductivity is replaced by magnetic behaviour (see e.g [67] and references there-in). In the rare-earth nickel borocarbides, some of the rare-earth ions are magnetic, and studies indicate that the rare-earth magnetic moments interact with the conduction electrons, in some cases suppressing the superconductivity [68].

In Ce-based heavy fermion compounds (e.g. $CeCu_2Si_2$, $CeIn_3$) external parameters such as pressure can be used to tune *between*, for example, antiferromagnetic order and superconductivity. A magnetic mediator (spin fluctuations) has been proposed for these materials [69].

This brings us to the uranium (heavy fermion) compounds. UGe_2 is ferromagnetic, but can be made into a (disordered) superconductor using pressure [70]. Several uranium compounds are antiferromagnetic and superconducting *at the same time* (e.g. URu_2Si_2 [71]) indicating that the magnetic environment is not a handicap to the type of superconductivity that develops in these materials. UPd_2Al_3 [72] is one of the most experimentally amenable of these compounds, and so is the sample used here.

These compounds, suspected of having a magnetic mediator, often have an unconventional superconducting energy gap (often labelled the superconducting order parameter), with nodes (gapless points in momentum space) and non-spherical symmetry. Indeed, Monthoux, Balatsky and Pines have shown that one type of magnetic mediator must give rise to an unconventional energy gap [73]. In previous chapters, we have seen evidence that multiple magnetic order parameters in the same volume interact; here we have a magnetic order parameter and a superconducting order parameter, generated by the same strongly-correlated electron system. The role of the magnetism in developing the superconductivity is a matter of lively debate, and in UPd_2Al_3 several authors have posited that the superconductivity is magnetically mediated [54, 75, 76].

Previous work has shown that the neutron inelastic response provides a unique probe of both the magnetic and superconducting order. An external magnetic field affects both the magnetic and superconducting components via different mechanisms. Initial studies at low-resolution by Metoki *et al.* [77] have indicated that the neutron inelastic response is affected in an observable manner by an external magnetic field. The experiments described in this chapter continue and extend this work, documenting the effect of an external magnetic field on the normal and superconducting states. Finally, to answer some specific questions about the nature of the low-energy response, a high-resolution

Please purchase PDF Split-Merge on www.verypdf.com to remove this watermark.

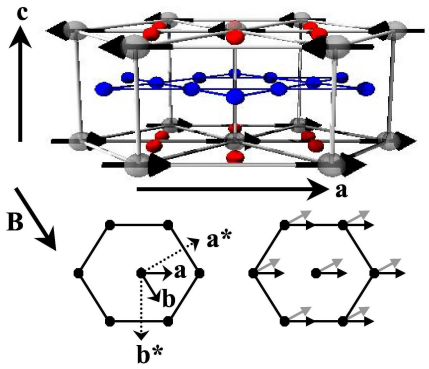

Figure 6.1: The structure of UPd_2Al_3. The grey atoms are U, the red atoms are Pd and the blue atoms are Al. The arrows on the uranium ions represent localized magnetic dipole positions and directions. The two hexagons are projections of the basal plane, with the reciprocal axes a^* and b^* marked as dotted lines on the left-hand hexagon. In the experimental work presented here, when a magnetic field **B** is applied, it is parallel to the b axis. The black arrows in the right-hand hexagon show one of the possible low-field magnetic domains. Above a certain applied field (2.3 T at 4 K) the moments rotate to lie along the a^* axis (grey arrows) [81].

neutron spin-echo study is discussed. First of all, an overview of the current experimental situation is given, along with a description of the two main models for the material.

6.2 Overview

6.2.1 Basic facts

UPd_2Al_3 was first discovered by Geibel and coworkers [72] in 1991. It has the hexagonal $PrNi_2Al_3$ P6/mmm structure, with lattice parameters $a = 5.37$ Å and $c = 4.19$ Å at room temperature [72]. There are no structural phase transitions observed from the lowest temperatures measured up to 300 K [78]. Below $T_N = 14.3$ K, UPd_2Al_3 becomes antiferromagnetic. In the ordered state the magnetic moments lie in the basal $a-b$ plane forming ferromagnetic sheets. These sheets are stacked antiferromagnetically $(+-+-)$ up the c axis (see Figure 6.1), giving a propagation vector $\boldsymbol{Q}_0 = [0\ 0\ \frac{1}{2}]$ [79]. The ordered magnetic moment per uranium atom is 0.85 μ_B. The magnetic moment is associated solely with the uranium atoms [80].

Below $T_{sc} = 1.8$ K, UPd_2Al_3 becomes superconducting. Krimmel *et al.* [79] observed that the magnetic Bragg peak remains present throughout the bulk of the material in the superconducting phase, and from specific heat studies [72] both phenomena originate from the same (strongly correlated) electron system as the superconductivity, and that there is no apparent phase separation. As the transition temperatures are easily accessible, and the magnetic moment is sizable, UPd_2Al_3 is ideal for experimental purposes. In addition,

Please purchase PDF Split-Merge on www.verypdf.com to remove this watermark.

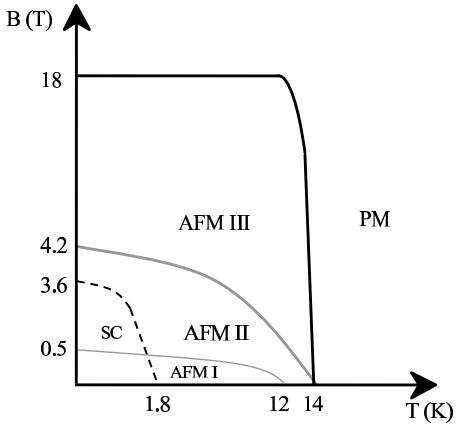

Figure 6.2: A schematic representation of the (B,T) phase diagram for UPd_2Al_3 for $B \parallel b$, based on data from Refs. [81] and [85]. The dashed line denotes the onset of superconductivity inside the antiferromagnetic phase. The thick grey line marks the moment rotation transition illustrated in Figure 6.1. The phases marked are described in the text.

large single crystals can be grown by the Czochralski method.

6.2.2 The effect of a magnetic field

Much of the experimental work presented here involves applying an external magnetic field to the sample. If the magnetic field is applied parallel to the c axis no change in the structure is recorded up to 35 T [82]. If the magnetic field is applied perpendicular to c there is a metamagnetic transition at 18 T (Figure 6.2) where the apparent magnetic moment roughly doubles [81]. Below 18 T, three phases have been seen [81, 83] if $\boldsymbol{B} \parallel b$. In phases I and II the moments point towards nearest(uranium) neighbours (black arrows in Figure 6.1). Phase I has all three possible domains; in phase II the domain with moments parallel to $\boldsymbol{B}$ disappears. In phase III the moments rotate to point along a^* (towards next nearest neighbours) perpendicular to $\boldsymbol{B}$ (grey arrows in Figure 6.1). Close to T_N phase II dominates in the zero field state. This has been confirmed by x-ray resonant scattering [84].

6.2.3 Bulk properties

Specific heat capacity

The specific heat is given in the upper panel of Figure 6.3, taken from Hagmusa *et al.* [85]. In the normal magnetically ordered state of UPd_2Al_3, the specific heat capacity obeys the relation

$$C = \gamma T + \beta T^3 \tag{6.1}$$

Please purchase PDF Split-Merge on www.verypdf.com to remove this watermark.

where the T^3 term is attributed to scattering by magnons. $\gamma = 150$ mJ/mol.K^2 and $\beta = 1.53$ mJ/mol.K^4 [82]. This value of γ is smaller than that extrapolated from the paramagnetic regime (210 mJ/mol.K^2 [72]), but indicates that we are dealing with a heavy fermion Fermi liquid. At T_{sc} there is a jump in the electronic specific heat of $\Delta C = 1.2\, C_{el}(T_{sc})$, implying that all of the heavy fermions take part in the formation of the superconducting state.

Resistivity

There are three principal features in the resistivity as a function of temperature: at T_{sc} the resistivity falls sharply to zero, marking the onset of superconductivity; at T_N there is a point of inflexion, and at ~ 80 K there is a broad maximum. This last point is thought to be linked to the Kondo effect, and is observed in other heavy fermion superconductors. The middle panel of Figure 6.3, from Dalichaouch *et al.* [86], covers the low temperature range. Two models have been proposed: the Bloch-Grüneisen model for a metal [87], and an Fermi-liquid antiferromagnet with an energy gap [86]. Both models fit the data well, and contain the T^2 component characteristic of a Fermi liquid. From Dalichaouch *et al.* [86], the strength of this T^2 dependence is 0.23 $\mu\Omega$.cm/K^2, a large value consistent with the heavy fermion hypothesis.

Magnetic susceptibility

The dc susceptibility of a single crystal is given in the lower panel of Figure 6.3, taken from Grauel *et al.* [83]. In the $a-b$ easy magnetic plane, Curie-Weiss-like behaviour is seen above ~ 150 K. Parallel to c, χ shows van Vleck-like paramagnetism. Several groups have attempted to model the paramagnetic susceptibility. Grauel *et al.* [83] found that a model of crystal field splitting of a localized tetravalent $5f$ state had the correct form, although the absolute values were a little too high (the solid lines in the figure). The broad maximum seen around 35 K was ascribed to van Vleck contributions from the two low lying singlets and the thermal population of the Γ_1 and Γ_6 states. A schematic of the proposed crystal field scheme is given in their paper [83]. Subsequently, Richter *et al.* [88] used *ab initio* crystal field theory to model the paramagnetic susceptibility. They concluded that it could not be a $5f^3$ state, but a $5f^2$ state was found to match the behaviour for T > 150 K.

6.2.4 Magnetic order

From the specific heat and resistivity data, the ordered state of UPd_2Al_3 looks like a classic Fermi liquid, with the antiferromagnetism generated by the itinerant $5f$ electrons. The susceptibility data indicates that a localized moment model applies for $T > 150$ K. Other experimental data indicate that there are two active electronic subsystems, one more localized and one less. This includes: specific heat measurements under pressure [87]; μSR data [89] revealing a strongly anisotropic susceptibility component (localized) and an isotropic component (itinerant), and high resolution photoemission spectroscopy [90], where two contributions are seen in the density of states, one close to the Fermi surface

Please purchase PDF Split-Merge on www.verypdf.com to remove this watermark.

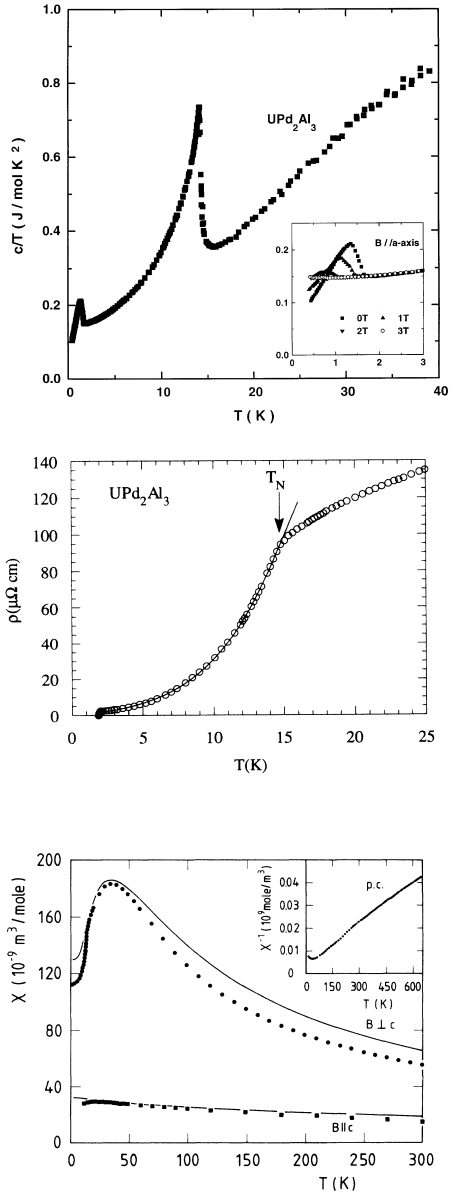

Figure 6.3: *Upper panel*: specific heat over temperature (C/T) of UPd_2Al_3 in zero field, taken from Hagmusa *et al.* [85]. Inset: C/T around the superconducting peak in magnetic fields of 0, 1, 2 and 3 T ($B \parallel a$). *Middle panel*: low temperature resistivity vs temperature of UPd_2Al_3 in zero applied magnetic field. This figure is taken from Dalichaouch *et al.* [86]. The solid line is a fit described in Ref. [86]. *Lower panel*: the dc susceptibility of a UPd_2Al_3 single crystal, taken from Grauel *et al.* [83]. The squares represent $\boldsymbol{B} \parallel c$ and the circles $\boldsymbol{B} \perp c$. The solid lines are the crystal field model mentioned in the text. The inset is the inverse susceptibility of a polycrystalline sample up to 650 K.

Please purchase PDF Split-Merge on www.verypdf.com to remove this watermark.

(itinerant) and the other much lower (localized). This has motivated the application of the dual model developed for UPt_3 [91]. These two models for the magnetic order will now be discussed.

The itinerant model

All three of the $5f$ electrons are assumed to be itinerant. The Fermi surface has been calculated by three groups in this paradigm [92, 93, 94], with broad agreement on the Fermi sheets found. The results of Knöpfle *et al.* [92] are shown in Figure 6.4, and were calculated using an electronic structure calculated using the local spin-density functional approximation (LSDA). The three Fermi sheets are: (i) 'party-hat', the largest but with major contributions from electrons other than the U $5f$; (ii) the 'cylinder', almost purely $5f$, and the 'cigars' with ~ 50 % $5f$ content, and (iii) the 'egg', with approximately 75 % $5f$ content. This system has an instability with respect to the wavevector $\boldsymbol{Q}_0 = [00\frac{1}{2}]$, and so magnetic order forms by nesting of the Fermi surface at this wavevector. Comparison with measured de Haas-van Alphen (dHva) frequencies is favourable. All of the observed frequencies could be classified, save for a few scattered points, but the 'egg' surface was not seen experimentally. Knöpfle *et al.* ascribe the absence of these frequencies to the local curvature of the Fermi surface, as this affects the amplitude of a dHvA oscillation. This absence may also occur because of the presumed high effective mass of the quasiparticles on the 'egg' surface, and so T was not low enough for oscillations from these quasiparticles to be observed.

The dual model

The $5f^2$ ground state calculated by Richter *et al.* [88] is assumed to extend to low temperatures. The antiferromagnetic order is created by exchange between the localized moments on the uranium ions. The itinerant properties are generated by the third $5f$ electron. The Fermi surface in this case has been modelled by Zwicknagl, Yaresko and Fulde [95], using the local density approximation (Figure 6.5). Again, three sheets were observed. The first consisted of a K-centred ellipsoid, but was deemed unimportant to the physics and is not shown in Figure 6.5. The second sheet was the 'cylinder and cigars' sheet, and the third sheet also consisted of K-centred ellipsoids which were strongly dependent on the Fermi energy. These surfaces provided a reasonable fit to the dHvA frequencies.

6.2.5 The superconducting state

UPd_2Al_3 is a Type II superconductor, with B_{c2} usually quoted as 3.6 T [72] although there is evidence that the critical field is anisotropic [96]. In the superconducting state, the electrons form coherent paired states (Cooper pairs) in momentum space. For the Cooper pairs to form, an attractive interaction between electrons is required. Usually, the Coulomb force means that electrons repel each other. In ordinary BCS superconductors, this interaction is provided by phonons, which mediate the interaction between two electrons.

Please purchase PDF Split-Merge on www.verypdf.com to remove this watermark.

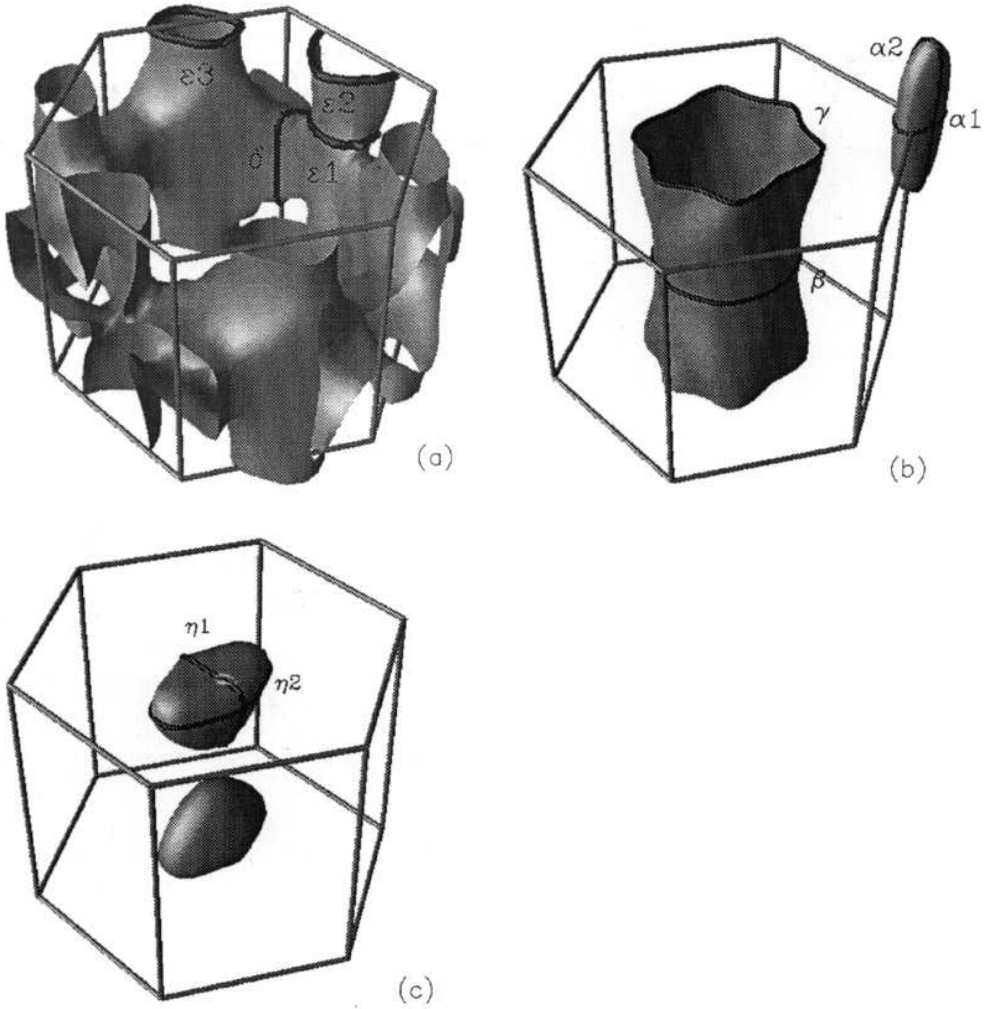

Figure 6.4: The calculated Fermi surfaces. The Greek letters mark particular extremal cross-sections. (a) is the 'party hat', (b) shows the 'cylinder' and the 'cigar', and (c) contains the 'egg'. Taken from Knöpfle *et al.* [92].

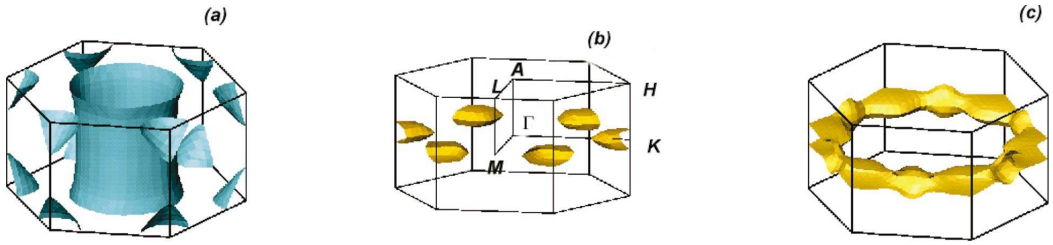

Figure 6.5: Two of the calculated Fermi surfaces from the Zwicknagl model. (a) is the 'cylinder' and 'cigar' sheet, (b) shows the K-centered ellipsoids, and (c) shows the same sheet with the Fermi energy shifted by 40 K. Taken from Zwicknagl *et al.* [95].

Please purchase PDF Split-Merge on www.verypdf.com to remove this watermark.

The pair formation must be energetically favourable compared to the normal state if the paired state is to form. When this happens for all of the electrons in the material, an energy gap forms at the Fermi surface. This gap acts as the (complex) order parameters in the Ginzburg-Landau phenomenological theory of superconductivity. For a normal BCS superconductor, the entire Fermi surface is uniformly gapped (s-wave symmetry), but different symmetries have been observed in more complicated superconductors, often accompanied by nodes. Indeed, some gapless superconductors have been found. It is not known if an unconventional gap is an indication of an unconventional mediator, although the converse has been shown for at least one case [73]. One reason for the great interest in UPd_2Al_3 is that it has an unconventional order parameter, and is suspected of being magnetically mediated. As we shall see, inelastic neutron scattering can contribute to this discussion.

6.3 Previous inelastic neutron scattering studies

6.3.1 Historical overview

The first inelastic neutron scattering on single crystals of UPd_2Al_3 was carried out at Risoe National Laboratory, where broad excitations with a strong dispersion along the c^* [001] axis up to ~ 8 meV at the magnetic zone boundary were reported [97]. The full-width half-maximum (fwhm) at the zone boundary is ~ 9 meV. In the basal plane strongly damped excitations were found, with poles and widths of similar extent, increasing up to ~ 4 meV. These studies, carried out with 0.3 meV resolution (fwhm) found no low energy gap in the excitations at the magnetic zone centre $\boldsymbol{Q}_0$, and no change when the material became superconducting. However, since the energy resolution was on the scale of ~ 3 K, it is perhaps not surprising that no effect was observed below T_{sc}.

Work on polycrystalline material at the ISIS spallation source by Krimmel *et al.* [98] then followed, giving an overview of the inelastic response function up to ~ 20 meV. This study gave no evidence for a discrete crystal field level scheme and the principal results were that (a) over the studied range of wavevectors a broad quasielastic contribution was present in the scattering at all measured temperatures with a fwhm of 9.8 meV at $T = 25$ K and 22.8 meV at 150 K, and (b) at $T = 25$ K a strong maximum in the scattered intensity with an energy transfer ~ 2.2 meV at $|\boldsymbol{Q}| \sim 1$ Å^{-1} was identified. The inelastic contributions appear to fit with the crystal field scheme of Grauel *et al.* [83] but could also be due to magnetic correlations persisting in the paramagnetic state.

Experiments with single crystals and a cold-source three-axis spectrometer were first attempted at Brookhaven National Laboratory in 1994, but were unsuccessful. In 1995, experiments were performed by the Tohoku University group using the JRR-3M research reactor (JAERI, Tokai) [99], and this motivated higher-resolution experiments at the Institut Laue-Langevin (ILL), Grenoble in 1996 [100, 101]. Subsequently, an independent effort was started by the group at the Advanced Science Research Centre in JAERI, Tokai [77, 102]. Over the following years, several papers have been published concentrating on the magnetic response in the vicinity of $\boldsymbol{Q}_0$, including polarization analysis,

Please purchase PDF Split-Merge on www.verypdf.com to remove this watermark.

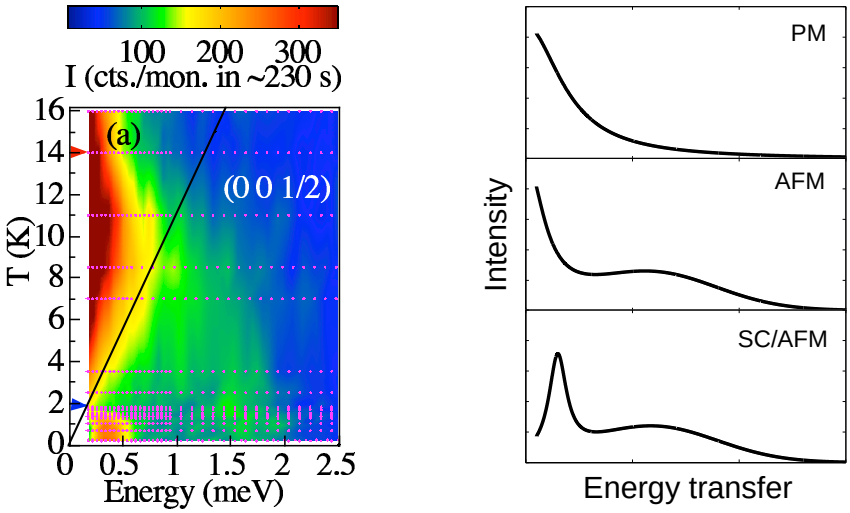

Figure 6.6: Contour plot of the (E,T) domain at $\boldsymbol{Q_0}$. The magenta points indicate actual data points. The black line shows k_BT. The blue arrow marks T_N and the red arrow T_{sc}. The white area marks the resolution limit due to Bragg peak contamination. Data taken from Bernhoeft *et al.* [103]. The side panels are representations of the neutron inelastic scattering response as a function of energy transfer in the paramagnetic (PM) state, the antiferromagnetic state (AFM), and the joint superconducting-antiferromagnetic state (SC/AFM).

temperature and field dependent studies. This has resulted in a disparate literature, masking rather than highlighting the fundamental importance and remarkable degree of experimental agreement between data collected on different samples by independent experimental groups.

6.3.2 At the magnetic zone centre $\boldsymbol{Q}_0$

Figure 6.6, based on data from [103], is an overview of magnetic response at $\boldsymbol{Q}_0$. From polarization analysis, this response is electronic in origin, and the fluctuations are in the basal plane only. The side panels are schematics of the dynamic response in the different temperature regimes. At high temperatures the response is, within the experimental energy resolution of 0.09 meV (fwhm), quasielastic. Between T_{sc} and $\sim T_N/2$ the quasielastic energy linewidth at constant intensity scales approximately with k_BT (the black line in Figure 6.6), indicating that the bare susceptibility is temperature independent. In addition to this low energy response, on cooling a distinct, albeit broad, inelastic features appears. This is the dispersive excitation seen at Risoe. This feature is unchanged on passing into the superconducting phase down to the lowest temperatures measured (0.15 K). In contrast, the low energy response is strongly renormalized in the superconducting state, with a distinct inelastic excitation appearing. For all temperatures studied this latter pole has little change in amplitude, width or position below

Please purchase PDF Split-Merge on www.verypdf.com to remove this watermark.

$T_{sc}/2$.

The thermal evolution of the normal state response along the hexagonal axis $[00q_L]$ and in the hexagonal plane $[q_H 0\frac{1}{2}]$ is given in Figure 6.7. The quasielastic intensity falls off rapidly on moving away from $\boldsymbol{Q}_0$. On heating to T_N the quasielastic feature becomes more extended in momentum space, but remains localized up to at least 80 K. The response across the Brillouin zone will be discussed in the relevant experimental section.

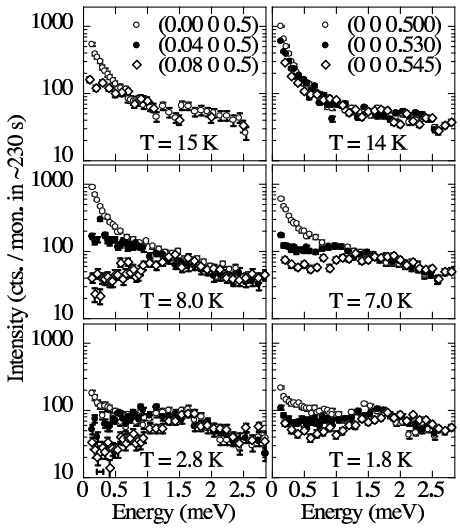

Figure 6.7: Comparison of the scattering in the hexagonal plane (q_h 0 1/2) (left) and along the hexagonal c^* axis (0 0 q_l) (right) at different temperatures in the normal state. Note the logarithmic vertical scale and different steps in reciprocal space (a reciprocal lattice unit corresponds to $a^* = 1.355$ Å^{-1} and $c^* = 1.500$ Å^{-1} along the two axes). At 15 K there are no data at (0.04 0 0.5). Only for temperatures $\sim T_N$ does the quasielastic response become more isotropic and extend significantly out into the zone in both the basal plane and along the hexagonal axis. Data taken on IN14 with fixed $k_f = 1.15$ Å^{-1}. Figure taken from Ref. [104].

6.3.3 In an applied magnetic field

Initial inelastic neutron scattering experiments in an external field up to 4 T, by Metoki *et al.* [77], show that an external field has a strong effect on the inelastic response at $\boldsymbol{Q}_0$. These initial, low-resolution measurements provided the motivation for the studies presented here.

The experimental work presented in this thesis investigates both the normal and superconducting states of UPd_2Al_3 as a function of applied magnetic field using three-axis spectrometry. To answer further questions about the low-energy response, a neutron spin-echo experiment was also performed.

Please purchase PDF Split-Merge on www.verypdf.com to remove this watermark.

6.4 Sample characterization

The sample used was a 2.7 g single crystal supplied by N. Sato of Nagoya University; it had previously been used in Refs. [100, 101, 103]. It was prepared by the Czochralski method, and had a nominal composition of $UPd_2Al_{3.03}$ in the melt. The transitions occur at $T_N = 14.3$ K and $T_{sc} = 1.8$ K. It was aligned to give an $a^* - c^*$ scattering plane for all experiments, with the b axis vertical. The superconducting phase diagram (Figure 6.8) was established from the susceptibility as measured by a mutual inductance technique, in the same 5 T cryomagnet as used for some of the neutron scattering work. Measurements were made by sweeping the applied magnetic field at a series of fixed temperatures. The critical field ($\boldsymbol{B} \parallel b$) was 3.3 T, consistent with the literature.

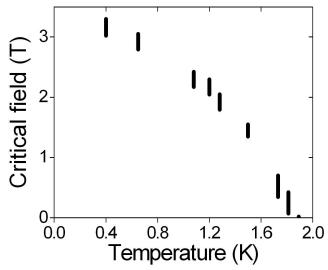

Figure 6.8: Experimental (B,T) phase diagram of the superconducting state in the sample of UPd_2Al_3 used, measured in the 5 T vertical cryomagnet (equipped with dilution insert) used in some of the experiments. The bars indicate the width of the anomaly observed as a function of magnetic field.

Please purchase PDF Split-Merge on www.verypdf.com to remove this watermark.

6.5 The normal state

The normal state, in both paramagnetic and antiferromagnetic phases, is altered by an external magnetic field. If the changes in the superconducting response are to be visualised, the changes in the normal response must be well understood. To provide this information the response at $\boldsymbol{Q}_0$, the magnetic zone centre, was examined in close detail. A study of particular features at other points in the Brillouin zone was carried out to complete the experimental picture.

6.5.1 At the magnetic zone centre

Experimental details

The IN14 three-axis spectrometer at the Institut Laue-Langevin (ILL) was used for this work. It is supplied with cold neutrons, and so has a good energy resolution compared to other three-axis spectrometers, although the available energy transfer range is shorter. A 14.9 T cryomagnet was used to generate the external magnetic field. The spectrometer was operated in fixed k_f mode, with $k_f = 1.5$ Å-1. This represented the best compromise between flux and energy resolution (0.1 meV hwhm), considering the beam attenuation caused by the cryomagnet tail. A vertically focussed pyrolytic graphite (PG) monochromator was used with 60' of collimation on k_i. A horizontally focussed PG analyzer was used with a Be filter and no collimation along k_f.

Results

Kita *et al.* [81] had examined the antiferromagnetic phases by neutron diffraction up to 6 T, using the $\boldsymbol{Q}$ dependence of the magnetic cross-section to identify the magnetic structure. In particular, the (1 0 1/2) Bragg peaks should drop to 38 % of its zero field value in Phase III (Figure 6.2) due to the change in the projection of the magnetic moment onto the scattering vector. At 14.9 T, the Bragg peak measured here had 43 % of the its zero field value, indicating that at 14.9 T, the UPd_2Al_3 is still in Phase III.

Figure 6.9 shows data taken at (1 0 0.5) at $T = 20$ K at 0, 4, 9 and 13 T. The signal appears to be purely quasielastic, with the intensity declining monotonically as a function of increasing magnetic field. Beyond 3 meV energy transfer there is almost no field-induced difference. Figure 6.10 shows similar data taken at 1.9 K, in the antiferromagnetic normal state, with scans taken at 0, 2, 4, 5, 7, 9, 11 and 13 T. The intensity of the quasielastic response increases up to 4 T, and then decreases, becoming very broad and flat by 13 T. This was confirmed by high-resolution measurements in fields up to 5 T (see Section 6.6.1), and is seen at both (0 0 0.5) and (1 0 0.5). The inelastic response, at 1.4 meV at 0 T, moves to higher energy transfers; at 15 T it is centred at 2.5 meV. Above 4 meV there is little change.

The momentum space width in the two accessible directions a^* and c^* at $\Delta E = 0.3$ meV was constant under applied magnetic field. The momentum width of the inelastic excitation only starts to increase at the highest applied fields used. The changes observed are therefore assumed to occur solely in the energy domain.

Please purchase PDF Split-Merge on www.verypdf.com to remove this watermark.

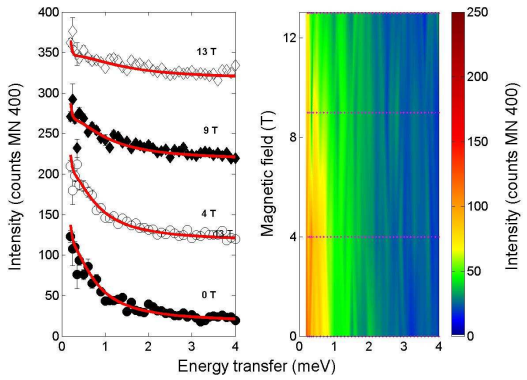

Figure 6.9: The magnetic field dependence of the inelastic response at $\mathbf{Q} = (1\ 0\ 0.5)$ in UPd_2Al_3 at 20 K, in the paramagnetic normal state, as measured on IN14 with $k_f = 1.5$ Å^{-1}. The left-hand panel shows four individual scans as a function of energy transfer, taken at 0 T, 4 T, 9 T and 13 T. The curves are separated by 100 counts. The fits are described in the text. The right-hand panel is an interpolated colour plot, with real data points are marked by dots. The white space marks the resolution cut-off.

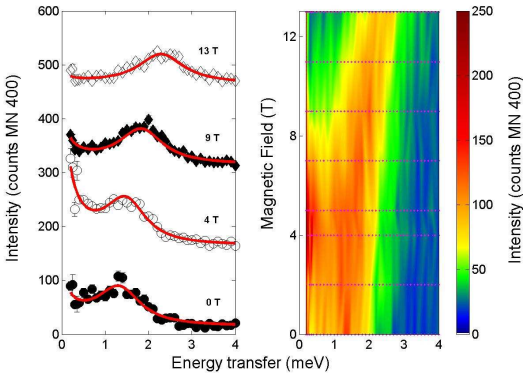

Figure 6.10: The magnetic field dependence of the inelastic response at $\mathbf{Q} = (1\ 0\ 0.5)$ in UPd_2Al_3 at 1.9 K, in the normal antiferromagnetic state, as measured on IN14 with $k_f = 1.5$ Å^{-1}. The left-hand panel shows four individual scans as a function of energy transfer, taken at 0 T, 4 T, 9 T and 13 T. These curves are separated by 150 counts. The fits are described in the text. The right-hand panel is an interpolated colour plot, including additional curves. Real data points are marked by dots. The colour scheme has been selected to highlight the inelastic excitation and the quasielastic response, and is the same as that used in Figure 6.9. The white space marks the resolution cut-off.

Please purchase PDF Split-Merge on www.verypdf.com to remove this watermark.

Analysis

A primitive model for the observed response is to split the dynamical susceptibility into two distinct components, and sum them incoherently to generate the total response function, $\chi = \chi_1 + \chi_2$. At this level, the independent contributions can be assigned to a low energy part, χ_1, and a high energy part, χ_2.

The next step is to adopt a standard mean-field type coupling between the two contributions, to give the full $5f$ neutron scattering amplitude, in an attempt to restore at least some of the correlations present. Although a dynamical coupling constant λ should be applied, in practice this is assumed to be constant for all energies and momentum transfers for simplicity. The two contributions are generated from the total magnetization $M = M_1 + M_2$ where $M_1 = \chi_1(H + \lambda M_2)$ and $M_2 = \chi_2(H + \lambda M_2)$. The appropriate mean-field form for the dynamic susceptibility is therefore

$$\chi = \frac{\chi_1 + \chi_2 + 2\lambda\chi_1\chi_2}{1 - \lambda^2\chi_1\chi_2}. \tag{6.2}$$

Therefore small changes can have large effects on the observed spectral form, because of the built-in positive feedback due to the Stoner-like denominator. This enhances the low frequency part, renormalizing the effective low-energy width at the same time. To see this, consider the response χ at low frequencies. The real parts of the $\chi_{1,2}$ tend to a constant, with the imaginary parts proportional to the frequency. As $\omega \to 0$, this gives a denominator $1 - \lambda^2 \mathrm{Re}\chi_1 \mathrm{Re}\chi_2$. At high frequencies, $\chi_{1,2}$ tend to zero, and the denominator goes to unity.

In a typical three-axis neutron scattering experiment, the measured quantity after all instrumental effects have been removed is the scattering function $S(Q, \omega)$, which is purely a property of the sample (Section 2). On taking into account the detailed balance factor and the magnetic form factor $f^2(\boldsymbol{Q})$, for magnetic scattering $S(\boldsymbol{Q}, \omega)$ reduces to the imaginary part of the magnetic susceptibility.

$$S(\boldsymbol{Q}, \omega) \propto \frac{f^2(\boldsymbol{Q})}{1 - \exp(-\hbar\omega/k_B T)} \chi''(\boldsymbol{Q}, \omega, T) \tag{6.3}$$

Because the susceptibility $\chi = \chi' + i\chi''$ is a causal quantity, the Kramers-Krönig relations apply

$$\chi'(\omega) = \frac{2}{\pi} \int_0^\infty \frac{\omega' \chi''(\omega')}{\omega^2 - \omega'^2} \mathrm{d}\omega' \tag{6.4}$$

$$\chi''(\omega) = -\frac{2\omega}{\pi} \int_0^\infty \frac{\chi'(\omega')}{\omega^2 - \omega'^2} \mathrm{d}\omega' \tag{6.5}$$

and so the imaginary part of the susceptibility can be written as

$$\chi''(T) = \pi\omega\chi(\omega, T) \tag{6.6}$$

if $\chi(\omega, T)$ is an even function of ω.

Please purchase PDF Split-Merge on www.verypdf.com to remove this watermark.

From the bulk measurements (Section 6.2.3) the system shows Fermi liquid-like electronic behaviour. A simple model of the response based on the effect of a random perturbation and the time taken to return to equilibrium was applied. The time is visualised via the energy linewidth Γ_1 of the quasielastic part of the response (χ_1), and is a function of all of the interactions and correlations inside the materials, represented by the total susceptibility χ, partially measured in a neutron scattering spectrum. $\Gamma_1 = C\chi^{-1}$ where C is a constant. This constraint was applied to a modelling using a Lorentzian lineshape for the quasielastic profile and a damped harmonic oscillator for the inelastic component.

To fit such functions to the measured intensity, the detailed balance factor and form factor must be taken into account. The fits described here are all at the same $\boldsymbol{Q}$, so $f^2(\boldsymbol{Q})$ can safely be neglected. The background (15 counts at 1.9 K and 20 counts at 20 K), an estimated elastic contribution, and instrumental resolution must also be accounted for. A full resolution ellipsoid is not used here; simply the energy resolution as estimated from a scan of the elastic incoherence. This means that the parameters obtained will not be comparable to those obtained in Ref. [103]. The parameters obtained here are intended to illustrate the trends in the response, rather than to provide absolute widths.

For the paramagnetic state data, the spectral form is clear, due to the absence of the inelastic excitation. Using $\Gamma(B) = C\chi^{-1}(B)$, where C is a constant with magnetic field, the fits illustrated in Figure 6.9 were obtained with $C = 72$ meV and a quadratic dependence for the energy linewidth $\Gamma(B)$ on the applied magnetic field. The energy linewidth parameters are shown in Figure 6.11a.

In the antiferromagnetic case, the inelastic pole χ_2 was assumed to have a constant amplitude and half-width half-maximum (0.6 meV) over all magnetic fields, with a shifting centre of mass. The C value determined from the paramagnetic state was used here. The fixed parameters (unvarying under magnetic field) used were

C (meV)	λ (arb. units)	I(χ_2) (arb. units)	Γ_2 (hwhm) (meV)
72	0.042	104	0.64

This model describes the data successfully and confirms that the magnetic correlation function of UPd_2Al_3 as measured here is consistent with Fermi-liquid-like behaviour over a large range of the parameter space from 1.9 K to 20 K, and 0 T to 15 T. The itinerant response is therefore well established.

The two fitted parameters - the centre of mass of the inelastic pole, and the quasielastic energy linewidth - are illustrated in Figure 6.11. The inelastic pole centre increases with applied magnetic field. This conclusion is supplemented with high-resolution data (0.05 meV fwhm) measured at (0 0 0.5) below 5 T, although here the measured inelastic pole has less apparent intensity due to the geometrical constraints on the cross-section. The quasielastic energy linewidth behaves quite differently. Globally, it increases with field, but locally there is a minimum close to 4 T.

The energy linewidths at both 2 and 20 K can be compared crudely with the inverse intensity, as estimated by summing over the inelastic energy window measured, and

Please purchase PDF Split-Merge on www.verypdf.com to remove this watermark.

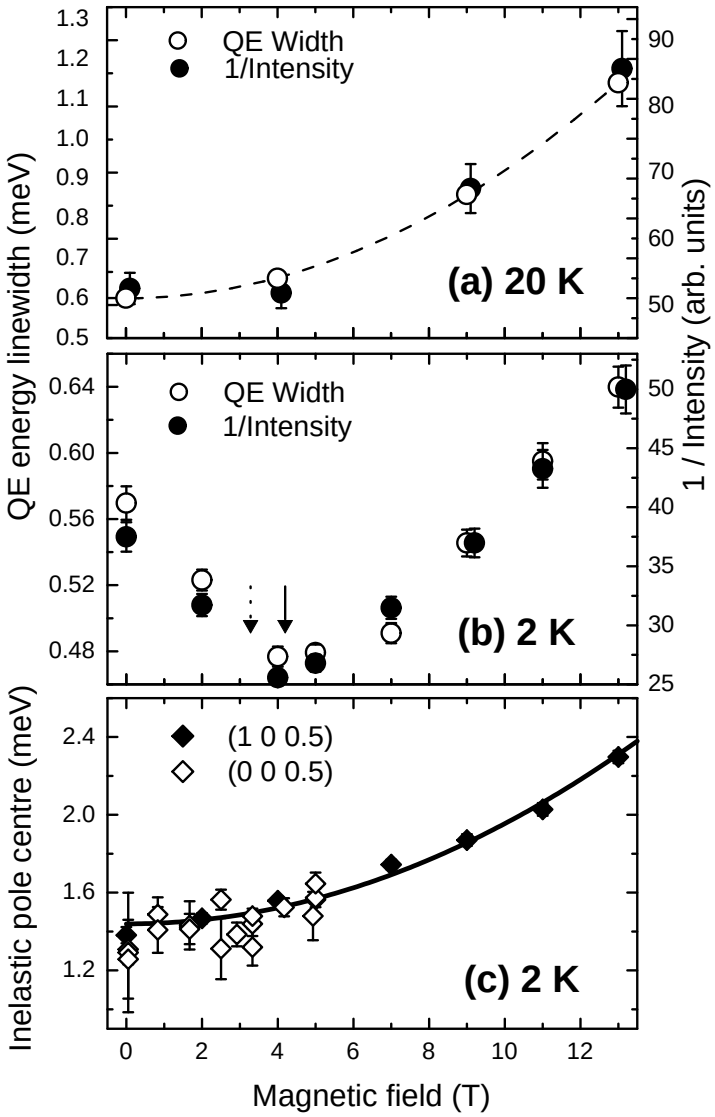

Figure 6.11: Panel (a) shows the effect of applied magnetic field on quasielastic energy linewidth (hwhm) at 20 K (open points). The linewidth is quadratic with respect to the applied magnetic field ($\Gamma = \Gamma_0 + \epsilon B^2$ where $\Gamma_0 = 0.6$ meV and $\epsilon = 0.00319$ meV.B^{-2}. Panel (b) shows the effect of applied magnetic field on the quasielastic energy linewidth (hwhm) at 2 K (open points), from the fits shown in Figure 6.10. In both panels (a) and (b) the closed points are the intensity of the non-Bragg response, summed over the energy window measured, and corrected for background. The dashed arrow in (a) indicates B_{c2} (3.3 T), and the solid arrow the approximate position of the moment rotation transition (4.2 T). Panel (c) shows the centre of the (high-energy) inelastic pole as a function of applied magnetic field at 2 K. The closed points are taken from the data shown in Figure 6.10, measured at $\mathbf{Q} = (1\ 0\ 0.5)$. The open points are taken from (high-resolution) data illustrated in Figures 6.18 and 6.19, measured at $\mathbf{Q} = (0\ 0\ 0.5)$. The line is described in the text.

Please purchase PDF Split-Merge on www.verypdf.com to remove this watermark.

correcting for background. As expected, considering the mean-field model described above, these two plots show the same dependence, reinforcing the reliability of the model.

Discussion

The inverse intensity may be considered to be proportional to the inverse imaginary susceptibility. In this case, the behaviour is reminiscent of an antiferromagnetic transition. It therefore seems that the changes in the quasielastic linewidth (and intensity) are directly related to the moment rotation at 4.2 T (Figure 6.2). As there is no change in the observed width in momentum space, the length correlations remain unaltered but the time correlations change. These antiferromagnetic fluctuations have a much longer lifetime at 4 T, as the system approaches the moment rotation. As there is no entropy change, this transition is invisible to the heat capacity, but is seen by neutron scattering.

The origin of the dispersive inelastic excitation is still a matter of debate. In both the itinerant and dual models it may simply be an ordinary spin wave excitation. Cooper *et al.* [74] have developed the spin wave theory for hexagonal close packed rare earth metals, including the effects of anisotropic exchange, axial and hexagonal anisotropy, and external magnetic fields. This can be applied to the hexagonal UPd_2Al_3. The general Hamiltonian for the system is

$$\begin{aligned} H &= -\sum_{i\neq j} J_{ij}\boldsymbol{S}_i\cdot\boldsymbol{S}_j - \sum_{i\neq j} K_{ij}S_{i\zeta}S_{j\zeta} + \sum_i \{[P_2^0 Y_2^0(\boldsymbol{S}_i) + P_4^0 Y_4^0(\boldsymbol{S}_i) \\ &\quad + P_6^0 Y_6^0(\boldsymbol{S}_i) + P_6^6(Y_6^6(\boldsymbol{S}_i) + Y_6^{-6}(\boldsymbol{S}_i))] + \lambda\beta\boldsymbol{H}\cdot\boldsymbol{S}_i\} \end{aligned} \tag{6.7}$$

where $\boldsymbol{S}_i$ is the total (orbital and spin) angular momentum of atom i, λ is the Landé factor and ζ is the direction of the hexagonal axis. The J_{ij} term is the anisotropic exchange; K_{ij} the axial anisotropy, the $Y_l^m(S)$ (operator equivalents of the spherical harmonics relative to this axis) describe the hexagonal anisotropy, and the final term is due to the external magnetic field $\boldsymbol{H}$. Other terms, such as the quadrupole-quadrupole interactions may be present but are not included here; their effects can be mimicked by giving J_{ij} and K_{ij} a temperature dependence. The branch of interest is acoustic, so the lattice can be treated as a Bravais lattice.

The magnetic structure of UPd_2Al_3 needs to be put into the (ζ,ξ,η) orthonormal coordinate frame. ζ is along the hexagonal axis, $\xi \parallel a$, and $\eta \parallel b^*$.

$$S_{i\zeta} = 0; \qquad S_{i\xi} = S\cos(\boldsymbol{Q}_0\cdot\boldsymbol{R}+\phi); \qquad S_{i\eta} = S\sin(\boldsymbol{Q}_0\cdot\boldsymbol{R}+\phi) \tag{6.8}$$

where $\phi = 0$ in the zero field state (Case IV in the notation used by Cooper *et al.*).

So far, the hexagonal anisotropy has been ignored, as it can introduce many harmonics, and prevent a simple description of the structure being made. However, evaluation of the spin-wave dispersion shows that it must be zero at $\boldsymbol{Q}_0$ (i.e. ungapped) unless there is hexagonal anisotropy. The calculation including the hexagonal anisotropy and magnetic field parallel to b is non-trivial; indeed conventional second-order perturbation theory gave an infinite anisotropy gap! Cooper *et al.* try a modified perturbation procedure and conclude that the energy gap of the excitation should vary quadratically with the

Please purchase PDF Split-Merge on www.verypdf.com to remove this watermark.

magnetic field and P_6^6 (the expression of the hexagonal anisotropy). The line in Figure 6.11 is a fit to the function of the form $c + aB^2$, where B is the applied magnetic field. c represents the effect of the hexagonal anisotropy at zero field, and places the spin wave centre of mass at 1.44 ± 0.01 meV; $a = (5.2 \pm 0.2) \cdot 10^{-3}$ meV.T^{-2}. This theory describes the observed behaviour.

At 4 T, the moment rotation is equivalent to making $\phi = \pi/2$. In the model described above, this does not affect the quadratic dependence of the dispersion on the magnetic field, but might affect frequency via the hexagonal anisotropy. However, a single quadratic dependence appears to fit the data accurately.

As an aside, a change in a magnetic structure like the rotation seen here is often ascribed to a 'spin-flop transition'. In such a transition, the spin-wave excitations develop an imaginary frequency due to the application of magnetic field. To stabilize the system, the structure shifts. For this to occur, the frequency of the excitations would have to decrease towards 0 meV as 4 T is approached. Experimentally this is not observed, and from the theory of Cooper *et al.* it is not expected as the excitation gap increases with external field.

In the dual model there is an alternative explanation for this inelastic pole: the crystalline electric field (CEF) excitations are coupled together by the itinerant electrons, giving an apparent dispersion through inter-site exchange. The mechanism was first developed for the anisotropic paramagnet by Becker, Fulde and Keller [105]. The width of the excitation is then a measure of the broadening of the CEF level brought about by the itinerant electrons. In the same way, the quasielastic scattering is the broadening of the ground state due to exposure to the itinerant part of the electronic subsystem. This theory is developed in Refs. [75, 76, 106]. The changes in the pole position of the excitation may then be brought about by (i) a decrease in the coupling by the itinerant electrons, so pulling the excitation upwards in energy towards its natural level, or (ii) a shift in the CEF energy level due to the external field. In principle, this could lead to a Zeeman splitting of the level, with one level eventually becoming the new ground state at ~ 4 T. There are several problems with this interpretation. No inelastic pole is seen in the paramagnetic state, although dispersive CEF excitations are still possible in the paramagnetic state [105]. This apparent absence could be due to significant broadening of the excitation. However, the localized quasielastic scattering is still visible at 20 K, and, unlike the data at 2 K, the observed energy linewidth does not decrease at 4 T. This decrease would be expected even for a broadened inelastic excitation if the crystal field levels underwent Zeeman splitting.

6.5.2 Dispersion away from the magnetic zone centre

Experimental details

To measure the inelastic response away from the magnetic zone centre, the thermal-source three-axis spectrometer IN8 was used, as it covers a larger energy transfer range, although the energy resolution is poorer than on IN14. Two sets of data, sampling two different Brillouin zones, were taken at both low and high fields:

Please purchase PDF Split-Merge on www.verypdf.com to remove this watermark.

(i) for $\boldsymbol{Q} = (0\ 0\ Q_L)$ where $1.0 < Q_L < 1.5$ at 0 T and 11.6 T using a 12 T cryomagnet. The spectrometer was operated at fixed $k_f = 2.662$ Å^{-1}, providing optimal flux with a vertically and horizontally focussing PG(002) monochromator.

(ii) for $\boldsymbol{Q} = (0\ 0\ Q_L)$ where $0.5 < Q_L < 1.0$ at 0 T and 12.5 T using a 14.9 T cryomagnet. The spectrometer was operated at fixed $k_f = 2.662$ Å^{-1}. A vertically and horizontally focussing Si(111) monochromator was used.

In both cases, a vertically and horizontally focussing Si(111) analyzer was used, with a PG filter to suppress third-order contamination and a radial collimator along k_f, to cut out incoherent scattering from the aluminium window of the cryomagnets.

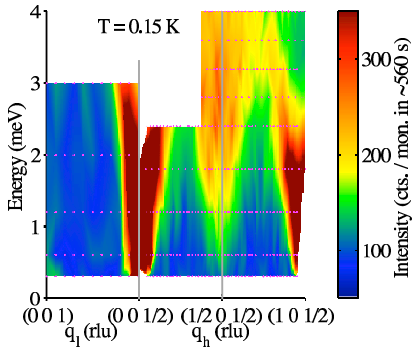

Figure 6.12: Contour map at 0.15 K showing the low-energy transfer response across the Brillouin zone, taken on IN14 with $k_f = 1.3$ Å^{-1}. The abscissa are scaled to constant length in reciprocal space. The colour scheme chosen leads to saturation close to $\boldsymbol{Q}_0$. The cross-section at the smallest energy transfers is inaccessible due to incoherent elastic scattering and, at $\boldsymbol{Q}_0$, due to the magnetic Bragg peak. Figure taken from Ref. [104].

Results

The inelastic response away from the magnetic zone centre is shown in Figure 6.12. The response at $\boldsymbol{Q}^* = (0.5\ 0\ 0.5)$ is discussed in Section 6.5.3. It is clear that the inelastic pole seen at $\boldsymbol{Q}_0$ is dispersive. It is well-defined close to the antiferromagnetic zone centre, and broadens rapidly in both momentum and energy space. The dispersion is much sharper along the c^* direction than in the basal plane, where secondary features are observed [107]. We therefore concentrate on the dispersion along the c^* axis, to avoid any confusion. Two different Brillouin zones were sampled.

Some examples of the data are shown in Figures 6.13 (constant-energy scans) and 6.14 (constant-**Q** scans). Figure 6.13 illustrates the steepness of the dispersion in zero field (103 ± 4 meV Å^{-2}, assuming quadratic behaviour), with several cuts across the inelastic excitation. A quadratic fit of the dispersion gives a stiffness of 67 ± 4 meV Å^{-}2. The lines in both panels are Gaussian fits of the 0 T data, assuming an excitation of equal weight on either side of the magnetic zone center. At 11.6 T, the excitation is

Please purchase PDF Split-Merge on www.verypdf.com to remove this watermark.

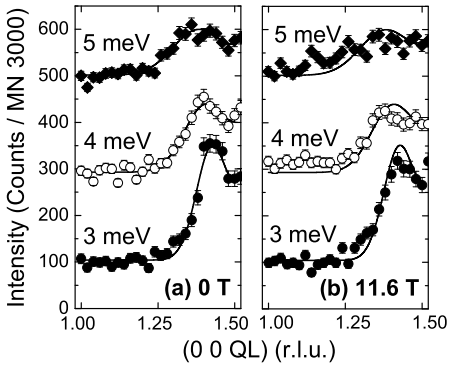

Figure 6.13: Constant-energy transfer neutron spectra at 3 K in (a) 0 T and (b) 11.6 T applied magnetic field. The curves are offset by 200 counts. The lines in both (a) and (b) are fits of the zero-field data in panel (a). Details are given in the text.

slightly broader in momentum space, with a lower peak intensity. This may be due to the small shift upwards in energy transfer, combined with the presence of the additional scattering, broadening the excitation seen in the constant-E cuts. Note that at ~ 4 meV, the background level appears to be higher at 11.6 T.

Figure 6.14 shows constant-$\mathbf{Q}$ scans at several positions at 0 T and 11.6 T. In these cuts, the inelastic excitation is no longer clearly visible; indeed it is difficult to assign any of the features unambiguously. Nevertheless, several broad trends can be noted.

Analysis

At (0 0 1.30) in zero field there is an increased amount of scattering between 4 and 10 meV. This appears to have evolved from the dispersive inelastic exitation. At (0 0 1.15) a similar feature with lower intensity is seen. Across the Brillouin zone in zero field from (0 0 1.3) to (0 0 1.0) there is an increase in the observed scattering between 4 and 10 meV energy transfer although the intensity decreases as we move away from $\boldsymbol{Q}_0$. This appears to have evolved from the dispersive inelastic excitation. At (0 0 1.0) the boundaries of this scattering are more difficult to discern as a signal was noted at 11 meV; this has been attributed to an optic phonon, due to its observed temperature dependence (measured up to 120 K). Unfortunately, the instrumental background in this region could not be obtained. In the absence of this information, this scattering is assumed to be electronic in origin.

The differences between the zero- and high-field data are shown in the right-hand panels of Figure 6.14. An S-like curve characteristic of a shift in excitation position is observed. The differences were fitted by taking the difference of two inelastic excitations at (0 0 1.45) and (0 0 1.3). At (0 0 1.15) and (0 0 1.0) the difference between the low- and high-field scans arises from an excitation in the high-field state alone.

The low-field behaviour is illustrated in Figure 6.15a, where fits to excitations are shown in bold with the measured half-width (in momentum or energy space accordingly).

Please purchase PDF Split-Merge on www.verypdf.com to remove this watermark.

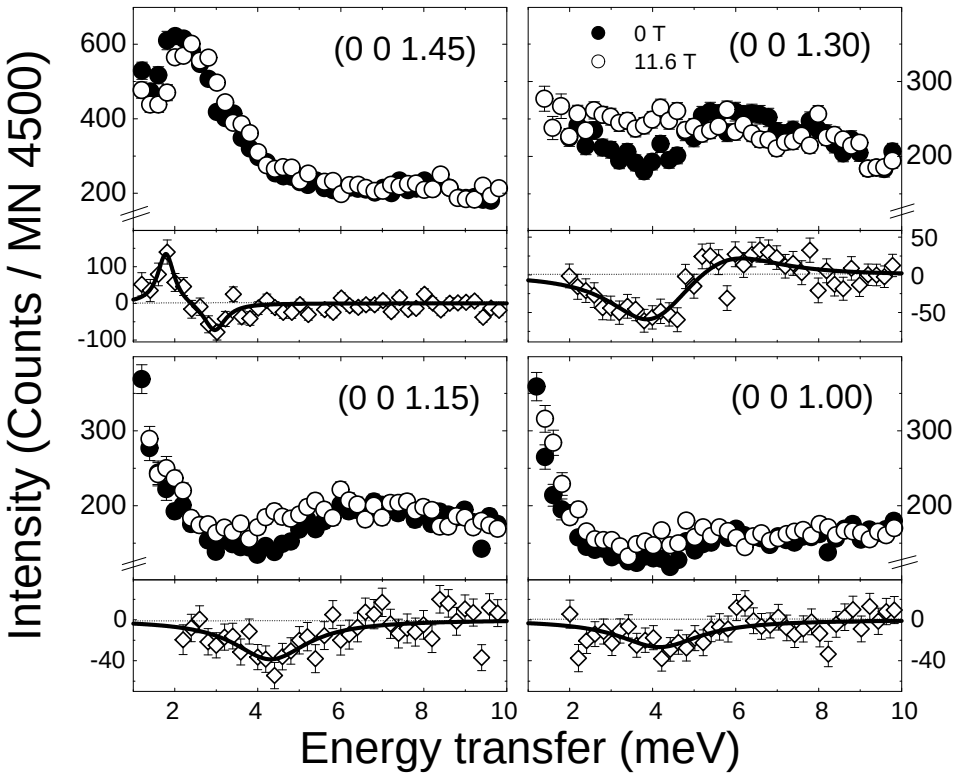

Figure 6.14: Constant-$\boldsymbol{Q}$ scans at 3 K at 0 T (closed points) and 11.6 T (open points). Under each scan, there is the subtraction $I_{0\mathrm{T}} - I_{11.6\mathrm{T}}$. The lines at (0 0 1.30) and (0 0 1.45) are fits of the difference between two Lorentzian lineshapes representing the dispersive inelastic pole at the two fields. At (0 0 1.00) and (0 0 1.15) only one Lorentzian lineshape is included in the fitting; the 0 T Lorentzian has been set to zero.

Please purchase PDF Split-Merge on www.verypdf.com to remove this watermark.

The filled circles represent excitations seen directly in the data, and the open circles excitations seen in the difference plots. The grey ellipses represent the broad features described above.

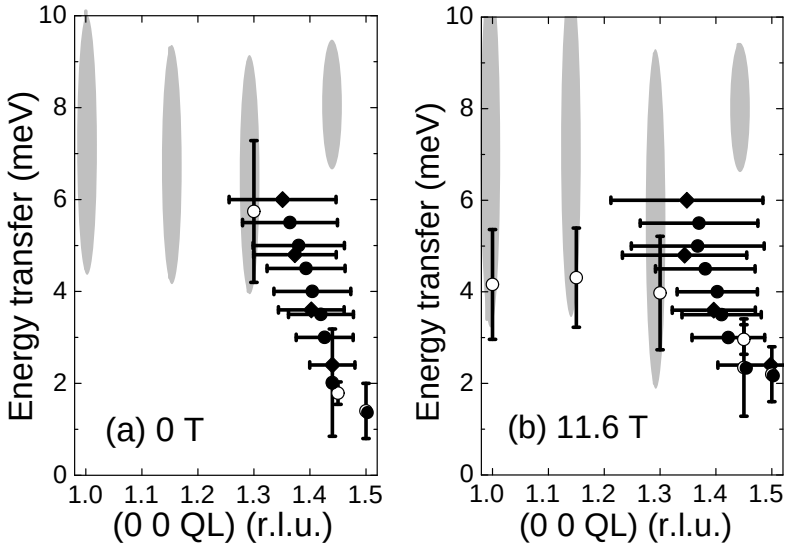

Figure 6.15: Representations of the inelastic response as a function of scattering vector and energy transfer at 3 K in (a) zero field and (b) high applied magnetic field. The solid black error bars indicate the half-width (in either momentum- or energy-space) of a peak, as determined by fitting data similar to that seen in Figures 6.13 and 6.14. The closed points were taken directly from data, and the open points from comparisons of the zero- and high-field data. The circles were measured at 11.6 T in setup (i). The diamonds at 12.5 T in setup (ii); these measurements were made in a different Brillouin zone, and have been mapped appropriately. The grey ellipses correspond to regions of relatively high intensity, measured from one estimated minimum to another (approximate full-width).

On applying magnetic field, there are several clear changes in the spectra (Figure 6.14). The overall behaviour is illustrated in Figure 6.15b, using the same conventions as in Figure 6.15a. The principal difference is the increase in scattering at 4.5 meV, apparently present across the Brillouin zone. Taking the difference of the high- and zero-field data sets, an excitation is observed centred close to $\sim$ 4 meV energy transfer, although the signal is broad and weak (Figure 6.14).

Please purchase PDF Split-Merge on www.verypdf.com to remove this watermark.

Discussion

The appearance of additional scattering in a high applied magnetic field is of great interest. Several explanations are considered here.

(i) a redistribution of the broad inelastic response seen at 0 T. This is unlikely as there is no change in the scattering observed for $\Delta E > 6$ meV, where the bulk of this broad lump of scattering is. In addition, the extra scattering has a relatively well-formed (Lorentzian) lineshape (Figure 6.14).

(ii) the quasielastic intensity at $\boldsymbol{Q}_0$ diminishes in high fields; at 11.6 T it contains little spectral weight. Is this spectral weight redistributed throughout the zone?

(iii) an excited crystal field level. In the dual model, this is not problematic. In the itinerant model, this might indicate that increasing the external magnetic field increases the localization of the apparent magnetic moments to the point that crystal field levels become visible. This would explain the loss in quasielastic scattering at $\boldsymbol{Q}_0$ too. However, the system must retain some itinerant character; Terashima *et al.* [108] have measured de Haas-van Alphen frequencies in elevated magnetic fields.

Several questions remain: is this signal present along the a^* axis in high field? at what field does it appear, or is the change gradual? If there is an abrupt change, the only significant alteration at 3 K is the moment rotation at ~ 4 T.

6.5.3 A 'soft spot' at $\boldsymbol{Q}^* = (0.5\ 0\ 0.5)$

Experimental details

The following data was gathered concurrently with the data presented in the previous two sections. The experimental setups are fully described above.

Results

A subsidiary maximum in the inelastic response was first observed at $\boldsymbol{Q}^* = (1/2\ 0\ 1/2)$ by Metoki *et al.* [109]. Figure 6.16 shows data taken at this point over a range of temperatures and fields, from 1.5 K (just inside the superconducting state) out to 80 K, well away from the magnetically ordered state, and from 0 T to 12.5 T. In the ordered state, an inelastic pole at ~ 3 meV is clearly visible. This pole is not affected in the superconducting state, and is unaffected by magnetic field up to 14.9 T. It seems plausible that it remains unchanged all the way to the metamagnetic transition, although this could not be confirmed due to limitations on the available magnetic field. As the temperature increases, the associated gap diminishes, and the inelastic pole becomes a localised quasielastic signal with diminished intensity above 20 K, disappearing after 80 K. This is a real change, and cannot be explained by changes in the thermal occupation factor. The quasielastic scattering at $\boldsymbol{Q}_0$ is strongly localized at all of these temperatures; it is never caused by contamination from the quasielastic scattering centred at $\boldsymbol{Q}_0$, which is strongly localized even at 80 K.

Please purchase PDF Split-Merge on www.verypdf.com to remove this watermark.

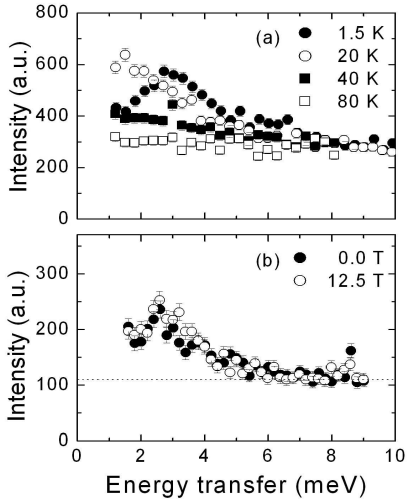

Figure 6.16: The inelastic response at $\mathbf{Q}^* = (0.5\ 0\ 0.5)$ in UPd_2Al_3 as measured on IN8. Panel (a): the temperature dependence of the response. Panel (b): the magnetic field dependence of the response, with $\boldsymbol{B} \parallel b$ axis, at 3 K. The dashed line is an estimate of the background. The two data sets were taken before and after a significant upgrade of IN8, and with different sample environments, and so the count rates are not directly comparable.

Discussion

A signal at $\boldsymbol{Q}^*$ indicates that there are antiferromagnetic correlations in the basal plane as well as along the c^* axis. UPd_2Al_3 has a sister compound, UNi_2Al_3. This has the same crystallographic structure and similar physical properties, although the ordering temperatures are lower: $T_N = 4.5$ K and $T_{sc} = 1.2$ K [110]. However, UNi_2Al_3 orders with at the wavevector (0.39 0 0.5) [111]. Inelastic neutron scattering carried out by Gaulin *et al.* [112] has revealed that the spectral weight of the spin fluctuations moves from the incommensurate position to the commensurate wavevector (0 0 0.5) as the energy of the fluctuations exceeds the energy scale of $T_N \sim 0.5$ meV. The electronic structure in these two materials is clearly very similar, with the UPd_2Al_3 eventually selecting the wavevector (0 0 0.5) whereas the UNi_2Al_3 develops at (0.39 0 0.5), close to (0.5 0 0.5). This leans towards the itinerant interpretation, as several wavevectors apparently encourage nesting of the Fermi surface. The slight differences between UPd_2Al_3 and UNi_2Al_3 are sufficient to give different results in the final ordered state.

It has been proposed [113] that the static Bragg peak observed at $\boldsymbol{Q}_0$ is merely the time-average of excitations at $\boldsymbol{Q}^*$ corresponding with hopping between two states with the symmetry required by $\boldsymbol{Q}^*$ (see Figure 6.17). This constant hopping then gives rise the dynamic scattering seen at $\boldsymbol{Q}^*$ in the ordered state. This interpretation is difficult to square with the observed moment rotation at 4 T. In addition, neutron spin-echo results

Please purchase PDF Split-Merge on www.verypdf.com to remove this watermark.

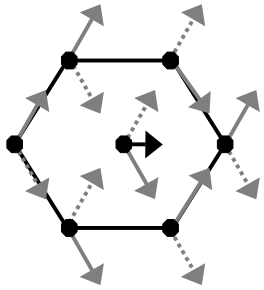

Figure 6.17: The grey arrows (solid and dashed) represent two configurations which, if static would give rise to a Bragg peak at $\boldsymbol{Q}^*$. The moments are proposed to fluctuate between the two configurations, giving rise to a reduced, static, time-averaged moment represented by the black arrow at $\boldsymbol{Q}_0$.

presented in Section 6.6.1 indicate that any dynamics of the magnetic Bragg peak must take place on a timescale greater than 10 ns.

It is surprising that the response at $\boldsymbol{Q}^*$ is not affected by the moment rotation in the basal plane. This indicates that the behaviour is independent of the actual magnetic structure, and is more directly related to the single-ion anisotropy.

Please purchase PDF Split-Merge on www.verypdf.com to remove this watermark.

6.6 The superconducting state

The superconducting state is investigated at 0.3 K and 1.4 K, and compared with the behaviour at 2.5 K, just outside the superconducting state. The low-energy response in the superconducting state is strongly renormalized, with a low-energy inelastic pole appearing at $\sim$ 0.35 meV. This renormalization is seen when using an external magnetic field to destroy the superconductivity. To complete the experimental picture of the superconducting state, a high resolution neutron spin-echo study is included.

6.6.1 Three-axis data under magnetic field

Experimental details

To obtain the high resolution needed to distinguish the low-energy inelastic response, IN14 was used with a fixed $k_f = 1.15$ Å^{-1} (energy resolution 0.06 meV hwhm). A 5 T cryomagnet was used with a dilution insert, so that the superconducting state could be fully probed. The cryomagnet was the same as that used to measure the superconducting phase diagram (Figure 6.8). A PG(002) monochromator was used with 60' collimation along k_i. A focussing PG(002) analyzer was used with no collimation along k_f.

Results

Figure 6.18 illustrates the evolution of the inelastic response at $\boldsymbol{Q}_0 = (0\ 0\ 0.5)$ at 0.3 K over a magnetic field range of 0 T to 5 T. One common feature is the dispersive inelastic excitation at $\sim$ 1.5 meV. This is always present, and changes little over the field range. The low-energy part of the response changes quite dramatically. The left-hand panels illustrate the disappearance of the inelastic pole at $\sim$ 0.35 meV, associated with the superconducting state, as the critical field B_{c2} is approached. The right-hand panels show the evolution of the quasielastic signal as the compound moves into the normal antiferromagnetic state. As magnetic field is applied, the intensity of the low energy inelastic pole, apparently centred at 0.35 meV, decreases and disappears completely between 2.92 T and 3.33 T, in agreement with the phase diagram in Figure 6.8. This is accompanied by a small shift downwards in the energy gap ($\sim$ 0.1 meV over 2.5 T). The inelastic response then assumes the normal state form with a quasielastic feature dominating, accompanied by the dispersive inelastic pole at $\sim$ 1.4 meV. This is consistent with the observations of Metoki *et al.* [77]. In Metoki's measurement, the low-energy inelastic pole appears to shift downwards in energy more dramatically than here; the higher resolution available on IN14 is able to resolve the inelastic component better as it loses intensity.

Further measurements were made at 0.3 K, 1.4 K and 2.5 K, to investigate the behaviour on leaving the superconducting phase by both magnetic field and temperature. Figure 6.19 shows the evolution in magnetic field of the response at these three temperatures. Close to the phase boundary (in either direction), the intensity diminishes.

Please purchase PDF Split-Merge on www.verypdf.com to remove this watermark.

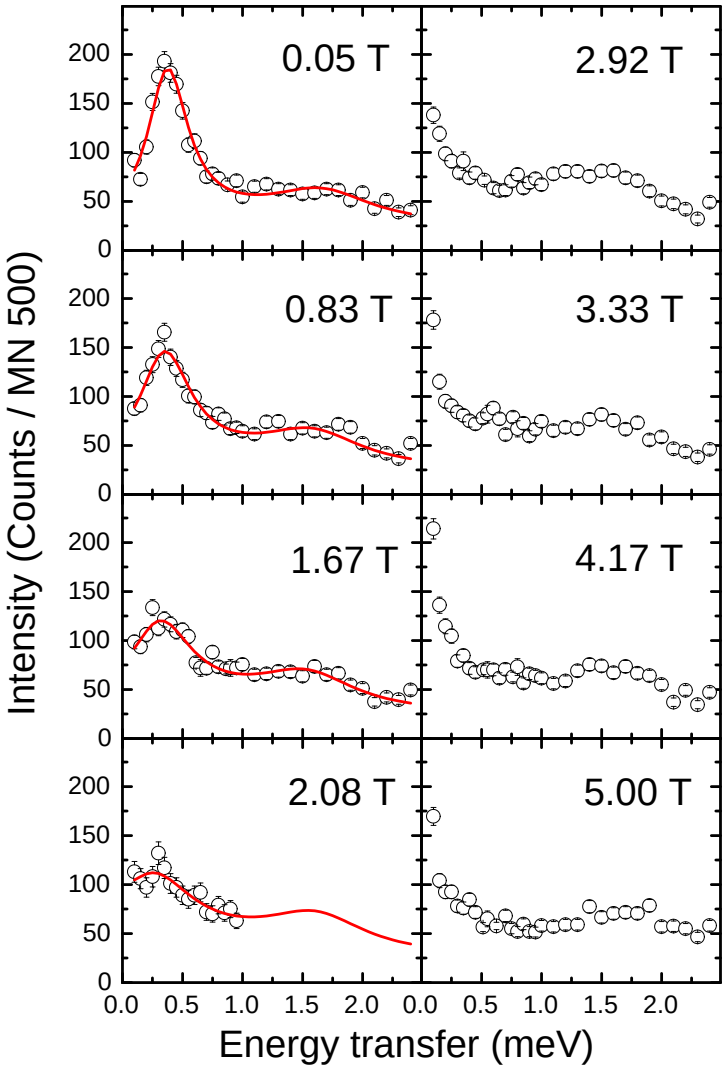

Figure 6.18: The inelastic response of UPd_2Al_3 at $\mathbf{Q} = (0\ 0\ 0.5)$ at 0.3 K, as a function of magnetic field, measured on IN14. The fits are described in the text.

Please purchase PDF Split-Merge on www.verypdf.com to remove this watermark.

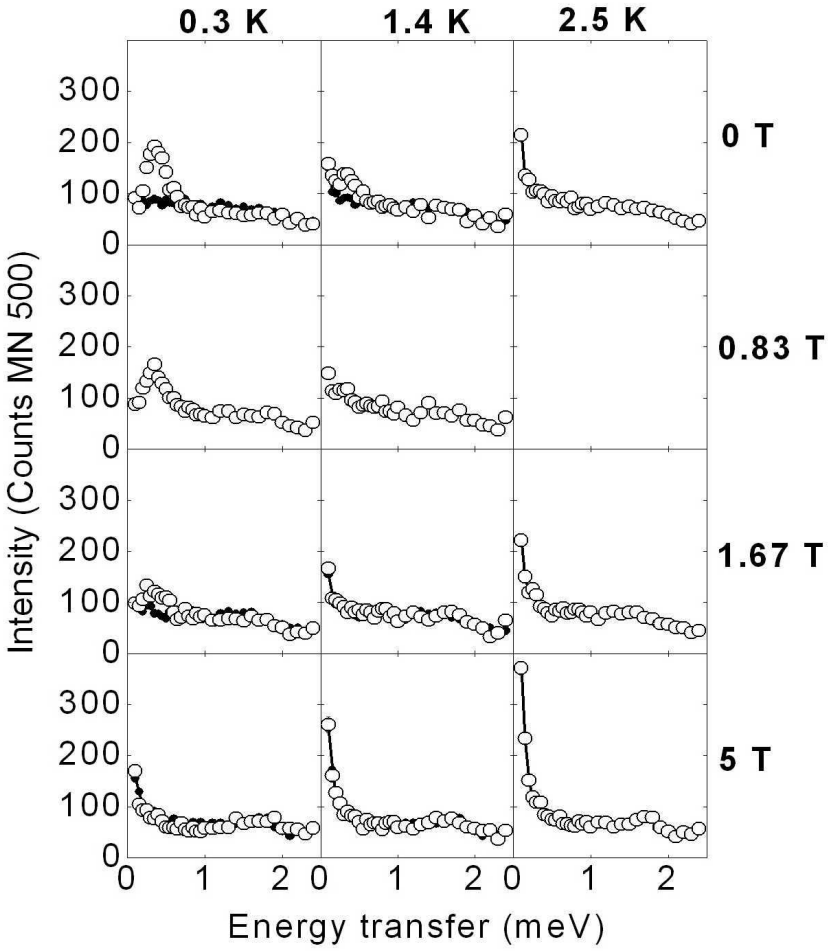

Figure 6.19: Inelastic response measured at $\mathbf{Q}$ = (0 0 0.5) on IN14. The open points are the raw data as measured under the conditions given in the panel rubric. The closed points (smaller than the open points) in selected panels are the raw data measured at 2.5 K, adjusted using a Bose temperature scaling to the value expected at 0.3 K / 1.4 K. In each case, the line represents the best estimate of the normal antiferromagnetic state response. This data was measured at k_f = 1.15 Å^{-1}. The error bars are smaller than the point size. [The lowest field measured was 0.05 T, to prevent the aluminium sample holder becoming superconducting, and help maintain a low temperature in the dilution insert.]

Please purchase PDF Split-Merge on www.verypdf.com to remove this watermark.

Analysis

The normal state data taken at 2.5 K was scaled using a Bose temperature factor to give the best estimate of the expected normal state antiferromagnetic response for a given applied field at 0.3 K / 1.4 K. At the higher end of the magnetic field range at 0.3 K and 1.4 K the system is in the normal state and the measured response overlays perfectly with the extrapolated data. The increase in the quasielastic strength at 5 T relative to 0 T is a physical increase and confirms the behaviour of the normal state described earlier in Section 6.5.1. This response changes on applying a given magnetic field.

It is clear that the inelastic pole at 0.35 meV is associated with the superconducting state. It diminishes in intensity as the boundary of the superconducting state, and the quasielastic response becomes visible. There is some overlap between the two (e.g. 2.08 T at 0.3 K; 0 T at 1.4 K) and the resolution of IN14 is not good enough to establish what is present at the lowest temperatures.

For the normal state responses, with a large quasielastic component, the fitting described in Section 6.5.1 can be carried out and is consistent with the results given in Section 6.5.1. Here, the focus is on the superconducting state, where the Fermi-liquid paradigm no longer applies, and so the $\Gamma_1 = C\chi_1^{-1}$ rule cannot be used in any case. The intensity was calculated in the same manner as in Section 6.5.1 using an input susceptibility assumed to consist of two inelastic poles, both described using damped harmonic oscillators. No quasielastic scattering was included, although at, for example, 2.08 T, it is evident that such a component is present. The other inelastic pole, diminished in intensity due to the different scattering vector (0 0 0.5), was assumed to be fixed in amplitude (46.2 arbitrary units) and linewidth (0.559 meV). The position is known to vary, but by very little over this field range, so this is justified. A λ of 0.04 was used and 25 counts of flat background were deducted. The intensity of the χ_1 inelastic pole was kept constant (56 arb. units) and the energy linewidth and position allowed to vary. The centre of mass of the inelastic pole is related to the width of the excitation (Figure 6.20), but there are not enough data points to establish the functionality concretely. In Figure 6.20, a simple linear fit is shown. The actual values obtained are given in Table 6.1.

Magnetic field (T)	Centre of mass (meV)	HWHM (meV)
0.05	0.351 ± 0.008	0.265 ± 0.009
0.42	0.317 ± 0.015	0.312 ± 0.011
0.83	0.315 ± 0.012	0.325 ± 0.011
1.25	0.278 ± 0.014	0.327 ± 0.014
1.67	0.267 ± 0.019	0.384 ± 0.014
2.08	0.21 ± 0.07	0.45 ± 0.15

Table 6.1: The centre of mass and half-width half-maximum of the inelastic pole seen in the superconducting state, as obtained from fits described in the text. These values are plotted in Figure 6.20.

The apparent broadening of the inelastic pole may be an indication of quasielastic

Please purchase PDF Split-Merge on www.verypdf.com to remove this watermark.

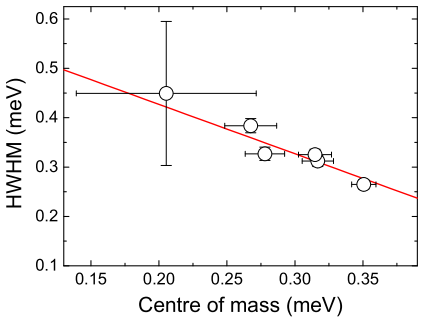

Figure 6.20: The half-width half-maximum of the inelastic pole associated with the superconducting phase as a function of its centre of mass. The points and appropriate field values are given in Table 6.6.1. Above 2.08 T, the presence of quasielastic scattering made the fit unusable. The line is of the form $y = mx + c$ where $c = 0.627$ meV and m was fixed at -1.

scattering; in the 2.08 T scan (Figure 6.18) there is clearly a quasielastic component, which distorts the fit used by broadening the model inelastic peak. From this it is not clear what the bare width of the pole is, and how much broadening might originate from the quasielastic components at $\boldsymbol{Q}_0$. To pin down exactly what is happening in the superconducting state, and in particular to find out if there is any quasielastic scattering left deep inside the superconducting phase, the neutron spin-echo technique was used, to take advantage of the extremely high energy resolution available from Larmor tagging the neutrons.

6.6.2 Neutron spin-echo study

The neutron spin-echo technique (see Section 2.6.4) offers a unique approach to this problem, because of the extremely high energy resolution available from Larmor tagging the neutrons. However, this method has rarely been applied to magnetic studies in single crystals because of several experimental difficulties.

Experimental details

In UPd_2Al_3 the region of interest is the antiferromagnetic zone centre $\boldsymbol{Q}_0$. For this reason a single crystal was used to focus on the relevant positions in momentum space. Elastic magnetic scattering from a single crystal will take place for a given crystal orientation only, and this effectively monochromatizes the scattered beam, which impinges on the detector at a relatively well defined angle. This allows the majority of the elastic intensity at $\boldsymbol{Q}_0$ to be separated from the quasielastic scattering close to $\boldsymbol{Q}_0$ by simply rotating the sample whilst maintaining a fixed scattering angle 2θ (a rocking scan).

The neutron spin echo spectrometer IN11A at the Institut Laue-Langevin (ILL), Grenoble, was used. The incident wavelength was set to 5.5 Å using a velocity selec-

Please purchase PDF Split-Merge on www.verypdf.com to remove this watermark.

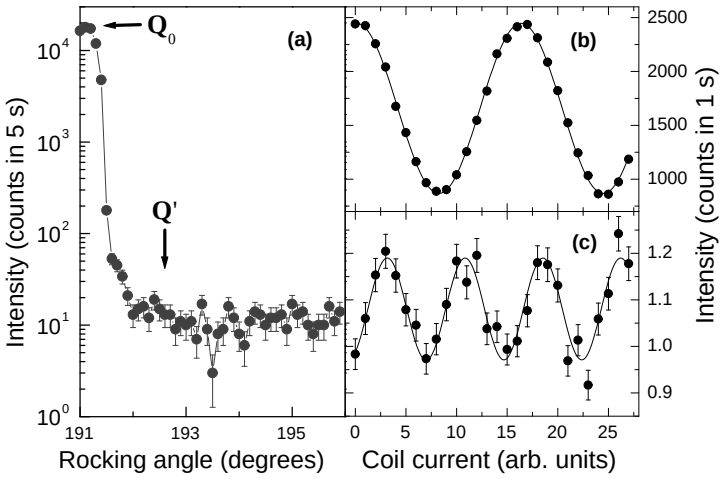

Figure 6.21: (a) Intensity observed on rotating the sample at a fixed scattering angle 2θ corresponding to the (0 0 0.5) magnetic Bragg peak at $T = 50$ mK. The arrows indicate the positions of the echo groups measured as a function of coil current at (b) $\boldsymbol{Q}_0$ = (0 0 0.5) with 5 s per point and (c) $\boldsymbol{Q'}$ = (0.015 0 0.5) with 15 minutes per point. The intensities are normalized to counts per second. The abscissa values of the coil current were chosen to illustrate different numbers of periods in the two cases (see text).

tor with a 16% spread. Using the lattice parameter measured independently for this sample at 50 mK, the wavelength selected by the crystal was found to be 5.52 Å. The first magnetic zone centre at (0 0 0.5) was selected for study, as a low 2θ angle reduces the overlap of the magnetic fields in the two arms of the spectrometer. A 2D detector with an angular coverage of 0.9 × 0.9 degrees was used.

Figure 6.21a shows the neutron scattering intensity observed in a rocking scan about the magnetic peak at $\boldsymbol{Q}_0$. On this basis an angular position 1.5° away from the Bragg peak, as indicated by the arrow in the figure, was selected to look for quasielastic scattering. This sample orientation corresponds to $\boldsymbol{Q'}$ = (0.015 0 0.5). From the previous three-axis spectroscopy results it is known that this position is sufficiently close to the magnetic zone centre to see a quasi-elastic signal at $T = 2$ K [102, 103].

By altering the magnetic field slightly in one arm, $\Delta\phi$ is shifted away from zero, and oscillations in P_{NSE} are observed. By altering the magnetic field, several periods over such *echo groups* were measured at a selection of Fourier times, at both the Bragg peak (Fig. 6.21b) with 5 s per point and $\boldsymbol{Q'}$ (Fig. 6.21c) with 15 minutes per point. Usually, the echo group amplitude and phase are established by a simple four-point measurement (of a maximum, minimum and two points in between). As the neutron phase is known, this is accurate, but because of the weakness of the signals here, we measured over several periods of the echo. By measuring more than one period, the existence of a real echo and the correct measurement of the amplitude was ensured, even considering the high sensitivity of the system to small changes in the magnetic field and the signal size at $\boldsymbol{Q'}$. The echo groups appear to have no envelope as the single crystal sample monochromatizes

Please purchase PDF Split-Merge on www.verypdf.com to remove this watermark.

the beam, so the echo groups could be fitted as simple sine waves to obtain the amplitude. At the Bragg peak, 45 point echoes were measured, covering 3 periods. An unexpected second wavelength was observed in the response for the smaller echo times. This was caused by the high beam monochromatization by the Bragg peak and the way that the neutron spin is flipped in magnetic neutron spin-echo. More details are given in Appendix 6.A. This would not have been spotted using the four-point method. At $\boldsymbol{Q}'$, a variety of different point numbers and periods were measured, in an attempt to find the best compromise with respect to time and accuracy.

Results

The amplitude of an echo group is a measure of the scattering fulfilling the echo condition at a particular Fourier term and so, after instrumental effects have been removed, is proportional to the intermediate scattering function $S(\boldsymbol{Q}, t)$. At $\boldsymbol{Q}_0$, the Bragg peak, echo groups were measured at 52 Fourier times, giving an amplitude $I(\boldsymbol{Q}_0, t)$ (Fig. 6.22a). This was normalized using an estimate of the magnetic scattering integrated over all energy, $I(\boldsymbol{Q}_0, 0)$, obtained using xyz polarization. Assuming that the signal $I(\boldsymbol{Q}_0, t)/I(\boldsymbol{Q}_0, 0)$ at $T = 50$ mK is generated by a *static* Bragg peak ($S(\boldsymbol{Q}_0, t)/S(\boldsymbol{Q}_0, 0) = 1$) it is justified to attribute observed deviations from 1 to instrumental resolution effects. This is the best estimate available of the spectrometer resolution as the standard resolution samples do not have the correct geometry and so the scattered beam would experience quite different magnetic field gradients to that from the UPd_2Al_3 sample used. These data are therefore used as a resolution correction for data measured at $\boldsymbol{Q}'$. At $\boldsymbol{Q}'$ a selection of Fourier times was examined in the superconducting state at 50 mK, in the antiferromagnetic state at 2 K, and in the paramagnetic state at 15 K (Fig. 6.22b). The data are normalized to $S(\boldsymbol{Q}', 0)$ and also corrected for resolution by normalization to the data taken at $\boldsymbol{Q}_0$.

Analysis

To analyse further the observed scattering function $S(\boldsymbol{Q}', t)$ as a function of Fourier time t we suppose that at all temperatures there is a superposition of a quasielastic (relaxing) signal with a static t-independent component (resulting from the tail of the Bragg peak and/or some instrumental background). In the simplest possible approach, assuming one clear relaxation path, the quasielastic scattering can be modelled as an exponential response (Eq. 2.53).[1] This is reinforced by the apparent observation of a quasielastic signal with a Lorentzian lineshape on three-axis spectrometers (Section 6.5.1). The data at $\boldsymbol{Q}'$ have therefore been fitted as

$$S(\boldsymbol{Q}', t)/S(\boldsymbol{Q}', 0) = y_0 + (1 - y_0)\exp(-\Gamma t) \tag{6.9}$$

where y_0 represents normalized background scattering and any static magnetic scattering (the tail of the magnetic Bragg peak). This function is constrained to be ≤ 1 for $t >$

[1] The simple exponential response is not exact in the low-temperature limit but nonetheless this fitting process provides a useful test for the presence of any dynamics.

Please purchase PDF Split-Merge on www.verypdf.com to remove this watermark.

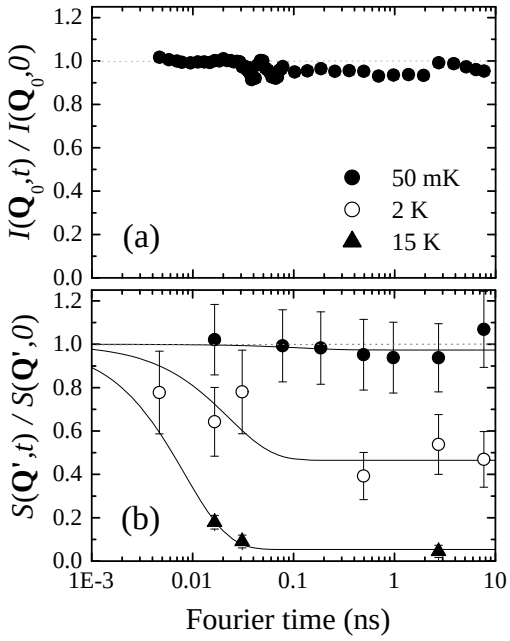

Figure 6.22: (a) Momentum and time-dependent intermediate scattering function $I(\boldsymbol{Q}_0, t)$ normalized to $S(\boldsymbol{Q}_0, 0)$ as a function of Fourier time at 50 mK (closed circles). (b) Momentum and time-dependent intermediate scattering function $S(\boldsymbol{Q'}, t)$ normalized to $S(\boldsymbol{Q'}, 0)$ and corrected for resolution using the measurements in panel (a) as a function of Fourier time at 50 mK (closed circles), 2 K (open circles) and 15 K (open triangles). The fits are described in the text. The dashed lines mark $S(\boldsymbol{Q}, t)/S(\boldsymbol{Q}, 0) = 1$.

0. This is reasonable if all dynamic scattering is included in $S(\boldsymbol{Q'}, 0)$ and a simple exponential is assumed. Neutron spin-echo cannot distinguish between neutron energy loss and neutron energy gain, and so the detailed balance factor will distort the exponential. For simplicity, this effect is ignored. The energy integration of $S(\boldsymbol{Q'}, 0)$ is limited by the instrumental transmission, and is estimated to cover the range from $\sim$ 2 meV neutron energy loss to $\sim$ 6 meV neutron energy gain, and so the major part of the quasielastic signal should be included. The fitted Γ and y_0 values are given in Table 6.2, with the measured $S(\boldsymbol{Q'}, 0)$.

At 2 K and 15 K, the scattering function clearly relaxes with t. At 15K, there is $\sim$ 8 times more dynamic scattering than at 2 K. The widths Γ obtained in the fits are of a similar order of magnitude to those observed at $\boldsymbol{Q}_0$ in Section 6.5.1. Values away from $\boldsymbol{Q}_0$ were calculated by Bernhoeft *et al.* [103] from three-axis data, and are the same order of magnitude as those found in here. This is reasonable considering the model dependencies and simplification in the analysis assumed in both the three-axis and spin-echo data.

The remanent static contribution y_0 at 15 K is attributed to background magnetic scattering. In the ordered state, the static signal is higher than this background level, and the most likely cause is contamination by the Bragg peak.

Please purchase PDF Split-Merge on www.verypdf.com to remove this watermark.

In the superconducting ordered state at 50 mK, the data suggests a constant $S(\boldsymbol{Q'},t)/S(\boldsymbol{Q'},0) = 1$, indicating that the scattering is purely static. This is supported by the quantitative fit: if an exponential fit is forced, the $y_0 \cdot S(\boldsymbol{Q'},0)$ given in the table is obtained, but no viable relaxation time can be extracted. The value of the static component $y_0 \cdot S(\boldsymbol{Q'},0)$ is, within statistical error, the same at 2 K and 50 mK; hence originating from the Bragg peak. Though a quasielastic component cannot be categorically eliminated, the maximum possible intensity would be 0.019 ± 0.025 counts per second, with an energy linewidth < 0.036 meV at $\boldsymbol{Q'}$.

We therefore conclude that *quasielastic scattering is absent deep inside the superconducting state* and any magnetic scattering observed on the timescales accessible by IN11 is static and results from the Bragg peak. Furthermore, at 50 mK there are no dynamics on shorter timescales than those measured here, indicating that there is no low temperature transition.

Our results allow us to interpret previous high-resolution diffraction experiments [77] which found a 1 % decrease in the observed scattering intensity on crossing below T_{sc}. Based on the spin-echo data presented here, we attribute those changes to the modification of the magnetization dynamics.

6.6.3 General discussion

The spin-echo results presented here were taken at $\boldsymbol{Q'}$, sufficiently close to $\boldsymbol{Q}_0 = (0\ 0\ 0.5)$ to probe the magnetic response possessing this (antiferromagnetic) periodicity. They can only be understood in the context of the electronic structure, and so the two principal model will be discussed here. First, however, before this can be assessed correctly, the order parameter must be considered, as this describes the way in which the condensate develops.

The superconducting order parameter

By probing the tunnelling conductivity of thin film superconducting junctions, Jourdan, Huth and Adrian [54] found a maximum superconducting gap energy of $\Delta = 235$ μeV at $T = 0$ K. The inelastic pole at 0.35 meV ($\sim 2\Delta$) is therefore thought to be generated by excitations across the energy gap out of the condensate. In this case, its presence at a position with antiferromagnetic symmetry indicates that the gap is periodic, and therefore has a wavevector dependence. This is crucial in understanding the neutron

	Γ (meV)	$S(\boldsymbol{Q'},0)$ (counts.s^{-1})	$y_0 \cdot S(\boldsymbol{Q'},0)$ (counts.s^{-1})
50 mK	–	0.108 ± 0.015	0.105 ± 0.017
2 K	0.18 ± 0.12	0.185 ± 0.035	0.086 ± 0.019
15 K	0.496 ± 0.076	0.854 ± 0.059	0.046 ± 0.021

Table 6.2: Γ and $y_0 \cdot S(\boldsymbol{Q'},0)$ values, obtained as described in the text, with the measured $S(\boldsymbol{Q'},0)$.

Please purchase PDF Split-Merge on www.verypdf.com to remove this watermark.

response. If the inelastic response *is* from the condensate, then $\Delta(k + \boldsymbol{Q}_0)$ must be the negative of $\Delta(\boldsymbol{k})$ over a sizable portion of the Brillouin zone. The observed scattering suggests a spatially anti-symmetry form for Δ:

$$\Delta(\boldsymbol{k}) = -\Delta(\boldsymbol{k} + \boldsymbol{Q_0}). \tag{6.10}$$

This gap can have either even or odd symmetry (a sum of cosines or sines respectively). As the gap wavevector dependence has to be imposed on top of the Fermi surfaces, the nature of the gap function is very important in understanding the electronic excitations. Several investigations of the gap symmetry have been carried out: (i) studies of the upper critical field in thin films found that the gap should have even symmetry, as the critical field decreased initially for all applied field directions [114]; (ii) angular-resolved magnetothermal transport measurements by Watanabe *et al.* [96] on a thin film found strong evidence for a single line node orthogonal to the c axis, and (iii) Oppeneer and Varelogiannis [94] have carried out self-consistent calculations and find that the gap equation has even symmetry. We therefore conclude that the gap has even symmetry, with a cosine-like form modulated in the c^* direction. It shall be shown that the inelastic neutron scattering data concurs with this assessment.

The mediator

In the same tunnelling experiments by Jourdan, Huth and Adrian [54], an anomaly was observed at 1.22 meV. In strongly coupled superconductors such as lead, a similar anomaly has been observed brought about by the interaction of the phonon density of states with the superconducting energy gap. It has therefore been proposed that this anomaly is a signature of the mediator in a strongly coupled superconductor. In UPd_2Al_3 the only excitation close to this energy is the dispersive inelastic part of the excitation spectrum at $\sim$ 1.5 meV. Jourdan, Huth and Adrian therefore suggested that this (magnetic) excitation might mediate the superconductivity. A full theory has been developed by Thalmeier and co-workers [76, 106], working in the dual model. In this approach, only the 'cylinder' Fermi sheet, being the purest $5f$ sheet, is used to develop the superconducting state.

We now return to the discussion of the electronic structure in the two models.

The itinerant model

The *itinerant* model assumes that all of the $5f$ electrons are delocalized. Figure 6.23a is an idealized sketch of the principal Fermi sheets as described by Knöpfle *et al.* [92]. As this sketch shows, the system has an instability with respect to the momentum transfer $\boldsymbol{Q}_0 =$ (0 0 0.5). This is seen for all of the illustrated surfaces; the 'cylinder' is in fact corrugated (see Figure 6.4), and so nesting of an appropriate vector is possible. Applying the caliper set by $\boldsymbol{Q}_0$, it is clear that - contrary to the other surfaces - the 'egg' sheet presents a high density of states (nesting). We therefore assume that the magnetic response as seen by inelastic neutron scattering arises from the 'egg' surface.

Please purchase PDF Split-Merge on www.verypdf.com to remove this watermark.

The dispersive inelastic feature in the antiferromagnetic normal state is anisotropic, with a much steeper dispersion in the c^* direction than in the a^* direction. The quasielastic scattering is also anisotropic, with shorter-range length correlations along the c^* direction than along the a^* direction. The stiffness of a dispersion can be related to the effective mass of the electrons, and is dependent on the Fermi surface topology. Bernhoeft [107] concluded that the 'egg' sheet was the only one in Knöpfle's model with the correct anisotropy in momentum space to fit the dispersion of the inelastic response.

The anisotropy of the observed quasielastic scattering indicates longer-range length correlations in the basal plane, and thus a softer magnetic basal plane (Section 6.2.3). Knöpfle *et al.* calculated the anisotropy of the magnetic susceptibility for their three sheets, and found that the 'egg' and the 'party hat' have the necessary anisotropy. As the quasielastic scattering is strongly coupled to the dispersive inelastic response, it therefore seems probable that 'egg' sheet is responsible for the observed magnetic inelastic response.

On entering the superconducting state, a superconducting energy gap opens as defined by the gap function $\Delta(\boldsymbol{k})$. It is known to have a wavevector dependence [102] with even symmetry [94, 96, 103, 114]. To illustrate this, a trapezoidal gap function is used in Fig. 6.23. This may be an oversimplification and a limited sum of cosines is the more likely form [94]. With such a gap function the 'egg' is completely gapped at low temperatures; there are no nodes. This is consistent with the observed absence of quasielastic scattering deep inside the superconducting state. Although the order parameter is unconventional, there are no normal quasiparticles on the 'egg' part of the Fermi surface in equilibrium with the condensate at low temperatures. Nevertheless, the order parameter does change sign.

If the gap function (a sum of cosines) decreases as the temperature is increased, then the 'egg' surface would start to generate quasielastic scattering at $\boldsymbol{Q}_0$ before passing through T_{sc}, thus explaining the behaviour near the superconducting phase boundary. This has indeed been observed in three-axis neutron spectroscopy (Figure 6.18). The itinerant model is therefore sufficient to explain all of these observations. As an aside, if the gap *did* have odd symmetry, both the 'cigar' and 'egg' would be completely gapped, and only the 'cylinder' would then have nodes. On heating, the 'egg' would remain gapped right up to T_{sc}. It is therefore safely eliminated as an option.

The dual model

In the *dual* model the $5f$ electrons are split into two electronic subsystems - a localized $5f^2$ ground state, and an itinerant third $5f$ electron. Considering the purely itinerant contribution in this model first, Fig. 6.23b is an idealized sketch of the Fermi surface calculated by Zwicknagl *et al.* [95]. The 'ellipsoid' replaces the 'egg', and for an even parity energy gap function, all of the arguments given above apply to the 'ellipsoid'. The stiffness in the c^* direction would be unaffected by a shift in the Fermi energy of 40 K, but would alter dramatically along the a^* direction (Figure 6.5c). The 'cigar' equivalents are here assumed to have similar anisotropy to that observed in the Knöpfle model, although this is not specified in the paper by Zwicknagl *et al.* The only difference is that the 'ellipsoid' will remain completely gapped right up to T_{sc}. If the gap were

Please purchase PDF Split-Merge on www.verypdf.com to remove this watermark.

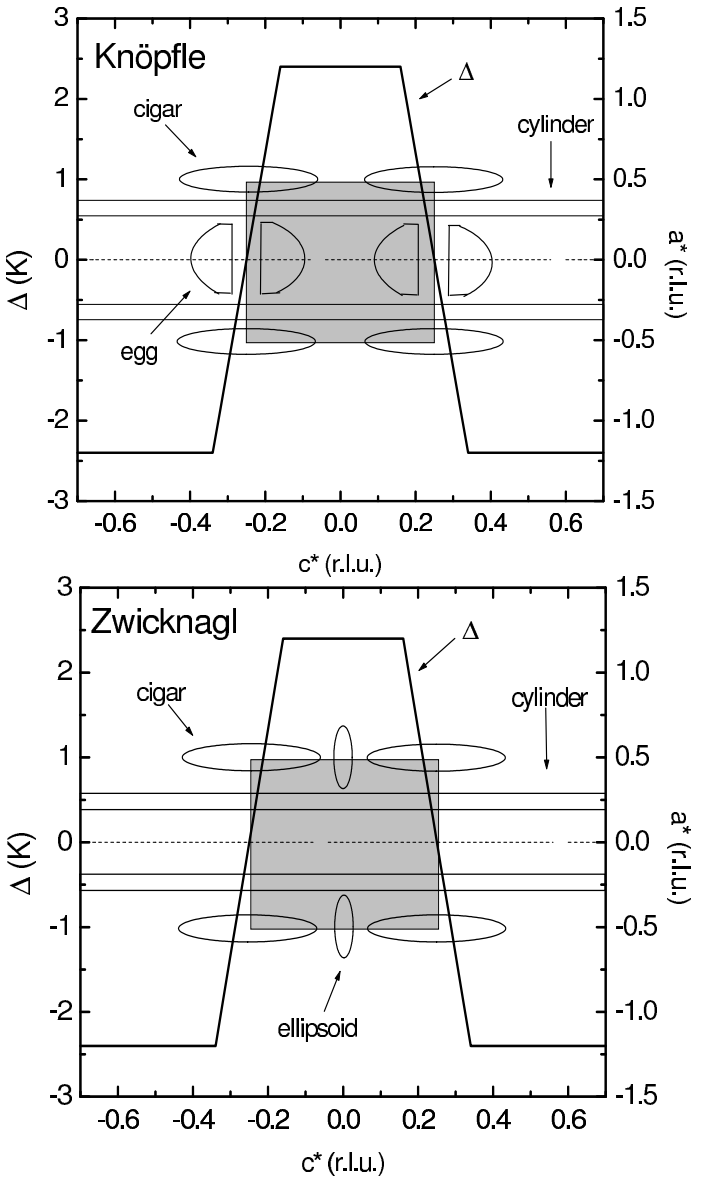

Figure 6.23: The panels superpose, on a common c^* axis, an even parity energy gap function (left-hand ordinate) and schematics of (a) the itinerant model Fermi sheets [92] and (b) the dual model Fermi sheets [95]. In both cases, the 'party hat' sheet is omitted. The grey area marks the first Brillouin zone. Based on Fig. 4 from Ref. [107].

Please purchase PDF Split-Merge on www.verypdf.com to remove this watermark.

odd, the 'ellipsoids' would always contain a node. At this point we note that if the superconductivity in this material were mediated by spin fluctuations [54, 75], it would have to be generated by fluctuations from either the 'egg' or 'ellipsoid' surfaces.

Moving now to the other part of the dual model, the localized $5f^2$ states are assumed to dominate the magnetic properties, which are described by a crystalline electric field (CEF) scheme. In the normal state, the quasielastic scattering seen at $\boldsymbol{Q}_0$ is generated when the ground state is broadened via coupling with the itinerant conduction electrons.

In the superconducting state, the gap develops, condensing most of the itinerant electrons. Given our spin-echo results, within this model it might be assumed that this has the effect of sharpening the ground state signal, eliminating the quasielastic signal at low temperatures and $\mathbf{Q_0}$. However, some coupling mechanism must still be active, to renormalize and broaden the CEF excitation at 1.4 meV. At the gap nodes, the itinerant electrons are in energetic equilibrium with the condensate, and those could still broaden the ground state. Therefore no quantitative microscopic mechanism is proposed here within the framework of this model.

Insight into the superconducting state

The above discussion has shown that the observed behaviour is fully consistent with the development of an even symmetry gap with a cosine-like form. The low-energy response deep inside the superconducting state is contained entirely in the low-energy inelastic response. Following the approach of Bernhoeft [107] the spin susceptibility of the excited quasiparticles below T_{sc} are considered. They are modified by the effects of (i) superconducting phase coherence and (ii) the presence of a gap in the excitation spectrum of the condensate. The susceptibility is calculated as $\chi_1 = \chi_n + \chi_c$, where χ_n is the normal (quasiparticle) component and χ_c the condensate component, assuming that it is generated solely by the itinerant component. A singlet ground state is assumed on the basis of thermodynamic, transport and tunnelling data [54, 72, 75, 89, 96]. The quasiparticle fraction is

$$\chi_n(\boldsymbol{q},\omega) = \sum_k \frac{1}{2}\left(1+\frac{\xi(\boldsymbol{k}+\boldsymbol{q})\xi(\boldsymbol{k})+|\Delta(\boldsymbol{k}+\boldsymbol{q})||\Delta(\boldsymbol{k})|\cos(\Phi(\boldsymbol{q})}{E(\boldsymbol{k}+\boldsymbol{q})E(\boldsymbol{k})}\right) \times\left(\frac{f(\boldsymbol{k}+\boldsymbol{q})-f(\boldsymbol{k})}{\omega-[E(\boldsymbol{k}+\boldsymbol{q})-E(\boldsymbol{k})]+i\Gamma}\right) \tag{6.11}$$

and the condensate fraction is

$$\begin{aligned}\chi_c(\boldsymbol{q},\omega) = &\sum_k \frac{1}{4}\left(1-\frac{\xi(\boldsymbol{k}+\boldsymbol{q})\xi(\boldsymbol{k})+|\Delta(\boldsymbol{k}+\boldsymbol{q})||\Delta(\boldsymbol{k})|\cos(\Phi(\boldsymbol{q})}{E(\boldsymbol{k}+\boldsymbol{q})E(\boldsymbol{k})}\right) \times\left(\frac{1-f(\boldsymbol{k}+\boldsymbol{q})-f(\boldsymbol{k})}{\omega-[E(\boldsymbol{k}+\boldsymbol{q})+E(\boldsymbol{k})]+i\Gamma}\right) \\ &-\sum_k \frac{1}{4}\left(1-\frac{\xi(\boldsymbol{k}+\boldsymbol{q})\xi(\boldsymbol{k})+|\Delta(\boldsymbol{k}+\boldsymbol{q})||\Delta(\boldsymbol{k})|\cos(\Phi(\boldsymbol{q})}{E(\boldsymbol{k}+\boldsymbol{q})E(\boldsymbol{k})}\right) \times\left(\frac{1-f(\boldsymbol{k}+\boldsymbol{q})-f(\boldsymbol{k})}{\omega+[E(\boldsymbol{k}+\boldsymbol{q})-E(\boldsymbol{k})]+i\Gamma}\right)\end{aligned} \tag{6.12}$$

Please purchase PDF Split-Merge on www.verypdf.com to remove this watermark.

Each element is a summation over the Brillouin zone of a product of a superconducting phase coherence factor and a Lindhard-style function [115]. The χ_n fraction arises from scattering between quasiparticle levels, and χ_c, the condensate fraction, from the creation and condensation of quasiparticle pairs. $\xi(\boldsymbol{k}) = \epsilon(\boldsymbol{k}) - \epsilon_F$ is the quasiparticle energy relative to the normal state Fermi energy, and $E(\boldsymbol{k}) = \sqrt{\xi(\boldsymbol{k})^2 + |\Delta(\boldsymbol{k})|^2}$ is the quasiparticle excitation energy above the superconducting state. The factor $\Phi(\boldsymbol{q})$ is the phase difference between $\Delta(\boldsymbol{k})$ and $\Delta(\boldsymbol{k}+\boldsymbol{q})$.

At T_{sc} the observed susceptibility changes abruptly, and this must be due to the development of superconductivity as the magnetic moment does not change, indicating the the Fermi surfaces are not altered. The spatial symmetries expressed in susceptibilities given above should not change, so the changes must have one of two origins: (i) changes in the two normal state components of χ, and possibly the coupling constant λ, and (ii) excitations out of the superconducting ground state.

In case (i), the cross-section is generated by quasiparticle-hole excitations from the normal state, subject to the phase coherence constraints of the superconducting state (the coherence factor in the equations above). To have significant spectral weight at $\boldsymbol{Q}_0$ nodes commensurate with $\boldsymbol{Q}_0$ on sheets of the Fermi surface with a significant density of states are required. Such a situation is energetically unfavourable and at odds with the data presented here and the available tunnelling data and angular-resolved thermal conductivity measurements [54, 96].

In case (ii), the response is dominated by the condensate response. This picture is supported by the apparent absence of quasielastic scattering in the superconducting condensate at low temperatures and the analysis of the Fermi surfaces with respect to the neutron scattering data given above, as well as the dramatic fall in the heat capacity at temperatures well below T_{sc} [72], signalling a loss of normal state quasiparticle excitations to the susceptibility, due to the opening of a gap on the strongly correlated sheets with a high density of states of the quasiparticle Fermi surface.

The coherence function acts in the opposite sense on the normal and condensate fractions. This excludes simultaneous enhancement of both the quasiparticle-hole contribution and the condensate fraction in the neutron scattering cross-section. To be explicit, at low temperatures, excitations of the condensate are restricted to quasiparticle states lying close to the Fermi surface ($1 - f(\boldsymbol{k}+\boldsymbol{Q}_0) - f(\boldsymbol{k}) \approx 1$) with the normal quasiparticle contribution to the bare susceptibility becoming progressively weaker on lowering the temperature. For excitations of minimal energy, the quasiparticle excitation energies are $\xi(\boldsymbol{k}) = \xi(\boldsymbol{k}+\boldsymbol{Q}_0) = 0$, and so the phase coherence term reduces to $1 \pm \cos(\Phi(\boldsymbol{Q}_0))$ for the normal and condensate fractions respectively. For a significant condensate response at wavevector $\boldsymbol{q}$, $\Delta(\boldsymbol{k}+\boldsymbol{Q}_0)$ must be the negative of $\Delta(\boldsymbol{k})$ over a sizable portion of the zone. As (enhanced) *inelastic* scattering is observed in the superconducting phase at the antiferromagnetic zone centres, we infer that the dominant contribution arises from the condensate. The condensate, in turn, is gapped, with $\Delta(\boldsymbol{k})$ displaying sign inversion on translation by $\boldsymbol{Q}_0$ over a major part of the zone. The observed scattering suggests the spatially anti-symmetric form of Δ given in Equation 6.10.

If the necessary symmetry is imposed $\Phi(\boldsymbol{Q}_0) = \pi$, and so for the normal fraction of the response $1+\cos(\Phi(\boldsymbol{Q}_0)) = 0$. The coherence factor eliminates normal state scattering

Please purchase PDF Split-Merge on www.verypdf.com to remove this watermark.

at the antiferromagnetic zone centre, leaving only the signature of the coherent superconducting state. In models with either no spatial periodicity or a periodicity matching the chemical lattice, the phasing enhancement from the coherence factor will be reversed. In such cases the coherence factor will give rise to a Hebel-Slichter peak in nuclear magnetic resonance experiments, as this probes $\boldsymbol{Q} = 0$. The susceptibility amplification is in that case a maximum for the gapless quasiparticle excitations from the normal fraction, and small for excitations from the condensate.

The most important aspect in all of this is the introduction of the energy gap in the denominator in the expression for χ_c (Equation 6.12). The normal state quasiparticle response does not acquire the corresponding gap, and is expected to remain quasielastic in form below T_{sc}. From the arguments above, it can therefore be neglected. In the itinerant model, the energy gap is easily introduced - the Fermi surfaces are affected directly. In the dual model, the mechanism is less clear. Sato *et al.* [75] claim that the normal quasiparticle excitations appear to be responsible for the inelastic pole in question, and the energy gap is inserted by hand. The mechanism for this is not made explicit, but the observed pole is held to be a measure of $\Delta(\boldsymbol{k})$, subject to a strong coupling renormalisation in position and width with a CEF excitation.

Conclusions

Inelastic neutron scattering is therefore able to contribute to our understanding of the superconducting order parameter, although no further information on the nature of the mediator has been obtained. It seems clear that the inelastic pole at ~ 0.35 meV is cause by excitations out of the superconducting condensate, and that the order parameter has even symmetry.

Please purchase PDF Split-Merge on www.verypdf.com to remove this watermark.

6.7 Summary

A series of inelastic neutron scattering experiments have been carried out on UPd_2Al_3. The normal antiferromagnetic and paramagnetic states were investigated, and found to display Fermi-liquid-like behaviour in external magnetic fields up to 15 T. The quasielastic signal increases in intensity dramatically at 4 T, before dying away at higher fields. This is attributed to the moment transition induced at 4.2 T. The external magnetic field also led to a shift in the dispersion of the 'high-energy' inelastic pole, and the excitation gap at the antiferromagnetic zone centre $\boldsymbol{Q}_0 = (0\ 0\ 0.5)$ (from 1.4 meV at 0 T to 2.5 meV at 15 T) was in accordance with the value expected from spin-wave theory. The rest of the dispersion was relatively unchanged.

Away from the magnetic zone centre, a broad, weak response was seen in all parts of the Brillouin zone studied at zero field as well as in high field. However, in high field, an additional response was seen at 4 meV, across the zone. Possible origins for this response are discussed.

At $\boldsymbol{Q}^* = (0.5\ 0\ 0.5)$ an inelastic excitation is seen at 2.5 meV. It is not affected by external magnetic fields up to 15 T, but in the paramagnetic state, it apparently becomes quasielastic. This is compared to the behaviour of UNi_2Al_3.

In the superconducting state, the renormalization of the inelastic response on exiting the superconducting phase was investigated. A neutron spin-echo experiment was carried out, and the high energy resolution available there revealed that deep inside the superconducting state, the quasielastic scattering is absent, within the experimental constraints. This observation is related to the calculated Fermi surfaces for this material, and the nature of the superconducting state is discussed.

Please purchase PDF Split-Merge on www.verypdf.com to remove this watermark.

6.A An unusual effect in neutron spin-echo from magnetic single crystals

6.A.1 Experimental observations

During the spin-echo measurements of the scattering function at the magnetic Bragg peak at $\boldsymbol{Q}_0 = (0\ 0\ 0.5)$, an unexpected second wavelength was seen at echo times < 36 ps. Ordinarily, an oscillation with a particular period is measured by altering $\Delta\phi$ by prescribed steps. This is achieved by changing the magnetic field in which the neutrons precess by small steps ΔB, which can be tuned to measure a particular number of points per period. Figure 6.24a is an example of such an oscillation from the Bragg peak at (0 0 0.5) taken at 78 ps. Figure 6.24b is the same measurement at 4.7 ps. An extra second wavelength has appeared. This wavelength has approximately half the frequency of the the ordinary echo group and the intensity of this new oscillation declines as the Fourier time is increased.

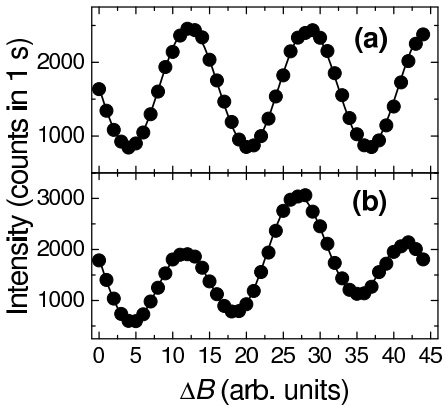

Figure 6.24: Sample echo groups measured at the Bragg peak (0 0 0.5). ΔB is the change in the magnetic field applied to the precessing neutrons. Each point was measured for 5 s, and then normalized to 1 s. The error bars are smaller than the point size. The x-axis is calibrated for the particular Fourier time to give ~ 3 periods in 45 points. (a) is an echo group measured at 78 ps. Over the measured range, it is a sine wave. (b) is an echo group measured at 4.7 ps. The fitted line consists of two sine waves.

For small Fourier times, the magnetic field in the spectrometer arms is small, and so the number of neutron precessions may be small, depending on the length of the arm. This can lead to a finite polarization remaining at the sample as the spins of neutrons with different velocities have not yet fanned out completely. On IN11, the 'small echo coil' setup is used in these cases. The coils used to generate the changes ΔB in the magnetic field are split and placed on both arms, so the precession angles before and after the sample are

$$\phi_1 = \gamma l_1 (B_1 + \Delta B_1/2)/v_1; \qquad \phi_2 = \gamma l_2 (B_2 - \Delta B_2/2)/v_2. \tag{6.13}$$

Please purchase PDF Split-Merge on www.verypdf.com to remove this watermark.

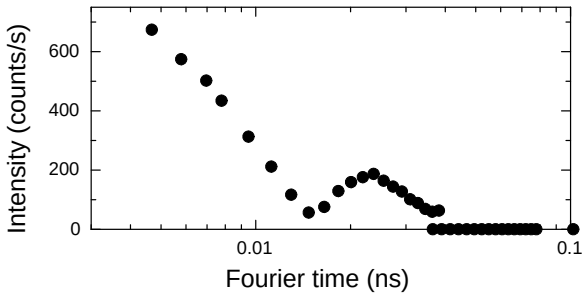

Figure 6.25: The intensity in counts per second of the second wavelength, observed at the magnetic Bragg peak position (0 0 0.5) as a function of Fourier time.

Usually, in the normal 'large echo coil' setup, ΔB is applied on the first arm only.

The second wavelength is only present when using the small echo coil setup on IN11, which is used for times below 38 ps in this experiment, and the large echo coil for times above 36 ps. There is some overlap, and this is clearly apparent when looking at the amplitude of the second wavelength (Figure 6.25).

6.A.2 The scattering process for a magnetic single crystal

This unexpected result is fundamentally a result of looking at magnetic scattering at a Bragg peak in a single crystal. In UPd_2Al_3 the moments all lie in the $a-b$ plane, and so at $\boldsymbol{Q}_0$, the scattering vector is always perpendicular to the magnetic signal. Assuming that all three of the possible magnetic domains in UPd_2Al_3 are present in equal quantities during the experiment, the magnetic correlations will be isotropic in the plane, and the case outlined in Section 2.6.4 is valid (normal paramagnetic NSE).

Figure 2.6 in Section 2.6.4 sketches out the effect of this magnetic scattering on the neutron spin. Part of the spin ($\boldsymbol{P}_{flipped}$) is effectively π flipped, and unwinds in the second arm to give an echo group at the detector when the field integral is changed, as described in Section 2.6.4. The other part, antiparallel to $\boldsymbol{P}_i$, does not meet the echo condition on precessing in the second arm.

If the incident wavelength distribution is large, there is a wide spread of neutron precession angles, and so at the sample the polarization appears white within its chosen plane. On integrating over all of the frequencies, only $P_{flipped}$ meets the echo condition and gives a signal at the detector. The other parts of the magnetic scattering simply add to the background.

The magnetic Bragg peak in a single crystal acts as a monochromator, and cuts the neutron velocity spread, and hence the spread of precession angles at the sample. For small Fourier times, the spread of precession angles may be significantly less than 2π at the sample. In the extreme case, there is only one wavelength, and hence a fixed precession angle. The π-flipped part of the signal behaves as expected. Because of the precession coils along the second arm, the other part continues to precess in the second

Please purchase PDF Split-Merge on www.verypdf.com to remove this watermark.

arm and arrives at the detector with a certain precession angle. When using the small echo coil, this precession angle is changed by $\Delta B/2$ during the measurement of the echo group. An additional signal will therefore be seen with an apparent frequency half that of the expected frequency, with the same intensity as the expected signal.

As more neutron velocities are included the spread of precession angles increases. The precession in the second arm then acts to disperse the spread of polarization at the detector, instead of amplifying it as at the echo condition and so the intensity of this signal drops as the Fourier time is increased. There will be a minimum when the range of precession angles covers 2π (complete cancellation), and then the intensity will increase again, but only to a limited value as a much smaller proportion of the spins do not cancel out. Assuming a 1% spread (hwhm) in the monochromated neutron wavelength, the range of precession angles covered at the smallest Fourier time will be 72°.

Normally, the phase of an echo group should be well defined, and consistent between measurements. For the second wavelength, the phase is dependent on the orientation of the polarization at the sample when $\Delta B = 0$. This is not a regular function.

This observation must be taken into account for all spin-echo experiments looking at a monochromating magnetic Bragg peak when the phase shift is induced by changing the field after the sample. The effect is easily eliminated if a full echo group is measured, so that the two frequencies can be extracted. The amplitude of the expected echo should then be used in further calculations. To illustrate the result if this is not done, the open points in Figure 6.26 are data taken at (0 0 0.5) in UPd_2Al_3 using the 4-point measurement method. The second wavelength cannot be extracted, and significantly perturbs the results. The closed points are taken from measurements made over more than one period, with the second spurious wavelength neglected. The 4-point method gives a characteristic extra scattering at small Fourier times. This is obviously spurious as it gives an (unphysical) $I(\boldsymbol{Q}_0, t)/I(\boldsymbol{Q}_0, 0)$ value greater than 1.

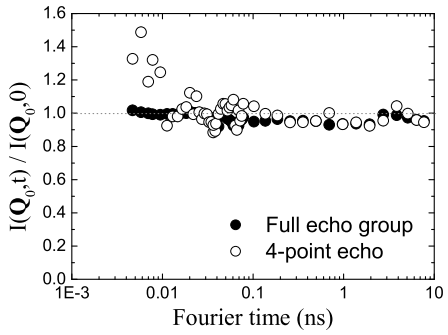

Figure 6.26: The momentum and time-dependent intermediate scattering function $I(\boldsymbol{Q}_0, t)$ normalised to $S(\boldsymbol{Q}_0, 0)$ as a function of Fourier time at 50 mK using the 4-point echo method (open circles) and the multiple-period echo method with the spurious wavelength ignored (closed circles).

Please purchase PDF Split-Merge on www.verypdf.com to remove this watermark.

Please purchase PDF Split-Merge on www.verypdf.com to remove this watermark.

Chapter 7

Conclusions and Perspectives

Please purchase PDF Split-Merge on www.verypdf.com to remove this watermark.

7.1 Conclusions

Inelastic polarized neutron studies of 3-$\boldsymbol{k}$ antiferromagnet UO_2

The 3-$\boldsymbol{k}$ magnetic state of UO_2 has been identified from polarization analysis of the spin-wave spectrum. Previously, the existence of a 3-$\boldsymbol{k}$ state had been suspected on the basis of indirect evidence, such as neutron diffraction carried out on artificially perturbed samples. The observed behaviour of the spin-waves is explained if the three magnetic propagation wavevectors of the 3-$\boldsymbol{k}$ state are considered coherently.

Diffraction from 3-$\boldsymbol{k}$ antiferromagnets

Continuing this theme, unexpected diffraction events are seen in cubic 3-$\boldsymbol{k}$ materials where the propagation wavevector is $\langle 00\frac{1}{2}\rangle$. This diffraction event is considered to be a sign of quantum correlations between the three coherent order parameters, and when this model is applied to the electronic orbitals of the U $5f$ electrons, it is shown to explain the apparent moment direction and form factor of this diffraction event.

The antiferromagnetic superconductor UPd_2Al_3

In UPd_2Al_3, the antiferromagnetic superconductor, the effect of magnetic field on the normal state (both paramagnetic and antiferromagnetic) has been mapped out. In the ordered state, the quasielastic signal at the magnetic zone centre increases in intensity dramatically at 4 T, before dying away at higher fields. This is attributed to the moment rotation induced at 4.2 T. The dispersive inelastic excitation at 1.4 meV behaves like a spin wave in an external magnetic field and shifts to higher energy transfers. Away from the magnetic zone centre, additional inelastic scattering is seen in a high applied magnetic field at ~ 4 meV in the parts of the Brillouin zone studied.

The low-energy inelastic magnetic response of UPd_2Al_3 contains a signature of the superconducting energy gap in the superconducting phase at the magnetic zone centre. This is the indication that the superconducting energy gap has the same symmetry as the magnetic lattice. Deep inside the superconducting state there is no quasielastic scattering at the magnetic zone centre, and this places serious constraints on the models of the superconductivity.

General

Understanding the interplay between multiple order parameters operating from the same electron system is an extremely interesting problem in modern condensed matter physics. If different types of order are generated from the same constituents, each type of order must respect the symmetry constraints imposed by the other types of order present. This is seen in the antiferromagnetic superconductor UPd_2Al_3, where the superconducting energy gap has the same symmetry as the antiferromagnetic lattice (and underlying Fermi surface). It is also seen in the 3-$\boldsymbol{k}$ magnetic structures studied here, where to fit

Please purchase PDF Split-Merge on www.verypdf.com to remove this watermark.

all three order parameters together, cubic symmetry is essential. This principle may be of use in understanding other mixed-order states.

7.2 Perspectives

Inelastic polarized neutron studies of 3-$\boldsymbol{k}$ antiferromagnet UO_2

The method outlined in Chapter 3 for examining the direction of the spin-wave fluctuations as a function of momentum transfer could easily be adapted to other (antiferromagnetic) materials. It would be interesting to use the method presented here on USb, to confirm the current theoretical picture. To see if this can be used to identify other types of multi-$\boldsymbol{k}$ structure, a 2-$\boldsymbol{k}$ structure with a sufficiently well-defined spin-wave spectrum would also be a possible candidate.

In addition to identifying multi-$\boldsymbol{k}$ structures, it would also be worthwhile to carry out experiments on materials with simpler magnetic structures, such as the archetypal antiferromagnet such as MnF_2 as the observations available provide extra information on the antiferromagnetic exchange.

Diffraction from 3-$\boldsymbol{k}$ antiferromagnets

Here, the next steps would be to look for $\boldsymbol{k}_3$ peaks in a non-actinide material, to illustrate the generality of the phenomenon. Such a material would have to have a magnetic unit cell larger than the nuclear cell, so that the $\boldsymbol{k}_3$ reflection does not coincide with a nuclear Bragg peak. One candidate is the cubic rare-earth antiferromagnet NdZn (propagation wavevector $\langle 00\frac{1}{2}\rangle$) [116]. In addition, for the form factor analysis, the key region of interest is the low $\boldsymbol{Q}$ regime; to investigate this area, one choice would be incommensurate 3-$\boldsymbol{k}$ materials. The solid solution $USb_{0.9}Te_{0.1}$ has $\boldsymbol{k} = \langle 00\frac{2}{3}\rangle$ [4].

The antiferromagnetic superconductor UPd_2Al_3

The results presented in Chapter 6, for both the normal and superconducting states, can be explained within the context of the itinerant model for the $5f$ electrons very easily. For the dual model to apply, certain aspects are not yet clear (the behaviour of the excitations under an applied field, and the low-energy response in the superconducting state), but the results here provide a series of constraints. The role of the scattering at $\boldsymbol{Q}^* = (0.5\ 0\ 0.5)$ is not yet understood, although it too appears to have an itinerant origin.

Please purchase PDF Split-Merge on www.verypdf.com to remove this watermark.

Conclusions

Études de la structure antiferromagnétique d'UO_2 par les neutrons polarisés

L'état 3-$\boldsymbol{k}$ d'UO_2 a été identifié par les particularités de ses ondes de spin. Avant, cet état 3-$\boldsymbol{k}$ a été postulé grace à des expériences indirectes, comme la diffraction neutronique sur des échantillons dans un champ magnétique. Les données ici sur les ondes de spin peuvent être expliquées seulement si les trois vecteurs de propagations sont considérés comme cohérents.

Diffraction par les structures 3-k antiferromagnétiques

Suivant cette thème, des pics de diffraction inattendus ont été observés dans les matériaux 3-$\boldsymbol{k}$ (ou $\boldsymbol{k} = \langle 0\ 0\ 1/2 \rangle$). Ces pics sont considérés comme la marque d'une corrélation quantique entre les trois vecteurs de propagation cohérents. Si ce modèle est appliqué aux orbitaux électroniques, des électrons $5f$ d'uranium, cela peut expliquer la direction effective du moment magnétique qui génère la diffusion, et le facteur de forme.

Le supraconducteur antiferromagnétique, UPd_2Al_3

L'effet d'un champ magnétique sur l'état normal (paramagnétique et antiferromagnétique) dans UPd_2Al_3 a été examiné. Dans l'état ordonné, la réponse quasiélastique au centre de la zone magnétique augmente rapidement à 4 T, et disparait dans les champs plus intenses. Il semble que ces phénomènes soient liés à la rotation des moments magnétiques à 4.2 T.

L'excitation dispersif à 1.4 meV agit comme une onde de spin dans un champ magnétique en bougeant aux transferts d'energie plus grands. Dans les autres parties de la zone magnétique dans l'espace réciproque, la diffusion inélastique augmente aux champs intensifs à ~ 4 meV.

La réponse inélastique au centre de la zone magnétique à petits transferts d'energie contient une signature du gap supraconducteur dans l'état supraconducteur. Cela indique que le gap possède la mme symétrie que le réseau antiferromagnétique. Aux températures les plus basses, il n'y a plus de diffusion quasiélastique au centre de la zone magnétique. Cette observation impose des limites sur les modéles de supraconductivité dans ce composé.

Général

L'interaction entre les paramètres d'ordre multiple dans le mme système électronique est une question intéressante dans la physique de la matière condensée. Les types d'ordre différents doivent respecter les contraintes symétriques imposées par eux-mêmes. Le gap supraconducteur dans UPd_2Al_3 est un bon exemple - il possède la mme symétrie que le réseau antiferromagnétique. Cela se voit également dans les structures magnétiques 3-$\boldsymbol{k}$, ou la symétrie cubique est essentielle. Ce principe peut être utile pour comprendre les autres états d'ordre mixte.

Please purchase PDF Split-Merge on www.verypdf.com to remove this watermark.

Perspectives

Études de la structure antiferromagnétique d'UO_2 par les neutrons polarisés

La méthode décrite en chapitre 3 pour sonder les fluctuations d'une onde de spin peut tre facilement adaptée aux autres composés (antiferromagnétiques). Il sera intéressant de poursuivre ces études sur USb pour confirmer la description donnée ici. Pour voir si on peut identifier d' autres états multi-k, il sera nécessaire d 'examiner un matériau 2-$\boldsymbol{k}$, par exemple ; mais il faut avoir des ondes de spin bien définies.

Il sera également une bonne prochaine étape d'étudier les structures magnétiques plus simples, comme le prototype MnF_2, pour voir si ces études offrent l'information complementaire sur l'échange antiferromagnétique.

Diffraction par les structures 3-$\boldsymbol{k}$ antiferromagnétiques

Ici, les prochaines étapes seraient de chercher pour les pics $\boldsymbol{k}_3$ dans un composé qui ne contient pas d' actinides, pour montrer que ce phénomène est général. Un tel matériau doit avoir une cellule magnétique plus grande que la cellule nucléaire pour que le pic $\boldsymbol{k}_3$ ne soit pas trouvé en-dessous un pic de Bragg nucléaire. Un candidat serait le composé cubique NdZn ($\boldsymbol{k} = \langle 0\ 0\ 1/2 \rangle$) [116]. En plus, pour l'analyse du facteur de forme, la région d'intérêt critique est la partie petit $\boldsymbol{Q}$. Pour sonder cette région, on aura besoin des matériaux incommensurables, par exemple $USb_{0.9}Te_{0.1}$ ou $\boldsymbol{k} = \langle 0\ 0\ 2/3 \rangle$.

Le supraconducteur antiferromagnétique, UPd_2Al_3

Dans le chapitre 6, les états normaux et supraconducteurs étaient étudiés. Les résultats peuvent être expliqués en utilisant le modèle itinérant pour les électrons $5f$. Un deuxième modèle, dit ≪dual≫, existe dans la littérature. Pour qu'il soit vrai, certains résultats ici doivent être expliqués (l'effet d'un champ magnétique sur les excitations dispersives et la réponse à basse énergies dans l'état supraconducteur). La diffusion notée à $\boldsymbol{Q}^* = (0.5\ 0\ 0.5)$ n'est pas bien comprise, mais il semble qu'il a une origine itinérante.

Please purchase PDF Split-Merge on www.verypdf.com to remove this watermark.

Please purchase PDF Split-Merge on www.verypdf.com to remove this watermark.

Bibliography

[1] Kouvel, J. S. and Kasper, J. *Journal of Physics and Chemistry of Solids* **24**, 529 (1963).

[2] Forgan, E. M., Gibbons, E. P., McEwen, K. A., and Fort, D. *Physical Review B* **62**, 470 (1989).

[3] Shirane, G. *Acta Crystallographica* **12**, 282 (1958).

[4] Burlet, P., Quezel, S., Rossat-Mignod, J., Vogt, O., and Lander, G. *Physica B* **102**, 271 (1980).

[5] Squires, G. L. *Introduction to the Theory of Thermal Neutron Scattering*. Cambridge University Press, (1978).

[6] Lovesey, S. W. *Theory of Neutron Scattering from Condensed Matter*. Clarendon Press, (1984).

[7] Moon, R. M., Riste, T., and Koehler, W. C. *Physical Review* **181**, 920 (1969).

[8] Brown, P. J., Nunez, V., Tasset, F., Forsyth, J. B., and Radhakrishna, P. *Journal of Physics: Condensed Matter* **2**, 9409 (1990).

[9] Blume, M. *Physical Review* **130**, 1670 (1963).

[10] Maleyev, S. V., Bar'yakhtar, V. G., and Suris, R. A. *Sov. Phys. Solid State* **4**, 2533 (1963).

[11] Brown, P. J., Forsyth, J. B., and Tasset, F. *Journal of Physics: Condensed Matter* **10**, 663 (1998).

[12] Regnault, L. P., Tasset, F., Lorenzo, J. E., Roberts, T., Dhalenne, G., and Revcolevschi, A. *Physica B* **267-268**, 227 (1999).

[13] Mezei, F. *Neutron Spin-Echo*. Springer-Verlag (1980).

[14] Jensen, J. and Bak, P. *Physical Review B* **23**, 6180 (1981).

[15] Caciuffo, R., Amoretti, G., Santini, P., Lander, G. H., Kulda, J., and du Plessis, P. V. *Physical Review B* **59**, 13892 (1999).

Please purchase PDF Split-Merge on www.verypdf.com to remove this watermark.

[16] Lander, G. H. and Stirling, W. G. *Physical Review B* **21**, 436 (1980).

[17] Bourdarot, F., Bossy, J., Burlet, P., B. Fak, P. M., Rebizant, J., Regnault, L. P., Spirlet, J. C., and Vogt, O. *Physical Review B* **56**, 14029 (1997).

[18] Schoenes, J. *Journal of Applied Physics* **49**, 1463 (1978).

[19] Amoretti, G., Blaise, A., Caciuffo, R., Fournier, J. M., Hutchings, M. T., Osborn, R., and Taylor, A. D. *Physical Review B* **40**, 1856 (1989).

[20] Faber, J. and Lander, G. H. *Physical Review B* **14**, 1151 (1976).

[21] Jones, W. M., Gordon, J., and Long, E. A. *Journal of Chemical Physics* **20**, 695 (1952).

[22] Henshaw, D. G. and Brockhouse, B. N. *Bulletin of the American Physical Society* **2**, 9 (1957).

[23] Frazer, B. C., Shirane, G., Cox, D. E., and Olsen, C. E. *Physical Review* **140**, A1448 (1965).

[24] Willis, B. T. M. and Taylor, R. I. *Physics Letters* **17**, 188 (1965).

[25] Dolling, G., Cowley, R. A., and Woods, A. D. B. *Canadian Journal of Physics* **43**, 1397 (1965).

[26] Cowley, R. A. and Dolling, G. *Physical Review* **167**, 464 (1968).

[27] Brandt, O. G. and Walker, C. T. *Physical Review Letters* **18**, 11 (1967).

[28] Allen, S. J. *Physical Review* **166**, 530 (1968).

[29] Allen, S. J. *Physical Review* **167**, 492 (1968).

[30] Sasaki, K. and Obata, Y. *Journal of the Physical Society of Japan* **28**, 1157 (1970).

[31] Ippolito, D., Martinelli, L., and Bevilacqua, G. *Physical Review B* **71**, 064419 (2005).

[32] Burlet, P., Rossat-Mignod, J., Quezel, S., Vogt, O., Spirlet, J. C., and Rebizant, J. *Journal of the Less Common Metals* **121**, 121 (1986).

[33] Ikushima, K., Tsutsui, S., Haga, Y., Yasuoka, H., Walstedt, R. E., Masaki, N. M., Nakamura, A., Nasu, S., and Onuki, Y. *Physical Review B* **63**, 104404 (2001).

[34] Wilkins, S. B., Caciuffo, R., Detlefs, C., Rebizant, J., Colineau, E., Wastin, F., and Lander, G. H. *cond-mat/0508394* , submitted to Physical Review Letters (2005).

[35] Giannozzi, P. and Erdös, P. *Journal of Magnetism and Magnetic Materials* **67**, 75 (1987).

Please purchase PDF Split-Merge on www.verypdf.com to remove this watermark.

[36] Giannozzi, P. PhD thesis, Université de Lausanne, (1987).

[37] Hälg, B. and Furrer, A. *Physical Review B* **34**, 6258 (1986).

[38] Osborn, R., Hagen, M., Jones, D. L., Stirling, W. G., Lander, G., Mattenberger, K., and Vogt, O. *Journal of Magnetism and Magnetic Materials* **76-77**, 429 (1988).

[39] Rossat-Mignod, J., Lander, G. H., and Burlet, P. *Handbook on the Physics and Chemistry of the Actinides*, volume 1, chapter 6. (1984).

[40] Kuznietz, M., Burlet, P., Rossat-Mignod, J., and Vogt, O. *Journal of Magnetism and Magnetic Materials* **69**, 12 (1987).

[41] Longfield, M. J., Stirling, W. G., Lidström, E., Mannix, D., Lander, G. H., Stunault, A., McIntyre, G. J., Mattenberger, K., and Vogt, O. *Physical Review B* **63**, 134401 (2001).

[42] Moncton, D. E., Axe, J. D., and diSalvo, F. J. *Physical Review B* **16**, 801 (1977).

[43] Longfield, M. J., Paixao, J. A., Bernhoeft, N., and Lander, G. H. *Physical Review B* **66**, 054417 (2002).

[44] Hannon, J. P., Trammell, G. T., Blume, M., and Gibbs, D. *Physical Review Letters* **61**, 1245 (1988).

[45] Hill, J. P. and McMorrow, D. F. *Acta Crystallographica A* **52**, 236 (1996).

[46] The structural refinement package used was the Cambridge Crystallographic Subroutine Library, available at http://www.ill.fr/dif/ccsl/html/ccsldoc.html.

[47] Lander, G. H. and Bernhoeft, N. *Physica B* **34**, 345 (2004).

[48] Brown, P. J. *Neutron Data Booklet*. Old City Publishing (2003).

[49] Meier, R. J. and Helmholdt, R. B. *Physical Review B* **29**, 1387 (1984).

[50] Freeman, A. J., Desclaux, J. P., Lander, G. H., and Faber, J. *Physical Review B* **13**, 1168 (1976).

[51] Sinha, S. K., Lander, G. H., Shapiro, S. M., and Vogt, O. *Physical Review B* **23**, 4556 (1981).

[52] Lander, G. H., Mueller, M. H., Sparlin, D. M., and Vogt, O. *Physical Review B* **14**, 5035 (1976).

[53] Loewenhaupt, M., Lander, G., Murani, A., and Murasik, A. *Journal of Physics C* **15**, 6199 (1982).

[54] Jourdan, M., Huth, M., and Adrian, H. *Nature* **398**, 47 (1999).

Please purchase PDF Split-Merge on www.verypdf.com to remove this watermark.

[55] Pagliuso, P. G., Petrovic, C., Movshovich, R., Hall, D., Hundley, M. F., Sarrao, J. L., Thompson, J. D., and Fisk, Z. *Physical Review B* **64**, 100503(R) (2001).

[56] Doran, C. and Lasenby, A. J. *Geometric algebra for physicists*. Cambridge University Press, (2003).

[57] Havel, T. F. and Doran, C. Geometric algebra in quantum information processing, quant-ph/0004031.

[58] Hestenes, D. *Space-Time Algebra*. Gordon and Breach, (1966).

[59] Lovesey, S. W. and Balcar, E. *Theory of Magnetic Neutron and Photon Scattering*. Oxford University Press, (1989).

[60] Bernhoeft, N. *Acta Crystallographica A* **55**, 274 (1999).

[61] Bernhoeft, N., Lander, G. H., Longfield, M. J., Langridge, S., Mannix, D., Brown, S. D., Nuttall, W. J., Hiess, A., Vettier, C., and Lejay, P. *Journal of Physics: Condensed Matter* **16**, 3869 (2004).

[62] Blackburn, E., Bernhoeft, N., McIntyre, G. J., Wilkins, S. B., Boulet, P., Ollivier, J., Podlesnyak, A., Juranyi, F., Javorsky, P., Lander, G. H., Mattenberger, K., and Vogt, O. *Philosophical Magazine* (2005).

[63] Bernhoeft, N., Paixao, J. A., Detlefs, C., Wilkins, S. B., Javorsky, P., Blackburn, E., and Lander, G. H. *Physical Review B* **69**, 174415 (2004).

[64] Hiess, A., Boudarot, F., Coad, S., Brown, P. J., Burlet, P., Lander, G. H., Brooks, M. S. S., Kaczorowski, D., Czopnik, A., and Troc, R. *Europhysics Letters* **55**, 267 (2001).

[65] Bethe, H. A. *Annalen der Physik* **3**, 133 (1929).

[66] Knöpfle, K. and Sandratskii, L. M. *Physical Review B* **63**, 014411 (2000).

[67] Timusk, T. *Physics World* **18**(7), 31 (2005).

[68] Eisaki, H., Takagi, H., Cava, R. J., Batlogg, B., Krajewski, J. J., Peck, W. F., Mizuhashi, K., Lee, J. O., and Uchida, S. *Physical Review B* **50**, 647 (1994).

[69] Mathur, N. D., Grosche, F. M., Julian, S. R., Walker, I. R., Freye, D. M., Haselwimmer, R. K. W., and Lonzarich, G. G. *Nature* **394**, 39 (1998).

[70] Saxena, S. S., Agarwal, P., Ahilan, K., Grosche, F. M., Haselwimmer, R. K. W., Steiner, M. J., Pugh, E., Walker, I. R., Julian, S. R., Monthoux, P., Lonzarich, G. G., Huxley, A., Sheikin, I., Braithwaite, D., and Flouquet, J. *Nature* **406**, 587 (2000).

[71] Broholm, C., Kjems, J., Buyers, W., Matthews, P., Palstra, T., Menovsky, A., and Mydosh, J. *Physical Review Letters* **58**, 1467 (1987).

Please purchase PDF Split-Merge on www.verypdf.com to remove this watermark.

[72] Geibel, C., Schank, C., Thies, S., Kitazawa, H., Bredl, C., Boehm, A., Rau, M., Grauel, A., Caspary, R., Helfrich, R., Ahlheim, U., Weber, G., and Steglich, F. *Z. Phys. B* **84**, 1 (1991).

[73] Monthoux, P., Balatsky, A. V., and Pines, D. *Physical Review B* **46**, 14803 (1992).

[74] Cooper, B. R., Elliott, R. J., Nettel, S. J., and Suhl, H. *Physical Review* **127**, 57 (1962).

[75] Sato, N., Aso, N., Miyake, K., Shiina, R., Thalmeier, P., Varelogiannis, G., Geibel, C., Steglich, F., Fulde, P., and Komatsubara, T. *Nature* **410**, 340 (2001).

[76] Thalmeier, P. *Eur. Phys. J. B* **27**, 29 (2002).

[77] Metoki, N., Haga, Y., Koike, Y., Aso, N., and Onuki, Y. *J. Phys. Soc. Jpn.* **66**, 2560 (1997).

[78] Krimmel, A., Fischer, P., Roessli, B., Geibel, C., Steglich, F., and Loidl, A. *J. Magn. Magn. Mater.* **149**, 380 (1995).

[79] Krimmel, A., Fischer, P., Roessli, B., Maletta, H., Geibel, C., Schank, C., Grauel, A., Loidl, A., and Steglich, F. *Z. Phys. B* **86**, 161 (1992).

[80] Paolasini, L., Paixao, J., Lander, G., Delapalme, A., Sato, N., and Komatsubara, T. *J. Phys.: Cond. Mat.* **5**, 8905 (1993).

[81] Kita, H., Dönni, A., Endoh, Y., Kakurai, K., Sato, N., and Komatsubara, T. *J. Phys. Soc. Jpn.* **63**, 726 (1994).

[82] de Visser, A., Nakotte, H., Tai, L., Menovsky, A., Mentink, S., Nieuwenhuys, G., and Mydosh, J. *Physica B* **179**, 84 (1992).

[83] Grauel, A., Böhm, A., Fischer, H., Geibel, C., Köhler, R., Modler, R., Schank, C., Steglich, F., Weber, G., Komatsubara, T., and Sato, N. *Phys. Rev. B* **46**, 5818 (1992).

[84] Gaulin, B., Gibbs, D., Isaacs, E., Lussier, J., Reimers, J., Schröder, A., Taillefer, L., and Zschack, P. *Phys. Rev. Lett.* **73**, 890 (1994).

[85] Hagmusa, I., Klaasse, J., Brück, E., Menovsky, A., and de Boer, F. *Physica B* **246-247**, 1998 (1998).

[86] Dalichaouch, Y., de Andrade, M., and Maple, M. *Phys. Rev. B* **46**, 8671 (1992).

[87] Caspary, R., Hellmann, P., Keller, M., Sparn, G., Wassilew, C., Köhler, R., Geibel, C., Schank, C., Steglich, F., and Phillips, N. *Phys. Rev. Lett.* **71**, 2146 (1993).

[88] Richter, M., Divis, M., Forstreuter, J., Koepernik, K., Steinbeck, L., and Eschrig, H. *Physica B* **230-232**, 519 (1997).

Please purchase PDF Split-Merge on www.verypdf.com to remove this watermark.

[89] Feyerherm, R., Amato, A., Gygax, F., Schenck, A., Geibel, C., Steglich, F., Sato, N., and Komatsubara, T. *Phys. Rev. Lett.* **73**, 1849 (1994).

[90] Takahashi, T., Sato, N., Yokoya, T., Chainani, A., Morimoto, T., and Komatsubara, T. *J. Phys. Soc. Jpn.* **65**, 156 (1995).

[91] Zwicknagl, G., Yaresko, A., and Fulde, P. *Physical Review B* **65**, 081103(R) (2002).

[92] Knöpfle, K., Mavromaras, A., Sandratskii, L., and Kübler, J. *J. Phys.: Cond. Mat.* **8**, 901 (1996).

[93] Inada, Y., Yamagami, H., Haga, Y., Sakurai, K., Tokiwa, Y., Honma, T., Yamamoto, E., Onuki, Y., and Yanagisawa, T. *Journal of the Physical Society of Japan* **68**, 3643 (1999).

[94] Oppeneer, P. and Varelogiannis, G. *Physical Review B* **68**, 214512 (2003).

[95] Zwicknagl, G., Yaresko, A., and Fulde, P. *Physical Review B* **68**, 052508 (2003).

[96] Watanabe, T., Izawa, K., Kasahara, Y., Haga, Y., Onuki, Y., Thalmeier, P., Maki, K., and Matsuda, Y. *Physical Review B* **70**, 184502 (2004).

[97] Petersen, T., Mason, T., Aeppli, G., Ramirez, A., Bucher, E., and Kleiman, R. *Physica B* **199-200**, 151 (1994).

[98] Krimmel, A., Loidl, A., Eccleston, R., Geibel, C., and Steglich, F. *J. Phys.: Cond. Mat.* **8**, 1677 (1996).

[99] Aso, N. PhD thesis, Tohoku University, (1996).

[100] Sato, N., Aso, N., Lander, G., Roessli, B., Komatsubara, T., and Endoh, Y. *J. Phys. Soc. Jpn.* **66**, 1884 (1997).

[101] Sato, N., Aso, N., Lander, G., Roessli, B., Komatsubara, T., and Endoh, Y. *J. Phys. Soc. Jpn.* **66**, 2981 (1997).

[102] Metoki, N., Haga, Y., Koike, Y., and Onuki, Y. *Phys. Rev. Lett.* **80**, 5417 (1998).

[103] Bernhoeft, N., Sato, N., Roessli, B., Aso, N., Hiess, A., Lander, G., Endoh, Y., and Komatsubara, T. *Phys. Rev. Lett.* **81**, 4244 (1998).

[104] Hiess, A., Bernhoeft, N., Metoki, N., Lander, G. H., Roessli, B., Sato, N. K., Aso, N., Haga, Y., Koike, Y., Komatsubara, T., and Onuki, Y. *cond-mat/0411041* (2005).

[105] Becker, K. W., Fulde, P., and Keller, J. *Zeitschrift für Physik B* **28**, 9 (1977).

[106] McHale, P., Fulde, P., and Thalmeier, P. *Physical Review B* **70**, 014513 (2004).

[107] Bernhoeft, N. *Eur. Phys. J. B* **13**, 685 (2000).

Please purchase PDF Split-Merge on www.verypdf.com to remove this watermark.

[108] Terashima, T., Haworth, C., Takashita, M., Aoki, H., Sato, N., and Komatsubara, T. *Phys. Rev. B* **55**, R13369 (1997).

[109] Metoki, N., Koike, Y., Haga, Y., and Onuki, Y. *Physica B* **259-261**, 660 (1999).

[110] Geibel, C., Thies, S., Kaczorowski, D., Mehner, A., Grauel, A., Seidel, B., Ahlheim, U., Helfrich, R., Petersen, K., Bredl, C., and Steglich, F. *Z. Phys. B* **83**, 305 (1991).

[111] Hiess, A., Brown, P., Lelievre-Berna, E., Roessli, B., Bernhoeft, N., Lander, G., Aso, N., and Sato, N. *Phys. Rev. B* **64**, 134413 (2001).

[112] Gaulin, B. D., Mao, M., Wiebe, C. R., Qiu, Y., Shapiro, S. M., Broholm, C., lee, S.-H., and Garrett, J. D. *Physical Review B* **66**, 174520 (2002).

[113] Bernhoeft, N. *J. Phys. Soc. Jpn.* **70A**, 7 (2001).

[114] Hessert, J., Huth, M., Jourdan, M., Adrian, H., Rieck, C. T., and Scharnberg, K. *Physica B* **230-232**, 373 (1997).

[115] Schrieffer, J. R. *Theory of Superconductivity.* Perseus Books Group, (1999).

[116] Amara, M., Morin, P., and Burlet, P. *Physica B* **210**, 157 (1995).

Please purchase PDF Split-Merge on www.verypdf.com to remove this watermark.

Résumé

Dans cette thèse, la coexistence de plusieurs paramètres d'ordre dans le même système électronique est étudiée. Les structures magnétiques, appelées multi-$\boldsymbol{k}$, où plusieurs vecteurs de propagation, $\boldsymbol{k}$, existent dans le même volume, sont considérés comme des systèmes modèles. L'effet de cette structure sur la réponse élastique et inélastique est étudié.

Dans certains composés d'uranium, type NaCl, avec des structures 3-$\boldsymbol{k}$, des pics de Bragg apparaissent à des positions imprévus dans l'espace réciproque. Ces pics sont identifiés avec des corrélations quantiques entre les trois paramètres de l'ordre magnétique. La structure 3-$\boldsymbol{k}$ joue également sur les dynamiques. Les fluctuations dans les ondes de spin dans le composé UO_2 peuvent être expliquées seulement si la structure est 3-$\boldsymbol{k}$, et les paramètres d'ordre sont correlés.

Dans le supraconducteur antiferromagnétique UPd_2Al_3, l'ordre magnétique et l'état supraconducteur sont crée par les mêmes fermions lourds. L'effet d'un champ magnétique externe sur les états normal et supraconducteur est étudié. Dans l'état normal, le matériau agit comme un liquide de Fermi. La réponse inélastique, vue par les neutrons, est renormalisée en entrant l'état supraconducteur. Une étude de la region de basse energie confirme que le gap d'energie supraconducteur possède la symétrie du reseau antiferromagnétique.

Abstract

In this thesis, multiple order parameters originating in the same electronic system are studied. The multi-$\boldsymbol{k}$ magnetic structures, where more than one propagation wavevector, $\boldsymbol{k}$, is observed in the same volume, are considered as prototypical models. The effect of this structure on the elastic and inelastic response is studied. In cubic 3-$\boldsymbol{k}$ uranium rocksalts, unexpected elastic diffraction events were observed at positions in reciprocal space where the structure factor should have been zero. These diffraction peaks are identified with correlations between the (orthogonal) magnetic order parameters. The 3-$\boldsymbol{k}$ structure also affects the observed dynamics; the spin-wave fluctuations in UO_2 as observed by inelastic neutron polarization analysis can only be explained on the basis of a 3-$\boldsymbol{k}$ structure

In the antiferromagnetic superconductor UPd_2Al_3 the magnetic order and the superconducting state coexist, and are apparently generated by the same heavy fermions. The effect of an external magnetic field on both the normal and superconducting states is examined. In the normal state, the compound displays Fermi-liquid-like behaviour. The inelastic neutron response is strongly renormalized on entering the superconducting state, and high-precision measurements of the low-energy transfer part of this response confirm that the superconducting energy gap has the same symmetry as the antiferromagnetic lattice.

Please purchase PDF Split-Merge on www.verypdf.com to remove this watermark.